Optimisation of Arterial Spin Labelling MRI for the assessment of perinatal brain injury

Magdalena Sokolska

University College London

A thesis submitted to University College London

for the degree of Doctor of Philosophy

in Magnetic Resonance Physics

2016

I, Magdalena Sokolska, confirm that the work presented in this thesis is my own. Where information has been derived from other sources, I confirm that this has been indicated in the thesis.

Abstract

Perinatal brain injury is a consequence of insufficient blood and oxygen supply to the brain during labour or delivery and can lead to impaired neurodevelopment or mortality. Hypoxic-ischemia triggers a chain of physiological reactions of the vasculature and measuring cerebral blood flow (CBF) has the potential to improve our knowledge of injury location and progression, as well as to deepen our understanding of the therapeutic processes involved in treatments. Quantitative regional CBF can be measured non-invasively with a magnetic resonance imaging technique called pseudo-continuous ASL (pCASL). However, the use of pCASL for neonatal CBF assessment in research or clinical practice is still uncommon due to several challenges specific to this patient group.

This thesis addressed some of the acquisition and quantification challenges and established a clinically feasible ASL protocol and processing pipeline for neonates with presumed hypoxic-ischemic encephalopathy (HIE). Specifically, a Bloch equation simulator was implemented to estimate the labelling efficiency of pCASL in neonates. The robustness of pCASL efficiency was investigated theoretically using the simulator and in vivo in a group of healthy adult volunteers. A high robustness of the pCASL efficiency against the angulation of the labelling plane was determined. Additionally, a problem of acoustic noise was studied theoretically and a method was proposed which resulted in a 6dB reduction of the acoustic noise. This thesis also developed an image analysis framework for robust motion correction and exclusion of corrupted datasets. The framework enabled the inclusion of all the acquired datasets (compared to seven out of twelve if no motion correction was used). Finally, the proposed developments and imaging framework was applied in a clinical study of neonates with presumed HIE. The new information provided by CBF was investigated separately and in combination with magnetic resonance spectroscopy (MRS), which is used routinely in HIE outcome prediction. In neonates at high risk of adverse outcome, lentiform nuclei and cingulate cortex were found to have elevated CBF values compared to neonates at low risk.

Acknowledgements

I would like to express my sincere gratitude to my primary supervisor Dr David Thomas for the continuous support and guidance throughout my PhD project. I am very grateful to him for his patience, insightful comments and constructive feedback on my thesis. I would like to thank Prof Xavier Golay for his contributions to the project, his advice and sharing his knowledge and experience.

I am very grateful to my collaborators Dr Cristina Uria-Avellanal, Dr Maïa Proisy, Dr Jorge Cardoso and Prof Nikki Robertson, for their support and feedback and all UCLH neonatal imaging team members. Work carried out as part of this thesis could not have been done without their contribution.

I would like to thank my friends and colleagues: Dr Marilena Rega, Dr Patxi Torrealdea, Dr Alvaro Villabona, Dr Claudia Godi, Dr Ruth Oliver, Dr Raj Ramasawmy, Dr Aaron Oliver-Taylor, Dr Alan Bainbridge and Dr Enrico De Vita for their help and support. Special thanks to Ivana Drobnjak for her advice and guidance throughout my time at UCL.

Finally, I would like to thank my family for their constant support and encouragement and the Engineering and Physical Sciences Research Council for providing the funding.

Academic output

M. Sokolska, C. Uria-Avellanal, M.J. Cardoso, M. Proisy, A. Bainbridge, S. Ourselin, D.Thomas, N. Robertson, and X. Golay *"Assessing brain damage after perinatal hypoxic-ischaemia using an automated protocol for combined regional analysis of the Cerebral Blood Flow and MR spectroscopy"*. Proceedings of 23rd ISMRM Meeting 2015

M. Sokolska, X. Golay, and D. Thomas *"Effect of labelling plane angulation on pCASL labelling efficiency - does it really matter? "*. Proceedings of 23rd ISMRM Meeting 2015

C. Godi*, **M. Sokolska***, F. Kennedy, S. Fallatah, X. Golay and R. Jäger *"Quantification of cerebral haemodynamics with QUASAR Arterial Spin Labelling (ASL) in patients with carotid atherosclerotic stenosis"*. Proceedings of 32nd Annual Scientific Meeting ESMRMB 2015

L. Haddow, **M. Sokolska**, S. Fallatah, R. Gilson, R. Jäger, X. Golay *"A study of the effect of early, untreated HIV on cerebral perfusion and arterial transit time in the basal ganglia using arterial spin labelling"*. 15th European AIDS Conference 2015

M. Sokolska, X. Golay, and D. Thomas *"Effect of labelling plane angulation on pCASL labelling efficiency - does it really matter? "*. Proceedings of 32nd Annual Scientific Meeting ESMRMB 2015

R. Ramasawmy, J. A. Wells, J.A. Meakin, **M. Sokolska**, A.E. Campbell-Washburn, S.P. Johnson, R.B. Pedley, M. F. Lythgoe, S. Walker-Samuel *"Pseudo-Continuous Arterial Spin Labelling (pCASL) in a Mouse Liver,"* Proceedings of 23rd ISMRM Meeting 2015

M. Sokolska, M. Proisy, C. Uria-Avellanal, A. Bainbridge, E. Cady, D. Thomas, N. Robertson, and X. Golay *"Combined use of arterial spin labeling and MRS to determine the severity of injury in neonates with hypoxic-ischaemic encephalopathy"*. Proceedings of 22nd ISMRM Meeting 2014

M. Sokolska, D. Thomas, A. Bainbridge, X. Golay, S. Taylor, S. Punwani, D. Pendse *"Renal Perfusion Imaging with Pseudo-continuous Arterial-Spin Labelling (pCASL) at 3.0T: Repeata-*

bility in Healthy volunteers". Proceedings of 22nd ISMRM Meeting 2014

M. Sokolska, D. Thomas, A. Bainbridge, X. Golay, S. Taylor, S. Punwani, D. Pendse *"Renal Pseudo- continuous Arterial Spin Labelling (pCASL) MRI: A Repeatability Study".* ERC 2014

M. Sokolska, X. Golay, D. Thomas *"Perfusion quantification using pseudo-continuous Arterial Spin Labelling: the impact of labelling efficiency estimation"* . Proceedings of 21th ISMRM Meeting 2013

M. Sokolska, A. Oliver-Taylor, X. Golay, D. Thomas *"Theoretical and practical investigation of acoustic noise level reduction in pseudo-continuous Arterial Spin Labeling".* Proceedings of 21th ISMRM Meeting 2013

M. Sokolska, A. Oliver-Taylor, X. Golay, D. Thomas *"Theoretical and practical investigation of acoustic noise level reduction in pseudo-continuous Arterial Spin Labeling".* Proceedings of ISMRM Perfusion Workshop 2012

Contents

List of Figures

List of Tables

List of Abbreviations

ATT	arterial transit time
B_0	external magnetic field
$B_1(t)$	envelope of RF pulse
B_{eff}	effective magnetic field
CBF	cerebral blood flow
CO_2	carbon dioxide
F	total flow through the vessels
FA	flip angle of RF pulse
G	magnetic field gradient
H^+	proton
I	current
J	total angular momentum
M	magnetisation
M_1	first moment of a gradient
M_1	first moment of a gradient
N	torque
NO	nitric oxide
O_2	oxygen
PLD	post labelling delay

PWI	perfusion weighted image
P_0	observed pressure of acoustic waves
RBF	renal blood flow
RF	radiofrequency pulse
S	measured signal
SPL	sound pressure level
TE	echo time
T_1	'spin-lattice' relaxation time
T_2	'spin-spin' relaxation time
T_2^*	apparent 'spin-spin' relaxation time
V	voltage
$VENC$	aliasing velocity in phase contrast imaging
$\Delta\omega$	frequency offset
Δf_{RF}	RF bandwidth
Δt	spacing of RF pulses in pCASL train
Δt_I	isodelay parameter
Ω	rotational angular velocity
Φ	magnetic flux through a loop of wire
α	labelling efficiency
δ_t	duration of RF pulse in pCASL train
δ_{RF}	offset of RF frequency
γ	gyromagnetic ratio
μ	nuclear magnetic moment
ω_0	Larmor frequency
ω_{RF}	carrier frequency of RF pulse

ω_{fr}	angular frequency of a rotating frame
ρ	spectral density function
σ	shielding parameter
τ	labelling duration
τ_{RF}	duration of RF pulse
$\vec{F_L}$	Lorentz force
$\vec{l}$	vector of magnitude equal to the length of wire
ξ	angulation error angle
f	flow
$g(t)$,G	system input function
$h(t)$,H	system transfer function
k_x, k_y	k-space points
$p(t)$,P	system output function
s	artery lumen
v	spin velocity
v_{eff}	effective spin velocity
ACA	anterior cerebral arteries
ASL	arterial spin labelling
ATP	adenosine triphosphate
CCA	common carotid artery
CPP	cerebral perfusion pressure
CPP	cerebrovascular resistance
DGM	deep grey matter
ECA	external carotid artery
EPI	Echo Planar Imaging

ETC	electron transfer chain
FOV	field of view
GA	gestational age
GM	grey matter
HIE	hypoxic-ischemic encepalopathy
ICA	internal carotid artery
MCA	middle cerebral arteries
MIP	maximum intensity projection
MRI	magnetic resonance imaging
MRS	magnetic resonance spectroscopy
NAA	N-acetyl asparate
NADH	nicotinamide adenine dinucleotide
NMR	nuclear magnetic resonance
PCA	posterior cerebral arteries
PLIC	posterior limb of the internal capsule
PNA	postnatal age
ppm	parts per milion
PRESS	Point RESolved Spectroscopy
SD	standard deviation
SNR	signal-to-noise ratio
SSD	summed square of differences
STEAM	STimulated Echo Acquisition Mode
TCA	trans-carboxylic acid cycle
WM	white matter

Chapter 1

Introduction

1.1 Motivation

Perinatal brain injury can result from insufficient delivery of oxygen (hypoxia) or blood (ischemia) to the brain during labor and/or delivery. A lack of oxygen or glucose delivered with blood results in molecular cell injury, which in turn causes cell death. Hypoxic-ischemia triggers a chain of physiological reactions of the vasculature in order to preserve sufficient blood flow to the brain, such as luxury perfusion, delayed post-ischemic hypoperfusion and abolished autoregulation. Different parts of the brain are susceptible to hypoxic-ischemic injury to a different extent; the most commonly affected are regions of the highest metabolic demand, such as basal ganglia and cortex. The degree of damage also depends on the nature and duration of hypoxic-ischemic event.

The best treatment available to date, that improves the outcome of neonates after hypoxic-ischemia, is therapeutic cooling. However, it does not provide neuroprotection in all cases. There is therefore a high demand for an effective treatment that would help prevent the brain damage from developing. Having a sensitive biomarker of injury could speed up clinical trials as well as aid prognosis of the outcome given to parents.

Measuring cerebral blood flow (CBF) has a potential to improve our knowledge of injury progression as well as deepen the understanding of the therapeutic processes involved in treatments. One magnetic resonance imaging technique, called arterial spin labelling (ASL), is capable of providing quantitative CBF maps non-invasively and without the need for exogenous contrast agents. It is therefore a good candidate to become a neonatal imaging biomarker.

The use of ASL for neonatal CBF assessment in research or clinical practice is still uncom-

mon due to several challenges specific to this patient group. One of these challenges is the much lower CBF values in neonates than that of healthy adults, which results in much lower signal-to-noise (SNR) of ASL. Recently proposed pseudo-continuous ASL (pCASL) provides higher SNR compared to previously used pulsed techniques. However, labelling efficiency of pCASL depends on the velocity of protons flowing through the labelling plane, which is different in neonates compared to that of healthy adults. Another challenge of using pCASL is acoustic noise produced by the scanner during the labelling period. A further challenge in neonatal ASL imaging is motion during the scan which might corrupt the scans. Elimination of motion is crucial, as motion artefacts can lead to misinterpretation of results or reduce the success rate of the technique.

This thesis develops a methodological framework that will address all these challenges and optimise the process of pCASL for neonatal imaging.

1.2 Scope and Objectives

The aim of this thesis is to establish a clinically feasible ASL protocol and processing pipeline for neonates with presumed hypoxy-ischemic encephalopathy (HIE) and investigate the new information provided by CBF in combination with magnetic resonance spectroscopy (MRS). Specific objectives are:

1. To find the appropriate labelling efficiency for neonates
2. To reduce the amount of acoustic noise
3. To reduce the effects of motion
4. To optimise the framework for neonates
5. To apply the framework to the study of neonates with presumed hypoxy-ischaemic encepahlopathy
6. To investigate new information provided by CBF in combination with magnetic resonance spectroscopy (MRS).

This thesis implements a Bloch equation simulator and estimates labelling efficiency for a range of measured velocities in arteries supplying the neonatal brain. Additionally, other factors influencing labelling efficiency, specifically angulation of labelling plane are considered. The

robustness of the pCASL efficiency is investigated theoretically using the simulator and in vivo in a group of healthy adult volunteers. The problem of acoustic noise is studied theoretically and a method, leading to the reduction of the acoustic noise is proposed. This thesis also develops an image analysis framework for robust motion correction and exclusion of corrupted datasets. Finally, the proposed developments and imaging framework is applied in the study of neonates with presumed hypoxy-ischemic encephalopathy and investigates the new information provided by CBF in combination with magnetic resonance spectroscopy (MRS), which is used routinely in HIE outcome prediction.

1.3 Thesis outline

The material in this thesis is organised as follows:

Chapter 2: Neonatal encephalopathy: from pathophysiology to imaging gives a background of a healthy brain physiology and physiological changes following hypoxia-ischemia in the neonatal brain.

Chapter 3: Introduction to magnetic resonance imaging and spectroscopy provides the basic theory of magnetic resonance imaging and spectroscopy.

Chapter 4: Introduction to neonatal perfusion quantification with arterial spin labelling introduces the concept of arterial spin labelling. It describes models that allow perfusion quantification and discusses sources of potential quantification errors in adults and in neonates.

Chapter 5: pCASL simulator for labelling efficiency estimation contains the theory of pseudo-continuous labelling and describes an implementation of a simulator which enables the estimation of labelling efficiency in neonates based on measured velocities of blood in vessels supplying the brain.

Chapter 6: Practical aspects of pCASL focuses on the practical aspect of the pCASL and provides solutions to address existing drawbacks such as acoustic noise and incorrect planning, which apply especially when scanning neonates. An effective method of acoustic noise reduction is given and the dependence of planning on labelling efficiency is investigated.

Chapter 7: Development of in vivo imaging framework for neonatal pCASL describes optimisation of the scanning protocol and development of an effective method for motion correction, resulting in a reduction of rejected datasets due to motion.

Chapter 8: Clinical application of pCASL in neonates with hypoxic-ischaemic encephalopathy presents a detailed regional analysis of CBF maps acquired in neonates who experienced a perinatal hypoxic-ischaemic event. This is additionally combined with brain MRS data to link the physiological and biochemical changes after hypoxia-ischaemia in the neonatal brain.

Chapter 9: Summary and future work summarises the work presented in this thesis and proposes future developments.

Appendix A: Renal pCASL: reproducibility study presents an application of pCASL quantification of renal blood flow. Although this work is not directly motivated by investigation of neonatal HIE at this stage, it benefits form the knowledge and experience gained during the development of the neonatal imaging framework described in chapter 7.

Chapter 2

Neonatal encephalopathy: from pathophysiology to imaging

2.1 Introduction

In this chapter a background of a healthy brain physiology and physiological changes following insufficient blood or oxygen delivery to developing brain tissue will be reviewed. This will be followed by description of the consequences of hypoxia-ischemia on the cellular level and its presentation in clinical imaging.

2.2 Normal brain physiology

Viability of the brain tissue depends on the delivery of glucose and oxygen, and clearance of the products of metabolism. High metabolic demand of the working brain means that it requires a continuous supply of glucose and oxygen (O_2) and, at the same time, clearance of carbon dioxide (CO_2) and other products of metabolism. This is provided by perfusion, which is the process of delivery of the nutrients to a capillary bed in the tissue, with cerebral blood flow (CBF) defined as the rate of that delivery to a tissue volume. The high level of metabolism in the case of brain is due to its primary role: the generation of electrical activity, which is required for neuronal signalling. Since there is no reserve store of O_2 and glucose, the continuous flow of blood is crucial to guarantee continuity of brain function.

CBF **reflects metabolic demand.** The higher the metabolism, the higher need for nutrients and therefore the higher CBF. This coupling between metabolism and CBF is reflected in the

heterogenous distribution of blood flow within the brain, with the majority of the flow received by grey matter (consisting mainly of the neuronal cell bodies), whereas white matter (consisting mainly of the myelinated axons) has much lower metabolic demand and therefore lower CBF. Within grey matter, delivery of fully oxygenated blood can change in response to stimulation, as observed with functional brain imaging studies.

In healthy neonates, the metabolic demand and therefore CBF is very low [16],[17]. This rapidly changes within the first days, weeks and years of life, during the time of the fastest development, and peaks at approximately 4-10 years of age, with CBF exceeding that of adults by 70% or more during this period [18], [19].

Brain is supplied by dense network of vessels. The high demand for blood flow to the brain is supported by the brain vasculature. Figure 2.1 shows a maximum intensity projection angiogram, showing the main vessels delivering blood to the brain. The biggest arteries - the common carotid arteries (CCAs) - derive from the aortic arch (left) and brachiocephalic artery (right) and split into the internal and external carotid arteries (ICA and ECA respectively) at the carotid bifurcation. The vertebral arteries originate from subclavian arteries, and combine together to form the basilar artery. The ICAs and vertebral system connect into the Circle of Willis (2.1 C) - a communicating pathway, that provides redistribution of the blood supply in case of vascular occlusion. The Circle of Willis is composed of anterior cerebral arteries (ACAs), and middle cerebral arteries (MCAs) which are derived from ICAs and connected by the anterior communicating artery, and posterior cerebral arteries (PCA), derived from the basilar artery, connected to MCAs by the posterior communicating arteries.

The arterial cerebral circulation can be divided into perforating and leptomeningeal arteries [20]:

- Perforating arteries arise from the Circle of Willis or from its immediate branches, and run perpendicularly to them. Perforating arteries penetrate brain parenchyma supplying blood to the basal ganglia, thalamus and deep white matter. Similar branches stemming from the basilar artery supply the brain stem.

- Leptomeningeal arteries consist of terminating branches of ACA, MCA and PCA. They travel across or in the depth of cortical sulci supplying blood to the cortex and subjacent white matter. An anastomotic (reconnecting) network created from the confluence of these terminating branches forms watershed zones, which protect the blood delivery to

the cortex in case of occlusion of the ACA, MCA or PC. Watershed zones are illustrated in figure 2.2.

Brain regions supplied by these arteries and their branches are presented in figure 2.3.

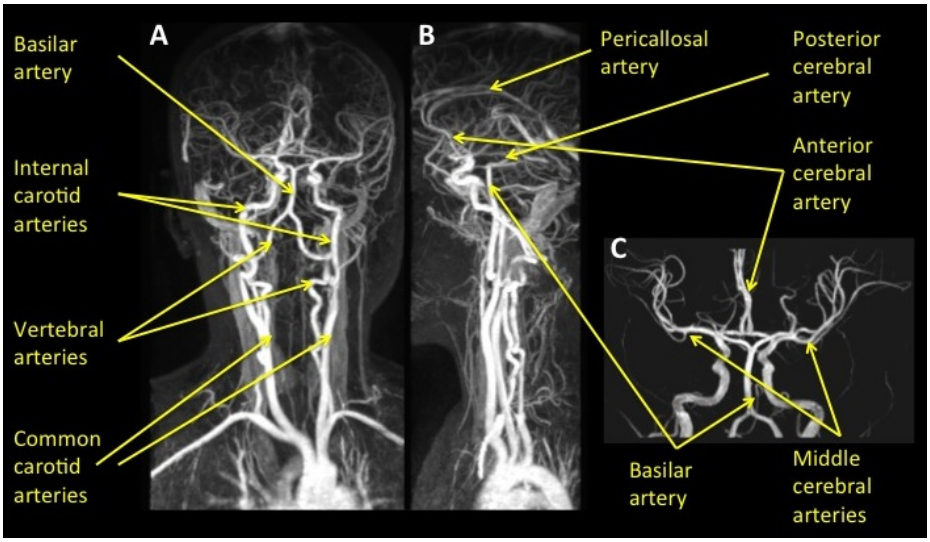

Figure 2.1: *Maximum intensity projection (MIP) angiography: coronal (A), saggital (B), Circle of Willis (C)* [1]

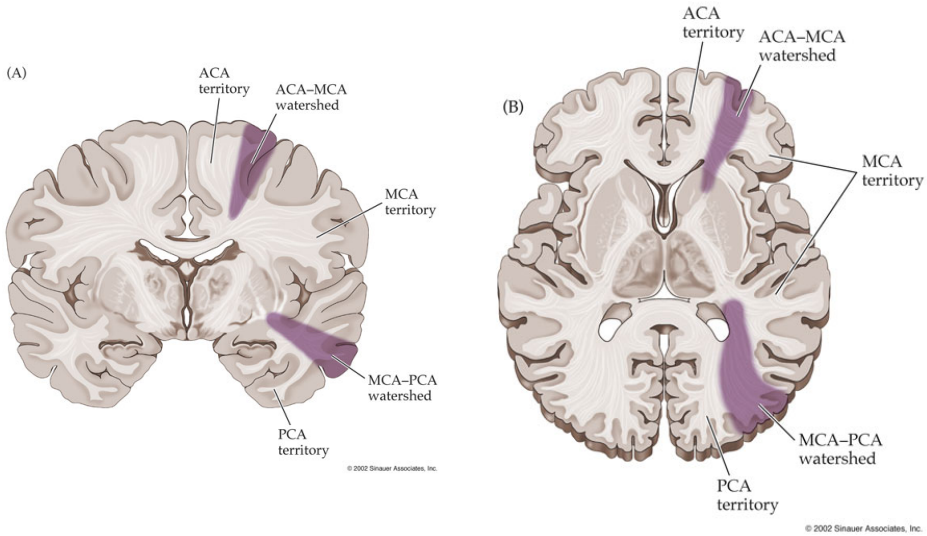

Figure 2.2: *Watershed zones (purple) as seen in the coronal (left) and transverse (right) orientations* [2]

[1] http://radiopaedia.org/images/545665

[2] http://missinglink.ucsf.edu/lm/ids_104_cns_injury/response%20_to_injury/watershed.htm

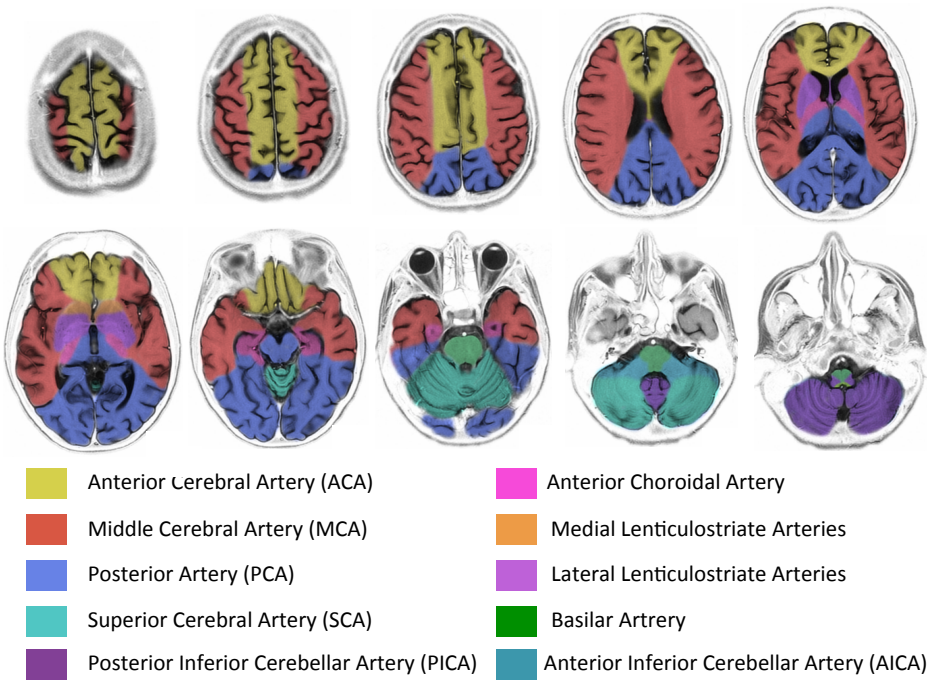

Figure 2.3: *Vascular territories of the major cerebral arteries*[3]

CBF is controlled by pressure and resistance. CBF depends on the net pressure gradient driving the blood through the vascular tree, the cerebral perfusion pressure (CPP, [Pa]), and the resistance that must be overcome along the way, the cerebrovascular resistance (CVR, [MPa $\cdot$ s $\cdot$ m^{-3}]). This relationship can be described by the following equation:

$$CBF = \frac{CPP}{CVR} \tag{2.1}$$

CVR is determined by arteriolar and capillary tone. The arteriolar smooth muscle controls CVR by relaxing (dilation, $CVR \downarrow$) and contracting ($CVR \uparrow$). The state of moderate contraction - muscular tone - ensures appropriate resistance for a given blood flow demand.

Arterial smooth muscles can be affected by a large number of factors. Some of the most common factors, their workings and influence on CBF are summarised in the table 2.1. A more detailed description of the cerebral blood flow regulation can be found in [21].

[3] http://radiopaedia.org/articles/cerebral-vascular-territories

Agent	Function	Effect on CVR	Mechanism	Effect on CBF
Arterial oxygen content C_aO_2 [22]	Substrate of oxidative glucose metabolism	Vasodilatation or vasoconstriction	Low levels trigger increase of CBF	$CBF \uparrow\downarrow$
Glucose	Substrate of energy metabolism in a cell		Low levels trigger increase of CBF	$CBF \uparrow$
CO_2 and H^+ [22], [23]	Product of oxidative glucose metabolism	Vasodilatation	Change of the pH at the arterial smooth muscle	$CBF \uparrow$
K^+ [22],[23]	Involved in neuronal signalling	Vasodilatation	Relaxes the muscle of arterioles	$CBF \uparrow$
Adenosine [22], [23]	Involved in energy metabolism and neural activity	Vasodilatation	Binds to the receptors and inhibits the activity release	$CBF \uparrow$
Nitric oxide NO [23]	Produced locally following glutamate receptor activity; produced by inflammatory cells	Vasodilatation, maintenance of vascular tone	Produces intracellular second messenger	$CBF \uparrow$
Arachidonic acid and its derivatives [23]	Involved in inflammation, fever and pain	Vasodilatation or vasoconstriction	Complex via hormones and enzymes	$CBF \uparrow\downarrow$
Sympathetic pathway [23]	Neural pathway	Vasoconstriction	Via transmitters	$CBF \downarrow$
Parasympathetic pathway [23]	Neural pathway	Vasodilatation	Via transmitters	$CBF \uparrow$

Table 2.1: *Summary of different mechanisms controlling CBF*

Autoregulation sustains constant CBF. Figure 2.4 shows the relationship between CBF and CPP together with vessel diameter. Constant CBF values can be sustained within a broad range of CPP by appropriate vasculature response: this is known as autoregulation. An increase in blood pressure triggers vessel constriction and therefore increase of cerebrovascular resistance, up to the point where any further constriction is impossible. Additional CPP increase may cause passive dilatation, resulting in linear increase of CBF with CPP and produces vasogenic edema [1],[4]. Similarly, if the CPP decreases beyond the limits of physiological vasodilatation, any further decrease in resistance is impossible and CBF decreases linearly with CPP, leading to ischemia. This passive link between CBF and CPP is called vasoparalysis.

Figure 2.4: *Cerebral Blood Flow in relation to Blood Pressure and artery lumen diameter. Dotted lines represent the lower and upper limits of CBF auto regulation. Red circles represent cerebral arteries (figure 2 from [1])*

Two ischemic CBF thresholds have been identified [24] and quantified using positron emission tomography (PET) in adults with cerebral ischema [25]. The first is a flow threshold of electrical failure in the cerebral cortex ($\sim$)20 ml/100g/min. The second one, is a threshold for cell membrane failure and cell death ($\sim$)15 ml/100g/min [25]. The condition of the ischemic brain with flow between the two thresholds is called penumbra [26] and is correlated with reversible neurological deficits [25]. It has been suggested, that the area of penumbra can be identified by imaging from the diffusion-perfusion mismatch area, i.e. the mismatch in the abnormality volume between diffusion and perfusion weighted MRI [27]. When the autoregulatory range is exhausted, the blood flow declines first in the most peripheral branches of the brain arteries (watershed zones).

Pre-term and neonatal autoregulation plateau is narrower compared to adults. Based on data acquired in neonatal lamb it was concluded that the autoregulation plateau is already present in the lamb foetus, but covers a narrower blood pressure range than in more mature animals, at the upper limit in particular [28]. Additionally, the mean arterial blood pressure is only slightly higher than the lower limits of autoregulation, meaning that the buffer provided by autoregulation is much smaller compared to adults. This indicates that the risk of ischemic injury is increased with minor hypotension, particularly within the watershed regions. In human neonates, this lower threshold has not been identified; CBF values associated with cell membrane failure in adults have been associated with subsequent normal outcome [3].

Glucose metabolism provides energy for neural activity. Metabolism of glucose and O_2 can be divided into four steps, illustrated in figure 2.5:

1. Glycolysis. In the first instance, glucose is taken up from the blood and undergoes glycolysis, in which the glucose is broken down into two pyruvate molecules. The free energy released in this process is used to form high-energy compounds: adenosine triphosphate (ATP) and reduced nicotinamide adenine dinucleotide ($NADH$). For each glucose molecule undergoing glycolysis two ATP and two $NADH$ are formed. Most of the pyruvate is transported into the mitochondria, where it is further metabolised by means of the Krebs Cycle. When the rate of pyruvate production by glycolysis is higher than that of pyruvate and O_2 metabolism, pyruvate is converted to lactate (reversibly), which then diffuses out of the cell and is carried away in the blood.

2. Krebs Cycle. The Krebs Cycle (or trans-carboxylic acid (TCA) cycle) is a complex chemical reaction pathway, in which pyruvate, a product of glycolysis, is further broken down to form CO_2 with the storage of energy in the form of $NADH$.

3. Electron transfer chain (ETC). In this step the electrons are transferred from $NADH$ to O_2 to form water and protons (H^+) are transferred across an inner mitochondrial membrane. The transfer of H^+ is against the electrochemical gradient and therefore storing the energy in H^+ gradient.

4. ATP synthesis. The ATP synthesis is driven by the proton gradient resulted from ETC.

The overall process of glucose metabolism can be written as:

$$Glucose + 6O_2 \rightarrow 6CO_2 + 6H_2O + 38ATP$$

where 2 ATP compounds are gained from step 1 and 36 from steps 2-4. ATP is used by the cells to maintain their activity, by sustaining the chemical (neurotransmitters) and ionic gradients.

A more complex picture of glucose metabolism and a key role of neuron-astrocyte metabolic interactions, can be found in [29].

2.3 Vascular pathophysiology during hypoxia - ischemia

Insufficient supply of oxygen (hypoxia) within the uterus following acute reduction of the uterine or umbilical circulation (ischemia) triggers a physiological reaction of the vasculature, which can be divided into two phases: during and after hypoxia-ischemia.

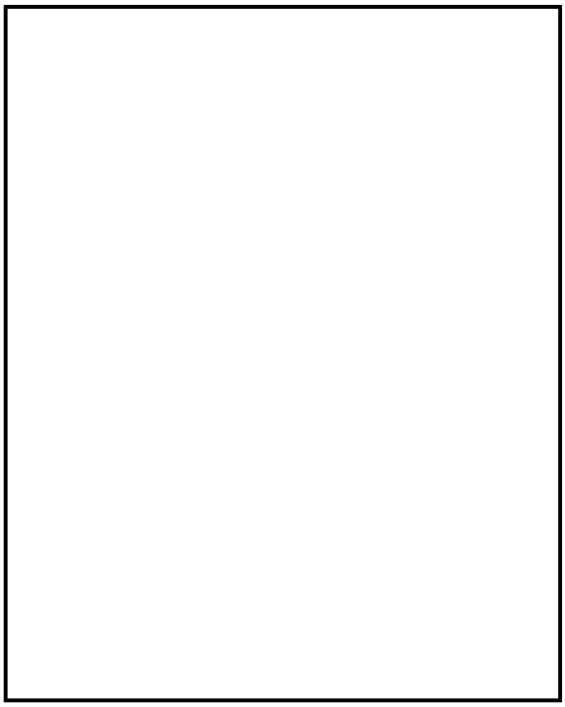

Figure 2.5: *Major steps of energy metabolism: glycolysis (cystol), Krebs cycle, electron transfer chain and ATP synthesis (mitochondria) (figure 1.5 from [2])*

2.3.1 Brain vasculature physiology under hypoxia - ischemia

Activation of sympathetic - adrenergic system. The sympathetic - adrenergic system activation redistributes the cardiac output to preserve blood flow in favour of the central organs: brain, heart and adrenal gland, at the expense of flow to the less vital organs (i.e. kidneys, intestine, muscle) [3]. Increased CO_2 and decreased O_2 partial pressure lead to vasodilation of the cerebrovascular bed causing hyperperfusion, according to table 2.1. Increase of CBF by vasodilatation is least effective in the white matter. Persisting deficit of oxygen drains the anaerobic energy reserves, which in turn reduces the cardiac output and blood pressure. If blood pressure falls below the lower level of autoregulation, a decrease in CBF is observed [3]. This CBF decrease mostly affects parasagittal watershed region of cerebrum and the white matter. A summary of cardiovascular reaction to asphyxia (severe deficit of oxygen supply to the body) is shown is figure 2.6.

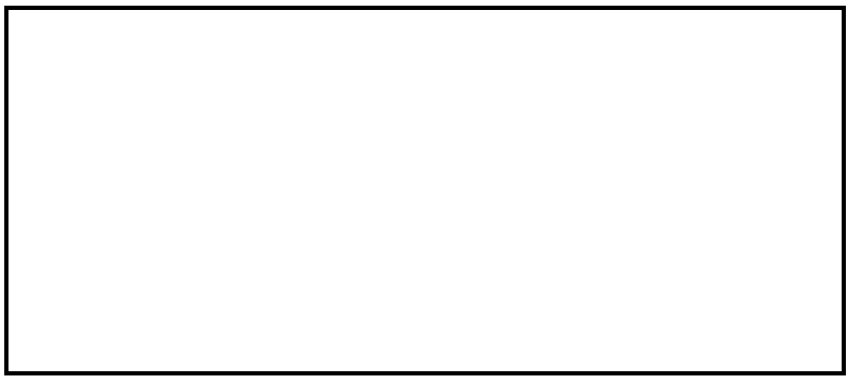

Figure 2.6: *Schematic representation of the cardiovascular response to asphyxia (figure 1 from [3]).*

2.3.2 Brain recovery from hypoxia - ischemia

Early post-ischemic deficit. The 'no-reflow' phenomenon is a failure of re-perfusion early after a period of cerebrovasculatory arrest and results from mechanical obstruction of the microcirculation by post-ischemic edema, observed in animal models [4]. The brain tissue volume of the no-reflow depends on the length and severity of ischemia: the longer and more severe ischemia, the greater the no-reflow volume. In case of complete ischemia, no-reflow is prominent after only 7 minutes of occlusion; this time extends to 3-7 hours for incomplete ischemia.

Luxury perfusion syndrome. Luxury perfusion syndrome (hyperaemia) is characterised by increased CBF relative to the metabolic needs of the brain. It lasts longer than would be needed to reoxygenate the brain (1-2 hours in dogs), indicating that the syndrome is most likely initiated by abnormal metabolism i.e. acute metabolic acidosis caused by accumulated lactate and CO_2 [30], as well as complete loss of tone in vessels [17] (see figure 2.7).

Figure 2.7: *Luxury perfusion and postischemic hypo perfusion of gerbil brain after 10 min bilateral carotid artery occlusion (figure 2 from [4])*

This phenomenon was also observed in asphyxiated term infants using Doppler ultrasonog-

raphy [5] (see figure 2.8). Here, however, the increased blood velocities indicating high CBF were observed from 12 hours after birth and increased over the course of the period of measurement in the neonates with the most severe hypoxic-ischemic encepalopathy (HIE) (see table 2.2 for details of HIE grading).

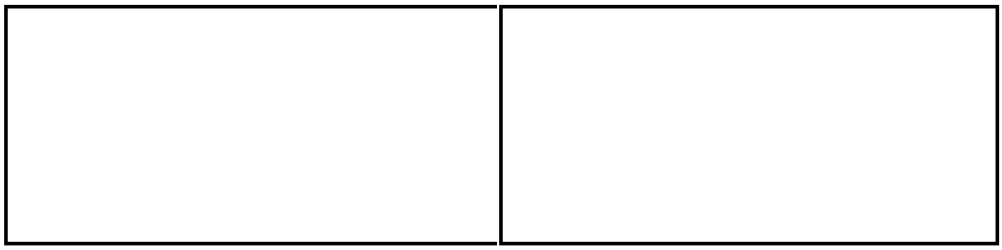

Figure 2.8: *Mean cerebral blood flow velocity in anterior (left) and middle (right) cerebral arteries in asphyxiated infants with different development of perineonatal hypoxic-ischemic encepalopathy and controls showing significant increase in measured velocities for most severe cases of HIE (figures 1 and 2 from [5])*

Delayed post-ischemic hypo-perfusion. Postischemic hypo-perfusion syndrome is a functional disturbance that develops due to increased arterio-artreriolar vascular tone. In the absence of no-reflow, it follows directly the luxury perfusion phase (see figure 2.7). It develops after about 5 min of ischemia (focal, complete or incomplete) and does not depend on the ischemia duration. At this time, the auto regulation, but not CO_2 reactivity begins to recover, and CBF stabilises at subnormal level [4],[31].

Abolished autoregulation and CO_2 reactivity. Abolished autoregulation and CO_2 reactivity is manifested by the pressure passive CBF and implies that CBF does not adjust to changes in cerebral metabolic demand. The lack of auto regulation i.e. no vascular response stimulated by hypercapnia or hypoxia, can be presumed to relate to the fact that the maximal vasodilatation has already developed as a result of asphyxia. Therefore further vasodilatation is impossible, regardless of the decrease in blood pressure. Abolished auto regulation has been observed in asphyxiated fetal sheep [32] and distressed newborn infants [33]. In neonates with extensive hypoxic-ischemic brain damage and isoelectric electroencephalogram (EEG), abolished CO_2 reactivity accompanying vasoparalysis was detected. In infants with signs of brain damage and burst suppression EEG, the pressure-flow autoregulation was abolished, whereas CO_2 reactivity was preserved. In the neonates with pressure-passive CBF, the average CBF was additionally increased (proportionately to the brain damage) compared to controls or mildly affected infants [17],[34].

2.4 Cellular injury

Lack of glucose and oxygen cause molecular cell injury. Neuronal cell death happens in two phases following a reversible global insult.

Primary cell death is related to a lack of O_2, which leads to disturbance in high energy oxidative glucose metabolism ('primary energy failure') and chemical imbalance and terminal depolarisation of the cell. As a result, the cell osmolality rises, causing a shift of water from the extracellular into the intracellular compartment [35]. The detailed description of this process can be found in [36]. This injury is established within a few minutes after the onset of hypoxia. However, primary cell death triggers a cascade of pathologic processes, but on its own doesn't contribute to large number of neuronal deaths.

Secondary/delayed cell death becomes apparent from about 1-100 hours after the injury. The mechanisms contributing include: excitotoxicity (damage and death of neurones by excessive stimulation by neurotransmitters, primarily glutamate) and apoptosis (programmed cell death). It is associated with hyperaemia, increased seizure activity cytoxic oedema, NO synthesis, accumulation of excitotoxins and mitochondrial failure. Mitochondrial failure is a key step leading to delayed cell death.

It has been demonstrated using a piglet model with continuous phosphorous-31 MRS monitoring [37], that the pattern of energy failure during and after hypoxic ischemia comes in two phases. Following an acute energy depletion in which some cells undergo primary cell death, the latent phase begins. This phase is characterised by the apparent recovery of oxidative metabolism. The second phase known as secondary energy failure, in which oxidative metabolism deteriorates leading to the secondary or programmed cell death. The latent phase, or the phase of pseudo-normalisation, is considered to be a "therapeutic window" for treatments, such as brain cooling.

2.5 Factors influencing the type and location of neural damage: animal models

The reaction of the brain under hypoxic-ischaemic conditions depends on the severity, pattern and type of the insult, as well as neonate's gestational age. [36]. As the origin of brain damage

in neonates is un-controllable and often unknown, the majority of the research on hypoxia-iscahemia and its impact on the brain has been carried out using animal models.

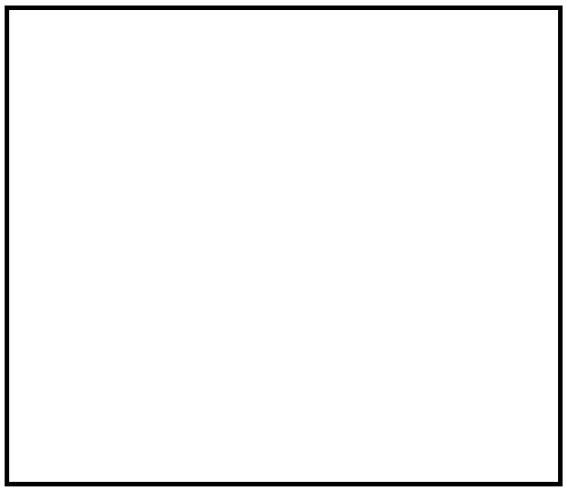

Figure 2.9: *Neuronal damage in nine brain regions of neonatal sheep following increasing durations of ischemia. These are ranked in order of total damage scores: The parasagittal cortex was the most severely damaged (bottom), whereas the thalamus (top) showed the least damage. The damage scores are on a linearised scale. 0 to 100:0, no neuronal lo.is; 100. total necrosis (figure 2 from [6])*

Duration of ischemia. Depending on the duration of ischemia, cell damage happens in different brain regions with different extent. This is illustrated in figure 2.9, which shows neuronal damage in nine brain regions of the developing sheep brain after *partial* ischemia, whereas *acute near-total* hypoxic ischemia of 10 minutes duration to the umbilical blood flow in lamb fetus produces damage to the nuclei of basal ganglia and the thalami [6].

Gestational age. If the baby is premature, it is more likely that the neurological disturbance will involve white matter (see section 2.7).

Temporal sequencing. Temporal sequencing appears to affect both the severity and the regional nature of the injury. Three repeated episodes of 10 min of ischeamia, repeated at 1h and 5h intervals, resulted in neuronal damage in striatum, but less in the cortex [38].

2.6 Clinical HIE grading

HIE grading system helps to diagnose, assess and aid prognosis of neonates after perinatal insult. It uses clinical observation like level of consciousness, muscle tone and complex reflexes

to assign one of the stages: mild (I), moderate (II) and severe (III). HIE stages are closely related to the outcome. The first grading system was proposed by Sarnat and Sarnat [13] (given in table 2.2).

	Mild HIE (I)	Moderate HIE (II)	Severe HIE (III)
Level of consciousness	Hyperalert	Lethargic	Flaccid
Muscle tone	Normal	Mild hypotonia	Severe hypotonia
Complex reflexes:			
Suck	Normal/Weak	Weak/Absent	Absent
Moro	Strong	Weak/Incomplete	Absent
Seizures	Absent	Common	Frequent/difficult to control

Table 2.2: *HIE grading according to Sarnat and Sarnat [13]*

2.7 Neonatal neuropathology

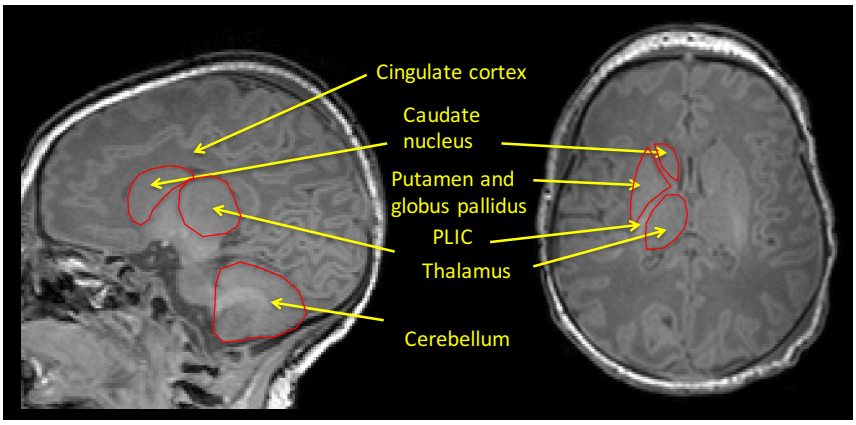

Figure 2.10: *T_1 weighted image of a typical neonate showing anatomies most often affected by hypxix-ischemia*

According to Inder *et al.* [36] the neuropathology of hypoxic-ischaemic encephalopathy in term neonates can be divided into 3 categories:

1. Selective neuronal necrosis. This is the most common neural injury in term infants resulting from HI. The brain regions injured the most often are: CA1 region of hippocampus, deeper layers of the cerebral cortex, putamen and thalamus.

2. Parasagittal cerebral injury is an injury of the cerebral cortex and subcortical white matter

in parasagittal and supermedial aspects of the cerebral convexities (i.e. the aspect of the cerebral hemisphere that lies in contact with the flat bones of the skull). The most prominent areas of neuronal necrosis are watershed regions of the cerebral cortex (border zones between the major cerebral arteries) and in the depths of sulci.

3. Basal ganglia and thalamic lesions. The basal ganglia consists of the lentiform nucleus (consisting of the globus pallidus and the putamen) and the caudate nucleus (as shown at the image 2.10). Together with the thalamus, they are extremely vulnerable to damage following acute near-total hypoxic ischemia. Often, the peri-Rolandic cortex is affected at the same time. In extreme cases, the damage to deep grey matter is termed 'Status Marmoratus'. Status Marmoratus initially involves basal ganglia and thalamus and is characterised initially by neuronal loss, gliosis and hypermyelination. This is apparent from about 8 months of age and characterised by marbled appearance of the basal ganglia. It is observed in only 5% of children with HI brain lesions [39].

Additionally, the most common lesions found in pre-term neonates are [36]:

1. Periventricular leucomalacia, which is a necrosis of white matter in a characteristic distribution, i.e. near the lateral ventricles.

2. Periventricular haemorrhage. Perilventricular haemorrhagic infarction is a haemorrhagic necrosis of periventricular white matter that is usually large and asymmetric.

3. Germinal matrix haemorrhage.

2.8 MR imaging findings and its relation to the neurodevelopmental outcome

MR imaging has been widely used for early evaluation of perineonatal hypoxic-ischemic encepalopathy. The most commonly used techniques are T_1, T_2 and diffusion weighted imaging. MRI allows determination of the type and severity of the insult and guides outcome prognosis. The most common imaging findings include brain swelling, abnormal signal/lesions in the basal ganglia and thalami, abnormal signal intensity in the posterior limb of the internal capsule (PLIC) and cortex, loss of gray/white matter differentiation [7]. Examples of abnormal images are shown in figures 2.11 to 2.14. The loss of normal signal intensity within PLIC is caused by edema or infarction and is associated with abnormal neurodevelopment outcome. Abnormal

signal in deep grey matter is linked to cerebral palsy, memory defects and feeding difficulties. The outcome depends on the severity and exact location of the damage [7]. Loss of gray/white matter differentiation can result from cytotoxic edema, with the outcome depending on the extent and location of the damage. Cortical involvement defined as abnormal highlighting on T_1 weighted images may represent ischemia and is usually accompanied by other lesions within the brain.

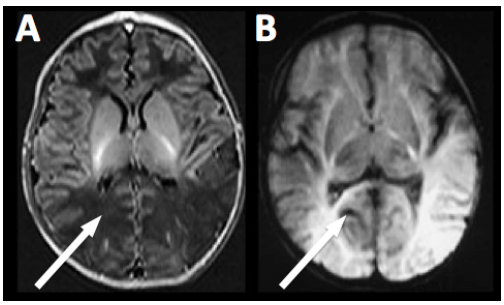

Figure 2.11: *T_1 (A) and T_2 (B) weighted images showing loss of gray/white matter differentiation in the posterior parietal and occipital lobes[4].*

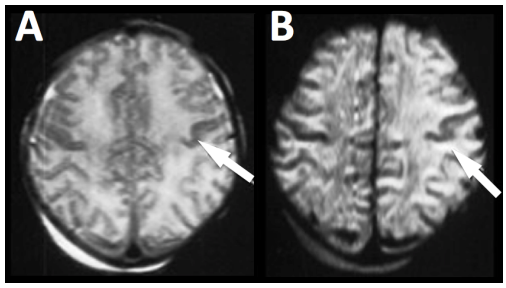

Figure 2.12: *T_2 (A) and diffusion weighted (B) images showing cortical and subcortical white matter abnormalities[4].*

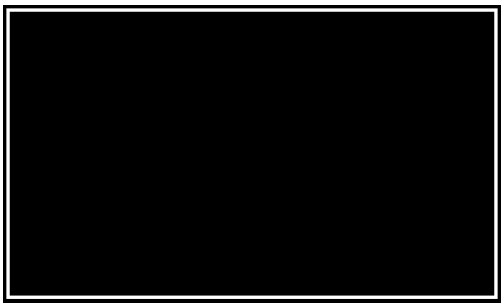

Figure 2.13: *T_1- weighted images showing posterior limb of the internal capsule. A - normal signal intensity (arrow) from myelin. B - loss of normal high intensity signal (arrow) in severe HIE. Also, there is abnormal high signal intensities in the thalamus and lentiform nuclei either side of the PLIC (figures 1a and 4c from [7])*

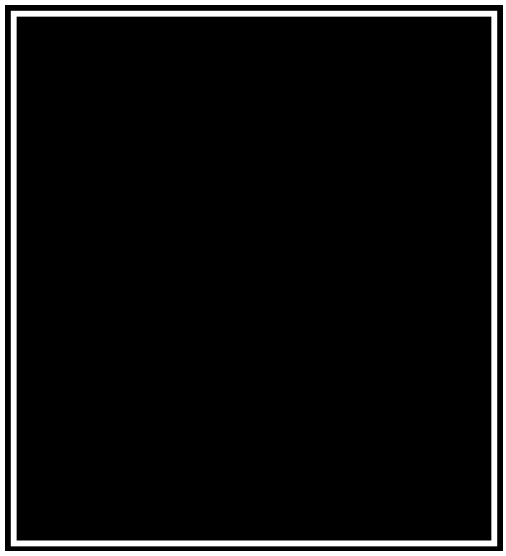

Figure 2.14: *MRI pattern suggestive of acute near total asphyxia. A - T_1-weighted image does not show a normal signal within the posterior limb of the internal capsule, but areas of increased signal intensity within thalami and basal ganglia. DWI (B-D) shows restricted diffusion in the ventrolateral thalami, lentiform nuclei, cerebral peduncles, and in the perirolandic cortex. Also note involvement of the hippocampi (figure 2 from [8])*

[4] http://www.mrineonatalbrain.com/

A summary of the above information of the injury type, affected brain region and the outcome is provided in table 2.3.

Time course		Typical site of brain injury	Disability
Acute, near-total	Moderate	Basal ganglia and thalami	Athetoid or dystonic CP, intact or mildly impaired cognitive development
	Severe or prolonged	Cerebral cortex added to basal ganglia and thalami	Severe, spastic quadriplegia, cortical visual impairment, microcephaly, cognitive deficit
Prolonged, partial	Moderate	Watershed regions	Moderate, spastic quadriplegia, variable cognitive deficit
	Severe	Extensive cortical pathology	Spastic quadriplegia, severe cognitive impairment, cortical visual impairment, microcephaly

Table 2.3: *Relationships between time course of asphyxial insult, site(s) of brain injury and type of disability [14]*

2.9 Neuro-imaging scoring system

One of the ways to evaluate the radiological findings is by a scoring system. The scores are based on the image intestines and contrast of the main brain areas affected by hypoxia-ischemia: deep grey matter and the intravascular zones. The more extensive injury, the higher the score is given. The scores can then be compared to clinical outcomes and use to help in outcome prediction. One example of such a scoring system was introduced by Barkovich *et al.* [15] and is shown in table 2.4.

2.10 Treatment

To date, a single, fully effective treatment for HIE has not yet been determined. This is due to the vast complexity of the biochemical and physiological processes and interactions, which are still not fully understood. However, as pointed out in section 2.4, there is a therapeutic window between reperfusion and secondary energy failure, in which a treatment should be most effective by blocking the path to cellular death. Recently, it has been shown that therapeutic

Score	Description
	Basal ganglia (BG)
0	Normal or isolated focal cortical infarct
1	Abnormal signal in thalamus
2	Abnormal signal in thalamus and lentiform nucleus
3	Abnormal signal in thalamus, lentiform nucleus, and perirolandic cortex
4	More extensive involvement
	Watershed (W)
0	Normal
1	Single focal infarction
2	Abnormal signal in anterior or posterior watershed white matter
3	Abnormal signal in anterior or posterior watershed cortex and white matter
4	Abnormal signal in both anterior and posterior watershed zones
5	More extensive cortical involvement
	Basal ganglia/watershed (BG/W)
0	Normal
1	Abnormal signal in basal ganglia or thalamus
2	Abnormal signal in cortex
3	Abnormal signal in cortex and basal nuclei (basal ganglia or thalami)
4	Abnormal signal in entire cortex and basal nuclei

Table 2.4: *Barkovich scoring system [15]*

cooling improves neurocognitive outcomes in early [40] and middle childhood [41]. Therapeutic hypothermia is a deliberate and closely controlled reduction of the body temperature to 33-34° for 72 hours, started within 6 hours after delivery. Hypothermia is currently the only treatment that has been recommended and introduced to the standard clinical care by the NICE interventional procedures guidance (IPG347)[5]. However, it does not provide neuroprotection in all cases. Therefore many other potential treatments are currently being investigated [42]. A combination of cooling and inhalation of Xenon gas has shown promising results in pre-clinical research [43], but its effectiveness hasn't been confirmed in a first clinical trial trial[6] [44].

[5] http://www.nice.org.uk/guidance/ipg347

[6] https://www.npeu.ox.ac.uk/toby-xe

2.11 Summary

This chapter presented anatomical, physiological and clinical background necessary to understand the origin and consequences of hypoxia-ischemia. Currently, none of the imaging techniques used in standard clinical practice evaluate perfusion, which could be beneficial to improve the knowledge of injury progression as well as deepen the understanding of the therapeutic processes involved in treatments. A review of research results measuring perfusion is given in chapter 4, section 4.2.

Chapter 3

Introduction to magnetic resonance imaging and spectroscopy

3.1 Introduction

This chapter gives an overview of the basics physical principles of nuclear magnetic resonance (NMR), formation of an image using NMR principles and magnetic resonance spectroscopy. It provides the basis for the imaging and spectroscopy techniques used and described in the subsequent chapters.

3.2 Physical principles of nuclear magnetic resonance

The nuclear magnetic moment μ is the foundation for MR spectroscopy and imaging. When put into an external magnetic field $\vec{B}_0$, the magnetic moment vector $\vec{\mu}$ experiences a torque $\vec{N} = \vec{\mu} \times \vec{B}$. Nonzero torque implies that the system's total angular momentum $\vec{J}$ changes according to $d\vec{J}/dt = \vec{N}$. On the other hand, the relationship between the magnetic moment μ and angular momentum $\vec{J}$ is given by : $\vec{\mu} = \gamma\vec{J}$, where γ is the gyromagnetic ratio and for protons of water it is equal to 42.6 MHz/Tesla (or 2.68 $\times 10^8$ rad/s/Tesla). Putting the above together yelds:

$$\vec{N} = \frac{d\vec{J}}{dt} = \vec{\mu} \times \vec{B} \rightarrow \frac{d\vec{\mu}}{dt} = \gamma\frac{d\vec{J}}{dt} = \gamma\vec{\mu} \times \vec{B} \tag{3.1}$$

which is the equation of motion for the magnetic moment μ of an isolated spin in the classical mechanics view. The solution to the above equation is of the form:

$$\begin{aligned} \mu_x(t) &= \mu_x(0)cos(\gamma B_0 t) + \mu_y(0)sin(\gamma B_0 t) \\ \mu_y(t) &= -\mu_x(0)sin(\gamma B_0 t) + \mu_y(0)cos(\gamma B_0 t) \\ \mu_z(t) &= \mu_z(0) \end{aligned} \tag{3.2}$$

or using rotation matrix notation:

$$\vec{\mu}(t) = \mathrm{R}_z(\gamma B_0 t)\vec{\mu}(0) \tag{3.3}$$

The angular frequency that μ precesses about B_0 is called the Larmor frequency:

$$\omega_0 = \gamma B_0 \tag{3.4}$$

The magnetic moment vectors of all protons contained in a unit volume (population) sum up and give a net magnetisation vector $\vec{M} = \sum_{n=1}^{n=Np} \vec{\mu}_n$. If there is no phase coherence between $\vec{\mu}$ within the population, then $\vec{M}$ is aligned with the direction of the main magnetic field. $\vec{M}$ is several orders of magnitude lower compared to B_0 (M_0 per unit volume at B_0 = 3 T is $\approx$ 0.04 μ T/ml [10]), therefore in order to detect $\vec{M}$, it needs to be tipped away from its equilibrium direction. This can be achieved by applying a short magnetic field of radio frequency (RF pulse). If the frequency of the RF pulse is equal to the Larmor frequency, the rotation is most efficient and it is said that the RF pulse is on resonance and it provides a continuously synchronised torque. The changes in the net magnetisation vector orientation can be then measured throughout the interaction of the protons' magnetic field with a coil detector.

3.2.1 Mathematical description: laboratory and rotating frames

The rotating frame is often used to simplify the description of $\vec{M}$ rotation compared to that of the laboratory frame, both mathematically and conceptually. Both the laboratory and rotating frames are right handed Cartesian coordinate systems (denoted by (x', y', z') and (x, y, z) in laboratory and rotating frame respectively), with z' and z axis of both systems aligned with main magnetic field direction $\vec{B}$. However, the xy plane of the rotating frame rotates around z slowing down the rotation of $\vec{M}$ and if the rotation frequency of the rotating frame is equal to Larmor frequency, $\vec{M}$ appear to be stationary. The biggest benefit of using the rotating frame is when considering the motion of $\vec{M}$ as a result of interaction with RF pulse.

Mathematical description of the frames. A time-dependent vector $\vec{m}(t)$ can be written in terms of its (x', y', z') components as:

$$\vec{m'}(t) = m_{x'}(t)\hat{x}' + m_{y'}(t)\hat{y}' + m_{z'}(t)\hat{z}' \tag{3.5}$$

where $(\hat{x}', \hat{y}', \hat{z}')$ are unit vectors in a laboratory frame. In the rotating reference frame, $\vec{m}$ can be expressed as:

$$\vec{m}(t) = m_x(t)\hat{x} + m_y(t)\hat{y} + m_z(t)\hat{z} \tag{3.6}$$

where $(\hat{x}, \hat{y}, \hat{z})$ are unit vectors in a rotating frame. The three components of $\vec{m}(t)$ in the rotating frame relate to those in a laboratory frame by:

$$\begin{bmatrix} m_x \\ m_y \\ m_z \end{bmatrix} = \begin{bmatrix} \cos\omega_{fr}t & -\sin\omega_{fr}t & 0 \\ \sin\omega_{fr}t & \cos\omega_{fr}t & 0 \\ 0 & 0 & 1 \end{bmatrix} \begin{bmatrix} m_{x'} \\ m_{y'} \\ m_{z'} \end{bmatrix} = \mathrm{R}\vec{m'} \tag{3.7}$$

where R is a rotation matrix, and ω_{fr} is the angular frequency of the rotating frame. Knowing the components in one frame allows computation of the components in the other frame:

$$\begin{bmatrix} m_{x'} \\ m_{y'} \\ m_{z'} \end{bmatrix} = \begin{bmatrix} \cos\omega_{fr}t & \sin\omega_{fr}t & 0 \\ -\sin\omega_{fr}t & \cos\omega_{fr}t & 0 \\ 0 & 0 & 1 \end{bmatrix} \begin{bmatrix} m_x \\ m_y \\ m_z \end{bmatrix} = \mathrm{R}^{-1}\vec{m} = \mathrm{R}^T\vec{m} \tag{3.8}$$

where R^T is a transpose of the matrix R.

The relation of the rate of change of the vector in time in two frames is given by:

$$\left(\frac{d\vec{m}(t)}{dt}\right)_{lab} = \left(\frac{d\vec{m}(t)}{dt}\right)_{rot} + \vec{\Omega} \times \vec{m}(t) \tag{3.9}$$

where Ω is a rotational angular velocity vector and subscripts 'lab' and 'rot' refers to the laboratory and rotating reference frames, respectively. The magnitude of Ω is equal to ω_{fr} and it points along the negative z axis: $\vec{\Omega} = -\omega_{fr}\hat{z}$ ($\vec{m}$ rotates around z clockwise, the direction of the angular velocity vector is defined by right-hand rule - if the fingers points towards the direction of the rotation, the thumb points towards the direction of the velocity vector). The above equation says that the rate of change of a vector seen in the laboratory frame is equal to the vector sum of rate of change of this vector seen from a rotating frame perspective and a cross product of angular velocity of one rotation frame (seen in laboratory frame) and vector $\vec{m}$.

Spin precession in rotating frame. The mathematical description of the net magnetisation $\vec{M}$ of spins in phase rotating in the laboratory frame with Larmor frequency ω_0 is similar to the equation of motion for a single magnetic moment $\vec{\mu}$, equation 3.1, and is given by:

$$\left(\frac{d\vec{M}}{dt}\right)_{lab} = \gamma\vec{M} \times \vec{B_0} = \vec{M} \times (\omega_0\hat{z}) \tag{3.10}$$

Therefore, if the rotating frame rotates with the angular velocity $\vec{\omega}_{fr}$, using equation 3.9 it can be rewritten as:

$$\begin{aligned}\left(\frac{d\vec{M}(t)}{dt}\right)_{rot} &= \left(\frac{d\vec{M}(t)}{dt}\right)_{lab} - \vec{\Omega} \times \vec{M} \\ &= \vec{M} \times (\omega_0\hat{z}) + \vec{M} \times (-\omega_{fr}\hat{z}) \qquad (3.11) \\ &= (\omega_0 - \omega_{fr})\,\vec{M} \times \hat{z} \qquad (3.12)\end{aligned}$$

If the frame rotates clockwise around z at Larmor frequency ω_0, then $(d\vec{M}/dt)_{rot} = 0$, indicating that from the point of view of the rotating frame, there is no change in time of $\vec{M}$, i.e. M is stationary in this frame.

RF pulse representation in the rotating frame

Radiofrequency (RF) pulses, oscillating at the same frequency as spins, are used to deliver an external energy and drive the spin system away from its equilibrium. An RF pulse of frequency ω_{RF} applied along x axis can be represented in the laboratory frame by the equation:

$$\vec{B}_1(t) = \hat{x}'B_1(t)\cos\omega_{RF}t - \hat{y}'B_1(t)\sin\omega_{RF}t \tag{3.13}$$

$B_1(t)$ is called the envelope and $\omega_{RF} = 2\pi f_{RF}$ is the pulse carrier frequency.

By matrix multiplication with the rotation matrix R, the RF pulse can be transformed to the rotating frame:

$$\begin{bmatrix} B_{1x}(t) \\ B_{1y}(t) \\ B_{1z}(t) \end{bmatrix} = \begin{bmatrix} \cos\omega_{fr}t & -\sin\omega_{fr}t & 0 \\ \sin\omega_{fr}t & \cos\omega_{fr}t & 0 \\ 0 & 0 & 1 \end{bmatrix} \begin{bmatrix} B_1(t)\cos\omega_{RF}t \\ -B_1(t)\sin\omega_{RF}t \\ 0 \end{bmatrix} = \begin{bmatrix} B_1(t)\cos(\omega_{fr} - \omega_{RF}) \\ B_1(t)\sin(\omega_{fr} - \omega_{RF}) \\ 0 \end{bmatrix} \tag{3.14}$$

If the angular frequency of the rotating frame ω_{fr} is equal to the carrier frequency ω_{RF}, then

$B_1(t)$ reduces to:

$$\begin{bmatrix} B_{1x}(t) \\ B_{1y}(t) \\ B_{1z}(t) \end{bmatrix} = \begin{bmatrix} \vec{B}_1(t) \\ 0 \\ 0 \end{bmatrix} \tag{3.15}$$

The representation of the RF pulse in the rotating frame is much simpler than in the laboratory frame, and has proven to be very popular in describing the MR experiment.

3.2.2 The Bloch Equations

The Bloch equations describe a time dependent behaviour of $\vec{M}$ in the presence of applied magnetic fields and relaxation. In general form it is given by:

$$\frac{d\vec{M}}{dt} = \gamma\vec{M} \times \vec{B} - \frac{M_x\hat{x'} + M_y\hat{y'}}{T_2} + \frac{(M_0 - M_z)\,\hat{z'}}{T_1} \tag{3.16}$$

where T_1 and T_2 are spin-lattice and spin-spin relaxation times and describe the return of the system to its equilibrium after perturbance, M_0 is a fully relaxed $\vec{M}$.

Excitation. The overall magnetic field is the sum of the static magnetic field B_0 and RF B_1 field:

$$\vec{B} = \vec{B}_1 + \vec{B}_0$$

where $\vec{B}_1$ is given by equation 3.13. Therefore equation 3.16 can be written as (ignoring relaxation processes):

$$\left(\frac{d\vec{M}}{dt}\right)_{lab} = \gamma\vec{M} \times \left(\hat{x'}B_1 \cos\omega_{RF}t - \hat{y'}B_1 \sin\omega_{RF}t + \hat{z'}B_0\right)$$

and after conversion to the rotating frame:

$$\begin{aligned} \left(\frac{d\vec{M}}{dt}\right)_{rot} &= \gamma\vec{M} \times \left[B_1\left(\hat{x}\cos(\omega_{RF} - \omega_{fr})t - \hat{y}\sin(\omega_{RF} - \omega_{fr})t\right) + \hat{z}\left(B_0 - \frac{\omega_{fr}}{\gamma}\right)\right] \\ &= \gamma\vec{M} \times \vec{B}_{eff} \end{aligned} \tag{3.17}$$

where $\vec{B}_{eff}$ is called the effective magnetic field. From the above equation it can be seen that in the rotating reference frame the magnetisation vector always precesses about $\vec{B}_{eff}$.

At resonance (i.e. $\omega_{RF} = \gamma B_0 = \omega_{fr}$) the effective field reduces to $\hat{x}B_1(t)$ and the magnetisation precesses about the applied B_1 field. If the frequency of the rotating frame is identical to the frequency of RF pulse, i.e. $\omega_{fr} = \omega_{RF}$, B_1 is demodulated. This is so called " RF reference frame". Another special case is when the frequency of the rotating frame is equal to

the Larmor frequency (i.e. $\omega_{fr} = \omega_0$). In this frame B_0 disappears and therefore this frame is called "B_0 rotating frame".

In the RF rotating frame the equation 3.17 simplifies to:

$$\left(\frac{d\vec{M}}{dt}\right)_{rot} = \gamma\vec{M} \times \left[B_1\hat{x} + \hat{z}\left(B_0 - \frac{\omega_{RF}}{\gamma}\right)\right] \tag{3.18}$$

Defining frequency offset $\Delta\omega$ as a difference between frequency of the spins and frequency of the RF pulse:

$$\Delta\omega = \gamma B_0 - \omega_{RF} \tag{3.19}$$

equation 3.18 can be expressed as:

$$\begin{aligned} \frac{dM_x}{dt} &= \Delta\omega M_y \\ \frac{dM_y}{dt} &= \gamma B_1(t) M_z - \Delta\omega M_x \\ \frac{dM_z}{dt} &= -\gamma B_1(t) M_y \end{aligned} \tag{3.20}$$

or, equivalently, in a matrix representation:

$$\frac{d\vec{M}}{dt} = \begin{bmatrix} 0 & \Delta\omega & 0 \\ -\Delta\omega & 0 & \gamma B_1 \\ 0 & -\gamma B_1 & 0 \end{bmatrix} \tag{3.21}$$

On resonance, the RF frequency is equal to Larmor frequency and $\Delta\omega = 0$. With the initial conditions $M_x = 0$, $M_y = 0$ and $M_z = M_0$, the closed-form solution to the above equation is given by:

$$\begin{aligned} M_x(t) &= 0 \\ M_y(t) &= M_0 \sin\left(\gamma \int_0^{\tau_{RF}} B_1(t)dt\right) \\ M_z(t) &= M_0 \cos\left(\gamma \int_0^{\tau_{RF}} B_1(t)dt\right) \end{aligned} \tag{3.22}$$

and therefore the RF flip angle FA can be defined as:

$$FA(t) = \gamma \int_0^{\tau_{RF}} B_1(t)dt = \int_0^{\tau_{RF}} \omega(t)dt \tag{3.23}$$

where τ_{RF} is the duration of the RF pulse. Off resonance, $\Delta\omega \neq 0$, the $\vec{B_{eff}}$ has two components: B_1 along $\hat{x}$ axis and $\Delta\omega/\gamma$ pointing along $\hat{z}$ and therefore magnetisation $\vec{M}$ will precess around $\vec{B_{eff}}$ with angular frequency ω_{eff}:

$$\omega_{eff} = \gamma B_{eff} = \sqrt{\Delta\omega^2 + \gamma^2 B_1^2} \tag{3.24}$$

$\vec{B_{eff}}$ makes the angle θ with $\hat{z}$ axis:

$$\theta = \arctan\left(\frac{\gamma B_1}{\Delta\omega}\right) \tag{3.25}$$

Relaxation. The general Bloch Equation in the rotating frame takes the form:

$$\left(\frac{d\vec{M}(t)}{dt}\right)_{rot} = \gamma\vec{M} \times \vec{B_{eff}} - \frac{M_x\hat{x} + M_y\hat{y}}{T_2} + \frac{(M_0 - M_z)\,\hat{z}}{T_1} \tag{3.26}$$

When $B_{eff} = 0$, equation 3.26 can be expressed in the rotating frame as:

$$\begin{aligned} \frac{dM_x}{dt} &= -\frac{M_x}{T_2} \\ \frac{dM_y}{dt} &= -\frac{M_y}{T_2} \\ \frac{dM_z}{dt} &= \frac{M_0 - M_z}{T_1} \end{aligned} \tag{3.27}$$

The solution to 3.27, with initial condition: $\vec{M}(0) = M_x(0) + M_y(0) + M_z(0)$ is:

$$\begin{aligned} M_x(t) &= M_x(0)\exp(-t/T_2) \\ M_y(t) &= M_y(0)\exp(-t/T_2) \\ M_z(t) &= M_z(0)\exp(-t/T_1) + M_0\left(1 - \exp(-t/T_1)\right) \end{aligned} \tag{3.28}$$

which, in the matrix representation takes form:

$$\vec{M}(t) = \begin{bmatrix} \exp(-t/T_2) & 0 & 0 \\ 0 & \exp(-t/T_2) & 0 \\ 0 & 0 & \exp(-t/T_1) \end{bmatrix} \vec{M}(0) + \begin{bmatrix} 0 \\ 0 \\ M_0\left[1 - \exp(-t/T_1)\right] \end{bmatrix} \tag{3.29}$$

An illustration of the evolution x, y and z components of the magnetisation after excitation pulse in the laboratory and rotating frames is presented in figure 3.1, computed for $T_1 = 200$ [ms] and $T_2 = 50$ [ms].

3.2.3 Signal detection

Precessing magnetisaton in the xy plane can be detected by measuring the voltage $V(t)$ it induces in a receive coil in accordance with Faraday's law of electromagnetic induction. The law states that a time-varying magnetic flux through a loop of wire, Φ, generates a voltage whose amplitude is proportional to the (negative of the) time rate of change of the flux [45]:

$$V(t) = -\frac{d\Phi}{dt} \tag{3.30}$$

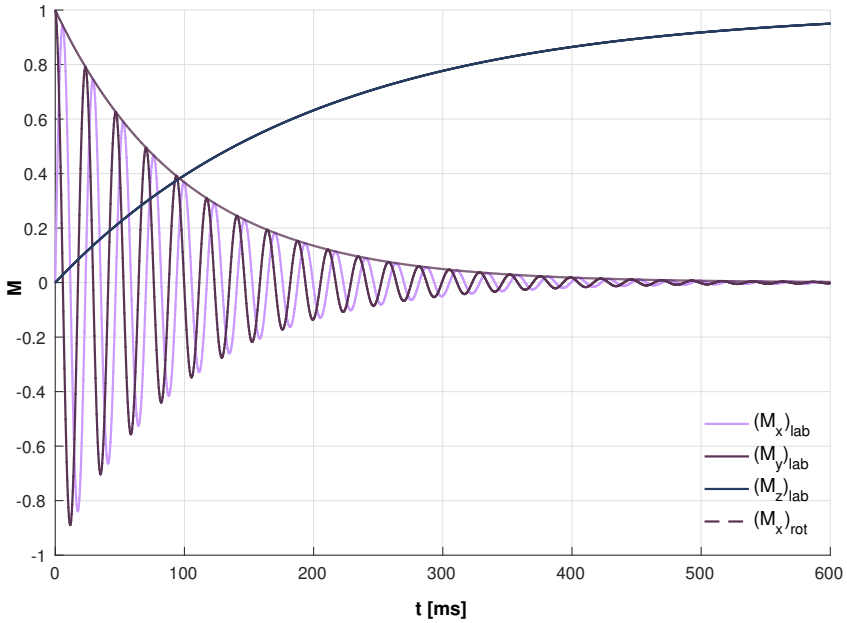

Figure 3.1: *Relaxation in laboratory and rotating frame.*

The magnetic flux can be written as:

$$\Phi = \int_{object} \vec{B_r}(\mathbf{r}) \cdot \vec{M}(\mathbf{r}, t) d\mathbf{r} \tag{3.31}$$

where $\vec{B_r}(\mathbf{r})$ is the receive coil B_1 field at the location $\mathbf{r}$. The full detailed derivation of the above equation can be found in [45]. Therefore the signal, $S(t)$, can be expressed as:

$$S(t) \propto V(t) = -\frac{\partial}{\partial t} \int_{object} \vec{B_r}(\mathbf{r}) \cdot \vec{M}(\mathbf{r}, t) d\mathbf{r} \tag{3.32}$$

After introduction of some assumptions and simplifications, of which details can be found in [45] and [9], the above can be rewritten as a signal expression:

$$S(t) = \int_{object} M_{xy}(\mathbf{r}, 0) \exp(-t/T_2^*(\mathbf{r})) \exp\left(-i\omega(\mathbf{r})t\right) d\mathbf{r} \tag{3.33}$$

where M_{xy} is a complex representation of the transverse magnetisation in the rotating frame, i.e. $M_{xy} = M_x + iM_y = M_{xy} \exp(i\phi)$, and $\omega(\mathbf{r})$ is spatially dependant resonance frequency. T_2^* is called an apparent T_2 and it given by: $1/T_2^* = 1/T_2 + 1/T_2'$, where T_2' is inversely proportional to the magnetic field inhomogeneity. By introducing a spin spectral density function $\rho(\omega)$ to characterise the frequency distribution of a spin system:

$$dM(\omega) = \rho(\omega) d\omega \tag{3.34}$$

and

$$M = \int_{-\infty}^{\infty} \rho(\omega) d\omega \tag{3.35}$$

where $M(\omega) = M_x(\omega) + M_y(\omega) + M_z(\omega)$, it can be shown that the signal generated can be expressed as [9]:

$$S(t) \propto \int_{-\infty}^{\infty} \rho(\omega) \exp(-t/T_2^*(\mathbf{r})) \exp(-i\omega t) d\omega. \tag{3.36}$$

On the other hand, the frequency spectrum $\hat{\rho}$ of the time signal $S(t)$ is:

$$S(t) = \frac{1}{2\pi} \int_{-\infty}^{\infty} \hat{\rho}(\omega) \exp(-i\omega t) d\omega. \tag{3.37}$$

Therefore the frequency spectrum of the time signal is directly linked to the spin spectral density function when T_2 relaxation is omitted.

3.3 Image formation

To obtain spatial localisation of the signal in the sample, the frequency of spins needs to be controlled. This can be achieved by augmenting the homogenous magnetic field with magnetic field gradients and creating a position dependant resonance frequency of the spins. The dependency of the spin frequencies on the spatial location can be used together with an RF pulse, which leads to a selective excitation, as only the spins at resonance with an RF pulse will experience excitation. If the field gradient is used to make an RF pulse spatially selective, it is called a slice selective gradient. The spatial encoding within a slice relies on creating a position dependant resonance response of the spins after excitation. The encoding can be employed in two forms: frequency and phase encoding, which is then decoded using a Fourier transform. If the gradients are used for spatial encoding, they are referred to as frequency and phase encoding gradients. The details of how slice selective and encoding gradients are used to form an MR image is described below.

3.3.1 Imaging gradients

Magnetic field gradient G is the linear variation of the z component of the magnetic field B_z in space and time, where z is the direction of the main magnetic field B_0. Since B_z can vary in any of the three orthogonal directions, the field gradient can be expressed as a vector:

$$\vec{G}(t) = \frac{\partial B_z(\vec{r},t)}{\partial x}\hat{x} + \frac{\partial B_z(\vec{r},t)}{\partial y}\hat{y} + \frac{\partial B_z(\vec{r},t)}{\partial z}\hat{z} \equiv G_x\hat{x}(t) + G_y\hat{y}(t) + G_z\hat{y}(t) \tag{3.38}$$

where G_x, G_y and G_z are the three orthogonal components of $\vec{G}$, $\vec{r}$ is a displacement vector from the gradient isocenter, $\hat{x}, \hat{y}$ and $\hat{z}$ are the unit vectors of the Cartesian coordinate system. The gradient amplitudes are given in mT/m (or G/cm). If the field gradient is applied, the additional

magnetic field at the position described by $\vec{r}$ is equal to $\vec{G}(t) \cdot \vec{r}$ and the total magnetic field at this location is given by:

$$\vec{B}(\vec{r},t) = \left(B_0 + \vec{G}(t) \cdot \vec{r}\right) \hat{z} = \left(B_0 + G_x x(t) + G_y y(t) + G_z z(t)\right) \hat{z} \tag{3.39}$$

3.3.2 Spacial selectivity

Selective excitation and refocusing. To obtain spatial selectivity (slice selection), an RF pulse is played out concurrently with a magnetic field gradient. In the presence of a gradient G_z, the Larmor frequency at the position z is given by:

$$f(z) = \frac{\gamma}{2\pi} B_0 + \frac{\gamma}{2\pi} \vec{G}(t) \cdot \vec{r} = f_0 + \frac{\gamma}{2\pi} G_z z \tag{3.40}$$

where f_0 is the Larmor frequency of the spins at the isocenter. To select spins at the position δz away from a isocenter, the carrier frequency of the RF pulse needs to be adjusted, from that at the isocenter, by the offset δf_{RF} given by:

$$\delta f_{RF} = \frac{\gamma}{2\pi} G_z \delta z \tag{3.41}$$

The RF pulse contains a bandwidth of frequencies Δf_{RF} which translates into a band of locations:

$$\Delta z = \frac{2\pi \Delta f_{RF}}{\gamma G_z} \tag{3.42}$$

where Δz is the width of the selected region. This dependency and its utilisation for offsetting the slices or controlling the slice width is illustrated in figure 3.2 and 3.3, respectively. The RF bandwidth Δf_{RF} is given by the full width at half maximum (FWHM) of the frequency profile, which, for small angles, can be approximated by the Fourier Transform of the pulse envelope.

Apart from spatial selection, the slice selection gradient causes a phase variation across the slice. To compensate for this phase dispersion, a slice refocusing gradient is applied after the RF excitation pulse. The maximal possible extent of the refocus of the phase dispersion across the slice is calculated based on the isodelay parameter Δt_I, which is the dephasing time that results in phase dispersion. The phase introduced by the slice selective gradient is given by:

$$\phi(z) = \gamma G_z z \Delta t_I \tag{3.43}$$

Across the slice this equals to:

$$\Delta\phi(z) = \gamma G_z \Delta z \Delta t_I \tag{3.44}$$

Substituting Δz with equation 3.42, the above simplifies to:

$$\Delta\phi(z) = 2\pi\Delta f_{RF}\Delta t_I \tag{3.45}$$

which states that the phase dispersion (in cycles) across the slice is approximately given by the product of the RF bandwidth and the isodelay [12].

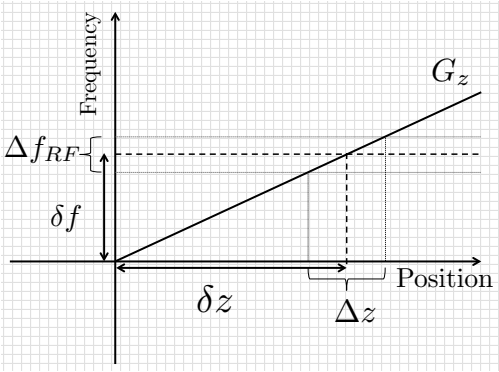

Figure 3.2: *RF carrier frequency offset δf_{RF} is used to offset the centre of the slice by a distance Δz from the gradient isocenter.*

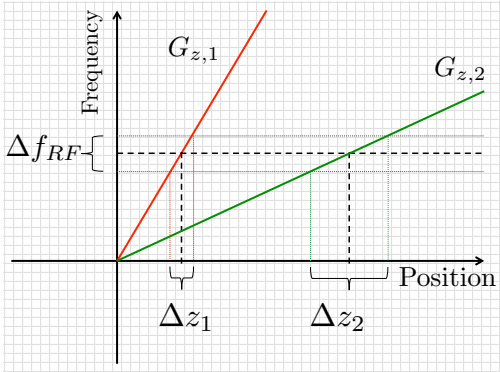

Figure 3.3: *The stronger gradient G_{z1} produces a thiner slice Δz_1 compared to a weaker gradient G_{z2} for s given band width Δf_{RF}*

3.3.3 Spatial encoding

Frequency encoding. Frequency encoding relies on the linear dependency of the spins' frequency on their spatial location, as illustrated in figure 3.4. This is achieved by applying a linear gradient field. In the presence of such a gradient applied in the x direction, the Larmor frequency at the position x is given by:

$$\Delta\omega(x) = \gamma G_x x \tag{3.46}$$

and the signal generated at the infinitesimal interval dx is (from equation 3.36):

$$dS(x,t) = \rho(x)\exp(-t/T_2^*)\exp(i\gamma x G_x t)dx \tag{3.47}$$

In general case, the total signal from the sample is:

$$S(t) = \int_{object} \rho(\mathbf{r})\exp(-t/T_2^*)\exp(i\gamma\mathbf{G_{FE}r}\cdot td\mathbf{r}) \tag{3.48}$$

where frequency encoding gradient $\mathbf{G_{FE}} = (G_x, G_y, G_z)$.

Phase encoding. To achieve phase encoding, a linear gradient field is applied for a duration T_{PE} and turned off before data acquisition (see figure 3.5). Therefore, at the position x:

$$dS(x,t) = \begin{cases} \rho(x)\exp(-t/T_2^*)\exp(i\gamma x G_x t)dx & 0 \leq t \leq T_{PE} \\ \rho(x)\exp(-t/T_2^*)\exp(i\gamma x G_x T_{PE})dx & T_{PE} \leq t \end{cases} \tag{3.49}$$

As a result of the first interval the spins accumulate different phases, depending on the frequency at which they oscillated. Therefore, after the first period of G_x, the phase will equal to:

$$\phi(x) = \gamma G_x x T_{PE} \tag{3.50}$$

In general, this can be written as:

$$\phi(\mathbf{r}) = \gamma \mathbf{G_{PE}} \mathbf{r} T_{PE} \tag{3.51}$$

where frequency encoding gradient $G_{PE} = (G_x, G_y, G_z)$. The total received signal is the sum of all the local phase-encoded signals and it's given by:

$$S(t) = \int_{object} \rho(\mathbf{r})\exp(-t/T_2^*)\exp(i\gamma \mathbf{G_{PE}} \mathbf{r} \cdot T_{PE})d\mathbf{r} \tag{3.52}$$

Comparing the above expression with 3.48 it can be appreciated that both phase and frequency gradients encode the signal by spatially varying the frequency of the spins. The main difference lies in the acquisition time: while the PE gradient is applied before the acquisition begins, the FE gradient is applied during the acquisition.

k-space To spatially encode a 2D plane, the phase and frequency encoding gradients are applied in perpendicular directions. The signal from spins at position x, y following both frequency and phase encoding is given by:

$$dS(t) = \rho(x,y)\exp(-t/T_2^*)\exp(i\gamma x G_{FE} t)\cdot\exp(i\gamma y G_{PE} T_{PE})dxdy \tag{3.53}$$

With a substitution:

$$\begin{cases} k_x(t) & = \frac{\gamma}{2\pi} G_{FE} \cdot t \\ k_y(t) & = \frac{\gamma}{2\pi} G_{PE} \cdot t \end{cases} \tag{3.54}$$

equation 3.53 becomes:

$$S(k_x, k_y) = \int\int \rho(x,y)\exp(-t/T_2^*)\cdot\exp(i2\pi(k_x x + k_y y))\cdot dxdy \tag{3.55}$$

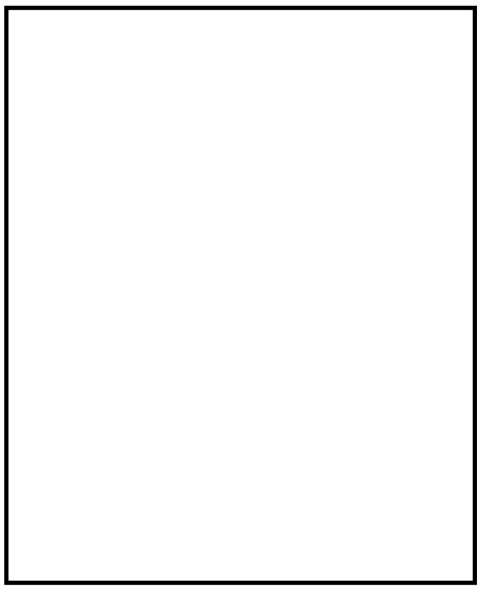

Figure 3.4: *Example of signal at 3 different locations in the presence of a frequency encoding gradient. Acquired signal is a composition of all frequencies (figure 5.7 from [9]).*

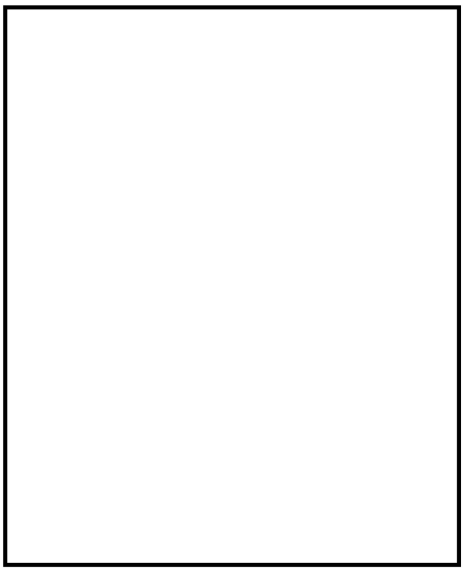

Figure 3.5: *Example of signal at 3 different locations after applying phase encoding gradient for a duration of T_{PE} (figure 5.9 from Liang2000).*

which, with the exemption of the T_2^*, term is the inverse Fourier transform of the spin density $\rho(x, y)$:

$$\rho(x, y) = \int\int S(k_x, k_y) \cdot \exp(-i2\pi(k_x x + k_y y)) \cdot dk_x dk_y \tag{3.56}$$

Position (x, y) and spatial frequency (k_x, k_y) are said to constitute a Fourier transform pair. The signal data matrix filled is called k-space. A Fourier transform of k-space data yields an image.

3.3.4 Echo formation

A signal measured in an MR experiment is called an echo. Echoes are created when magnetisation, tilted away from the equilibrium with an excitation RF pulse, first dephases and then gets refocused. There are two ways of refocusing the spins: (i) using refocusing gradient, or (ii) using a 180° refocusing RF pulse. Depending on the refocusing type, the echo is called gradient or spin echo.

Gradient Echo. A gradient echo (or field echo) is created by rapid dephasing and rephasing of the transverse magnetisation, by changing spins precession frequencies. However, since the rephasing gradient can only compensate dephasing caused by the dephasing gradient, dephasing due to main magnetic field inhomogeneities or T_2 relaxation is not refocused. The amplitude of

the echo, acquired at the echo time, TE, is therefore given by:

$$S_{GE} = S_0 \exp\left(-\frac{TE}{T_2^*}\right) \tag{3.57}$$

An example of a gradient echo sequence is shown in figure 3.6.

Spin Echo. A spin echo is created by applying a $180°$ refocusing RF pulse, which refocuses the spins that naturally dephased after $90°$ excitation pulse. The $180°$ refocusing RF pulse reverses the accrued phase, therefore the amplitude of the echo will not depend on inhomogeneities:

$$S_{SE} = S_0 \exp\left(-\frac{TE}{T_2}\right) \tag{3.58}$$

An example of a spin echo sequence is shown in figure 3.7.

Figure 3.6: *Example of gradient echo. An echo is formed by first dephasing and then rephasing of the spins, achieved by rapid switching of the gradient (figure 8.9a from [10])*

Figure 3.7: *Example of spin echo. After dephasing, the spins are refocused by a 180° pulse (figure 8.10a from [10])*

3.3.5 Pulse sequence

A pulse sequence is a series of events including RF pulses, gradients and data acquisition, with precisely defined timing. First, an RF pulse is played out together with a slice selective gradient, causing an excitation of a two-dimensional plane (a slice). Next, phase encoding is applied orthogonal to the slice selection direction. The frequency encoding gradient is applied in the third orthogonal direction and the signal is acquired. The sequence is then repeated for each phase encoding steps until k-space is filled. Fast Fourier Transform (FFT) of the k-space data yields an image. The pulse sequence is usually visualised using a pulse sequence diagram, with time on the horizontal and amplitude on the vertical axis. An example the gradient-echo pulse sequence diagram is shown in figure 3.8.

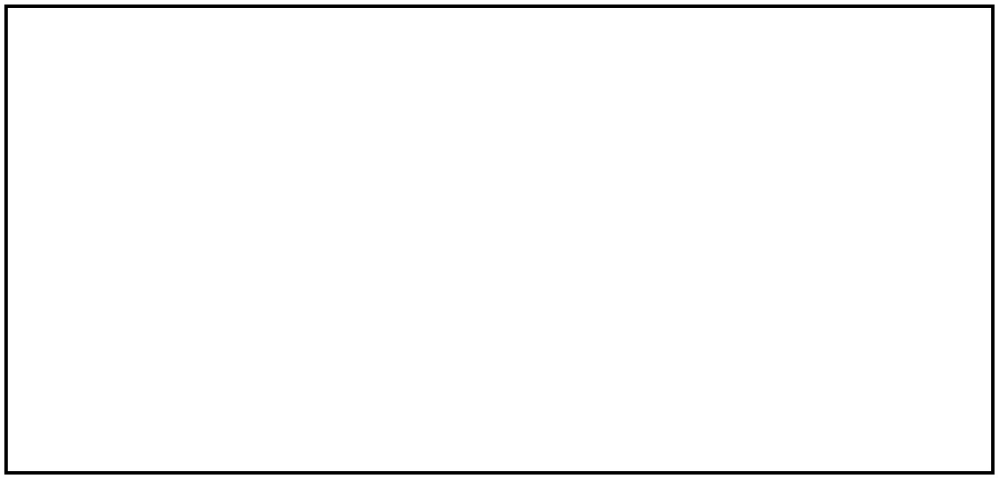

Figure 3.8: *Example of a simple gradient-echo pulse sequence and k-space path. After a selective RF pulse (A), phase encoding rephrasing gradients are applied (B). Next, an echo is formed and recorded during frequency encoding gradient (B-D). This is repeated for each phase encoding step till a full k-space is filled in. (Figures 7.19 and 7.23 from [10])*

The number of acquired points, M and phase encoding steps, N is dictated by the required field of view (FOV):

$$\begin{cases} FOV_{FE} = M \cdot \Delta x & = \frac{2\pi}{\gamma G_{FE} \Delta t} \\ FOV_{PE} = N \cdot \Delta y & = \frac{2\pi}{\gamma \Delta G_{PE} T_{PE}} \end{cases} \tag{3.59}$$

3.4 Fast imaging: Echo Planar Imaging

One of the fastest MRI techniques is Echo Planar Imaging (EPI) [46]. EPI is capable of producing a 2D image in tens of milliseconds, and it is therefore broadly used in applications that benefit from such acquisition speed (e.g. arterial spin labelling). In EPI, the full k-space is acquired after a single RF excitation pulse by using bipolar readout gradients and 'blipped' phase encoding gradients, which generate a train of echoes (as illustrated in figure 3.9). Due to the speed of acquisition, EPI suffers from a range of artefacts like ghosting, chemical shift artefacts, distortions and blurring. More details on the EPI artefacts and their prevention can be found in [12].

3.5 Imaging moving spins: Phase Contrast

Phase contrast is an imaging method which enables quantification of the velocity of moving spins by applying flow encoding gradients. Spins moving in the direction of the flow encoding

Figure 3.9: *Echo-planar sequence and the k-space path (figures 16a and 16b from [10]).*

gradient field G of duration T with velocity v accrue a phase ϕ_v:

$$\phi_v = \gamma \int_0^T Gvt \cdot dt = \left[\frac{1}{2}\gamma v G t^2\right]_0^T = \frac{1}{2}\gamma v G T^2 \tag{3.60}$$

where GT^2 is referred as the first moment of the gradient M_1. Typically, a bipolar gradient waveform is used, which is composed of two flow encoding gradients with the same amplitude but opposite polarity (applied in the time from T to $2T$), therefore the total phase shift is:

$$\phi_v = -\gamma v M_1 \tag{3.61}$$

To avoid contribution to the phase from external factors, like B_0 inhomogeneities, the scan is usually performed with the inverted polarity of the bipolar gradient. The subtraction of the phase images on pixel-by-pixel basis yields:

$$\Delta\phi_v = \gamma v \Delta M_1 \tag{3.62}$$

The dynamic range of $\Delta\phi_v$ is limited to $\pm\pi$ and it is therefore only possible to reliably determine the flow velocity for phase values within this range, unless unwrapping algorithms are used in post processing. The maximum velocity that produces a phase shift of π radians is called $VENC$ (Velocity ENCoding) and is given by:

$$VENC = \frac{\pi}{|\gamma \Delta M_1|} \tag{3.63}$$

and the velocity can be calculated from:

$$v = \frac{\phi_v}{\pi} VENC, \quad \text{where } -VENC < v < VENC \tag{3.64}$$

3.6 Magnetic Resonance Spectroscopy

3.6.1 Principles

Magnetic resonance spectroscopy (MRS) is a MR technique that allows non-invasive measurement of selected biochemical compounds in-vivo. MRS is possible owing to a phenomenon called chemical shift, in which protons in different molecular environments experience different amounts of shielding of the magnetic field by the electron clouds of neighbouring atoms. Therefore the effective magnetic field, $B_{0,eff}$ is different to that applied, B_0, and can be expressed in terms of a shielding parameter, σ:

$$B_{0,eff} = B_0 (1 - \sigma) \tag{3.65}$$

and the resonance frequency becomes:

$$\omega_{0,eff} = \gamma B_{0,eff} = \omega_0 (1 - \sigma) \tag{3.66}$$

Chemical shift enables differentiation of different chemical environments based on their resonance frequencies. σ is very small and the resulting frequency offset depends on B_0, therefore the chemical shift is usually defined in parts per million (ppm) of the resonance frequency measured relative to a reference compound (ω_{ref}): $10^6 (\omega_{eff} - \omega_{ref}/\omega_{ref})$ ppm.

In addition to chemical shift effect, protons in liquid samples usually experience the magnetic field of their nuclei through polarisation of the electrons in the molecular bonds between them. The effective magnetic field experienced by one nucleus depends on the spin state of the neighbouring coupled nucleus. This is so called J-coupling and the effect is B_0 independent. Since the technique is relatively insensitive only compounds present in millimolar concentrations are detectable using clinical in vivo MRS.

Although many studies have investigated nuclei such as phosphorous-31 (^{31}P) and some carbon-13 (^{13}C), proton (^{1}H) spectroscopy is by far the most popular, given its natural abundance and higher SNR, and no need for specialised hardware which allows performance of proton spectroscopy on most commercial MRI scanners. Therefore the rest of this section will focus on ^{1}H MRS.

3.6.2 Information content

An example spectra obtained from a phantom containing the main brain metabolites acquired at different TE are shown in the figure 3.10. The most important compounds detectable by proton

MRS in the human brain are listed below, together with their chemical shifts:

Lactate (Lac) 1.3 ppm. In the normal human brain the concentration of lactate methyl is very low, therefore it is not usually detected. However, lactate is increased, and therefore detectable, in pathological conditions resulting from hypoxia or ischemia, when glucose metabolism by the means of the Krebs cycle is no longer sustained (see chapter 2 for more details on the Krebs cycle). Lactate can be also elevated in pathologies such as tumours and mitochondrial diseases, in which Krebs cycle is inefficient.

N-acetyl aspartate (NAA), 2 ppm. NAA is the most abundant amino acid in the central nervous system; its decrease can represent neuronal loss, and increase is observed in neuronal development. However, the exact functions and roles of this amino acid are unclear.

Creatine (Cr) 3 ppm & 3.9 ppm. Creatine is a compound involved in energy metabolism. Cr is converted to phosphocreatine , which is the short-term energy storage form of the tissue. Therefore the total measured Cr (sum of PCr and Cr) may reflect the energy potential available.

Choline (Cho) 3.2 ppm. The Cho peak consists of free choline, phosphocholine and glycerophosphocholine. These compounds are involved in membrane synthesis and degeneration, and their levels can be elevated in diseases like tumours, where increased membrane turnover is involved.

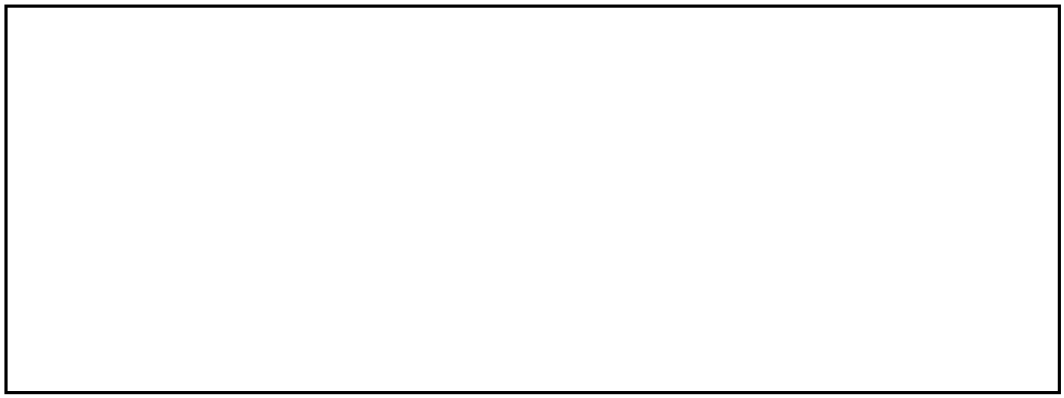

Figure 3.10: *Example of MR spectroscopy obtained in a phantom containing the main brain metabolites in normal concentrations plus lactate.TE = 30 ms (a), 135 ms (b) and 270 ms (c) (figure 15.1 from [10]).*

3.6.3 Acquisition

The spatial localisation of a single voxel is achieved by applying three slice selective pulses in mutually orthogonal directions. This is illustrated in figure 3.11 [11], where black, green and red represent slice selection in x, y and z direction, respectively. Two most commonly used sequences for spatial localisation are: STimulated Echo Acquisition Mode (STEAM) and Point RESolved Spectroscopy (PRESS).

1. STimulated Echo Acquisition Mode - STEAM. The STEAM sequence consists of three 90° orthogonal slice selective pulses, which produce a stimulated echo. Spin-echoes from the second or third pulse are dephased by large crusher gradient applied between the second and third pulse. Any other undesired coherence is also removed using crusher gradients applied during the echo time. An example of the STEAM pulse sequence (without crusher gradients) is given in figure 3.12.

2. PRESS - Point RESolved Spectroscopy. The PRESS sequence uses one 90° and two refocusing 180° pulses to generate a spin echo in the localised volume. Additional crusher gradients are applied around the refocusing pulses to dephase any undesired coherence pathways and therefore select only the desired spin-echo signal. An example of the PRESS pulse sequence (without crusher gradients) is given in figure 3.13.

PRESS is characterised by higher SNR compared to STEAM, but STEAM can be performed with shorter TE. However, the performance of the two sequences is comparable in clinical brain spectroscopy, and the choice of sequence depends on the availability from the MRI vendor or the particular application that is required [11].

3.6.4 Processing and analysis

The main goal of MRS analysis is to measure the concentration of the compounds present in the spectra. Metabolite concentrations are proportional to their respective peak areas, however, measuring them in vivo can be challenging due to resonance overlap, baseline distortions, and poor approximation of conventional models such as Gaussian or Lorentzian functions as lineshapes. Therefore many studies report relative amounts (ratios) of each metabolite, for example Lac/NAA in the case of HIE neonates.

The following steps are performed to obtain a readable spectrum:

Figure 3.11: *Voxel localisation (figure 1a from [11])*

Figure 3.12: *Example of STEAM pulse sequence (figure 1b from [11])*

Figure 3.13: *Example of PRESS pulse sequence (figure 1c from [11])*

1. Fourier transform data from time to frequency domain to represent the data as spectral intensity as a function of frequency.
2. Correction of phase and timing error, associated with the scanner receiver pathway and the start of recording the data
3. Correction of frequency errors resulting from subject's motion
4. Spectral fitting in time or frequency domain.

3.7 Summary

This chapter presented a basic theory of magnetic resonance imaging and spectroscopy. It described the magnetic resonance phenomenon, how field gradients and RF pulses are used for MR image formation and quantification of moving spins. It also illustrated how chemical shift of different molecular environments is used to identify the brain metabolites.

The aim of this chapter was to provide background of the mathematical formalism, image formation, basic imaging techniques and spectroscopy for the following chapters, in which these concepts will be used.

Chapter 4

Introduction to neonatal perfusion quantification with arterial spin labelling

4.1 Introduction

This chapter begins with a short overview of the neonatal cerebral blood flow measurement methods. It then provides an introduction to a concept of the arterial spin labelling, describes models that allow perfusion quantification and discusses sources of potential quantification errors. It finished with a review of the recent work on perfusion measurement in neonates, which provides the basis for in-vivo protocol development described in chapter 7.

4.2 Motivation

Cerebral circulation in preterm and high risk infants has been a subject of numerous studies, aiming to determine pathological mechanism of cerebral damage as well as evaluate maturation in developing brain. In normal developing preterms, cerebral blood flow (CBF) was found to be much lower than in adults and changed rapidly during first weeks of life, reflecting first low and then increasing brain activity and metabolism [47],[48],[49]. In premature infants with intraventricular haemorrhage and hemorrhagic intracerebral involvement, abnormalities in CBF were observed, [50] indicating the role of impaired CBF in brain damage [51]. Term and preterm infants, as well as infants with HIE, were also found to have much lower CBF compared to

adults [16]. Additionally, different patterns of HI brain injury emerged from CBF maps [52]: watershed, basal ganglia and total cortical pattern.

A variety of different methods has been employed to study neonatal brain perfusion. CBF in high risk and normal neonates has been investigated using radioisotopes: Xenon clearance [47], positron emission topography (PET) [50], [53], [16], and single-proton emission computer tomography (SPECT) [54], as well as non-invasive Doppler ultrasonography and near- infrared spectroscopy (NIRS) [55], [56]. Magnetic resonance imaging (MRI) methods have also been used: phase contrast (PC) [57], arterial spin labelling (ASL)[58],[49] and dynamic bolus tracking [59], [52], requiring an injection of a gadolinium contrast agent. Table 4.1 sums up the quantification of CBF derived from different methods in neonates with different pathological conditions. However, the direct comparison of CBF values provided might be difficult, as each of the method has its own limitations and different accuracy.

Method	N	GA	Weight at birth(g)	Postnatal Age (d)	Condition	CBF Range mL/100g/min
Xe clearance [47]	42	28-33	1510	0-5	preterm	5.6-36.8
Xe clearance [56]	16	27-39	1753	9-74h	preterm	7.2-22.0
PET [16]	16	26-36	1355	2.0-39	preterm	5.0-23
	14	term	3180	2.0-40	HIE or ECMO	9.0-73
NIRS [55]	9	25-44		1.0-10.0		12.0-33
NIRS [56]	16	27-39	1753	9-74h	preterm	6.21-21.0
PC MRI [57]	13	27-38	-	33-97	mild HIE	18-30
	7	term	-	45-49	mild HIE	25-60
MRI ASL [58]	23	28-34	-	63 (median)	preterm	21.3 ($\pm$ 5.1)
	6	37-42	-	2 (median)	normal	16.6 ($\pm$ 5.9)

Table 4.1: *Summary of measured CBF values in studies using different techniques; ECMO - status after common carotid ligation and extracorporeal membrane oxygenation; HIE - hypoxic-ischemic encephalopathy, GA - gestational age*

ASL is a method of choice for CBF measurement in neonatal population. It is truly non-invasive as it does not require injection or inhalation of radioisotopes (as opposed to Xenon clearance, PET, SPECT) or other contrast agents (like dynamic bolus tracking MRI), therefore allowing CBF quantification and repeated measurements safely as many times as required. Additionally, it capable is of providing regional CBF maps, in contrast to ultrasound, NIRS

or phase contrast MRI. However, ASL protocol and CBF quantification needs to be carefully designed to reflect neonatal physiology, which in turn requires an understanding of underlying model assumptions and potential quantification errors.

4.3 Introduction to arterial spin labelling

Arterial spin labelling is capable of imaging and quantifying CBF non-invasively by using water as an endogenous, freely diffusible tracer. The principle behind ASL is to measure the flow rate of arterial blood delivered to imaging voxels within the slice of interest. This is achieved by magnetically labelling blood water protons with one or several RF pulses applied to the arterial input of the imaging slice. Such prepared water molecules then travel with the blood and reach the tissue at a rate proportional to the local CBF. The image is acquired after a delay, sufficient to allow labeled spins to reach the imaged slice. The presence of labelled blood water and unlabelled tissue water within a voxel gives rise to the MR signal change. An analogous image is then acquired without the labelling and subtraction of the two yields a perfusion weighted image. Since the signal from the static tissue in both control and label images is identical, it subtracts out leaving only the signal of labelled arterial blood water delivered during the delay time. The signal-to-noise ratio (SNR) of a single subtraction image is very low; the signal change due to the perfusion is in the order of 0.5-1.5% of the full signal [60]. Therefore usually multiple repeats of labelled and control conditions are performed and averaged in a post processing step, resulting in a mean perfusion weighted image (PWI).

The feasibility of the ASL concept was demonstrated by Williams *et al.* [61] and Detre *et al.* [62] in 1992. Williams used adiabatic fast passage (AFP) for flowing spin inversion, whereas Detre used a train of pulses to saturate arterial spins in the neck. Williams method gave rise to continuous ASL methods (CASL), in which the labelling is carried out by using a long (2-4s) continuous radiofrequency (RF) pulse while applying a magnetic field gradient in the flow direction. However, due to specialist hardware requirements of AFP (i.e. gradient and RF amplifier duty cycle), there was a limited usage of this method in the clinical setting. A different approach to labelling was proposed by Edelman *et al.* [63] in 1994, called EPISTAR. He applied pulsed adiabatic inversion to a slab of arterial blood proximal to the imaging slice. Additionally, he used Echo Planar Imaging (EPI [46]), a fast imaging technique, which significantly increased the time resolution between control and label experiments. As a consequence, motion artefacts were reduced and multiple signal averages were acquired to compensate for the low SNR of

pulsed approach. Also, the power deposition of such a scheme was lower than that of the long pulse in CASL. Introduction of pulsed labelling in ASL (PASL) allowed for more common usage of ASL in clinics, since no additional hardware was required. This also accelerated ASL development: since EPISTAR, a number of other PASL schemes were proposed to enable better and more accurate quantification as well as reduction of confounding effects like magnetisation transfer (MT). However, PASL suffers from lower SNR compared to CASL label due to lower signal difference between control and label [64].

Recently, pseudo-continuous ASL (pCASL) was introduced by Dai *et al.* [65]. Here, a train of pulses accompanied by gradients is used to invert flowing spins in a "pseudo-continuous" manner. pCASL has the advantages of CASL, namely the higher SNR, but can be easily realised on common clinical scanners without additional hardware. Since the main difference between CASL and pCASL is only in the implementation of the inversion of the flowing spins most of the considerations of CASL are the same in pCASL. In the descriptions below, pCASL will be used to represent both CASL and pCASL. In case of any differences between these two methods, they will be considered separately.

4.4 Perfusion quantification with ASL

Quantification of perfusion from ASL data requires a theoretical model, which accounts for the label delivery and wash out as well as the relaxation of the label. Two main approaches are used to derive such a model: modification of the Bloch equations and the General Kinetic Model.

4.4.1 Bloch Equation

In their original work, Detre *et al.* [62] proposed modification of the Bloch Equation to account for delivery and clearance of protons, proportional to the local flow:

$$\frac{dM_t(t)}{dt} = \frac{M_t^0 - M_t(t)}{T_{1t}} + f\left(M_a(t) - M_v(t)\right) \tag{4.1}$$

where f is the flow in ml / (g $\cdot$ s), T_{1t} relaxation time of the tissue in the absence of flow or exchange between blood and brain water, M_t is the longitudinal magnetisation of brain tissue, M_t^0 is fully relaxed M_t and M_a and M_v are the longitudinal magnetisation of arterial and venous blood water, respectively. The first part of equation 4.1 describes the return of the M_t to equilibrium after a perturbation, as given in detail in chapter 3, section 3.27. Term $f\left(M_a(t) - M_v(t)\right)$ represents the delivery of the label into the tissue and its clearance by the venous outflow. As-

suming a single compartment model, the water, a freely diffuseable tracer, exchanges rapidly across the capillary walls and the magnetisation of water leaving the voxel ($M_v(t)$) is proportional to the average magnetisation of the whole voxel. Since the volume of the water in the tissue differs from that in the blood $M_v(t) = M_t(t)/\lambda$ where λ is the blood/brain partition coefficient (concentration of the tracer in brain tissue relative to that of the blood). This very simple model was later expanded to account for inversion efficiency ([61]), spin relaxation during the transit time (time delay between blood labelling and its arrival to the acquisition plane) ([66],[67]) as well as different relaxation times for water protons in the blood and tissue [68] and restricted capillary water permeability [69].

4.4.2 General Kinetic Model

Buxton *et al.* [64] proposed a general kinetic model for ASL perfusion quantification. In this model, he considered the difference of control and label signals to be a measure of how much of the original label, created by the inversion pulse, has been delivered to the voxel and survives at the time of the measurement. Therefore the difference in magnetisation ΔM becomes a bolus of an agent delivered by cerebral blood flow and kinetic modelling used in tracer kinetics can be rewritten as:

$$\Delta M = 2 \cdot M_{a,0} \cdot f \cdot \int_0^{t'} c\left(t\right) \cdot r\left(t' - t\right) \cdot m\left(t' - t\right) dt \tag{4.2}$$

where $M_{a,0}$ is the equilibrium magnetisation of arterial blood that fills up the voxel, $c(t)$ is the delivery function (normalised arterial concentration of magnetisation arriving at the voxel at time t), $r\left(t' - t\right)$ is the residue function describing the wash out of labelled spins from a voxel, and $m\left(t' - t\right)$ accounts for longitudinal magnetisation relaxation effects. With the assumptions of (i.) uniform plug flow of arterial blood, (ii.) single compartment model i.e. rapid exchange between the protons of arterial blood arriving into the voxel and tissue, (iii). blood relaxation time T_{1a} during arterial transit time ATT until exchange into the tissue and T_{1t} after reaching the extravascular space, the model can be summarised using the following equations:

$$c(t) = \begin{cases} 0, & t \leq ATT \\ \alpha \cdot e^{-t/T_{1a}}, \text{(PASL)} & ATT < t \leq ATT + \tau \\ \alpha \cdot e^{-ATT/T_{1a}}, \text{(pCASL)} & ATT < t \leq ATT + \tau \\ 0, & ATT + \tau < t \end{cases} \tag{4.3}$$

$$m(t) = e^{-t/T_{1t}} \tag{4.4}$$

$$r(t) = e^{-f \cdot t/\lambda} \tag{4.5}$$

where τ is bolus width (PASL) or labelling duration (pCASL) and α - inversion efficiency, describing the fraction of the maximum possible change in longitudinal relaxation between the label and control. The above can be solved by applying equations 4.3 - 4.5 to 4.2 for PASL:

$$\Delta M = \begin{cases} 0 & t \leq ATT \\ \frac{2M_{a,0} \cdot \alpha \cdot f}{\delta R} e^{-R_{1a} \cdot t} \cdot \left(1 - e^{-\delta R(t-ATT)}\right) & ATT < t \leq ATT + \tau \\ \frac{2M_{a,0} \cdot \alpha \cdot f}{\delta R} e^{-R_{1a} \cdot (ATT+\tau)} & \\ \qquad \cdot \left(1 - e^{-\delta R(t-ATT)} \cdot e^{-R_{1app} \cdot (t-ATT-\tau)}\right) & ATT + \tau < t \end{cases} \tag{4.6}$$

and for pCASL:

$$\Delta M = \begin{cases} 0 & t \leq ATT \\ \frac{2M_{a,0} \cdot \alpha \cdot f}{R_{1app}} e^{-R_{1a} \cdot ATT} \cdot \left(1 - e^{-R_{1app}(t-ATT)}\right) & ATT < t \leq ATT + \tau \\ \frac{2M_{a,0} \cdot \alpha \cdot f}{R_{1app}} e^{-R_{1a} \cdot ATT} \cdot e^{-R_{1app}(t-\tau-ATT)} & \\ \qquad \cdot \left(1 - e^{-R_{1app} \cdot \tau}\right) & ATT + \tau < t \end{cases} \tag{4.7}$$

where $\delta R = R_{1a} - R_{1app}$, $R_{1app} = R_{1t} + f/\lambda$, $R_{1a} = 1/T_{1a}$ and $R_{1t} = 1/T_{1t}$. Terms: $\left(1 - e^{-R_{1app}(t-ATT)}\right)$ and $\left(1 - e^{-R_{1app} \cdot \tau}\right)$ describes the approach to the steady state. For pCASL, t=0 represents the beginning of the labelling.

The above form of function $m(t)$ assumes that the protons start relaxing with tissue relaxation time T_{1t} immediately after arriving at the imaging voxel. A more realistic description of the exchange is to assume that the water proton spend time T_{ex} in the vasculature before exchanging [70]:

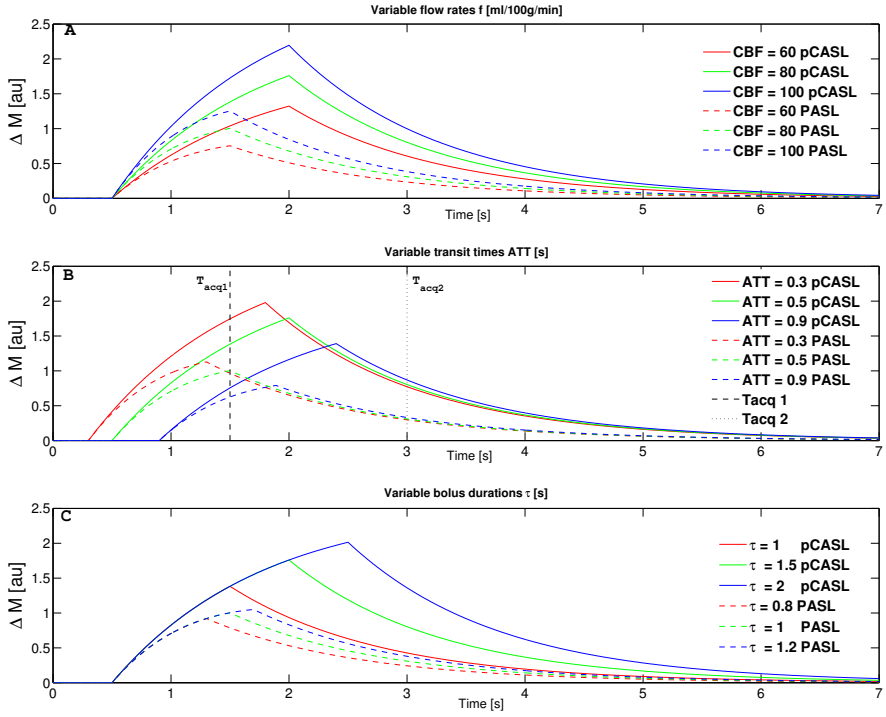

Figure 4.1: *Kinetic Model: theoretical curves of pulsed and pseuo-continuous ASL signal. A - variable flow rates, B - variable transit times, C - variable bolus durations. Other parameters:* $T_{1a} = 1.7s$, $T_{1t} = 1.3s$, $\alpha = 1$, $\lambda = 0.9$, τ *1.5s (pCASL) and 1s (PASL),* ATT *= 0.5s.*

$$m(t) = \begin{cases} e^{-t/T_{1a}} & t < T_{ex} \\ e^{-T_{ex}/T_{1a}} e^{-(t-T_{ex})/T_{1t}} & t \geq T_{ex} \end{cases} \tag{4.8}$$

Using equations 4.6 and 4.7 (i.e. assuming a rapid exchange), theoretical curves of the ASL signal ΔM are plotted in the Figure 4.1 for PASL and pCASL: A - for variable flow rates f, B - variable arterial transit times ATT, and C - variable bolus length τ. Other parameters used for the simulation were $T_{1a} = 1.7$s, $T_{1t} = 1.3$s, $\alpha = 1$, $\lambda = 0.9$, τ = 1.5s (pCASL) and 1s (PASL), ATT = 0.5s. For PASL, time $t = 0$ is the time of the inversion pulse, whereas for pCASL $t = 0$ is the beginning of the labelling train.

Recently, a simplified solution to equation 4.2 was proposed [71] for use in the clinical setting for PASL:

$$CBF = \frac{6000 \cdot \lambda \cdot \Delta M \cdot e^{\frac{TI}{T_{1,a}}}}{2 \cdot \alpha \cdot TI_1 \cdot M_{t,0}} \tag{4.9}$$

and for pCASL:

$$CBF = \frac{6000 \cdot \lambda \cdot \Delta M \cdot e^{\frac{PLD}{T_{1,a}}}}{2 \cdot \alpha \cdot T_{1,a} \cdot M_{t,0} \left(1 - e^{\frac{-\tau}{T_{1,a}}}\right)} \tag{4.10}$$

where CBF is given in units of ml/100g/min by multiplication of f by a factor of 6000.

4.4.3 Quantification errors

To obtain quantitative CBF values, T_{1a}, T_{1t} M_{0a}, λ and α need to be estimated or measured. With the use of the kinetic model it can be easily visualised, how a particular systematic error can affect the quantification of the perfusion for PASL and pCASL approaches and how they differ in terms of bolus delivery. The most significant quantification errors will now be discussed together with the potential solutions.

Arterial transit time ATT. Arterial transit time ATT is the time taken by the labelled blood to travel from the labelling region to the imaging voxel. It differs across brain regions [72]. If the transit time is unknown, quantification and interpretation of the ASL signal can be incorrect, especially in the presence of large transit time differences between the regions within one imaging slice. This is shown in the figure 4.1 B, in which ΔM is plotted for 3 different ATT values. If the acquisition is performed at T_{acq1} immediately after the end of the labelling in pCASL, three different perfusion signals ΔM would be recorded, even though the value of the perfusion is the same for these three cases. A solution to this problem was proposed by Alsop *et al.* [67]. They introduced a delay time between the labelling and acquisition, termed post labelling delay, PLD (in case of pCASL). If this delay is longer than the longest transit time: $PLD > ATT$, all the labelled spins will be delivered to the imaging voxel before the start of acquisition (T_{acq2} in figure 4.1 B). This way the dependence on the transit delay of the ASL experiment is greatly reduced. The labelled spins, that took longer to reach the tissue voxel, would, indeed, experience less relaxation, since they would spend more time relaxing with the blood T_{1b}, which is usually longer than than that of the tissue $T_{1b} > T_{1t}$. However, this is a small effect for grey matter. Another approach to minimise uncertainty of transit delay is to acquire data at the multiple time points [64] and fully characterise the inflow of labelled signal.

Arterial transit artefact. In the case of very big differences in the transit times between different brain regions or very short post labelling delays, the measured signal might be a mixture of signal arising from the water perfused to the tissue and the arterial blood signal, which is still in the large vessels at the time of the measurement. This problem can be partially removed by assuring appropriate PLD or by applying appropriate bipolar crushing gradients to reduce vascular ASL signal by dephasing the moving spins [73]. However, this increases the effective echo time, which will introduce T_2 (or T_2^*) contrast and result in reduction in SNR.

Unknown bolus duration and dispersion. Under the assumption of plug flow, i.e. the flow with the constant fluid velocity across any cross-section, the duration of the bolus in pCASL is equal to the duration of the labelling pulse. In PASL, the width of the labelled bolus can be controlled with the use of the QUIPSS II (Quantitative Imaging of Perfusion with a Single Subtraction II) technique [74], [75]. This technique produces a well defined bolus by saturation of the arterial blood after time TI_1, which also gives the bolus a well defined edge. In reality, however, the blood travels with the range of velocities, which can be different in different parts of the arterial tree and causes bolus dispersion. To account for that, models of bolus dispersion have been proposed [76], [77].

Labelling efficiency α. The blood exposed to labelling flows in the vessels with mean velocity ranging from 40 to 60cm/s [78]. This does not present a problem for PASL, since all the spins are uniformly inverted with a single inversion pulse and inversion efficiency is usually assumed to be the same for all velocities and equal to the efficiency of the inversion pulse for static spins. In the case of CASL and pCASL, on the other hand, the inversion efficiency depends heavily on the blood velocity. For laminar flow, i.e. the flow where the velocities are distributed across the crossection, the degree of inversion will be different for the blood traveling with different velocities within an artery. Additionally, if the labelling plane is not perpendicular to the direction of the flow, the efficiency might be also decreased. This, in the context of pCASL will be investigated and discussed in details in the chapter 5.

Fully relaxed magnetisation of arterial blood $M_{a,0}$. $M_{a,0}$ can be measured directly in the posterior sagittal sinus [60], however most commonly $M_{a,0}$ is estimated from M_0 of the tissue and dividing by λ.

Control for Magnetisation Transfer effects. All ASL techniques, pulsed or continuous, rely on perfect cancellation of the static tissue signal after subtraction of labeled from control images. For this to be fulfilled, Magnetisation Transfer (MT) effects in both images must be the identical. MT is the exchange of longitudinal magnetisation between protons in two pools: the free water pool and pool of protons bounded to macromolecules. Protons in macromolecules, due to very short T_2 have a very broad resonance frequency compared with free water protons. Therefore the RF pulse on resonance at the labelling plane, when applied with gradients, will saturate longitudinal magnetisation in the macromolecular pool at the imaging plane. Next, the saturated protons bound to macromolecules exchange with those in free water and reduce its MR signal [79]. If the MT effect is different for control and label images, the resulting difference image will mis-represent the signal change due to the perfusion and yield incorrect quantification. Balancing magnetisation transfer in control/label experiments has been a consideration since the first ASL experiments and prompted the development of labelling/control designs of continuous and pulsed ASL.

MT in CASL. In the first CASL experiment the control image was created with a pulse similar to the labelling RF pulse, but with the labelling plane placed distal to the imaging slice [61], which was well above the brain. The major drawback of this approach is that only one imaging plane experiences identical saturation effects due to applied gradients during labelling and therefore MT effects in other slices are not appropriately balanced. A solution to this problem was proposed by Zhang *et al.*[80] by using a small, separate labelling coil. This has been shown to enable multi slice CASL imaging in humans [81]. It is also possible to compensate MT effects using a single coil, as demonstrated by Alsop *et al.*[82] by employing a double inversion during the control imaging (double adiabatic inversion, DAI). During the passage through the first plane, flowing spins get inverted, however, this process is reversed within the second plane and the spins are returned to the original magnetisation direction. By assuring that the power in the control and label experiments are matched, the MT effects are balanced. In practice, however, it is difficult to satisfy the adiabatic conditions for double inversion, and therefore this solution suffers from reduced effectiveness of spin labelling.

MT in PASL. In the original single slice EPISTAR [63], the thick, labelling slab was positioned about 1cm below the imaging plane. The gap was designed to reduce the effect of imperfect profiles of the inversion slab. For the control, an identical slab was positioned on the

other side, above the imaging slice with 180 ° flip angle was used with identical bandwidth, and total RF irradiation as the inversion pulse. This ensured that the MT effects (already reduced compared to CASL by using a short RF pulse) are the same in both label and control images. However, true compensation is present only for a single slice. What is more, the venous blood inverted in the control can enter the imaging slice and produce artefacts, which would manifest themselves as negative perfusion signal. A variation of EPISTAR is PICORE (proximal inversion with a control for off-resonance effects) proposed by Wong *et al.* [75]. PICORE label is performed in the same way as in EPISTAR, but the inversion pulse in control is performed non-selectively, with the same frequency offset. This assures the identical MT effects on the imaging slice and at the same time reduces the inflow artefact seen in EPISTAR. However, the gradients played out during control and label experiments are different and therefore eddy-current effects may differ. An improved version of EPISTAR [83] consisted of a labelling pulse, identical as in the previous version, and two inversion pulses at the same location as the labelling slab, rather than a single pulse above imaging slice as in the original version. This allowed multislice acquisition as the MT effects were identical in both label and control pulses.

Another alteration to EPISTAR, TILT (Transfer Insensitive Labelling Technique) introduced by Golay *et al.* [84] enabled multislice acquisition by splitting one inversion pulse into two pulses for labelling. For the control, the second pulse is phase shifted by 180 °, which brings the magnetisation back to its relaxed state. The efficiency of this approach is low in the presence of inhomogeneities of RF pulses. In PULSAR (Pulsed Star Labelling or Arterial Regions) [85], the inversion was done with a single adiabatic pulse, whereas in control, double inversion pulses of half of the power were applied, as in EPISTAR.

A different approach was presented by Kwong *et al.* [66] and Kim, which was named by Kim: Flow-Sensitive Alternating Inversion Recovery, FAIR [86]. Here, selective and non-selective pulses are employed to produce control and label, respectively. Provided, that both pulses have identical effects on static spins in the imaging plane, the difference image is free from MT artefact and represents only the inflowing spins. The blood entering the imaging slice is inverted by nonselective RF (label), but fully relaxed if selective RF was applied. The problem with this approach is to produce as sharp inversion pulse over the entire slice to match the nonselective inversion.

The most common designs of ASL experiment are presented in the figure 4.2.

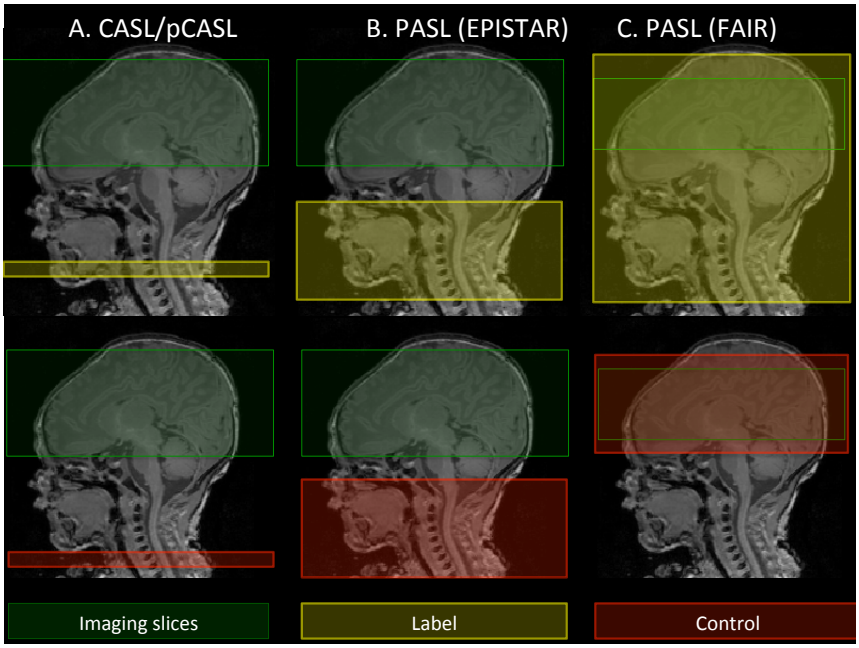

Figure 4.2: *ASL designes for CASL/pCASL (A), PASL (B) and FAIR (C). The colour boxes represent: the imaging slices (green), label (yellow) and control (red) pulses position.*

4.5 Considerations in neonatal ASL experiment design and CBF quantification

4.5.1 Cerebral blood flow rate and perfusion signal

CBF in the neonates is low, which means that the perfusion signal ΔM is correspondingly lower than that found in adults. This is presented in figure 4.3, which shows the signal change for two CBF values: 60 ml/100g/min (red line, adult) and 20 ml/100g/min (blue line, neonate), simulated using the general kinetic model (equations: 4.2, 4.3 - 4.4). Each of the flow values was also used to plot perfusion signal of two labelling schemes: pseudo-continuous ASL (pCASL, solid line) and pulsed ASL (PASL dashed line) for comparison. As expected, the pCASL technique provides higher perfusion signal compared to PASL and therefore pCASL is a method of choice for neonatal perfusion imaging [87]. A consequence of low CBF in neonates is reduction in SNR, which means that more repetitions of control/label pairs are needed to reliably quantify perfusion.

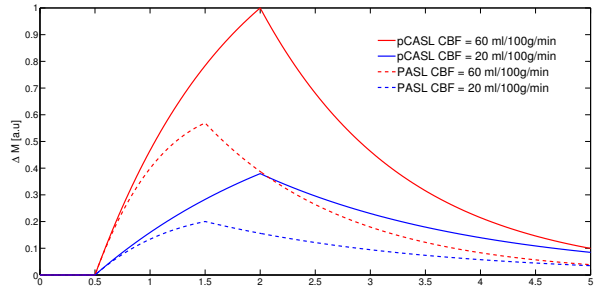

Figure 4.3: *Buxton Model: theoretical curves ΔM for pCASL and PASL. Other parameters for the simulations were: $T_{1a} = 1.7$ s, $T_{1t} = 1.3$s for adults (red), $T_{1a} = 1.5$ s, $T_{1t} = 2$s for neonates (blue), $\alpha = 1$, $\lambda = 1$, $\tau = 1.5$s for pCASL and 1s for PASL*

4.5.2 Labelling duration

In pCASL, the labelling duration is controlled by the operator and can depend on hardware limitations. Figure 4.4 shows the implications of changing the labelling duration in pCASL: the longer τ the greater the signal. To understand further the reason for increased signal for longer labelling, the dependency of labelling duration vs approach to the steady state is plotted in the figure 4.5. It shows the term related to the approach to the steady state: $1 - \exp\left(-\tau/T_1'\right)$ where $1/T_1' = 1/T_{1t} + f/\lambda$ (equation 4.7 for $ATT + \tau < t$). Steady state is the level at which the perfusion signal is maximum for given flow f and T_1'. Prolonging the labelling duration brings the state closer to the steady state. It can be seen from the Figure 4.5 that the steady state is reached more slowly in case of neonates, with lower CBF values, than for adults. In order to match the level of steady state in neonatal group with that of adults with 1.5s labelling duration, τ of 2.4s would have to be used. However, the longer duration of labelling means longer acquisition times which in turn reduces the temporal resolution of the method and its efficiency i.e. number of averages which can be acquired in a given scan time. Longer acquisition might be also more prone to motion artefact. Also, long labelling duration might be not feasible due to hardware limitations (CASL RF amplifier or gradient duty cycle) or SAR limits (pCASL) as well as decay of the label. Therefore the labelling duration of 1.5s is commonly used in practice. Moreover, in the case of neonates and young infants with long T_{1a}, the flowing blood might not fully relax before the control condition and therefore create negative voxels after subtraction of the label and control images, which has been reported by [88]. In their PASL experiment, the labelling slab covered almost the whole infant body. Additionally, the infants imaged had a heart condition causing the mixing of the blood from systematic and pulmonary circulation and cross-contamination of the label and control acquisitions. The amount of negative voxel was

much reduced by reduction of the labelling slab width. When using a labelling method with a thin labelling plane, i.e. pCASL in babies without any heart disease, the mixing and negative voxels, however, should not be an issue.

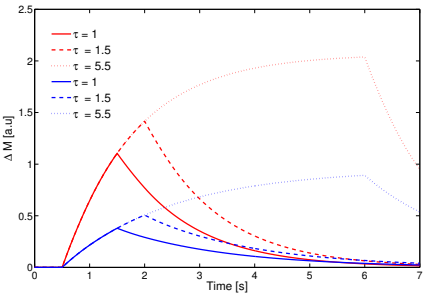

Figure 4.4: *Buxton Model: the effect of labelling duration τ on the pCASL signal. Other parameters for the simulations were: $T_{1a} = 1.7$ s, $T_{1t} = 1.3s$,CBF = 60 ml/100g/min for adults (red), $T_{1a} = 1.5$ s, $T_{1t} = 2s$, CBF = 20 ml/100g/min for neonates (blue), $\alpha = 1$, $\lambda = 1$,$\tau = 1.5s$*

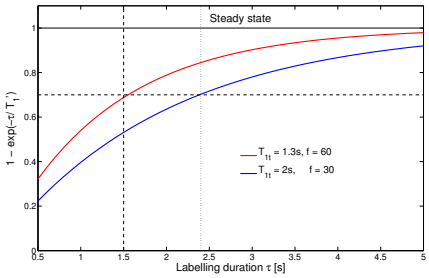

Figure 4.5: *Buxton Model: the approach to the steady state for pCASL. Other parameters for the simulations were: CBF = 60 ml/100g/min, $T_{1t} = 1.3s$ and $\lambda = 0.9$ for adults (red), CBF = 30 ml/100g/min, $T_{1t} = 2s$ and $\lambda = 1$ for neonates (blue)*

4.5.3 Arterial blood relaxation time T_{1a}.

Arterial blood relaxation time T_{1a} depends on the haematocrit (Hct). Haematocrit is the volume of the blood occupied by the red blood cells and can vary hugely in the neonatal population (28-67%), with significant changes within days [89]. It has been shown for a narrow range of Hct levels of healthy adults, that the relationship between haematocrit and T_{1a} can be described as [90]:

$$\frac{1}{T_{1a}} = a \cdot Hct + b \tag{4.11}$$

Varela et al. [89] found a similar dependency in a neonatal population: $a = 0.5$ s $^{-}1$ and $b = 0.37$ and the range of T_1 of the venous blood T_{1v} to be 1393ms to 2035 ms.

The kinetic model of ΔM for a range of T_{1a} and T_{1t} in adults and in neonates is plotted in Figure 4.6 and 4.7. This clearly shows, that the T_{1a} has a significant effect on ΔM as opposed to T_{1t} and therefore the knowledge of T_{1a} is crucial for appropriate CBF quantification.

4.6 Findings and limitations of neonatal ASL studies

ASL in neonates has proven feasible and useful by a number of groups. Licht *et al.* [91] used ASL to assess CBF in 23 term neonates with severe congenital heart defect. They used PASL

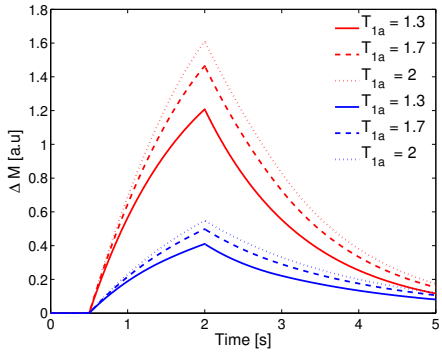

Figure 4.6: *Buxton Model: the effect of T_{1a} on the pCASL signal. Other parameters for the simulations were: T_{1t} = 1.3 and CBF = 60 ml/100g/min for adults (red), T_{1t} = 2s and CBF = 20 ml/100g/min for neonates (blue), $\alpha = 1$, $\lambda = 1$, $\tau = 1.5s$*

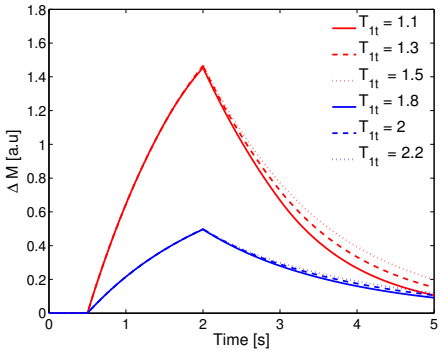

Figure 4.7: *Buxton Model: the effect of T_{1t} on the pCASL signal. Other parameters for the simulations were: T_{1a} = 1.7 and CBF = 60 ml/100g/min for adults (red), T_{1a} = 2s and CBF = 20 ml/100g/min for neonates (blue), $\alpha = 1$, $\lambda = 1$, $\tau = 1.5s$*

that had been previously validated in children [88]. They confirmed the previous findings of much lower CBF compared to healthy adults (mean of 19 ml/100g/min ranging from 7 to 43 ml/100g/min vs 40-60 ml/100g/min in healthy adults [82]) and found association between low CBF baseline and poor CO_2 reactivity with periventricular leukomalacia (PVL). There were two major limitations of the study. First, the absence of a control group. Second, the assumption of a constant value of blood T_1 for adults and neonates (1.2s at 1.5T). It has been shown by Lu *et al.* [90], that blood T_1 is dependent on haematocrit. This finding was also confirmed in neonates by Varela *et al.* [89]. Since the values of haematocrit in neonates can range from 0.27 to 0.7 [89], this results in a range of T_1 of blood between 1.4 and 2s at 3T, which has a significant effect on CBF quantification.

Miranda *et al.* [58] looked at CBF in healthy, unsedated term and preterm neonates at term-equivalent age. Apart from global CBF in the whole brain (WB) they also reported regional values of CBF in basal ganglia (BG) cortical grey matter (GM) and white matter (WM), which were found higher at pre-terms than term infants. In both groups, CBF was the highest in BG (39 and 30 ml/100g/min for pre terms and terms respectively), and was approximately twice of that in cortical GM (19.3 and 15.8 ml/100g/min for pre terms and terms respectively). WM perfusion was the lowest (14.8 and 10.3 ml/100g/min for pre terms and terms respectively). WB perfusion was lower in term controls (16.6 ml/100g/min) compared to preterm infants (21.3 ml/100g/min). This was the first imaging study carried out in heathy infants, permitted by the non-invasive nature of ASL MRI. However, a similar limitation in this study was present, i.e. a fixed T_1 of the blood equal to 1.5s.

Wintermark *et al.* [92] investigated changes in CBF before, during and after therapeutic hypothermia in asphyxiated neonates. Three groups were enrolled to the study: 11 HIE neonates that received hypothermia, 7 neonates who were not cooled and 4 controls without brain injury. They found that CBF values in the first week of life were significantly different in neonates developing brain injury compared to the ones that did not indicating that the severity of the encephalopathy has an effect on brain perfusion, regardless of hypothermia. Also, despite hypothermia, some asphyxiated cooled neonates (that later exhibited injury) displayed hyperperfusion in brain areas (up to 78 ml/100g/min in BG, 19 ml/100g/min in WM and 64 ml/100g/min in GM injury), similarly to infants that were not cooled and also developed BG, WM or GM injury (up to 88 ml/100g/min in BG, 15 ml/100g/min in WM and 88 ml/100g/min in GM). For comparison, in controls, the mean CBF was 28, 3 and 39 ml/100g/min in BG, WM and GM respectively.

Pienaar *et al.* [93] used the pseudo-continuous method of labelling in ASL to study the correlation between abnormal perfusion and diffusion weighted images (DWI) in non-cooled HIE infants. Diffusion weighted images are used to identify the areas of metabolic stress or evolving necrotic injury. Decrease in apparent diffusion coefficient (ADC) is associated with complete energy failure in adult ischaemic stroke. The main finding of their work was the correlation between regions of increased perfusion and low ADC intensity on DWI. The WB CBF ranged from 13 to 33 ml/100g/min in healthy controls (2 days to 4 weeks of life at the scan) and from 10 to 70 ml/100g/min in HIE babies (0 to 4 days of life at the scan, with regional CBF ranging from 70 to 160 ml/100g/min). However, the post labelling delay of 1s might have skewed the results of CBF quantification, as it is likely that not all the labelled blood has reached the imaging slice by the time of imaging. Additionally, the labelling duration of 1.2s might not have been enough to reach the required steady state.

Massaro *et al.* [94] aimed to correlate the injury seen on conventional MRI and that on ASL images. Reported CBF was: in WB 24 and 19 ml/100g/min, in BG 52 and 31 ml/100g/min, in thalamus 52 and 29 ml/100g/min and in WM 12 and 10 ml/100g/min in HIE and control group respectively. The HIE infants and controls were scanned in the second week of life. They found increased CBF in BG and thalamus in infants with HIE and no qualitative injury on conventional MRI compared with healthy controls. The quantification, however, might have been affected by the choice of short PLD of 1.025s as well as choosing a fixed tissue and blood T_1 of 1.2s and 1.6s respectively.

Recently, Boudes *et al.* [87] compared the performance of pulsed and pseudo-continuous

ASL in asphyxiated newborns. The authors found that both methods were feasible and the quantified CBF with each technique was strongly correlated. Mean CBF quantified in a single slice was highest in the most affected neonates (33.51 $\pm$16.73 and 32.41 $\pm$ 14.43 ml/100g/min for PASL and pCASL respectively) and lower in lest affected neonates (27.48 $\pm$8.21 and 24.65 $\pm$ 8.82 ml/100g/min for PASL and pCASL respectively) as well in the control group (27.22 $\pm$ 8.23 and 24.27 $\pm$ 5.83 ml/100g/min for PASL and pCASL respectively). The authors used blood T_1 of 1.8s for all neonates. In addition, the pCASL images were characterised by significantly superior image quality compared to PASL, which was quantified using an image quality score.

4.7 Summary

This chapter provided a motivation for choosing pCASL for neonatal perfusion measurements, reviewed arterial spin labelling techniques, CBF quantification and model limitations resulting in quantification errors. Also, a short summary of the recent work on neonatal perfusion measurement was given. This gave the motivation for detailed analysis of pCASL labelling that follows in chapter 5 and theoretical background for the protocol optimisation presented in chapter 7.

Chapter 5

pCASL simulator for labelling efficiency estimation

5.1 Introduction

In this chapter, a detailed theory of continuous and pseudo-continuous labelling will be introduced, together with the theoretical basis for labelling efficiency changes due to magnetic field inhomogeneity and orientation of the flow direction to the labelling plane. Next, a method for efficient numerical simulation of the Bloch equations for labelling efficiency estimation will be given, which will be then used to investigate the changes of labelling efficiency for a range of velocities, inhomogeneities and orientations. Following the simulations, in-vivo validation of the simulator will be described. Finally, the simulator will be used to estimate labelling efficiency in neonates. An additional application of the simulator for renal blood flow quantification in healthy adults is given in an appendix.

5.2 Theoretical background

5.2.1 Labelling efficiency

In the previous chapter the perfusion signal of pseudoontinuous Arterial Spin Labelling (pCASL) was modelled and it was shown that accurate quantification of CBF depends heavily on accurate estimation of labelling efficiency α (equations 4.7 and 4.10 in chapter 4). Labelling efficiency is defined as the maximum difference in longitudinal magnetisation M_z after control and label

pulses:

$$\alpha = \frac{M_{z,C} - M_{z,L}}{2M_0} \tag{5.1}$$

where $M_{z,C}, M_{z,L}$ are the longitudinal magnetization after the control and label pulses, respectively and M_0 is fully relaxed magnetisation. For perfect inversion after labelling ($M_{z,L} = -M_0$) and perfect non-inversion after control ($M_{z,C} = M_0$), $\alpha = 1$. Therefore to estimate labelling efficiency, knowledge of $M_{z,C}$ and $M_{z,L}$ is necessary. $M_{z,C}$ and $M_{z,L}$ can be calculated theoretically from the solution of the Bloch equations, described in detail in section 3.2.2 of chapter 3.

5.2.2 Continuous ASL (CASL)

Magnetic labelling in CASL is achieved through velocity-driven adiabatic inversion [61]. A constant RF pulse $B(t) = B_1 \exp(-i\omega_{RF}t)$ with amplitude B_1 is applied concurrently with a field gradient G in the direction of the flowing spins. The frequency offset of this pulse is chosen to define labelling plane at position r_0 (with respect to the gradient isocenter) according to equation 3.41: $\delta\omega_{RF} = r_0\gamma G$. The moving spins will experience variable angular frequency offset, which in the reference frame rotating at frequency $\omega_{RF} = \gamma B_0 + \delta\omega_{RF}$ is defined, similarly to 3.19, as:

$$\Delta\omega(t) = \gamma B_0 + \gamma G r(t) - \omega_{RF} = \gamma G\left[r(t) - r_0\right] \tag{5.2}$$

where $r(t)$ is position of the spin in relation to the magnet isocenter. The effective magnetic field $\hat{B}_{eff}$ will have $\hat{z}$ component equal to $\Delta\omega(t)/\gamma$ and $\hat{x}$ component given by the magnitude of the RF pulse:

$$\vec{B}_{eff} = \frac{\hat{z}\Delta\omega(t)}{\gamma} + \hat{x}B_1 \tag{5.3}$$

As the spins flow through the field gradient the $\hat{z}$ component of B_{eff} changes from parallel to anti-parallel and so does the direction of the $\vec{B}_{eff}$ (Figure 5.1 (a - f)). If the adiabatic condition is met, the spins magnetisation will nutate around $\vec{B}_{eff}$ and therefore follow its direction. The adiabatic condition for spins flowing with velocity v is given by:

$$\frac{1}{T_{2b}} \ll \frac{G \cdot v}{|\vec{B}_{eff}|} \ll \frac{\gamma}{2\pi}|\vec{B}_{eff}| \tag{5.4}$$

where T_{2b} is the T_2 relaxation time of the arterial blood. At low velocities, the inversion efficiency is reduced, as the T_2 relaxation dominates. If the velocity of the spins is too high, then the change of B_{eff} is too rapid for the magnetisation to follow and the efficiency is also reduced.

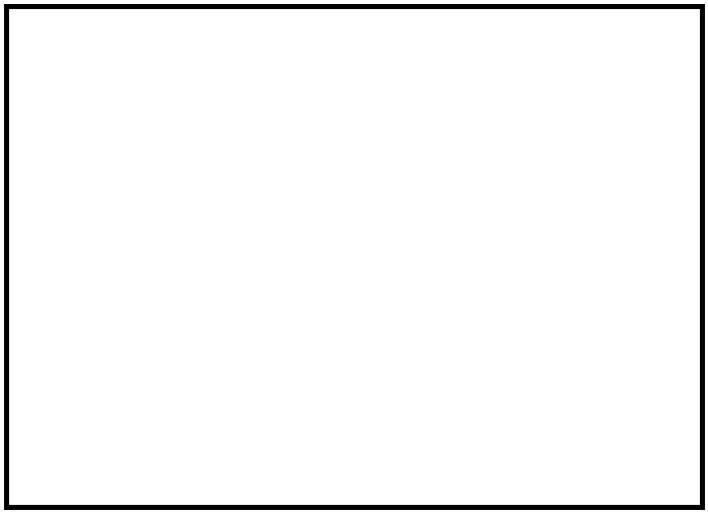

Figure 5.1: *Flow driven adiabatic passage (figure 17.6 from [12])*

5.2.3 Pseudo-Continuous ASL (pCASL)

Pseudo-continuous ASL [65] was designed to perform flow driven inversion in a way that does not require a long RF pulse and therefore additional hardware, as in case of CASL. To achieve this, the inversion of flowing spins is realised by using a train of short RF pulses and gradients. To understand the principles of the pCASL labelling train design, firstly, the rectangular train of pulses is considered in the presence of a constant gradient. RF_r pulse train with rectangular width δ_t and spacing Δt can be mathematically represented as a convolution of comb and rect functions:

$$RF_r(t) = \frac{1}{\Delta t}\mathrm{comb}\left(\frac{t}{\Delta t}\right) * \mathrm{rect}\left(\frac{t}{\delta_t}\right) \tag{5.5}$$

where $*$ is the convolution and comb and rect functions are given by:

$\mathrm{comb}_{\Delta t}(t) = \sum_{n=-\infty}^{\infty} \delta\left(t - n\Delta t\right) = \frac{1}{\Delta t}\mathrm{comb}\left(\frac{t}{\Delta t}\right)$

and

$$\mathrm{rect}\left(t/\delta_t\right) = \begin{cases} 1 & |t| < \frac{\delta_t}{2} \\ 0 & \textit{otherwise.} \end{cases}$$

The Fourier transform of such defined $RF_r(t)$ is given by:

$$F\{RF_r\left(t\right)\} = \mathrm{comb}\left(f\Delta t\right) \cdot \delta_t \mathrm{sinc}\left(\pi\delta_t f\right) \tag{5.6}$$

since $F\{\mathrm{comb}_{\Delta t}\left(t\right)\} = \frac{1}{\Delta t}\mathrm{comb}_{\frac{1}{\Delta t}}\left(f\right)$, and

$$\frac{1}{\Delta t}\mathrm{comb}_{\frac{1}{\Delta t}}\left(f\right) = \sum_{N=-\infty}^{\infty} \delta\left(f - N\frac{1}{\Delta t}\right) = \sum_{N=-\infty}^{\infty} \delta\left(f - N\Delta f\right) = \mathrm{comb}(f\Delta t).$$

Therefore, RF_r will result in a number of aliased (repeated) frequencies: $\frac{N}{\Delta t}$ with their Fourier response modulated by broad sinc function. In a presence of a constant gradient G applied during RF_r train, these frequencies will correspond to labelling planes positioned at $r_{a,N} = \frac{2\pi N}{\gamma G \Delta t}$, where γ is the gyromagnetic ratio.

The presence of these undesired aliased labelling planes can be reduced by choosing a RF pulse with its Fourier response dropping more rapidly, for example Hanning pulse. The train of Hanning pulses $RF_h(t)$ can be written as a convolution $*$ of comb and Hanning function:

$$RF_h(t) = \frac{1}{\Delta t}\mathrm{comb}\left(\frac{t}{\Delta t}\right) * H\left(\frac{t}{\delta_t}\right) \tag{5.7}$$

where Hanning function is defined as: $H(t) = \begin{cases} 0.5 + 0.5\cos(2\pi t) & |t| < \frac{1}{2} \\ 0 & \textit{otherwise.} \end{cases}$

and its Fourier transform given by:

$$F\{RF_h(t)\} = \mathrm{comb}\left(f\Delta t\right) \cdot \delta_t \mathrm{sinc}\left(\pi \delta_t f\right) \frac{1}{2\left(1 - \delta_t^2 f^2\right)}. \tag{5.8}$$

The Fourier response of Hanning pulse train drops quadratically faster than that of a square pulse, however it is too broad to supress all aliased planes. The spatial selectivity of the RF train can be further improved by increasing the gradient amplitude G_{max} during each of the Hanning pulses in relation to the average gradient G_{ave} played out between the consecutive pulses Δt (Figure 5.2).

This way the position of the first aliased labelling plane $r_{a,1} = \frac{2\pi}{\gamma G_{ave} \Delta t}$ will fall outside the excitation profile of RF_h pulse frequency response (the half width of Hanning pulse can be approximated to $r_{hw} = \frac{2\pi}{\gamma G_{max} \delta_t}$). Hence, in order to avoid aliased labelling planes the condition:

$$r \gg r_{hw} \Rightarrow \frac{G_{max}}{G_{ave}} \gg \frac{\Delta t}{\delta_t} \tag{5.9}$$

needs to be fulfilled. To achieve the position-dependent frequency offset $\Delta\omega$ (5.2) during the time between the pulses, the average gradient between the pulses (G_{ave}) needs to be comparable to G used in CASL. Additionally, an average $B1$ over the same period of time should be comparable to that of CASL.

There are two variations of control experiment: 'balanced' [95], and 'unbalanced' [96]. 'Balanced' scheme has a control gradient train identical to that of label. In the 'unbalanced' variation, G_{ave} is equal to zero for control condition. Additionally, for both methods, the phase of every other RF pulse in the control pulse train is π shifted, reversing the effect of the previous

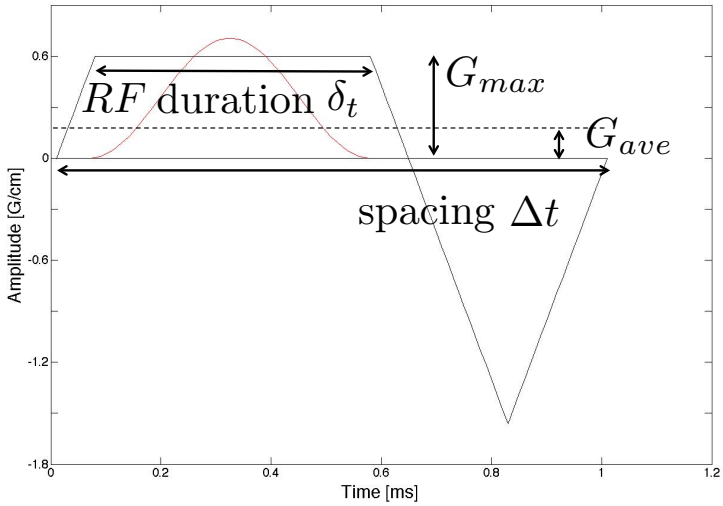

Figure 5.2: *A single module of pCASL labelling train*

pulse. For labelling planes located at r_0 outside scanner isocenter, the frequency offset of the RF pulses is given by:

$$\delta\omega_{RF} = \gamma G_{max} r_0 \tag{5.10}$$

and the phase increment between consecutive pulses at the location r_0, sometimes referred to as 'tracking phase' [97]:

$$\Delta\phi = \gamma G_{ave} r_0 \Delta t \tag{5.11}$$

and for the control condition, the phase of the n-th pulse of the train:

$$\Delta\phi_n = \gamma G_{ave} r_0 \Delta t + \pi \cdot \frac{(1+(-1)^n)}{2} \tag{5.12}$$

On the other hand, if the proton moves through the gradient field, with its initial position r_0 and velocity v_0, the true phase accrued between the pulses is given by:

$$r(t) = r_0 + v_0 t; \Delta\phi = \phi(t_0, \Delta t)$$

$$\begin{aligned}
\Delta\phi_{true} &= \gamma \int_0^{\Delta t} G(t) \cdot r(t) dt \\
\Delta\phi_{true} &= \gamma \int_0^{\Delta t} G(t) \cdot (r_0 + v_0 \cdot t)\, dt \\
\Delta\phi_{true} &= \gamma \cdot G_{ave} \cdot r_0 \cdot \Delta t + \frac{1}{2} \cdot \gamma v_0 G_{ave} \Delta t^2
\end{aligned} \tag{5.13}$$

The velocity dependant component $\frac{1}{2} \cdot \gamma v G_{ave} \Delta t^2$ is small and therefore there is usually no need to account for in the in $\Delta\phi$ calculations. However, for high v_0 or for large gradient inhomogeneities the velocity dependant phase accrual might become a source of discrepancies between $\Delta\phi_{true}$ required to track the spins phase and that subscribed, $\Delta\phi$.

Pseudo-Continuous ASL (pCASL) in a presence of B_0 inhomogeneities and correction methods

Two types of magnetic field inhomogeneities can influence the labelling efficiency: δB_0 and position dependent inhomogeneities, δG_{inh}.

B_0 inhomogeneities. The presence of B_0 inhomogeneities, δB_0, changes of the resonance condition which shifts the labelling plane by $\Delta r = r_0 - r_0'$, as illustrated in the image 5.3. The new position of the labelling plane can be found from:

$$\frac{\gamma \delta B_0}{\Delta r} = \frac{\gamma G_{max} r_0}{r_0} \Rightarrow r_0' = r_0 - \frac{\delta B_0}{G_{max}} \tag{5.14}$$

Additionally, the true phase accrued between two consecutive pulses of the pCASL RF train becomes:

$$\Delta\phi = \gamma G_{ave} r_0 \Delta t + \frac{1}{2} \cdot \gamma v_0 G_{ave} \Delta t^2 + \Delta\phi_{error} \tag{5.15}$$

where:

$$\Delta\phi_{error} = \gamma \delta B_0 \Delta t + \frac{1}{2} \cdot \gamma v_0 \delta B_0 \Delta t^2 \tag{5.16}$$

G_{inh} inhomogeneities. The position dependent inhomogeneities, δG_{inh}, can influence the labelling efficiency in two ways: affecting the phase increment between two pulses, similarly to the δB_0 and by changing the rate of the frequency sweep required for pseudo-adiabatic inversion (see equations 5.2 and 5.4 with $G = G_{ave} + \delta G_{inh}$) and therefore the phase accrued between the pulses. Similarly to δB_0, the true phase accrued between the pulses is given by 5.15 with:

$$\Delta\phi_{error} = \gamma \delta G_{inh} (r_{G_{inh}} - r_0) \Delta t + \frac{1}{2} \cdot \gamma v (G_{inh}) \Delta t^2 \tag{5.17}$$

where $r_{G_{inh}}$ is the point of crossing of the G_{inh} with ω axis. Changes of the position and the thickness of the labelling plane are given by:

$$\delta\omega_{RF} = \gamma G_{max} r_0 + \gamma \delta G_{inh} (r_{G_{inh}} - r_0) \Rightarrow r_0 = \frac{\delta\omega_{RF} - \delta G_{inh}}{\gamma (G_{max} + \delta G_{inh})} \tag{5.18}$$

Additionally, δG_{inh} might further deteriorate the efficiency by changing $\frac{G_{max}}{G_{ave}}$ fraction:

$$\frac{G'_{max}}{G'_{ave}} = \frac{G_{max} + \delta G_{inh}}{G_{ave} + \delta G_{inh}} \tag{5.19}$$

which might mean that 5.9 is no longer met and the aliased labelling planes are not appropriately separated from the main labelling plane.

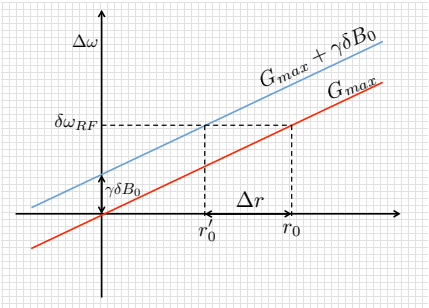

Figure 5.3: *The shift of the labelling plane as a result of* δB_0

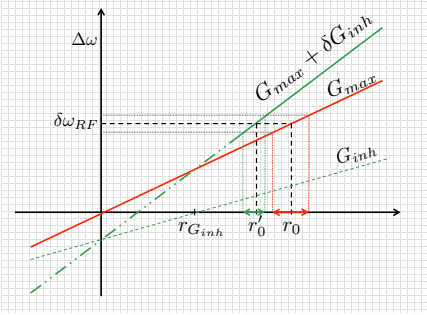

Figure 5.4: *The shift of the labelling plane and thickness change as a result of* δG_{inh}

Methods of $\Delta\phi$ correction. The methods for B_0 inhomogeneity correction rely on finding an additional phase increment, $\Delta\phi_{add}$ can be added to $\Delta\phi$ to minimise the effect of $\Delta\phi_{error}$:

$$|\Delta\phi_{error} - \Delta\phi_{add}| = 0$$

so that the corrected phase increment is equal to:

$$\Delta\phi_{corrected} = \gamma G_{max} r_0 + \Delta\phi_{error} - \Delta\phi_{add} \tag{5.20}$$

Several methods of finding $\Delta\phi_{add}$ has been proposed. In multiphase pCASL (MP-PCASL) [97], images are acquired with eight-phase tagging cycle, with $\Delta\phi_{add}$ ranging from 0 to 7π/4 every π/4. Then, multiple signal averages are fitted to the function of expected inversion response to the phase changes (modified Fermi function, or more recently a cos function [98] at 7T) to yield the PWI and $\Delta\phi_{error}$ on a per-voxel basis. A modification of this approach is to acquire images with two different $\Delta\phi_{add}$ values and determine the $\Delta\phi_{error}$ from a look-up table [99]. Both approaches rely on an accurate definition/prediction of the response function.

An extension to MP-PCASL is optimised pCASL (OptPCASL) [100],[98]. In OptPCASL method, $\Delta\phi_{error}$ is found at each main artery location from a pre scan and a mask of perfusion territories, and compensated for with the use of additional gradients in xy plane.

A different approach is to find δB_0 and δG_{inh} from a B_0 map acquired at the level of the labelling plane [101]. From the map, $\Delta\phi_{error}$ as well as an additional gradient can be calculated and added to the refocusing gradient of the pCASL train. The advantage of the last approach is that it does not require any assumption related to inversion response function and corrects for velocity dependent phase accrual, as stated in the equation 5.17, and has greater SNR efficiency compared to MP-PCASL, in which multiple acquisitions are repeated with sub-optimal $\Delta\phi_{add}$. However, it does require an additional scan, and therefore, similarly to OptPCASL, requires more scanning time.

pCASL for spins traveling through labelling plane not perpendicular to the flow direction

The usual assumption made for pCASL is that the spins flow through the labelling plane positioned perpendicularly to the direction of the flow. However, this might not be always the case for all feeding arteries simultaneously, given their anatomy and relative position/orientation to each other. Since the normal to the labelling plane designates the direction of the pCASL gradients, any deviation from the normal means that the rate of change of the spins' position in the gradient field (with the respect to the labelling plane) is different to that of the spins velocity along the direction of the artery (see image 5.5).The new value of effective velocity will be equal to:

$$v_{eff} = |\vec{v}| \cdot cos\,(\xi) \tag{5.21}$$

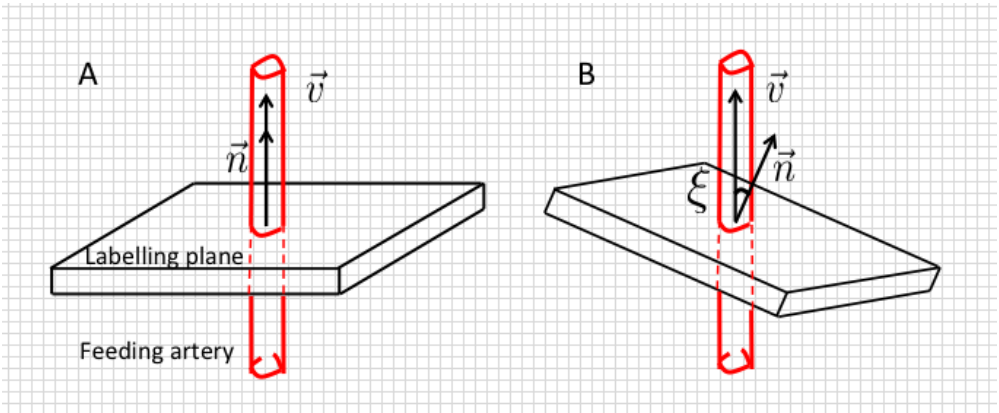

Figure 5.5: *Spins traveling though the labelling plane within an artery perpendicular to the labelling plane (A) and in one that makes an angle ξ with the normal to the labelling plane (B)*

5.3 Bloch equation simulator

To estimate the theoretical labelling efficiency for spins moving with a range of velocities in different scenarios, a Bloch equation simulator was implemented in Matlab. A particle with starting magnetisation vector $\vec{M}_0$ aligned with the direction of the main magnetic field B_0, was moving with a velocity υ through a total distance r, in the presence of RF pulses and field gradients. After each time interval dt, the location of the particle was updated according to: $r_{n+1} = r_n + \upsilon \cdot dt$. To find $\vec{M}$ at each location r_i, the Bloch equation was solved using the matrix representation [102]. In this representation, the solution of the Bloch equations is equivalent to rotation around $\vec{B}_{eff}$ in the B_{eff} rotating frame. Since $\vec{B}_{eff}$ is not constant during adiabatic inversion, the numerical solution is found by integration of small, finite rotations of the magnetisation vector $\vec{M}$. During each time step dt, $\vec{M}$ will process about $\vec{B}_{eff}$ by the angle:

$$\varphi = 2\pi\gamma|\vec{B}_{eff}|dt \tag{5.22}$$

In the case of pCASL, the selective pulses are interleaved with refocusing gradients. During an RF pulse, $\vec{B}_{eff}$ is considered in ω_{RF} rotating frame, and therefore equal to:

$$|\vec{B}_{eff}| = \sqrt{\left(\frac{\hat{z}\Delta\omega(t)}{\gamma}\right)^2 + B_1^2} \tag{5.23}$$

where $\Delta\omega(t)$ is defined by equation 5.2 and the angle θ that $\vec{B}_{eff}$ makes with $\hat{z}$ direction of the ω_{RF} rotating frame is equal to $\theta = \arctan\left(\frac{B1}{\Delta\omega/\gamma}\right)$. In the absence of the RF pulse, the $\vec{B}_{eff}$ frame rotates with the frequency at the isocenter, equal to γB_0, and therefore $\Delta\omega$ and $|\vec{B}_{eff}|$ reduces to $\gamma Gr(t)\hat{z}$ and $\frac{\Delta\omega(t)}{\gamma}$ respectively. The angle that the ω_{RF} frame rotates about the isocenter frame within the duration of the pulse δ_t can be found from: $\psi = \delta\omega_{RF}$. All the above can be combined into one rotation matrix R: and applied to magnetization vector $\vec{M}$ for each time point dt:

$$R = R_z(\psi)^{-1}R_z(\phi)^{-1}R_y(\theta)^{-1}R_z(\varphi)R_y(\theta)R_z(\phi) \tag{5.24}$$

where:

$$R_y(\theta) = \begin{bmatrix} \cos\theta & 0 & -\sin\theta \\ 0 & 1 & 0 \\ \sin\theta & 0 & \cos\theta \end{bmatrix} \quad R_z(\varphi) = \begin{bmatrix} \cos\varphi & \sin\varphi & 0 \\ -\sin\varphi & \cos\varphi & 0 \\ 0 & 0 & 1 \end{bmatrix}$$

$$R_{z,\psi} = \begin{bmatrix} \cos\psi & \sin\psi & 0 \\ -\sin\psi & \cos\psi & 0 \\ 0 & 0 & 1 \end{bmatrix}$$

which can be seen as changing the coordinate system to one aligned with the phase ϕ of applied RF pulse $R_z(\phi)$ (changing in accordance to 5.11 and 5.12), next from ω_{RF} frame to the one where $\vec{B}_{eff}$ is aligned with $\hat{z}$: $R_y(\theta)$, then rotation around the direction of B_{eff} $R_z(\varphi)$ and return to the original reference frame by inverse transformations $R_z(\phi)^{-1}$ and $R_y(\theta)^{-1}$. Finally, $R_z(\psi)^{-1}$ accounts for the rotation of ω_{RF} rotating frame with respect to the isocentre frame after each pulse.

In the case of CASL, the RF pulse is applied constantly and therefore R simplifies to:

$$R = R_y(\theta)^{-1} R_z(\varphi) R_y(\theta) \tag{5.25}$$

The effect of T_1 and T_2 relaxations are accounted for by 3.28:

$$W(t) = \begin{bmatrix} \exp(-dt/T_2) & 0 & 0 \\ 0 & \exp(-dt/T_2) & 0 \\ 0 & 0 & \exp(-dt/T_1) \end{bmatrix} \tag{5.26}$$

and

$$Q(t) = \begin{bmatrix} 0 \\ 0 \\ M_0 \cdot [1 - \exp(-dt/T_1)] \end{bmatrix}$$

Therefore for each iteration, a new orientation of $\vec{M}$ was found as a result of the rotations and relaxations:

$$\vec{M}_{n+1} = WR\vec{M}_n + Q \tag{5.27}$$

5.3.1 Methods

Velocities and B_1. Simulations were performed for spins moving through the labelling plane with a range of velocities (1-100cm/s), over a distance of 20 cm. The time step was $4e^{-6}$s. The pCASL RF pulse and gradient trains were matched to that implemented on the Philips scanner ('balanced' variety): G_{max} = 6mT/m, G_{ave} = 0.6 mT/m, Hanning shaped RF pulses with mean B_1 = 1.175 μT for δ_t = 0.5ms and Δt = 1ms (FA =18°, max B_1 = 4.7μT) and B_1 = 0.65 μT

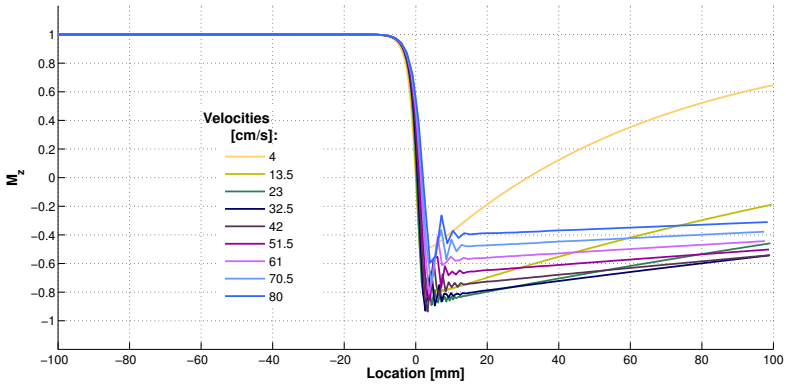

Figure 5.6: *M_z simulation results plotted against the location r. Labelling plane was set at $r = 0$ and T_{1b} and T_{2b} were set to 1.65s and 0.2s respectively. Scanner default settings of the pCASL train was used: FA = 18°, G_{max} = 6 mT/m, G_{ave} = 0.6 mT/m , Δt = 1ms, δ_t = 0.5ms*

(FA = 10°, max B_1 = 2.6μT) to illustrate the effect of the mean B_1 on the labelling efficiency for a range of velocities. The matrix R was pre-computed for each spin location using explicit solutions of matrix multiplications.

A realistic distribution of flow velocities in the arteries can be modelled by a laminar flow. This ensures an appropriate weighting by velocity, as the higher flow velocity the greater volume of the blood delivered by this velocity:

$$\alpha_{weighted}(\upsilon_{max}) = \frac{1}{2\upsilon_{max}^2}\int_0^{\upsilon_{max}} \upsilon\alpha(\upsilon)d\upsilon \tag{5.28}$$

where $\alpha(\upsilon)$ is the efficiency for the particle moving with the velocity υ.

Inhomogeneities. δB_0 and δG_{inh} were considered separately:

1. The influence of δB_0 was tested in two steps: For the first step, a constant filled of 0.0352 [Gauss] (150 [Hz], estimated from field inhomogeneity at the level of labelling plane in [101]) was added to the pCASL gradient train. $\Delta\phi_{add}$ was calculated from equation - 5.16 to compensate for the $\Delta\phi_{error}$ and added $\Delta\phi$ with accordance to equation 5.15. For the second step, the M_z for labelled and control conditions was obtained for $\Delta\phi_{error}$ ranging from $-\pi$ to π and the efficiency calculated according to 5.1.

2. To study the influence of δG_{inh}, additional linear gradient of 0.02 [Gauss/cm] (similarly to [101]) was added to the pCASL gradient train. δG_{inh} gradient was centred at isocenter for simplicity (i.e. $r_{G_{inh}} = 0$.) To illustrate the correction with the additional gradient, the refocusing part of the pCASL gradient train was re-computed to compensate for the

phase accrued in δG_{inh} (δG_{add}). $\Delta\phi_{error}$ was calculated based on equation 5.17 and compensated for with $\Delta\phi_{add}$, ignoring the velocity dependant component.

The pCASL train parameters were matched to the scanner default with FA =18° and the velocity of moving spins was 50 [cm/s].

Alignment. To quantify the labelling efficiency loss due to imperfect alignment with the vector normal to the labelling plane, the simulations were performed for angles ξ equal from 0 (i.e. flow perpendicular to the labelling plane) to 80° (i.e. flow almost parallel to the labelling plane). This was done for the velocities ranging from 1 to 80 cm/s with a step size of 5 cm/s. Additionally, the weighted efficiency was also estimated, as described in 5.3.1.

5.3.2 Results

Velocities and B_1. The results of the Bloch equation simulations of M_z inversion for spins flowing with a range of velocities are shown in the figure 5.6. The calculated efficiencies $\alpha(\upsilon)$ and weighted efficiencies $\alpha_{weighted}(\upsilon_{max})$ for two different mean B_1 are shown in figures: 5.7 and 5.8. It can be noticed in figure 5.7, that the efficiency rapidly increases with the velocity up to about 22cm/s and then slowly decreases. This is consistent with the adiabatic condition prediction 5.4 for slowest and fastest spins and additionally, increasing tracking error $\Delta\phi_{error}$ for the fastest spins. For more realistic laminar flow model, the weighted efficiency reaches its maximum for velocities around 38cm/s and the maximum is flat within a broad range of velocities. Changing the average B_1, as seen in the figure 5.8, improves the efficiency of the slower spins. However, this compromises the efficiency of the spins flowing with the higher velocities. In a cardiac cycle, a range of velocities are expected. Therefore the best parameter choice should provide as little dependency of labelling efficiency on velocity as possible.

Inhomogeneities. The shift of the labelling plane and influence of $\Delta\phi_{error}$ as a result of δB_0 is shown in the figure 5.9. The direction of the shift depends on the sign of the additional δB_0, in the accordance with equation 5.14. The additional phase $\Delta\phi_{add}$ almost perfectly corrects for the shift of the labelling plane and the deterioration of the M_z inversion. In case of the δG_{inh}, the additional gradient in a combination with $\Delta\phi_{add}$ also produce a very good correction. On its own, $\Delta\phi_{add}$ corrects for the labelling plane shift, but only some inversion loss, as shown in figure 5.10. This is due to the velocity dependant part or the true phase accrual between the pulses: $\frac{1}{2}\cdot\gamma\upsilon(G_{ave}+G_{inh})\Delta t^2$ that with G_{inh} became a significant component of the true $\Delta\phi$.

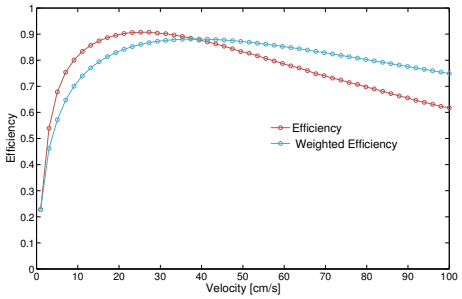

Figure 5.7: *pCASL Labelling efficiency for FA = 18°, G_{max} = 6 mT/m, G_{ave} = 0.6 mT/m, Δt = 1ms, δ = 0.5ms*

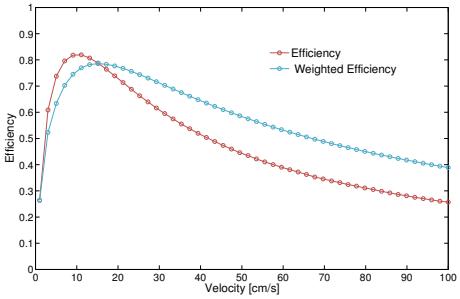

Figure 5.8: *pCASL Labelling efficiency for FA = 10°, G_{max} = 6 mT/m, G_{ave} = 0.6 mT/m, Δt = 1ms, δ = 0.5ms*

The results of the Bloch equation simulations of M_z inversion for spins flowing with a range of velocities and phase offsets $\Delta\phi_{error}$ are shown in the figures 5.11 and 5.12 with the labelling efficiency in the figure 5.13. It can be clearly seen, that spins traveling at different velocities are affected differently. For the slowest spin, the efficiency is preserved for the broadest range of $\Delta\phi_{error}$. The higher the velocity, the quicker deterioration of the efficiency with the increased phase offset. Again, the velocity dependant part or the true phase accrual between the pulses: $\frac{1}{2} \cdot \gamma v_0 \left(G_{ave} + \delta B_0\right) \Delta t^2$ became a significant component of the true $\Delta\phi$, which is not compensated for if δB_0 is unknown.

A very important observation is that for $\Delta\phi_{error} = 180°$, control and label conditions are swapped, as predicted by equation 5.2.3, and the labelling efficiency is equal to 0 for $\Delta\phi_{error} = 90°$.

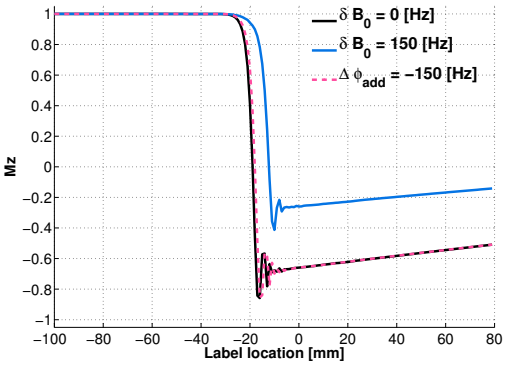

Figure 5.9: *M_z simulation results for δB_0=150 [Hz] (blue),with additional $\Delta\phi_{add} = 54°$ (pink) and inhomogeneity free (black). Other parameters were set to the scanner default, with v = 50 [cm/s]*

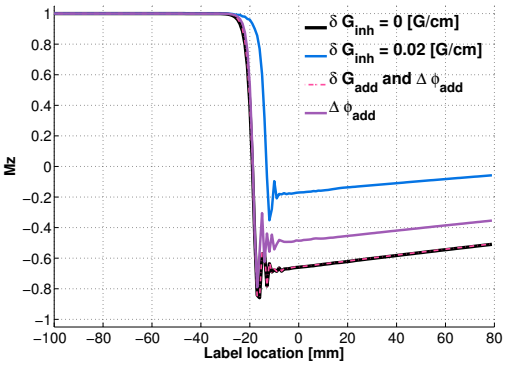

Figure 5.10: *M_z simulation results for δG_{inh}=0.02 [G/cm] (blue), with additional δG_{add} and $\Delta\phi_{add} = 61°$, with only $\Delta\phi_{add} = 61°$ (lilac) and inhomogeneity free inversion (black). Other parameters were set to the scanner default, with v = 50 [cm/s]*

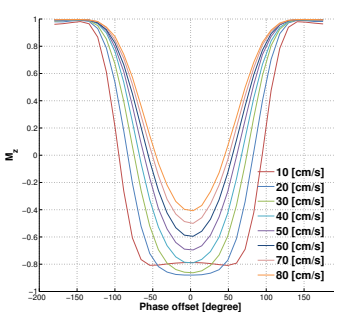

Figure 5.11: *M_z simulation results for a range of velocities as a function of phase offsets; label condition*

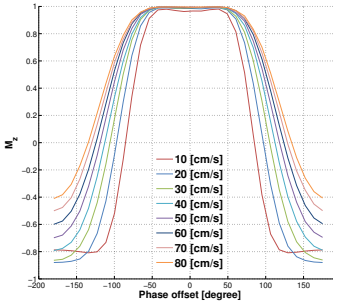

Figure 5.12: *M_z simulation results for a range of velocities as a function of phase offsets; control condition*

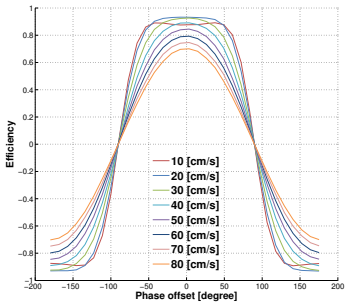

Figure 5.13: *Labelling efficiency for a range of velocities as a function of phase offset*

Aligment. Figures 5.14 and 5.15 show labelling efficiency and weighted labelling efficiency, respectively as a function of the angle ξ. Overall, the inversion process is remarkably robust to the angle between the labelling plane and the flow direction for the flow velocities. This is especially the case for velocities greater than 20 cm/s. For the highest velocities, improvement of efficiency can be observed for high values of ξ as higher ξ reduces $\cos(\xi)$ and therefore, according to equation 5.21, this shifts towards the lower v', for which the efficiency is at its highest. However, for the velocities in the lower range (i.e. less than 20cm/s), the lower the velocity, the quicker reduction of the labelling efficiency with ξ.

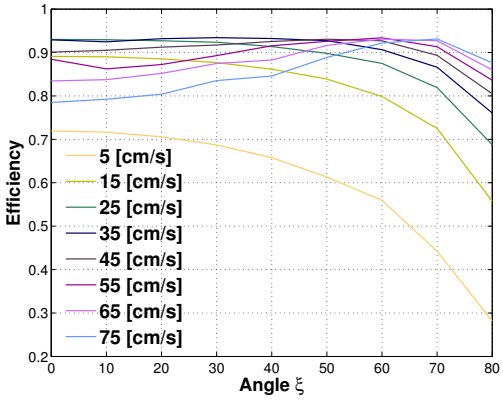

Figure 5.14: *Efficiency as a function of ξ for a range of velocities*

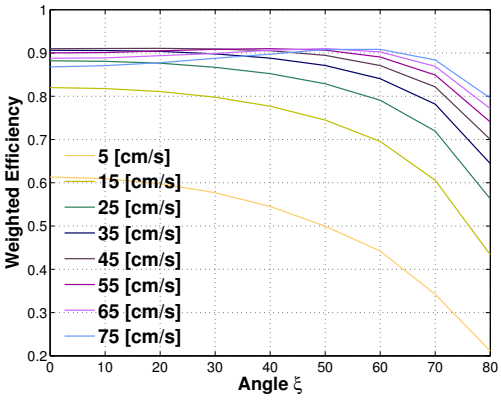

Figure 5.15: *Weighted efficiency as a function of ξ for a range of velocities*

5.3.3 Discussion

Different aspects affecting the labelling efficiency were described and simulated: the field inhomogeneities and angulation of the labelling plane in respect to the vessel. This was done for a range of velocities and different B_1 values. The simulation results are consistent with those presented in the literature [65],[99],[101], which reflects the reliability of the presented implementation.

The labelling efficiency increases with proton velocity till around 25-30 cm/s and does not change till velocity reaches 50-55cm/s, which is the range of the velocity values most commonly present in feeding arteries in adults. Also, in presence of inhomogeneities, the efficiency of the fastest protons decreases the fastest, as true phase accrual between the pulses changes with velocity (see equations 5.16 and 5.17). However, for velocities in the range between 25-55cm/s and small inhomogeneities, this is a small effect. Therefore many studies in which pCASL is employed, assume a single value of α for all subjects to be 0.85 [71]. This is likely to be a good estimation for adult volunteers and for patients, for which mean velocities in the main feeding arteries do not deviate significantly from the normal range. However, this is not the case for the neonates, for which the velocities are much lower and might be dependant on the pathology. Therefore the labelling efficiency in neonates will be investigated later in section 5.5 of this chapter.

An important finding here is that the labelling efficiency is sustained for large miss-aligment of labelling plane with the plane perpendicular to the flow, apart from the spins traveling with the slowest velocities. This indicates, that the poisoning of the labelling plane is especially important in the neonatal group.

5.4 Validation of pCASL simulator

5.4.1 Motivation

In order to use the simulator for labelling efficiency estimation for clinical studies, it needs to be validated. The validation was performed by changing the labelling plane angulation ξ and/or flip angle of the Hanning pulses, as this was easily achievable on the scanner and did not require any changes in the sequence code, making the validation process more robust.

5.4.2 Methods

Simulations. The change of labelling efficiency α with the angulation of the labelling plane ξ ($\xi = 0$ represents flow perpendicular to the labelling plane) was first investigated using Bloch Equation simulations, similarly to those described in section 5.3.1. Angulation of the labelling plane was modelled by calculating the effective velocity that spins experience with respect to the vector perpendicular to the labelling plane according to the equation 5.21: $v_{eff} = |\vec{v}| \cdot cos\,(\xi)$ (see section 5.2.3 for more details). ξ was varied from 0 to 80°; the input velocities ranged from 1 to 100 cm/s over a distance of 20 cm with a step size of 1 cm/s. Laminar flow was assumed (see equation 5.28). The pCASL gradient (G_{max} = 6mT/m, G_{ave} = 0.6 mT/m) and RF pulse train (Hanning shaped RF pulses of 0.5ms/1ms duration/spacing, flip angle FA=18°) were matched to that implemented on our Philips 3T scanner. To provide predictions of the relative change in labelling efficiency large enough to be detectable in vivo, a pCASL train with FA=8° was also simulated. FA=8° was chosen based on the previous simulations (see section 5.3.2). T1/T2 of the blood was assumed to be 1.65s/0.2s.

In vivo experiments. Two healthy volunteers (1 female, mean age 26yrs) underwent pCASL scans on a 3T Philips Achieva scanner. The pCASL labelling plane was carefully positioned using a vessel survey scan. In addition to the standard pCASL acquisition (ξ= 0°, FA=18°), two different angles were chosen for ξ: 30° and 60° with FA=18° (volunteer 1) and FA=8° (volunteer 2). An example scan plan for $\xi = 30°$ is shown in the figure 5.16. The center of the labelling plane was positioned on the right carotid artery (CA) to keep the same distance between the labelling plane and the imaging slices for each ξ. Each scan was repeated twice in a randomized fashion. pCASL protocol was: 30 control/label pairs, labelling duration: 1.65s, post labelling delay: 1.8s, GE-EPI readout: FOV 240x240, acq. matrix 64x64 TR/TE 4000/15ms, BS, 20 slices. An M0 image was also acquired with the readout identical to that of pCASL but without background suppression.

Processing. All datasets were motion corrected (DTI-TK [1]), pairwise subtracted and averaged before correction for blood T_1 relaxation and registration to a study template. M_0 images were chosen to manually draw a mask in the cortex of the right hemisphere to minimize the effect of the saturation artifact caused by overlap of the labelling plane in the left hemisphere in the angulated cases (bright stripe in figures 5.17 showing the scan plan and 5.21 showing the final

[1] http://dti-tk.sourceforge.net/pmwiki/pmwiki.php

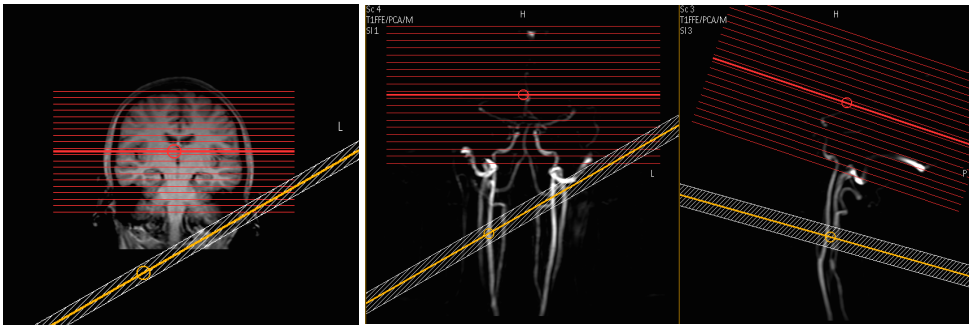

Figure 5.16: *Example of the planning of the scan with ξ = 30° on coronal scout, coronal and sagittal vessel survey. The yellow line and white slab is the position of the centre and thickness of the labelling plane; red lines indicate the position of the imaging slices.*

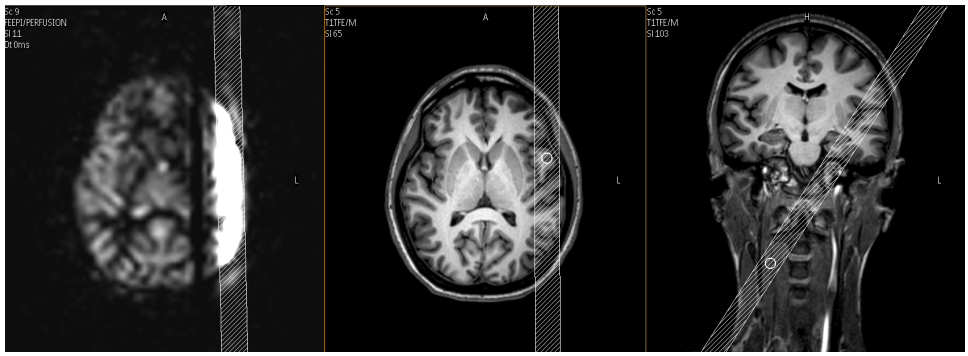

Figure 5.17: *Example of the planning of the scan with ξ = 60° on axial perfusion weighted image, axial and coronal T_1 slices. The white slab is the position of the labelling plane; bright stripe in perfusion weighted image is caused by the labelling plane cutting through the brain tissue.*

CBF map). The mean perfusion weighted signal within the mask for a given ξ and labelling efficiency α, $PWI_{\xi,FA}$, was then used to estimate the labelling efficiency from the data:

$$\alpha_{\xi,FA} = \alpha_{0,18} \cdot PWI_{\xi,FA}/PWI_{0,18} \tag{5.29}$$

where $PWI_{0,18}$ is the mean perfusion weighted signal for the standard acquisition, i.e. ξ=0 and FA = 18°, for which $\alpha_{0,18}$ was assumed to be 0.89, based on the simulation results for an average flow of 40cm/s. The ratios between $\alpha_{0,18}$ and $\alpha_{\xi,FA}$ were also compared to the results of simulations to find v_{max} that best explained the data. Additionally, cerebral blood flow (CBF) was calculated using a standard equation using $\alpha_{0,18}$ in all cases to demonstrate potential CBF estimation error.

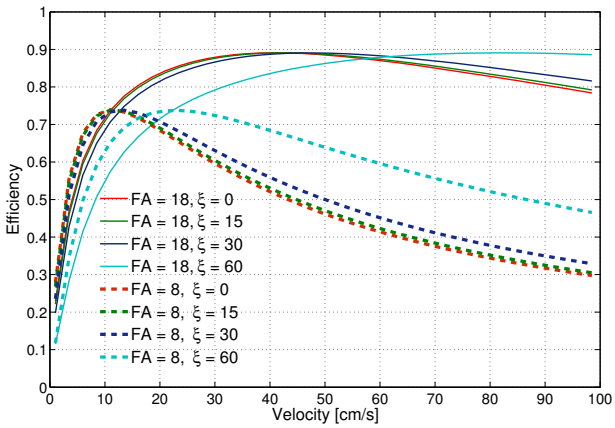

Figure 5.18: *Simulated efficiency for different ξ and flip angles for a range of v_{max}. Labelling plane was set at $r = 0$ and T_{1b} and T_{2b} were set to 1.65s and 0.2s respectively. Scanner default settings of the pCASL train was used: G_{max} = 6 mT/m, G_{ave} = 0.6 mT/m , Δt = 1ms, δ_t = 0.5ms*

5.4.3 Results

The results of the Bloch Equation simulations for ξ values of 0°,15°, 30° and 60° and 2 flip angles plotted against the maximum velocity of the laminar flow distribution are presented in figure 5.18. Figures 5.19 and 5.20 show the measured and simulated labelling efficiencies for volunteer 1 and 2 respectively. The error bar for measured efficiency is the uncertainty assuming 15% error in PWI measurement, and for the simulated efficiency it was estimated from the simulations for a broad range of velocities. In both cases, the $\Delta_{\xi,FA}/PWI_{0,18}$ ratios, and therefore estimated $\alpha_{\xi,FA}$, follow the prediction of the simulations. CBF was measured at 54.6 ($\xi = 0°$), 58.1 ($\xi = 30°$) and 60.3 ($\xi = 60°$) [ml/100g/min] for volunteer 1 and 21.7 ($\xi = 0°$, FA = 8°), 22.6 ($\xi = 30°$, FA = 8°), 30.1 ($\xi = 60°$, FA = 8°) and, 41.5 ($\xi = 0°$, FA = 18°), [ml/100g/min] for volunteer 2, which is in agreement with expected values in this age group. Figure 5.21 illustrates the CBF maps computed for volunteer 1, showing good grey matter contrast for all 3 values of ξ. The data was best explained by the $v = 60$ and $v = 60$ cm/s for volunteer 1 and 2 respectively.

5.4.4 Discussion

The Bloch Equation Simulator predicted changes in the labelling efficiency which were confirmed by in vivo experiments. This proved the validity of the simulator and assumptions made to model labelling plane angulation.

Additionally, this work confirmed high robustness of the pCASL efficiency against angu-

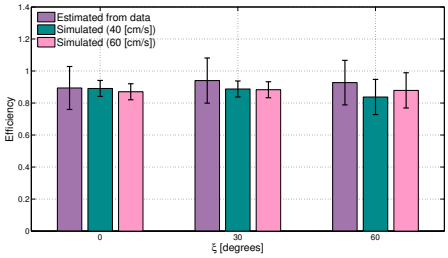

Figure 5.19: *Results of measured and simulated labelling efficiency for different ξ and flip angles for volunteer 1 (FA = 18°)*

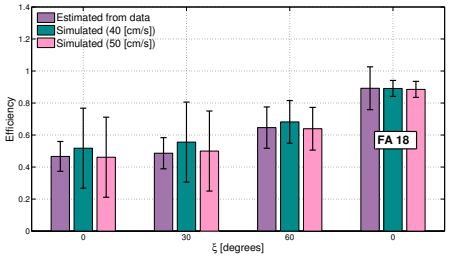

Figure 5.20: *Results of measured and simulated labelling efficiency for different ξ and flip angles for volunteer 2 (FA = 8°)*

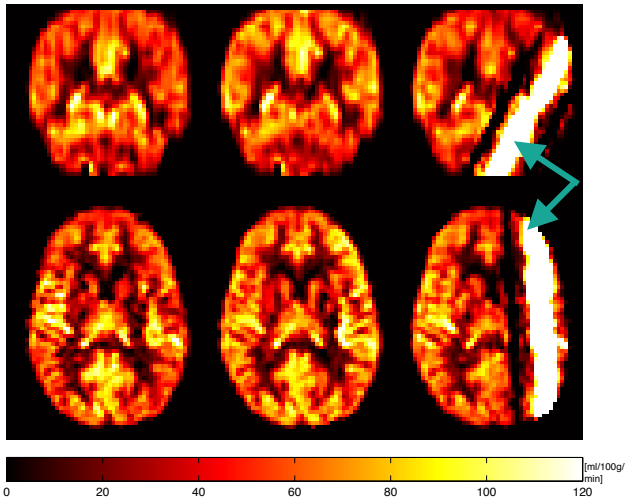

Figure 5.21: *CBF maps computed for volunteer 1 acquired with $\xi = 0°$ (first column), $\xi = 30°$ (second column) and $\xi = 60°$ (third column); top row - coronal view, bottom row - transverse view. Green arrows point to the artefact caused by the labelling plane cutting through the brain tissue.*

lation of the labelling plane when using the standard 18° pulse train, as predicted by Bloch Equation simulations. FA=8° was used here to better demonstrate the agreement of the simulations with in-vivo data, as this predicts much larger changes, bearing in mind that this is not a part of a standard, recommended protocol. In this study, the center of the labelling plane was positioned on the right CA for consistency. If centered mid-way between the carotid arteries, it would have caused a difference in the distance between the labelling plane and imaging slices of 3.6cm/10cm for ξ 30°/60° and therefore introduce differences in the arterial transit time for left and right hemisphere.

5.5 pCASL labelling efficiency estimation in neonates

5.5.1 Motivation

The average velocity in the feeding arteries in neonates is much lower than in adults [47], [57] and can be even lower in neonatal pathology [5]. The aim of this section is to obtain labelling efficiency for neonatal group, based on blood velocities measured in this cohort, described in details in chapter 8.

5.5.2 Methods

To obtain the velocity, quantitative phase contrast (QFlow, see section 3.5 in chapter 3) images were acquired in 10 neonates at the level of the labelling plane. A detailed description of this cohort can be found in chapter 8. Two protocols have been used with the following parameters: TR/TE = 12/6.1ms, FA =10°, FOV = 100x100x4mm, 20 averages and VENC = 60 cm/s (in agreement with [57]) for 4 neonates , and TR/TE = 13/7ms, FA =10°, FOV = 120x120x4mm, 20 averages and VENC = 20 cm/s (in agreement with [103]). Both protocols were optimised for neonates in their respective studies. The change of protocol was dictated by the low range of velocities measured in the studied cohort, which was much lower than 60 cm/s and therefore reduction of VENC was appropriate, to improve the accuracy of velocity measurement (the accuracy of velocity measurement is the highest, for VENC just above the expected velocity. See 3.5 in chapter 3)

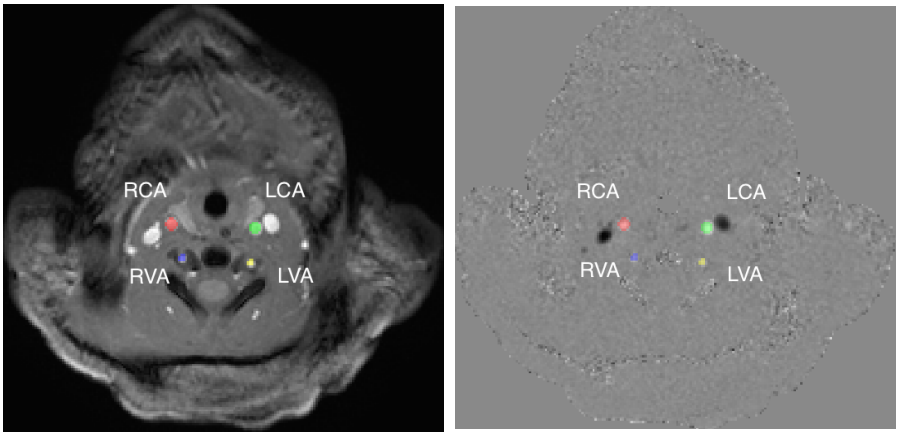

Figure 5.22: *Magnitude (left) and phase (right) images acquired with QFlow sequence with overlaid manual segmentations of four arteries.*

The QFlow data was acquired without cardiac gating with 20 averages, therefore the measured velocities represent the mean value within a cardiac cycle. Right and left common carotid

arteries (RCA, LCA), and right and left vertebral arteries (RVA,LVA) were manually segmented using ITK-SNAP[2]. An example segmentation is shown in the figure 5.22. These segmentations were used to find mean and maximum velocities, as well as the lumen (the interior of a vessel) of each artery (i.e. number of segmented voxels times voxel size in mm^2). The mean from all 4 ROI were then added to estimate the total flow:

$$F_{total} = \sum_{i=1}^{4} v_{mean,i} \cdot s_i \tag{5.30}$$

where s_i is the artery lumen. Bloch equation simulations were performed using the simulator for velocities ranging from 1 to 40 cm/s every 0.2 cm/s. The maximum velocity found in each ROI was used to estimate efficiency assuming laminar flow. The mean efficiency was then calculated as a sum of efficiencies weighted by the amount of flow they contribute:

$$\alpha_{total} = \frac{1}{F_{total}} \sum_{i=1}^{4} v_{mean,i} \cdot s_i \cdot \alpha_{weighted}(v_{max,i}) = \sum_{i=1}^{4} w_i \cdot \alpha_{weighted}(v_{max,i}) \tag{5.31}$$

where $\alpha_{weighted}$ is defined by equation 5.28. Using the weighting additionally addresses the issue of reliability of the velocity measurement with smallest areas due to the partial volume, i.e. the accuracy of velocity estimation is lower for smaller vessels.

Comparsion to other methods of efficiency estimation

For comparison, the method of Aslan *et al.* [104] was also used for α estimation. First, the total flow to the brain was calculated, according to equation 5.30. High resolution anatomical scans were segmented automatically, as described in methods section of chapter 8. The grey, white and deep grey matter, cerebellum and brain stem segmentations were summed up and binarised, and the total volume of brain, V, calculated. To obtain the total CBF in ml/100g/min from PC measurement, $tCBF_{PC}$, the brain tissue density ρ 1.06 [g/ml] [105] was assumed:

$$tCBF_{PC} = \frac{F_{total}}{V \cdot \rho} \tag{5.32}$$

Next, the total $tCBF_{PC}$ was equated to the brain CBF measured with ASL, $tCBF_{ASL}$ (calculated with α = 1) and α was found from:

$$tCBF_{PC} = \frac{1}{\alpha_{PC}} \cdot CBF_{ASL,\alpha=1} \Rightarrow \alpha_{PC} = CBF_{ASL,\alpha=1}/tCBF_{PC} \tag{5.33}$$

The agreement between methods of efficiency estimation was assessed using Bland-Altman plot and limits of agreement (2 · SD).

[2]http://www.itksnap.org/pmwiki/pmwiki.php

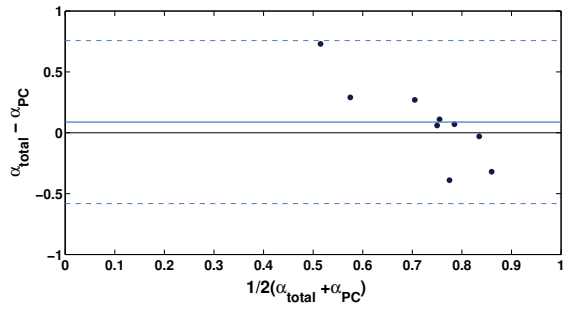

Figure 5.23: *Bland-Altman plot of agreement between two efficiency estimation methods: based on simulations, α_{total} and Aslani, based on phasc-contrast flow, α_{PC}. The solid line represents bias and the dashed lines limits of agreement (2 · SD)*

5.5.3 Results

The results for each ROI are presented in the table 5.1. The mean velocity for all neonates measured in CCAs was 9.55 [cm/s], ranging from 2.7 [cm/s] to 27.2 [cm/s] and 7.3 [cm/s] for VSs ranging from 3.2 [cm/s] to 25.7 [cm/s], which is in a broad agreement with the literature [57]. The labelling efficiency, estimated based on these measurements, was 0.77, ranging from 0.58 to 0.88.

Comparsion to other methods of efficiency estimation

The mean and total efficiencies based on the simulations as well as the total flow are presented in table 5.2. The Bland-Altman plot and limits of agreement between α_{total} and α_{PC} are shown in the figure 5.23. The mean difference between the two methods (solid line) is greater than zero, indicating that α_{total} gives on average higher results, compared to α_{PC}. The agreement between the two methods is overall poor, as indicated by very broad limits of agreement (dashed lines in figure 5.23).

	Left CCA				Right CCA			
N	v_{max} [cm/s]	v_{mean} [cm/s]	s [cm^2]	α_w	v_{max} [cm/s]	v_{mean} [cm/s]	s [cm^2]	α_w
1	15.6	9.5	0.055	0.80	24.3	12.5	0.068	0.86
2	10.7	6.2	0.088	0.73	10.7	5.7	0.110	0.73
3	15.5	8.0	0.094	0.80	14.4	7.3	0.094	0.79
4	23.6	12.3	0.056	0.86	21.3	8.5	0.079	0.85
5	32.4	27.0	0.076	0.89	33.9	27.2	0.040	0.89
6	10.4	6.2	0.076	0.73	8.4	5.0	0.040	0.68
7	5.3	2.9	0.117	0.57	4.7	2.7	0.065	0.53
8	18.1	9.0	0.108	0.82	16.8	8.6	0.055	0.81
9	19.8	9.1	0.108	0.84	17.1	9.2	0.056	0.81
10	8.5	5.4	0.061	0.68	7.9	4.5	0.037	0.78
11	18.5	12.0	0.041	0.83	16.5	11.1	0.018	0.81
Mean	16.2	9.8	0.080	0.78	16.0	9.3	0.060	0.78
SD	7.6	6.4	0.025	0.09	8.4	6.6	0.027	0.10
	Left VA				Right VA			
N	v_{max} [cm/s]	v_{mean} [cm/s]	s [cm^2]	α_w	v_{max} [cm/s]	v_{mean} [cm/s]	s [cm^2]	α_w
1	9.7	7.2	0.012	0.71	10.7	8.4	0.012	0.73
2	5.9	3.5	0.026	0.60	9.6	5.9	0.033	0.71
3	5.7	3.6	0.021	0.59	8.6	6.1	0.018	0.69
4	10.4	1.1	0.037	0.73	15.4	10.3	0.021	0.80
5	26.3	24.0	0.012	0.87	28.7	25.7	0.014	0.80
6	5.7	4.4	0.008	0.58	7.1	4.3	0.027	0.64
7	10.0	4.0	0.012	0.72	7.4	3.8	0.015	0.65
8	10.3	6.7	0.018	0.72	16.6	7.7	0.026	0.81
9	11.4	6.5	0.018	0.74	14.7	7.5	0.021	0.79
10	4.4	3.2	0.012	0.65	4.5	3.4	0.012	0.65
11	12.7	8.6	0.014	0.76	9.3	5.7	0.012	0.70
Mean	10.2	6.6	0.017	0.70	12.1	8.1	0.019	0.72
SD	6.0	6.2	0.008	0.09	6.7	6.2	0.007	0.07

Table 5.1: *Blood velocity and labelling efficiency measurements from the carotid and vertebral arteries in neonatal subjects. v_{max} - maximum blood velocity, v_{mean} - mean blood velocity, s - artery lumen, α_w - efficiency assuming laminar flow distribution of velocities.*

N	α_{mean}	α_{total}	F_{total} [ml/min]	V [cm^3]	$tCBF_{PC}$ [ml/ 100g/min]	$tCBF_{ASL,\alpha=1}$ [ml/ 100g/min]	α_{PC}
1	0.78	0.82	94.0	402	22.0	18.8	0.85
2	0.69	0.72	87.5	289	28.5	12.2	0.43
3	0.72	0.78	98.3	369	25.1	18.1	0.72
4	0.81	0.84	97.6	422	21.8	12.5	0.57
5	0.86	0.88	226.3	381	56.0	8.2	0.15
6	0.66	0.70	49.2	384	12.1	12.3	1.02
7	0.62	0.58	37.1	346	10.1	9.8	0.97
8	0.79	0.81	106.1	357	28.0	19.6	0.70
9	0.80	0.82	106.8	380	26.5	20.0	0.75
10	0.69	0.70	34.4				
11	0.77	0.80	52.9				
Mean	0.74	0.77	90.005	370	25.6	14.6	0.68
SD	0.07	0.09	53.101	38	13.2	4.5	0.27

Table 5.2: *Results of estimated labelling efficiency in neonatal subjects. α_{mean} - labelling efficiency averaged for four vessels, α_{total} - total simulated labelling efficiency, F_{total} - total flow of blood based on phase-contrast measurement of velocities, V - brain volume, $tCBF_{PC}$ - total CBF based on phase-contrast flow estimation, $tCBF_{ASL,\alpha=1}$ - CBF based on ASL, α_{PC} - labelling efficiency based on Aslani's method using phase-contrast flow.*

5.5.4 Discussion

This section presents an estimation of labelling efficiency in neonates using simulator and quantitative flow measurement for arterial blood flow velocities estimation.

1. No gating was used due to technical restrictions (incubator monitoring), which could produce more accurate results if efficiency in the cardiac phases was included. However, using 20 averages, the measured velocity should be equal to the mean velocity in the cardiac cycle [57]

2. Manual segmentation of the arterial cross-section was used. This could influence the estimation of the total flow F_{total}

3. The B_0 field map was not acquired, and therefore there was no information available about the amount of B_0 inhomogeneities in the neck area of neonates. This could affect the simulation estimation of efficiency, α_{total}. However, given the small size of the neonate, the expected inhomogeneities are less than in adults. Additionally, in the current implementation on Philips scanner, additional shimming is performed on the level of the labelling plane, reducing B_0 inhomogeneities.

4. Velocity estimation for each artery might have been underestimated due to the partial volume effects, i.e. the spins flowing fastest share the same voxels with the slower spins. This could have given a rise to an underestimation of labelling efficiency, especially for the velocities in the lower range, accordingly (see figure 5.7).

5. The Bland-Altman plot shows that the two methods of α estimation are not in a good agreement. α_{PC} results are characterised much larger distribution compared to methods using simulation. Aslan's method relies on a reliable CBF quantification using pCASL as well as accurate brain volume estimation. This, however, might not be the case in HIE neonates, as discussed later in this thesis.

6. The simulations show a dependency of the labelling efficiency on velocity, which is especially apparent in the flow range measured in neonates. Therefore, ideally the blood velocity at the level of labelling plane should be measured and used to compute α on a subject-by-subject basis. This will ensure more reliable CBF quantification. In this work, a single average efficiency value is used.

5.6 Summary and conclusions

This chapter describes the theory, implementation, validation and usage of the Bloch equation simulator for pCASL labelling. The simulator provides the flexibility to estimate the labelling efficiency for any design of RF and gradient train. Moreover, it allows inclusion of the magnetic field inhomogeneities (static and gradient) to study the effects of compensation for these inhomogeneities. It therefore helps to understand the influence of changes in the train design on the labelling efficiency as well as different real-life scenarios, such as imperfect positioning of the labelling plane or an inhomogenous B_0 field, for a range of velocities and realistic model of the laminar flow. The results of the simulations presented here are consistent with the results in the literature and were confirmed in-vivo, demonstrating their reliability and robustness. The knowledge and experience gained from implementation of the simulator was later used in designing the acoustic noise reduction strategies described in Chapter 6.3. The pCASL parameters used for simulations are kept consistent with those used by the Philips scanners, as both pCASL studies were carried out using these scanners and therefore the results for the 'unbalanced' variety of pCASL was not presented here. However, it is available on the simulator.

The Bloch equation simulator is an important tool in estimation of labelling efficiency in new applications, as presented in this chapter and in appendix A, for which it has not been estimated and reported. Also, it enables quantification of efficiency on subject-by-subject basis. Another important area of usage for the simulator is pre-clinical research, where high magnetic (B_0) fields are used. The simulator described here was used for estimation of labelling efficiency in rats kidneys and liver (see the third position in the list below). The simulator will be made publicly available after publishing the PhD thesis.

List of abstracts that benefited from work presented in this chapter:

M. Sokolska, X. Golay, and D. Thomas *Effect of labelling plane angulation on pCASL labelling efficiency does it really matter?*. Proceedings of 23rd ISMRM 2015

M. Sokolska, C. Uria-Avellanal, M.J. Cardoso, M. Proisy, A. Bainbridge, S. Ourselin, D.Thomas, N. Robertson, and X. Golay *Assessing brain damage after perinatal hypoxic-ischaemia using an automated protocol for combined regional analysis of the Cerebral Blood Flow and MR spectroscopy*. Proceedings of 23rd ISMRM 2015

R. Ramasawmy, J. Wells, **M. Sokolska**, J.Meakin, S.Johnson, A.. Campbell-Washburn, R. Pedley, M.Lythgoe, and S. Walker-Samuel *Separation of arterial and portal blood supply to mouse liver and tumour tissue using pseudo-Continuous Arterial Spin Labelling (pCASL)* Proceedings of 23rd ISMRM 2015

M. Sokolska, Maia Proisy, Cristina Uria-Avellanal, Alan Bainbridge, Ernest Cady, David Thomas, Nicola Robertson, and Xavier Golay *Combined use of arterial spin labeling and MRS to determine the severity of injury in neonates with hypoxic-ischaemic encephalopathy* . ISMRM 2014

M. Sokolska, D. Thomas, A. Bainbridge, X. Golay, S. Taylor, S. Punwani, D. Pendse *Renal Perfusion Imaging with Pseudo-continuous Arterial-Spin Labelling (pCASL) at 3.0T: Repeatability in Healthy volunteers.* Proceedings of 22nd ISMRM 2014

M. Sokolska, X. Golay, D. Thomas *Perfusion quantification using pseudo-continuous Arterial Spin Labelling: the impact of labelling efficiency estimation.* Proceedings of 21th ISMRM Meeting 2013

M. Sokolska, A. Oliver-Taylor, X. Golay, D. Thomas *Theoretical and practical investigation of acoustic noise level reduction in pseudo-continuous Arterial Spin Labeling.* Proceedings of ISMRM Perfusion Workshop 2012

Chapter 6

Practical aspects of pCASL

6.1 Introduction

The previous chapter described the theory of pCASL. This chapter focuses on the practical aspect of the methods and provides some solutions to address the existing drawbacks. In section 6.2, an investigation into the effect of angulation of the labelling plane on spin tagging efficiency is presented, which is an extension of work of the previous chapter. Section 6.3 discusses the acoustic noise properties of the pCASL labelling train and methods for its reduction.

6.2 Effect of labelling plane angulation on pCASL labelling efficiency

6.2.1 Motivation

pCASL, introduced in detail in chapter 5, is emerging as the method of choice for non-invasive measurement of tissue perfusion in research and clinical practice [71]. The labelling efficiency α, knowledge of which is essential for accurate CBF quantification as discussed in chapters 4 and 5, usually takes a value based on the idealistic model that assumes spins flowing perpendicularly to the labelling plane. In practice, it might not be always possible to meet this assumption for all feeding arteries at the same time, either due to anatomical variation, lack of appropriate anatomical scans or lack of angulation flexibility in the pCASL implementation. In chapter 5, the theoretical background for the effect of the angulation on efficiency was given and it was found that, even for large offsets of the labelling plane from desired perpendicular position, ξ, the labelling efficiency was preserved, which was then confirmed in vivo in two healthy vol-

unteers. This is a very important finding in the context of clinical practice, clinical trials and research, as it reassures users of the easiness of its application. The work presented here is extended to a larger group of volunteers, and other sub optimal positions of the labelling plane, that could arise in a clinical setting, are also tested. Additionally, a more detailed characterisation of α with increase of ξ for spins at different velocities is explored.

6.2.2 Methods

Simulations. The method of the labelling efficiency estimation using Bloch Equation simulations was described in detail in chapter 5 section 5.4.2. The definition of the angle ξ here is consistent to that introduced in chapter 5 section 5.2.3, (see figure 5.5). As previously described, pCASL gradient amplitudes, as well as RF amplitudes and durations were consistent with the Philips scanner implementation: G_{max} = 6mT/m, G_{ave} = 0.6 mT/m, Hanning shaped RF pulses of 0.5ms/1ms duration/spacing, flip angle $FA = 18°$.

The initial results revealed, that even large labelling plane offsets from perpendicularity result in a small change in labelling efficiency (see figure 5.18). Given relatively low test-retest reproducibility of pCASL (reference), a larger ξ, i.e. $\xi > 15°$ and reduced flip angle of the pCASL labelling train provides a detectable difference and therefore is more informative about the limits of ξ that ensure sustained labelling efficiency.

Imaging protocol. 8 healthy volunteers underwent scans (4 females, mean age 28 years) after providing a written consent. The scans were performed on a 3T Philips scanner, using the 32 channel head coil and standard pCASL vendor implementation (unless indicated otherwise). The flow chart representing the protocol is shown in figure 6.1.

The core protocol included: T1 MPRAGE (TI 812ms, TR/TE 6.8/3.1ms, TFE factor 230, FOV 200x200x180mm, 1x1x1mm SENSE 2, scan duration 5min), phase contrast (PC QFlow, VENC = 60 cm/s, non-gated), proton density image (TR=9s) and pCASL with three labelling plane angles, chosen based on the work presented in the previous chapter: $\xi = 0°$, 30° and 60°, performed twice with 20 repetitions in a pseudo-randomised fashion. The labelling plane was always carefully positioned on the vessel survey and centred on the right carotid artery to maintain the same distance of the labelling plane from the imaging slices for each ξ. Other pCASL parameters were: labelling duration: 1.65s, post labelling delay: 1.8s, GE-EPI readout: FOV 240x240, acq. matrix 64x64 TR/TE 4000/15ms, BS, 20 slices. The second part of the protocol consisted of two scans with reduced flip angle of the labelling train ($FA = 8°$) and

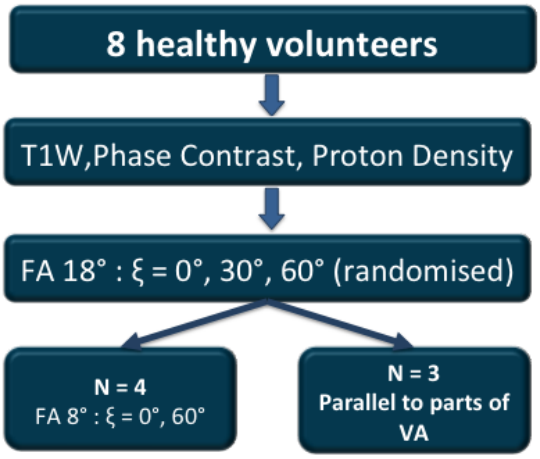

Figure 6.1: *Flow chart of the study protocol*

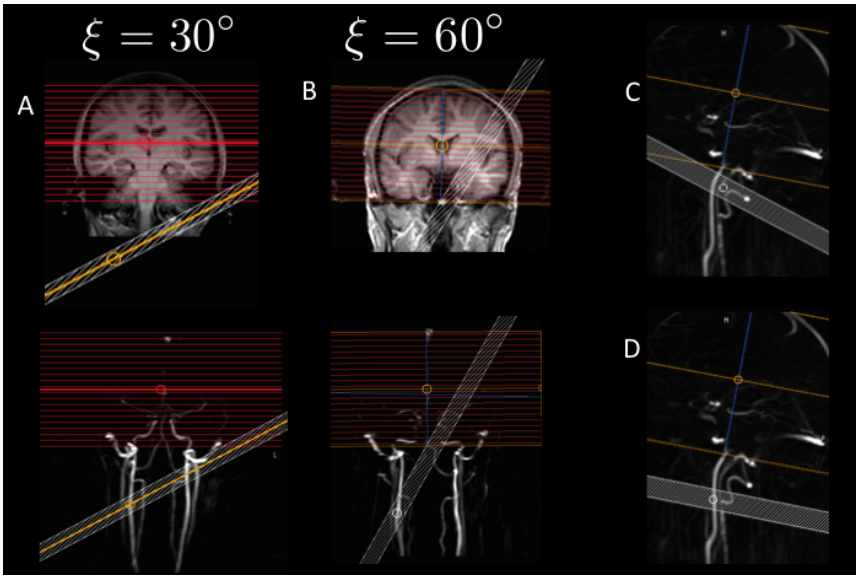

Figure 6.2: *The position of the labelling plane for $\xi = 30°$ (A), 60° (B) and parallel to the vertebral arteries: top kink (C) and bottom kink (D)*

two labelling plane angles ($\xi = 0°$ and 60°) (5 volunteers) or standard $FA = 18°$ but labelling plane positioned parallel to the flow direction on the parts of the vertebral artery. The position of the labelling plane for $\xi = 30°$ and 60° and parallel to the vertebral arteries (top and bottom) are shown in figure 6.2. PC and proton density images were acquired three times, distributed in time equally during scan duration.

Post-processing. All datasets were motion corrected by registering all raw images to the volunteer template (i.e. a mean of data acquired with $FA = 18^\circ$ and $\xi = 0^\circ$) using DTI-TK[1] software. Each dataset was then pairwise subtracted, averaged (all acquired repetitions for given ξ and FA), corrected for blood T_1 relaxation during the labelling delay with $T_{1,a}$ assumed to be 1.65s and divided by the proton density image. Cortical voxels were defined using FSL FAST segmentation algorithm [106] and after converting to a binary map and restricting to only cover right hemisphere, carotid and vertebral territories were segmented manually using ITK-SNAP[2], based on anatomical knowledge.

For vascular territories, the watershed regions were avoided. An example of segmentation into cortex, carotid and vertebral territory is presented in figure 6.3. Mean signal in such defined regions were then calculated for each acquisition and a paired two-sided Student's t-test was used to test the significance of the signal change between different labelling plane orientations and F-test to test differences in the variance ($p < 0.05$ was considered statistically significant for both tests).

Efficiency estimation For each combination of labelling plane angulation and pCASL flip angle (ξ, FA) a relative labelling efficiency was calculated by dividing the mean signal from each post-processed acquisition by the signal from the standard acquisition where $FA = 18^\circ$ and the labelling plane is perpendicular to the arteries:

$$\alpha_{rel,\xi,FA} = PWI_{\xi,FA}/PWI_{0,18} \tag{6.1}$$

This calculation was done for all segmented regions: cortex and both CA and VA segmented territories. Additionally, the mean velocity of the blood was measured in CA and VA, using PC Qflow scans, as shown in figure 6.4. Simulated relative labelling efficiencies were calculated for these velocities using the results obtained in previous chapter 5 for each acquisition type (section 5.4.3).

6.2.3 Results

Figure 6.5 shows results of relative labelling efficiency estimated based on the Bloch Equation simulations and in vivo imaging data, plotted for a range of measured velocities. α_{rel} from CA and VA territories were calculated based on the velocity measured in the respective arteries.

[1] http://dti-tk.sourceforge.net/pmwiki/pmwiki.php

[2] http://www.itksnap.org/pmwiki/pmwiki.php

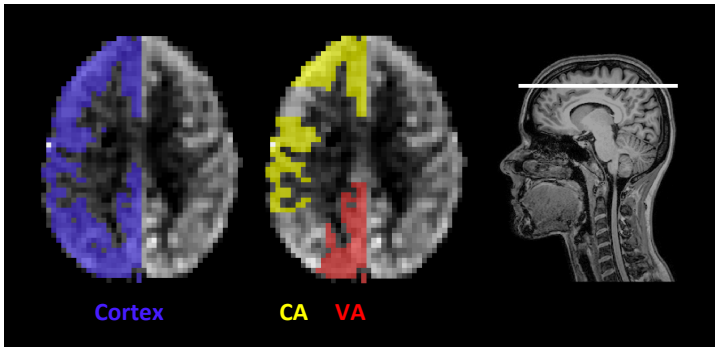

Figure 6.3: *Example segmentation of voxels within cortex, carotid artery (CA) and vertebral artery (VA) for a single slice.*

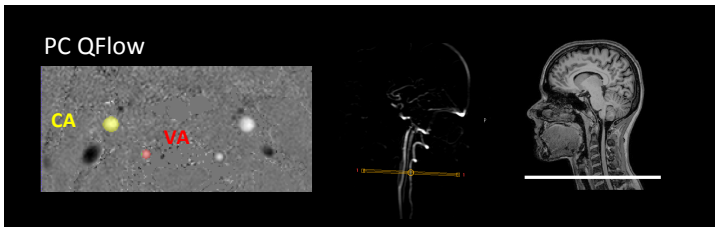

Figure 6.4: *Segmentation of feeding arteries for velocity measurement*

Although the range of relative labelling efficiencies in the in-vivo data is larger than expected from simulations, the general trend and predicted order of the acquisitions are similar: the highest α_{rel} was measured for $\xi = 30°$ (close to 1), then $\xi = 60°$ both with the standard $FA = 18°$ followed by the $\xi = 60°$ and $\xi = 30°$ with reduced $FA = 8°$. This confirms the model prediction, that for pCASL $FA = 8°$, the labelling efficiency improves with increase of ξ.

Mean and standard deviation of α_{rel} computed across all volunteers for different regions is presented in table 6.1. On average, there is no change of the relative labelling efficiency for $\xi = 30°$, and only a small decrease for $\xi = 60°$, especially in the VA territory. For $\xi = 60°$, the standard deviation is also higher, indicating bigger spread of the data. When comparing PWI between acquisitions, no statistical significant difference was found between means or variances of PWI for $\xi = 0°$ and $\xi = 30°$ or $\xi = 60°$ for any of the regions of interest (p ranged from 0.16 to 0.96 for t-test and 0.07 to 0.69 for F-test). A large reduction of α_{rel} is observed for the least desired position, i.e. along the blood direction in the higher 'kink'. Although there is no average α_{rel} change for the bottom 'kink', the standard deviation for that acquisition is elevated in VA territory, similar to that of the top 'kink' location. To better visualise the spread of the data for each acquisition type, the results of α_{rel} for all volunteers are shown in figure 6.6.

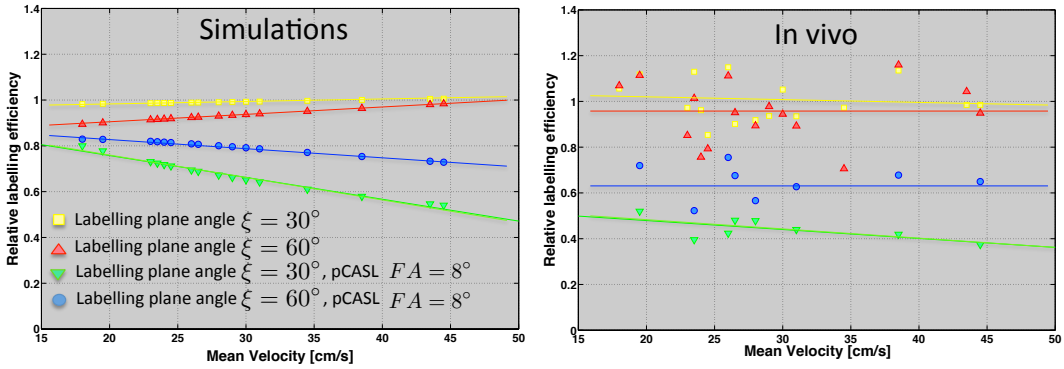

Figure 6.5: *Relative efficiency estimated based on simulations and in vivo data (carotid and vertebral territories) for a range of measured velocities*

ROI	$\xi = 30°$	$\xi = 60°$	bottom 'kink'	top 'kink'
Cortex	1.01 (0.08)	0.98 (0.16)	1.00 (0.11)	0.87 (0.09)
CA	1.02 (0.08)	0.97 (0.13)		
VA	0.99 (0.10)	0.93 (0.12)	0.99 (0.19)	0.84 (0.18)

Table 6.1: *Mean relative labelling efficiency for four different positions of the labelling plane. Standard deviation is given in brackets.*

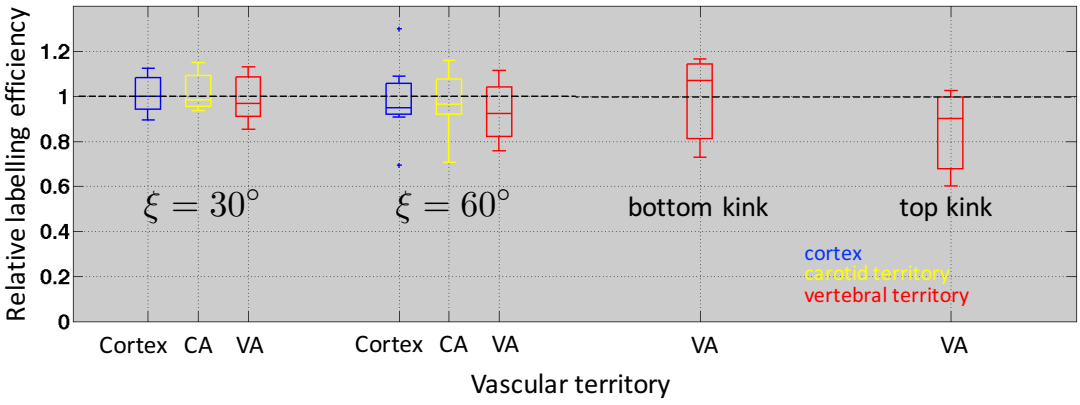

Figure 6.6: *Relative efficiency for four different positions of the labelling plane ($\xi = 30°$, $\xi = 30°$ bottom and top 'kink') and different territories: cortex (blue), carotid artery (CA, yellow), vertebral artery (VA, red). The boxes represent the 25th and 75th percentile, the line across is the median and whiskers are the spread of the data ($FA = 18°$)*

6.2.4 Discussion and conclusions

This study confirmed high robustness of the pCASL efficiency against the angulation of the labelling plane, even as high as 30° in larger number of volunteers. It also found, that labelling plane positioned on parallel part of vertebral arteries resulted in a large data variation. Therefore the highest attention while positioning the labelling plane should be given to ensure accurate position on the vertebral arteries.

The findings presented here are important in the context of neonatal protocol development for two reasons. Firstly, the lower velocities of blood in supplying arteries found in neonates, especially in posterior circulation, are more susceptible to higher angulations of the labelling plane. Secondly, the position of the neonatal head and neck in the scanner can be tilted to allow space for a tracheal tubes used as part of breathing support, which makes the position difficult to predict. A constant distance between the labelling plane and FOV could therefore result in disadvantageous labelling plane position on parallel part of vertebral arteries.

6.3 Acoustic noise level of pCASL and its reduction

6.3.1 Motivation

Although pCASL offers higher signal-to-noise ratio (SNR) than pulsed ASL and provides better quality CBF maps, concern has been raised about acoustic noise levels experienced by scanner operators and patients undergoing the scan, leading to patient anxiety and discomfort. This is especially a concern in imaging unsedated infants, where exposure to high levels of acoustic noise might increase stimulation and chances of waking up [107], which in turn might result in motion artefacts in the images and make diagnosis impossible. This chapter therefore addresses the need to reduce the Sound Pressure Level (SPL) produced by the pCASL sequence. In this section the theory of acoustic noise generation and reduction is introduced. This is then applied to pCASL labelling trains and simulations are performed to find the best labelling train with reduced SPL while maintaining labelling efficiency. The proposed labelling pulse train is then tested on a healthy volunteer for in-vivo confirmation of the result.

6.3.2 Theoretical background

Source of the acoustic noise in MRI

Acoustic noise during MRI scan is produced by undesired vibrations of the gradient coils in their assembly. This vibration is a consequence of the Lorentz forces $\vec{F_L}$ acting upon the gradient coil, generated by rapidly changing currents I in the coils in the presence of a static magnetic field $\vec{B_0}$. The magnitude of $\vec{F_L}$ is described by 6.2 [108]:

$$\vec{F_L} = \int_l I\vec{dl} \times \vec{B_0} \tag{6.2}$$

where $\vec{l}$ is a vector of magnitude equal to the length of wire and its direction is along the wire and $\times$ is a cross product. The resultant force deflects the coil structure. Changes of the Lorentz force with alternating electric currents cause the coil vibrations. These are then transferred through the gradient coil assembly into the air, producing airborne acoustic waves with pressure P. The measure of an effective sound pressure relative to the reference, P_{ref}, is the SPL, expressed in decibels (dB):

$$SPL = 10\log_{10}\left(\frac{P_0^2}{P_{ref}^2}\right) = 20\log_{10}\left(\frac{P_0}{P_{ref}}\right) \tag{6.3}$$

where P_0 is the observed pressure in μ Pa and P_{ref} is a standardised reference value of 20 μ Pa (the threshold of human hearing).

Several methods for the acoustic noise reduction have been proposed, which can be broadly divided in to two categories:

1. mechanical, by changes in the design of gradient coils structure [108], assembly [109] or MR suite [110];

2. non-mechanical (altering the gradient output), by controlling the acoustic response of the scanner by changing the gradient waveform shape [111] or frequency content of the pulse sequence [112], [113], [114] .

Since manufacturers optimise mechanical methods, and further modifications via these methods are not practically possible, non-mechanical methods were investigated.

Acoustic transfer function

Assuming a linear electromechanical system, for any arbitrary physical input $g(t)$, $G(f)$ the system output $p(t)$, $P(f)$ is given by [112]:

$$p(t) = \int_0^\infty h(\tau)g(t-\tau)d\tau \tag{6.4}$$

or in frequency domain:

$$P(f) = H(f) \cdot G(f) \tag{6.5}$$

where $h(t)$, $H(f)$ is the transfer function. This can be calculated as the complex ratio of output response to an input excitation spectrum:

$$H(f) = \frac{P(f)}{G(f)} \tag{6.6}$$

Once the transfer function is determined, it can be applied to any input signal to predict the expected acoustic noise [112]. The input in the frequency domain can be computed using Fast Fourier Transform of the gradient waveform.

Sources of acoustic noise in pCASL

The main source of acoustic noise in the pCASL labelling module is a long train (1.5-2s) of rapidly changing gradient waveforms (that accompany RF pulses) (see figure 5.2) repeated many times over a 4-6 minute scan. Here, the pCASL train is considered to be the input function $g(t)$. The elements of the pCASL train and their impact on the acoustic noise and the labelling efficiency are as follows:

RF spacing Δt. The spacing between pulses Δt dictates the duration of the single gradient module in the train, which in turn defines the fundamental the frequency f = 1/(Δt) and its harmonics at multiples of the peak frequency: f_n = nf [112], (figure 6.7). If the fundamental frequency or any of the harmonics coincides with a peak of the transfer function $H(f)$, the system response $P(f)$ and therefore acoustic noise will be increased. It is possible to adjust Δt so that f and all f_n avoid the maximum of $H(f)$ and target $H(f)$ minima.

RF duty cycle. Decreasing RF duty cycle ($\frac{\delta_t}{\Delta t}$) has a significant effect on the noise levels by reduction of the amplitude and the shape of the negative gradient lobe: there is more time available to achieve the same gradient moment, which results in reduction of the slew rate and therefore the gradient waveform is less sharp. This results in a spectrum with the lower relative the harmonics contribution, as can be seen in figure 6.8 ($G_2(f)$). For fixed G_{max} and the same spacing between the pulses Δt, change in duty cycle from 50% to 33% reduces the acoustic noise from 109.7dB to 107dB. However, to maintain the average B_1 between the pulses, the

flip angle (FA) of pulses in the train needs to be increased. Additionally, the condition in equation 5.9, i.e. $\frac{G_{max}}{G_{ave}} \gg \frac{\Delta t}{\delta_t}$ is no longer fulfilled and to sustain the efficiency, G_{max}/G_{ave} ratio needs to be increased, by either increasing G_{max} or the amplitude of the negative lobe to decrease G_{ave}. Also, with more time between the pulses, the pCASL 'phase tracking' error of the phase shift between consecutive pulses from equation 5.11 increases and is more susceptible to gradient or main magnetic field inhomogeneities (see section 5.2.3 in chapter 5).

Gradient amplitude. The amplitude of the selective gradient G_{max} defines the width of the labelling plane. The higher the gradient, the thinner the selectivity of the RF pulses and more efficient aliasing reduction (equation 5.9). However, the amplitude of the gradient has a direct implication in terms of the acoustic noise: the higher the gradient the higher the noise. Based on Fourier Transform of the gradient train alone, reduction of G_{max} from 1 to 0.6 G/cm can reduce acoustic noise from 114.1 to 109.7 dB (more than 50 %). Increasing G_{max}/G_{ave} ratio while keeping G_{max} fixed, i.e. increasing the amplitude of the negative lobe, can have a marginal influence on the acoustic noise, depending on the train design. If the negative gradient fills up the whole time between 2 consecutive pulses, then increasing the ratio, resulting in increased gradient moment, needs only a small increase in gradient amplitude.

Flip angle. The flip angle needs to be chosen to assure an adequate mean B_1 as discussed previously in section 5.2.3. This puts the constrains on the possible duty cycle.

6.3.3 Methods

Train design and simulations. To find the pCASL train design $G(f)$ that results in the lowest theoretical gradient system response $P(f)$, the default pCASL gradient train (G_{max} = 6mT/m, G_{ave} = 0.6 mT/m, Δt = 1ms, δ_t = 0.5ms) was modified using different search strategies summarised in table 6.2. For each strategy, ten Δt values were considered, starting from 1 ms with 0.1 ms increment, while δ_t was either fixed or increased proportionally to Δt. The average amplitude of RF pulse over Δt was fixed, the amplitude of positive gradient lobe was always 0.6 G/cm and the amplitude of the negative lobe was matched so that G_{max}/G_{ave} was equal to 10, 15 or 20 depending on the strategy. Bloch equation simulations were performed as described in chapter 5 to analyse changes in labelling efficiency as a result of changes in pCASL pulse and gradient train design.

Next, theoretical total SPL for each design was calculated based on the FFT of the gradient

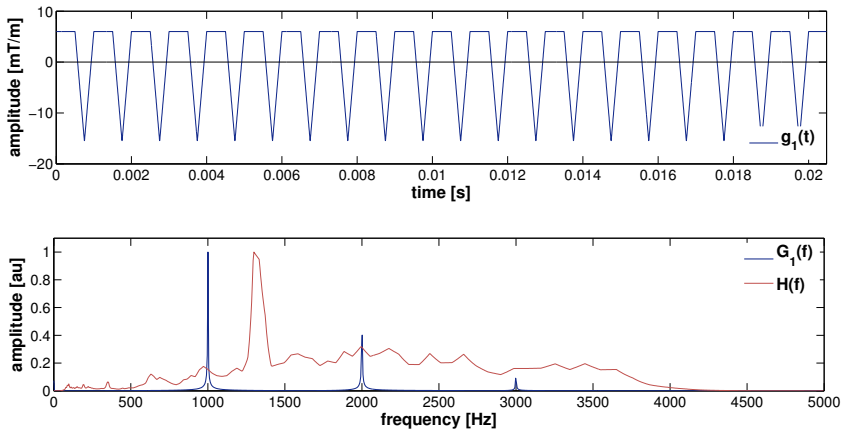

Figure 6.7: *Default pCASL gradient train $g_1(t)$ (Δt = 1ms, δ_t = 0.5ms) and an example transfer function with overlaid the $G_1(f)$ (FFT of $g_1(t)$), normalised*

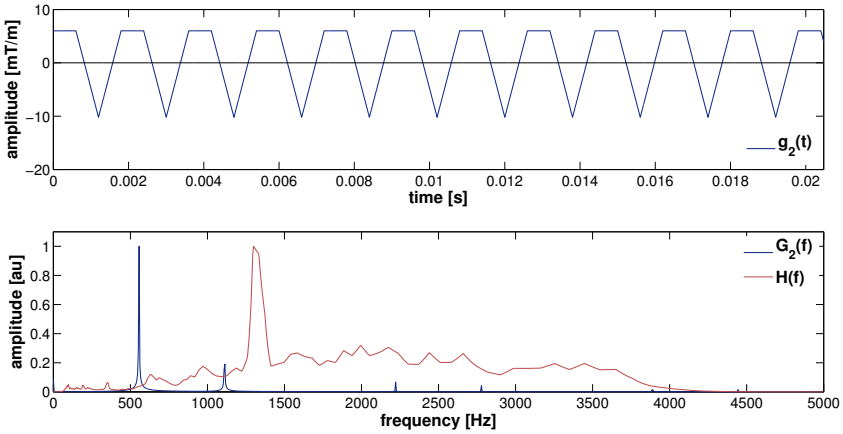

Figure 6.8: *pCASL train $g_2(t)$: Δt = 1.8ms, δ_t = 0.6ms and an example transfer function with overlaid the $G_2(f)$ (FFT of $g_2(t)$), normalised. By changing Δt the minima of a transfer function are targeted, and by changing δ_t, the amplitudes of f_n are reduced*

train and the scanner transfer function provided by the manufacturer (Philips), according to equation 6.3, where P_0 was the power of system response spectrum calculated based on equation 6.5 for each train design. The flow chart presented in figure 6.9 summarises the method of choice of the strategies to be tested on the scanner.

SPL **measurements.** Real system response was measured with a Brüel and Kjaer 2260 integrating sound level meter on a 3T Philips scanner for the 2 strategies that showed the best theoretical SPL reduction and best labelling efficiency (i.e. strategy 3 and 6 in table 6.2) . Measurements were performed at the location of the patient's ear in the presence of a phantom with linear frequency weighting (i.e. no weighting accounting for perceived 'loudness' of

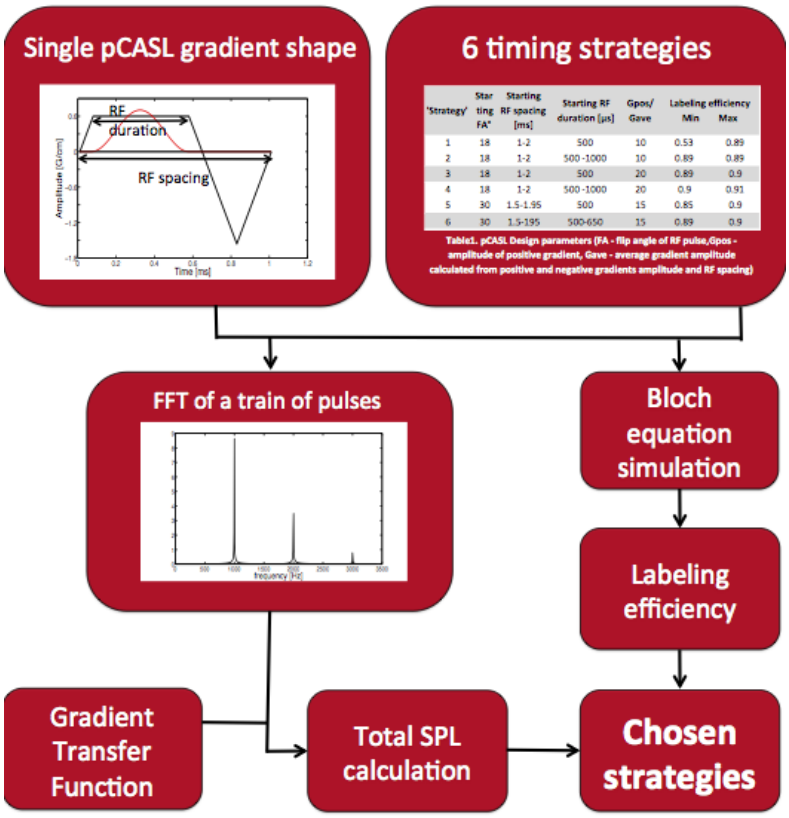

Figure 6.9: *Flow chart representing a method for strategy selection*

different frequencies by the human ear was employed). The acoustic noise of the EPI readout module was also measured for comparison.

Imaging. A healthy volunteer (27yrs) underwent a series of pCASL perfusion scans to evaluate the labelling efficiency of four labelling train designs resulted from two best 'strategies' in vivo, chosen based on the lowest measured SPL with the highest simulated labelling efficiency and compared to the scanner default setting. The labelling train parameters were: $\delta_t = 0.5ms$, $G_{max}/G_{ave} = 20$, Δt = 1.3 with FA = 24°, $\Delta t = 1.8$ s with FA = 33° (strategy 3 design), and $G_{max}/G_{ave} = 15$, $\delta_t = 0.5ms$, Δt = 1.5, with FA = 27°, $\delta_t = 0.63ms$, Δt = 1.8, with FA = 33° (strategy 6 design). The scanner default pCASL labelling train was also used for comparison. Other pCASL parameters were: labelling duration: 1.65s, post labelling delay: 1.5s, GE-EPI readout: FOV 240x240mm, acq. matrix 64x64 TR/TE 4000/15ms, 30 averages.

Post-processing. As described previously in 6.2.2, all data was motion corrected by registering all raw images to the volunteer template using DTI-TK[3] software. Each dataset was then pairwise subtracted, averaged (all acquired repetitions for given acquisition), corrected for blood T_1 relaxation during the labelling delay with $T_{1,a}$ assumed to be 1.65s. A single mask including brain tissue was created manually using ITK-SNAP[4], which was then used to quantify mean perfusion weighted signal for each labelling strategy. Next, relative labelling efficiency was calculated by dividing the mean signal from each post-processed acquisition by the signal from the standard acquisition:

$$\alpha_{rel,strategy} = PWI_{strategy}/PWI_{default} \tag{6.7}$$

Strategy	Δt [ms]	δ_t [ms]	G_{max}/G_{ave}	Efficiency min	Efficiency max
1	1-2	0.5	10	0.53	0.89
2	1-2	0.5 -1	10	0.89	0.89
3	**1-2**	**0.5**	**20**	**0.89**	**0.9**
4	1-2	0.5 -1	20	0.9	0.91
5	1.5-1.95	0.5	15	0.85	0.9
6	**1.5-1.95**	**0.5-0.65**	**15**	**0.89**	**0.9**

Table 6.2: *pCASL train design parameters used to find of the best search strategy; chosen strategies are highlighted in bold.*

6.3.4 Results

The results of the theoretical and measured SPL reduction is shown in figure 6.11. Analysis of the system response spectra indicated that a reduction of up to 10dB in total SPL is possible compared to the default scanner settings. A reduction of 6dB compared to the default scanner setting was achieved for Δt =1.8s (δ_t = 0.5ms for strategy 3 and δ_t = 0.6ms for strategy 6) and 4dB for Δt = 1.3s and δ_t = 0.5ms. Bloch equation simulation showed (table 6.2), that by choosing high G_{mean}/G_{ave} and/or adjusting the δ_t, the labelling efficiency was preserved. Relative labelling efficiency is shown in Figure 6.12, suggest that there is a slight loss of labelling efficiency for chosen strategies compared to default setting, however a larger number of volunteers

[3] http://dti-tk.sourceforge.net/pmwiki/pmwiki.php

[4] http://www.itksnap.org/pmwiki/pmwiki.php

should be scanned to establish statistical significance of this change. Additionally, no loss in the quality of PWI was observed, as shown in figure 6.11.

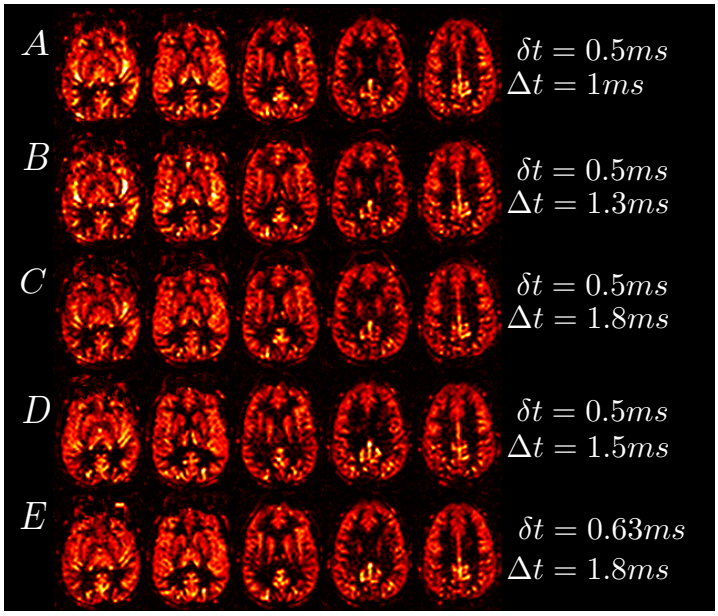

Figure 6.10: *PWI images: default (A), strategy 3 (B,C), strategy 6 (D,E).*

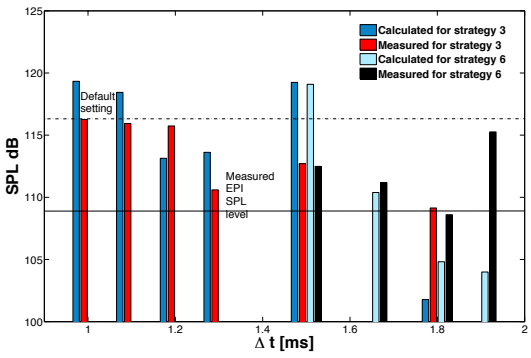

Figure 6.11: *Measured SPL of pCASL labeling module and EPI readout module; phantom experiment*

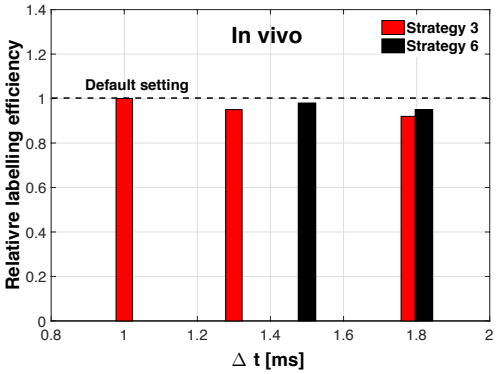

Figure 6.12: *Relative signal of each strategy compared to the standard acquisition without altering the labelling train*

6.3.5 Discussion and conclusions

The study presented here shows that, acoustic noise level can be reduced and therefore patients' comfort during scanning can be improved by adjusting the timing values of pCASL gradient waveform, without compromising labelling efficiency. A small adjustment of Δt and δ_t can reduce the acoustic noise by 6dB and reduce labelling module noise levels to that of EPI readout.

An important property of the presented approach is, as opposed to, for example, smoothing the gradient shape, is that it does not require any sequence programming and the parameters can be easily adjusted by any operator. However, smoother gradient forms might provide further improvement.

In this work, the provided transfer function $H(f)$ was used to identify best search strategy. However, the differences between the calculated and measured SPL levels were found. This discrepancy could be explained by the fact that $H(f)$ depends, apart from the scanner design, on the room acoustics and the position of the microphone [112]. In this case, a potentially better approach would be to first identify the best fundamental frequency f by measurement with the noise meter for variable Δt and constant duty cycle, then probe different δ_t to Δt and G_{max} to G_{ave} ratios and finally, match the appropriate flip angle of RF pulse. Unfortunately, it was impossible to test this approach due to the hardware changes in the scanner carried on by Philips shortly after presentation of this work at the ISMRM Perfusion Workshop. This change reduced the acoustic noise of the pCASL labelling module to the level of EPI readout (data not shown), and therefore the project was discontinued.

Similar work was presented at the same ISMRM Perfusion Workshop and later published by Meer *et al.* [115]. The authors carried out very similar experiments on 3T Philips Intera system: SPL predictions, measurements and in-vivo tests on 9 healthy volunteers. The authors were provided with response functions for five different spatial positions in the scanner bore and incorporated it to simulate SPL levels as a function of the Δt depending on the labelling plane position. Similarly to work presented here, they found a significant change of acoustic noise levels with Δt. Additionally, the authors also identified (simulated and measured) changes in SPL levels with the position of the labelling plane from the scanner isocenter. This finding was used to determine best Δt: 1.4ms which led to a SPL reduction of 6.5dB. In-vivo measurement confirmed, that there was no statistical significant reduction of the labelling efficiency, although the mean reported values were lower. In the final conclusions the authors recommend adjusting Δt to between 1.1 and 1.4ms, which is in line with the work presented in this chapter.

6.4 Summary

This chapter presented two important practical aspects of pCASL: labelling plane position and acoustic noise reduction. Both aspects are very important for development of clinically feasible and optimum neonatal protocol. However, the findings presented in this chapter also translate to

other patient groups, in clinical or research studies, to achieve reproducible results and increase patient comfort.

List of abstracts that benefited from work presented in this chapter:

M. Sokolska, X. Golay, and D. Thomas *Effect of labelling plane angulation on pCASL labelling efficiency does it really matter?*. Proceedings of 23rd ISMRM 2015

M. Sokolska, A. Oliver-Taylor, X. Golay, D. Thomas *Theoretical and practical investigation of acoustic noise level reduction in pseudo-continuous Arterial Spin Labeling.* Proceedings of ISMRM Perfusion Workshop 2012

Chapter 7

Development of in vivo imaging framework for neonatal pCASL

7.1 Introduction

This chapter describes the development of the imaging framework for the neonatal pCASL. This includes optimisation of the scanning protocol and development of an effective method for motion correction. Sequence optimisation steps were performed as part of clinical neonatal pCASL study, described in detail in chapter 8.

7.2 Development of scanning protocol

Readout choice

Ideal readout sequence for neonatal ASL would provide a rapid volume acquisition, with resolution appropriate to neonatal brain anatomy sizes. However in practice, the voxel size in ASL needs to be large enough to provide high perfusion signal relative to noise. Previous ASL studies in neonates [58], [92] [49], have used voxels of the same size as in adults, which range between 3x3 and 4x4 mm^2, with slice thickness of 5.5 to 6 mm. A recently published study [49] was carried out on 3.0 Tesla Philips Achieva System (Philips Medical Systems, Best, The Netherlands), where they used a quadrature body coil for transmission, an 8-element phased-array SENSE head coil for reception and EPI readout. This set up is identical for the one available for this project, and therefore the same EPI readout parameters were chosen as a starting point (matrix 64x64, FOV 240x240, 3.75x3.75 in plane resolution, 6mm slice thickness, 1mm gap, TE 20ms).

SENSE factor was set up to 2.3. Tests with thinner slices resulted in reduction of SNR in PWI, therefore this readout setup was kept throughout the study.

Positioning of the labelling plane

As shown in section 6.2 of the previous chapter, the labelling plane in pCASL should be positioned over parts of the feeding arteries where all vessels are straight in order to ensure minimum variability of the labelling efficiency. On the other hand, labelling plane should be distanced enough from the brain to avoid saturation artefacts. The best way to find straight parts of the vessels is to perform a Time of Flight (ToF) sequence and use Maximum Intensity Projection (MIP) reconstruction. An example of the labelling plane position overlaid on the ToF MIP scans is shown in figure 7.1 (FFE, TE/TR 4.4/16ms, FOV 160x132x90mm, acquisition matrix 160x132).

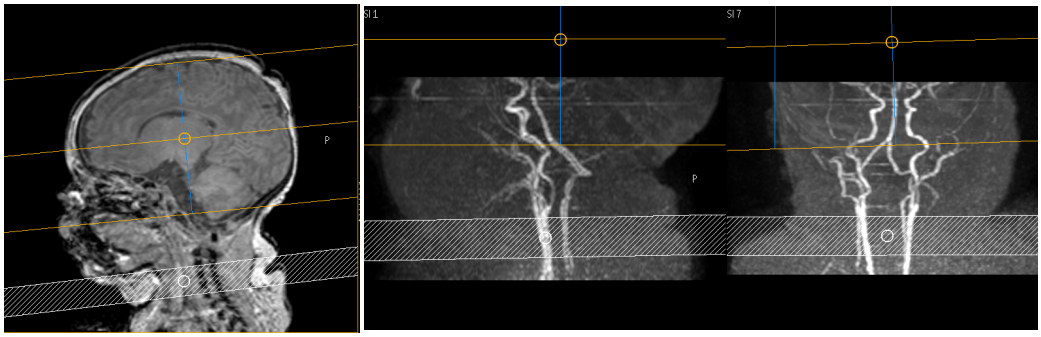

Figure 7.1: *Recommended position of the imaging volume (orange) labelling plane (white) on sagittal view of T_1 weighted image and MIP of ToF in sagittal and coronal projections.*

Background suppression optimisation

To further improve the SNR and reduce the number of averages required, background suppression pulses can be used [116]. Background suppression pulses are a series of inversion pulses following saturation, with a time delay in-between, chosen to suppress the signal from the static tissue [117]. The evolution of magnetisation after saturation and 2 inversion pulses is illustrated in figure 7.2 and can be found from the following equation:

$$M_z(T_1) = 1 + (-1)^{n+1} \exp\left(\frac{T_{acq}}{T_1}\right) + 2\sum_{i=1}^{n}(-1)^i \exp\left(\frac{TI_{BS,i}}{T_1}\right) \tag{7.1}$$

Delays between the pulses can be found by solving the above equation using the function "fsolve" in Matlab. Ideally, the M_z of each tissue type should be equal to 0, in order to achieve

best suppression of the background signal. However, any small deviation from expected T_1 values or physiological noise could result with negative values of M_z. To avoid this, the target value of $M_z(T_1)$ can be set to 20% of the original value. The T_1 values should be appropriate for the neonatal group [118]: 1.913 - 2.254s for grey matter and 2.556 - 2.934s for white matter. The time for the first BS pulse should be fixed to the earliest possible time after labelling train.

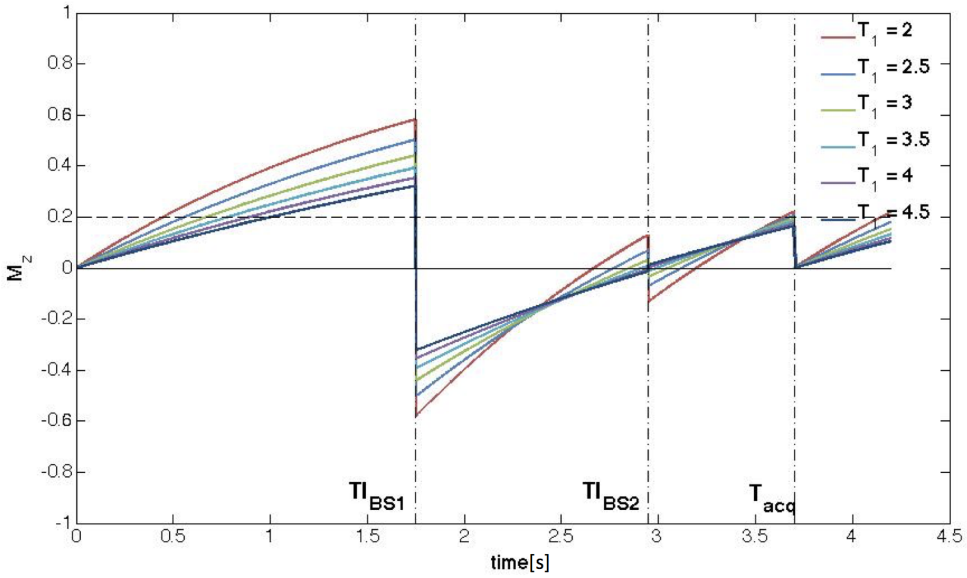

Figure 7.2: *Evolution of tissue longitudinal magnetisation with background suppression pulses*

Fat/SENSE artefact

The fat artefact in an EPI based readout is a result of a chemical shift in the phase encoding direction. Additionally, in cases of misalignment between the SENSE reference scan and ASL, the SENSE reconstruction can introduce 'wrapping' artefact. This is caused by the incorrect coil sensitivity estimation due to motion. An example of the combination of Fat/SENSE artefact and can be clearly visible in the further part of this chapter, in figures 7.11 and 7.12 (before motion correction). To reduce this artefacts, two steps were undertaken:

1. Addition of fat saturation pulses (not used initially following the manufacturer's advice)
2. When possible, and addition of SENSE reference scan before the ASL acquisition.

Additional SENSE acquisition extends the imaging protocol time and can only provide the improvement if there is no more motion within ASL scan. Fat saturation is commonly used for ASL experiments, but it might affect the CBF quantification [119],

Post labelling delay

Identification of the optimal post labelling delay (defined previously in chapter 4), is crucial for accurate CBF quantification. As discussed in section 4.2, if PLD is shorter than theATT, the traveling blood will still occupy arteries, producing bright signal and CBF around arteries becomes overestimated, and underestimated in other regions, since the bolus duration in the voxel would be different to that assumed. Therefore the PLD should be longer than the longest ATT. On the other hand, when PLD is too long, the labelled blood would have relaxed (which reduces SNR) and fewer repetitions are possible within the acquisition time, according to [70], [120]:

$$SNR_{eff} = \frac{PWI}{\sqrt{\tau + PLD + t_{acq}}} \tag{7.2}$$

where SNR_{eff} is an effective SNR of an ASL experiment and t_{acq} - image acquisition time. Establishing the optimal PLD in a neonatal group can be challenging, as there are many factors influencing ATT, that vary between neonates, like velocity in the feeding arteries [57], [121], sedation drug used, cooling or the overall condition of he neonate after HIE.

7.2.1 Methods

To better understand the spatial distribution and the range of ATT in neonates, two experiments aiming to measure perfusion weighted signal at different PLD were performed:

1. Multiple, short and low resolution acquisitions at different PLDs, similar to [120] (long acquisition)

2. An acquisition of a single slice at different PLDs in Look-Locker sampling scheme, similar to [122] (short acquisition).

The main differences between the two protocols is their duration and coverage. Although approach 1 has a better coverage, it was found too lengthy and impractical to perform on all neonates. Protocol 2 was proposed to offer shorter ATT survey, compromising the coverage.

Multiple PLDs in multi low-resolution acquisitions

Two neonates underwent the multiple low resolution scans at a range of PLDs in addition to an acquisition with PLD = 1500ms (3 x 20 control-label pairs,2min48s each). The details of the low resolution scans were as follow: 15 control-label pairs, acquisition matrix 64x64, voxel size 4.5 x 4.5 x 6 mm (reconstructed voxel 3x3x6mm), labelling duration τ = 1700ms, SENSE

factor 2.3, 12-16 slices, TE = 20ms, TR = 3170 - 4678ms and 5 PLDs: 800ms, 1300ms, 1600ms, 1900ms, 2300ms, scan duration: 1.5min - 2.5min for each PLD. Before analysis, all images were registered to the mean of the standard resolution image and the motion corrupted data removed with the procedure described below in section 7.3. PWIs at each PLD were computed. A histogram of all image intensities within a brain mask was also computed (30 bins were used) to visualise the intensity composition for PWIs at each PLD.

An acquisition of a single slice at different PLDs with Look-Locker sampling

Look-Locker sampling with EPI readout [122] was used to acquire multi PLD information. Here, only one slice was acquired, which was positioned at the level of thalamus and basal ganglia. 15 PLDs were acquired, ranging from 50 to 3998ms after the end of labelling in steps of 151ms, with TE/TR = 16/151 ms, flip angle α = 30°. Two repetitions were acquired in 24 seconds. Before analysis, the intensities of the images were corrected for T_1 relaxation and multiple excitation, by multiplying each voxel by $\exp(\tau/T_{1b})$ and $(cos\alpha^{-1})^{n-1}$ (where n - number of pulses experienced by blood protons, T_{1b} - T_1 of arterial blood) respectively. It was assumed, that the arterial protons during first five PLDs experience only one excitation pulse as they move through the vasculature. The mask was created by applying a threshold to segment the brightest voxels. The intensity of these voxels, with the mean and standard deviation was also plotted to visualise the evolution of arterial signal over time.

7.2.2 Results

Multiple PLDs in multi low-resolution acquisitions. Three chosen slices of PWI acquired at different PLDs are shown in figures 7.3 and 7.5 and the corresponding histograms of brain PWIs in figures 7.4 and 7.6. For the first neonate, the quality of PWI at higher PLDs (1900 and 2300 ms) is much worse compared with others. This was due to the motion artefacts, which persisted through the motion correction, as well as the lower signal due to the relaxation of labelled blood. For both subjects, there is some signal coming from residual label in arteries in image acquired at 800ms, however, this is not visible at the later PLDs. From PLD 1300 ms onwards, a well perfused cortical ribbon is visible. The analysis of the histograms confirms this - at PLD 800 there are many high intensity voxels compared to the late PLDs.

An acquisition of a single slice at different PLDs with Look-Locker sampling. Two examples of single slice Look-Looker sampling are shown in figures 7.7 and 7.8 for two neonates

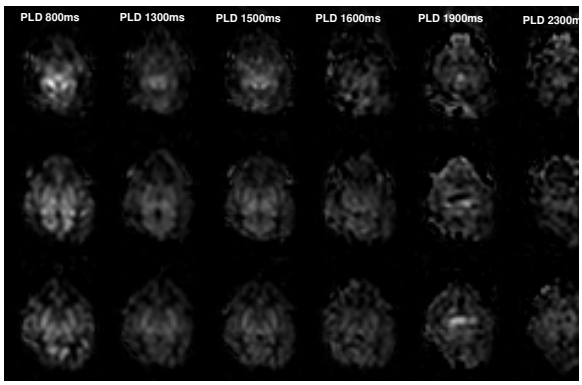

Figure 7.3: *3 slices of PWI acquired at different PLDs (neonate 1)*

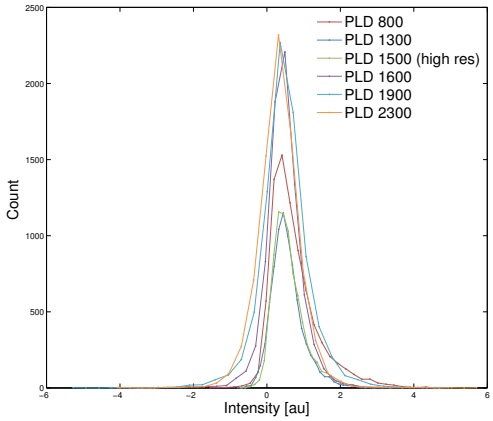

Figure 7.4: *Histogram of masked PWI acquired at different PLDs (neonate 1)*

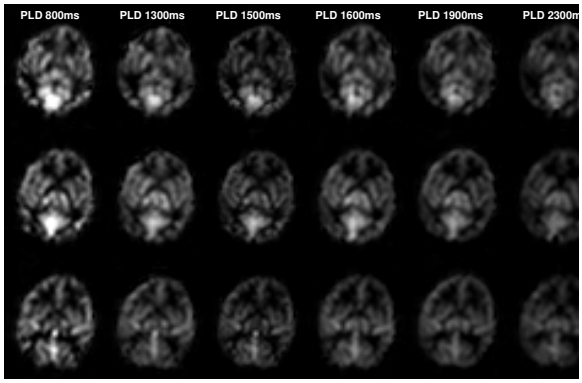

Figure 7.5: *3 slices of PWI acquired at different PLDs (neonate 2)*

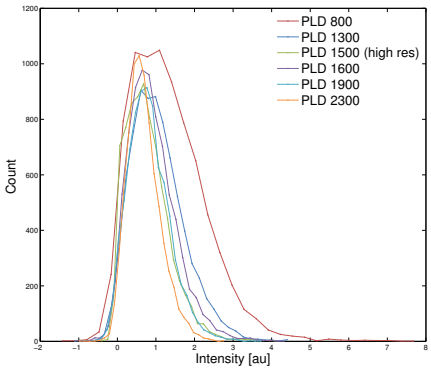

Figure 7.6: *Histogram of masked PWI acquired at different PLDs (neonate 2)*

with different ATT patterns. In the first neonate (figure 7.7), the vascular signal reduces much more slowly compared to the second neonate (figure 7.8) and is still is visible in the image acquired at PLD = 1.107s. For the second neonate the vascular signal reduces rapidly and is not visible in the image acquired ad PLD 0.65s.

7.2.3 Summary

This section described the development of the imaging protocol in neonates and justified the choices made:

1. Readout: although 2D, EPI readout has been used due to acquisition speed.

2. ToF scan: Given variable size of neonates and the inconsistent position of the head and

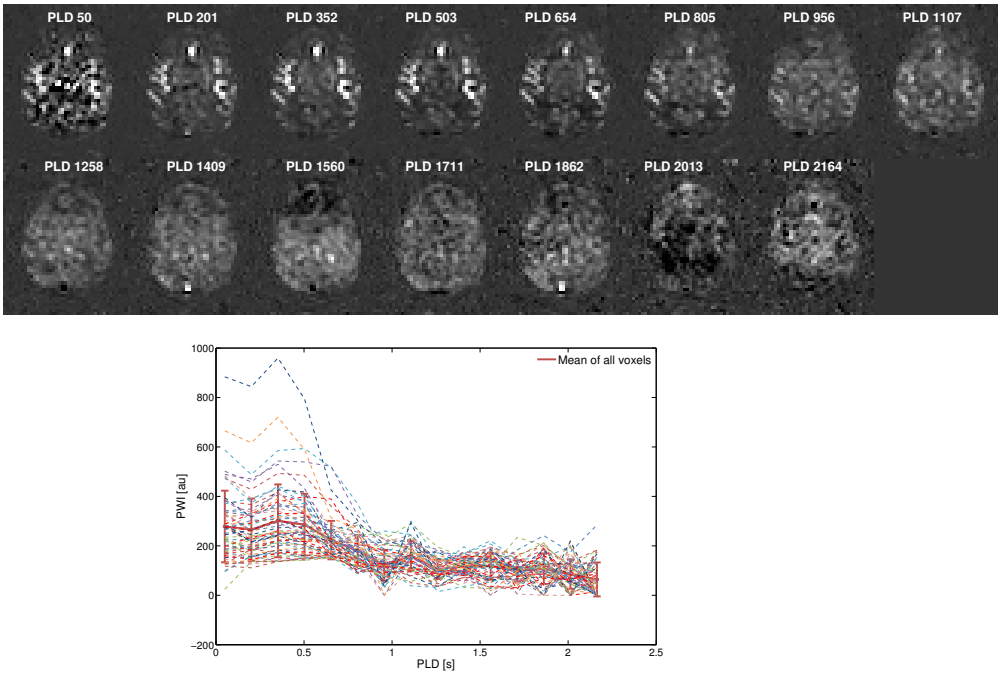

Figure 7.7: *Difference image of a single slice Look-Locker acquisition and arterial ROIs plotted for a range of PLDs [ms]. Neonate with long ATT*

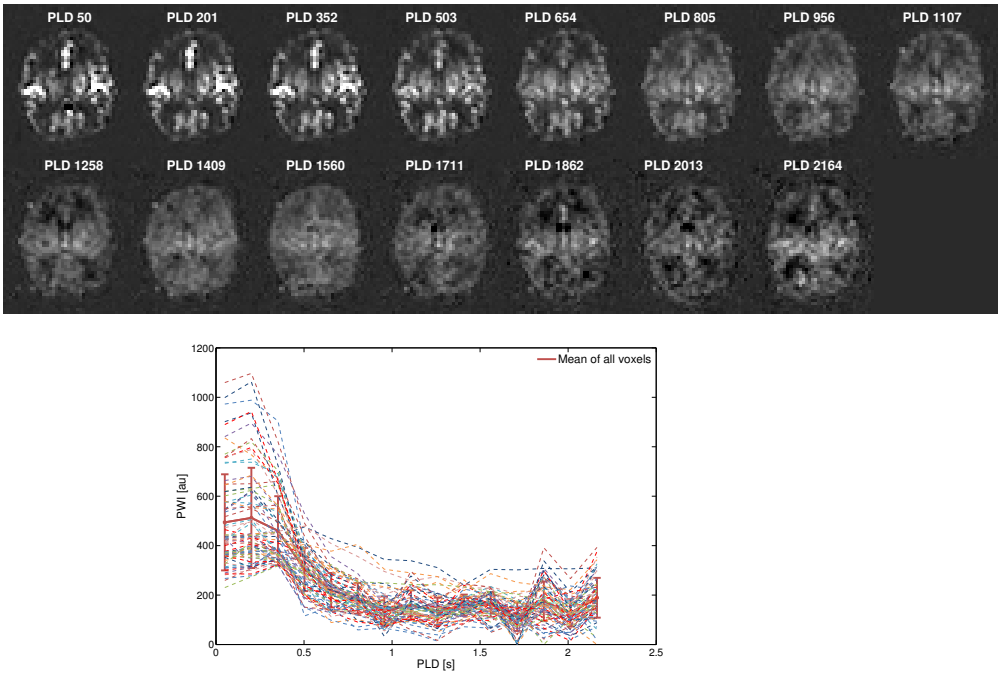

Figure 7.8: *Difference image of a single slice Look-Locker acquisition and arterial ROIs plotted for a range of $PLDs[ms]$. Neonate with short ATT*

neck in the incubator between babies, it is advantageous to find the best labelling plane position using ToF MIP. In addition, the structural scans should also be used to ensure a minimum distance between the labelling plane and brain tissue.

3. BS: For labelling duration of 1.7s and PLD 2s, optimised BS pulses were at 1750ms and 2974ms.

4. Optimum PLD: The method in which multiple, low resolution PLDs are acquired as separate scans gave an initial insight into the temporal distribution of the blood to different parts of the brain in neonates and guided the PLD change from the initial setting of 1.5 to 1.8s. However, due to the long acquisition time, this method was adopted in only two neonates, one of which had an unusually high CBF value due to HIE. Since some residual arterial signal was still observed in some neonates, PLD was increased to 2s. The single slice PLDs with Look-Locker sampling benefits from very short acquisition time and therefore can provide very useful information about arrival times before the main scan. This can be used to choose the appropriate PLD for each baby. From these limited examples it is clear, that ATT differs between babies. Therefore it might be that estimating ATT for each neonate might add to clinical picture or help investigating the treatment effects. However, the relevance of this, given a single slice acquisition, has yet to be established.

7.3 Motion and motion correction

Motion correction and elimination of any intensity differences between control and label images that do not represent perfusion is a crucial part of ASL image processing. In ASL, multiple repetitions of the control-label pairs are acquired to improve the SNR. This assumption is only true if all the voxels correspond to a fixed location in the brain which does not change during the duration of the scan. However, this is usually not the case and given that the difference of the signal between a single control and labelled images is relatively small, the difference in signal due to motion can be significantly larger and produce artefactual perfusion values.

The amount of motion during an ASL scan in neonates can vary substantially, depending on the baby's preparation. Some babies are 'fed and wrapped' without any sedation, but some are administered an oral dose of chloral hydrate or intravenous morphine (in case of ventilated babies). None of these methods, however, guarantees motion free scans. Examples of different

extent of motion are shown in figures 7.9 and 7.10, showing translation and rotation computed from the transformation matrix after rigid registration. If the baby did not move throughout the duration of the scan, motion correction might not be necessary, given the magnetic field drift is not large (the scanner drift is demonstrated here as the smooth and consistent translation in the phase encoded direction y, as seen in [123]). In some cases, when the baby is unsettled or awake, the amount of motion makes it impossible to create a meaningful perfusion weighted image without additional data processing steps: identification of corrupted data and its exclusion, image registration, or a combination of both.

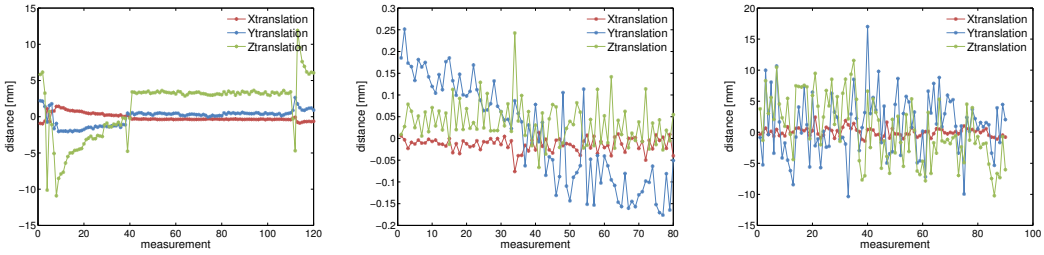

Figure 7.9: *Translation in x, y and z direction computed from the transformation matrix after rigid registration for different amount of motion: from the left: severe intermittent motion, drift of magnetic field during the scan, very severe motion. Please note different distance scales*

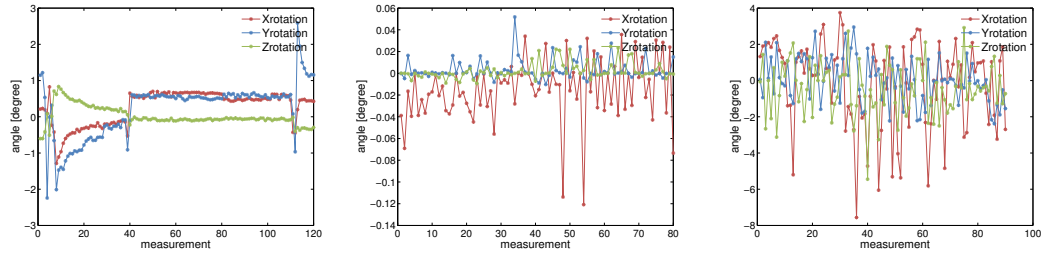

Figure 7.10: *Rotations around x, y and z axis computed from the transformation matrix after rigid registration for different amount of motion: from the left: severe intermittent motion, drift of magnetic field during the scan, very severe motion. Please note different distance scales*

There is a limited literature on the best strategy in neonates with severe motion artefacts, and therefore a detailed analysis was performed.

7.3.1 Background

Outlier exclusion

Existing intensity based methods. One of the methods for improving the quality of PWI is based on identifying and discarding the corrupted images from the data series. This can be done based on a visual inspection, however, due to an impracticality and potential bias, an automated method is preferred. Most commonly, after pairwise subtraction, a mean difference between control and labeled image m_i is calculated for each pair $i = 1 : N$, where N is the number of averages:

$$m_i = \frac{1}{K} \sum_{j=1}^{K} v_{ij} \tag{7.3}$$

where K is the number of voxels within a mask, and v_{ij} - intensity of the jth voxel of the ith difference image within the mask. Next, the mean μ_m and standard deviation σ_m over all m are computed:

$$\mu_m = \frac{1}{N} \sum_{i=1}^{N} m_i \text{ and } \quad \sigma_m = \sqrt{\frac{1}{N-1} \sum_{i=1}^{N} (m_i - \mu_m)^2} \tag{7.4}$$

The pairs for which the condition:

$$|m_i - \mu_m| > p \cdot \sigma_m \tag{7.5}$$

is fulfilled, are discarded from the final averaging. The constant p; when set to 2 [124] it means that the 95% of the data is kept. An extension to this method proposed by Tan *et al.* [125], is to calculate both the m_i as well as the standard deviation for each subtracted pair:

$$s_i = \sqrt{\frac{1}{K-1} \sum_{j=1}^{K} (v_{ij} - m_i)^2} \tag{7.6}$$

and the mean μ_s and standard deviation σ_s across all s_i, where:

$$\mu_s = \frac{1}{N} \sum_{i=1}^{N} s_i \text{ and } \sigma_s = \sqrt{\frac{1}{N-1} \sum_{i=1}^{N} (s_i - \mu_s)^2} \tag{7.7}$$

Similarly, if

$$|m_i - \mu_m| > p \cdot \sigma_m$$

or

$$s_i - \mu_s > q \cdot \sigma_s \tag{7.8}$$

with q empirically found to be 1.5 [125], such volume is classified as an outlier. If

$$\ln (max(s_i) - min(s_i)) < 1 \tag{7.9}$$

all the pairs were considered 'stable' and included in the final PWI. This step is design to minimise over-filtering, i.e. exclusion of good data since a certain number of s_i will always fall outside $\mu_s \pm q \cdot \sigma_s$. Constants p, q and exclusion criterions are empirically chosen, and can be adjusted to better remove motion corrupted volumes for given dataset. The main drawback of this method is the fact that, especially in the presence of severe motion, the calculated standard deviation will be artificially increased by the presence of the outliers and therefore not all corrupted data will be correctly identified.

Investigated new intensity based methods.

1. The first proposed method of outlier detection is to further extend the method proposed by [125] and use criterion 7.9 as a stopping criterion, i.e. keep excluding difference images until 7.9 is fulfilled.

2. An alternative approach is to identify volumes - control or labels - that are not aligned with the mean image using sum of square differences (SSD) - commonly used similarity measure. The SSD is very sensitive to voxels with large intensity differences, which makes it a good candidate to identify volumes that are not aligned with the rest. The procedure of finding outliers can be designed in a similar way than above, but instead of calculating a difference image m_i, SSD between the acquisition I_i and the mean of all acquisitions $\bar{I}$ is calculated instead, as defined below:

$$SSD_i = \frac{1}{K} \sum_j |I_j - \bar{I}|^2 \tag{7.10}$$

   The rejection of the data is performed until an empirically found exit criterium is reached, such as:

$$\ln\left(max(SSD_i) - min(SSD_i)\right) < 5 \tag{7.11}$$

3. The extension of the above approach is to restrict the analysis to the regions of the biggest motion, rather than the brain mask. For this purpose, the use of Robust Principal Component Analysis (RPCA) [126] was investigated. If the motion artefact in the SSD_i is sparse, RPCA can separate sparse and low rank components in the image. The assumption is that the high intensity due to motion can be decomposed and used to identify the most corrupted volumes better.

Registration based methods. The final method of identifying the outliers is to register all the images together and use the given transformation matrix as a guidance. In [127],[58], if the absolute translations or rotation between successive volumes was greater than 2 mm and 1.5° respectively, such volumes were discarded.

Registration

The relative motion between acquired volumes can be represented by a geometrical transformation, that maps the corresponding anatomy from the one image to the another. This transformation can be determined by image registration. The transformation is then used to transform one image into the coordinate system of the other one by resampling, which requires interpolation. Image registration is a common approach in reduction of motion artefacts, however due to the big voxel sizes and low contrast between different tissue types in ASL data, it can be challenging.

In a typical implementation of ASL data registration, the first image is chosen as a common space and the remaining images from that dataset are registered to that common space. However, this can give rise to interpolation asymmetries: the target image will not be resampled and therefore will have a different amount of blurring compared to the rest of the volumes [128],[129]. This might especially be an issue if the chosen common space happens to be significantly missaligned relative to all other volumes. Additionally, the performance of the registration algorithm might be compromised due to large transformation needed for the alignment, which will then affect negatively all the volumes. The solution to these problems is to create an unbiased, common space template so that all the volumes can be treated the same way and the transformation needed is minimised. Such computed common template will represent an "average" head position.

7.3.2 Methods

Outlier exclusion. To find the best method of outlier exclusion, two datasets, one with severe and one with moderate motion between scans, were used to assess and compare the performance of methods described above (see list below). Each dataset consisted of 40 control - label pairs (80 volumes). Mean and standard deviation of PWI was computed alongside mean SNR, defined as PWI divided by SD across the all the difference images (tSD). The calculations were performed within the region of the brain defined by the mask. "inexact_alm_rpca" [1] function

[1] http://perception.csl.illinois.edu/matrix-rank/sample_code.html#RPCA

was used for RPCA computation. Two slices with the most pronounced artefact were chosen to demonstrate the change in perfusion image after discarding the data points identified. All the tested methods of outliers detection are listed as follows:

(A) No outlier identification

(B) Outlier identification based on visual inspection

(C) Outlier rejection based on equation 7.5 only with $p = 2$ [124]

(D) Outlier rejection based on equation 7.5 and 7.8, with restriction 7.9 with $p = 2$ and $q = 1.5$ [125]

(E) Method D extended by repeating it until 7.9 is fulfilled

(F) Identification of misaligned volumes based on SSD

(G) Identification of misaligned volumes based on the combination of SSD and RPCA

(H) Identification of misaligned volumes based on the transformation matrix from rigid registration to the mean

Registration. Two different registration strategies were tested:

(A) Registration to the first image

(B) Registration to refined mean image

The same two datasets with variable amount of motion were chosen to assess the performance of these approaches. A rigid transformation with normalised mutual information [130] was used. Rigid transformation only alters the image orientation, preserving object's size and shape and is therefore best suited for alignment of ASL data. Normalised mutual information was chosen as a similarity measure to accommodate the intensity differences in control and labelled images.

The refined mean image was computed by first creating a mean image, next registering all volumes to the mean image and iterating the process 3 times (established empirically as the number of iteration that do not reduce tSD of registered images significantly). This was done using "scalar_rigid_population" implemented in the DTI-TK software package [2]. To reduce the computational time, every other control image was used to create a mean.

[2] http://dti-tk.sourceforge.net/pmwiki/pmwiki.php

Registration with outlier rejection. To further reduce the contribution of motion to the final PWI image, the combination of the registration and outlier rejection was also tested. Two methods of outlier rejection that performed best in the previous section were identified and added as as step after registration. Additionally, a motion free dataset was chosen to assess the influence procedure on the image SNR.

Validation Twelve neonatal datasets were used to validate the motion correction and rejection regime. Each dataset consisted of 40 control-label pairs. Similarly, mean and standard deviation of PWI and mean SNR, as defined above. This was computed for all datasets without any motion correction, standard data rejection and best rejection regime, for both non-registered and registered data. The amount of motion was assessed visually and the datasets were divided in three categories: motion free, moderate and severe motion to assess the motion correction and rejection regime in each category. Resulted PWIs were also visually assessed in terms of artefacts and definition of grey and deep grey matter.

7.3.3 Results

Outlier exclusion. Table 7.1 presents the results of the analysis. All the methods were capable of improving PWIs for both datasets, in terms of reduction in SD and increase in SNR for case of severe and moderate motion. The change of the quality of the PWI maps for data with severe motion can be observed in figures 7.11, 7.12 and 7.13. The bright rim around the brain observed in PWI and tSD before discarding corrupted data, indicating misalignment of volumes, are much reduced after exclusion. Although the number of volumes contributing to the final PWI decreased, the reduction of tSD resulted in increase in SNR. Method C and D - rejection based on the deviation from the mean signal or in combination with deviation in standard deviation, resulted in the smallest amount of improvement, both qualitatively and quantitatively. This is the result of significant inflation of both SD of the mean σ_m and SD of the standard deviation σ_s in case of big motion artefacts. This seems to be solved by iterating the rejection of the data until all difference images m are considered 'stable' by meeting the condition 7.9. In case of method H, the improvement of PWI in terms of SNR is similar to method C and D. This is due to the limitations of the registration algorithm, namely, some of the volumes get mis-registered and therefore the registration transformation does not always reflect the amount of rotation and/or translation necessary for the perfect alignment. The PWI, SD and SNR for moderate motion is shown in figures 7.14, 7.15 and 7.16. Visually, the improvement provided by all methods is

similar. However, quantitatively, method E provides the highest SNR, even though the lowest number of repeats are used to create the PWI. Method F and G identified the same volumes as outliers and produced the same results of Mean PWI and SNR. This indicates that there are no benefits in restriction of calculations to the motion affected regions using RPCA.

Method	No Pairs Used	Mean PWI (SD)	SNR = PWI / tSD
Severe motion			
A. None	40	0.7644 (1.0860)	0.1835
B. Visual rejection	28	0.4273 (0.4013)	0.3457
C. Mean	37	0.6074 (0.7524)	0.2436
D. Mean + SD	35	0.5130 (0.5729)	0.2748
E. Mean + SD + loop	**26**	**0.4263 (0.4100)**	**0.3599**
F. SSD	29	0.4467 (0.4668)	0.3505
G. PCA	29	0.4467 (0.4668)	0.3505
H. Rigid transf. mat	33	0.5305 (0.5800)	0.3307
Moderate motion			
A. None	40	0.6624 (0.5325)	0.5619
B. Visual rejection	34	0.6412 (0.4895)	0.8659
C. Mean	37	0.6602 (0.5136)	0.7417
D. Mean + SD	36	0.6655 (0.5155)	0.8285
E. Mean + SD + loop	**31**	**0.6550 (0.4809)**	**0.9041**
F. SSD	37	0.6537 (0.5062)	0.8057
G. PCA	37	0.6537 (0.5062)	0.8057
H. Rigid transf. mat	39	0.6458 (0.5207)	0.6837

Table 7.1: *Summary of mean, standard deviation and SNR of the whole brain PWI for each exclusion method. The best performer highlighted in bold.*

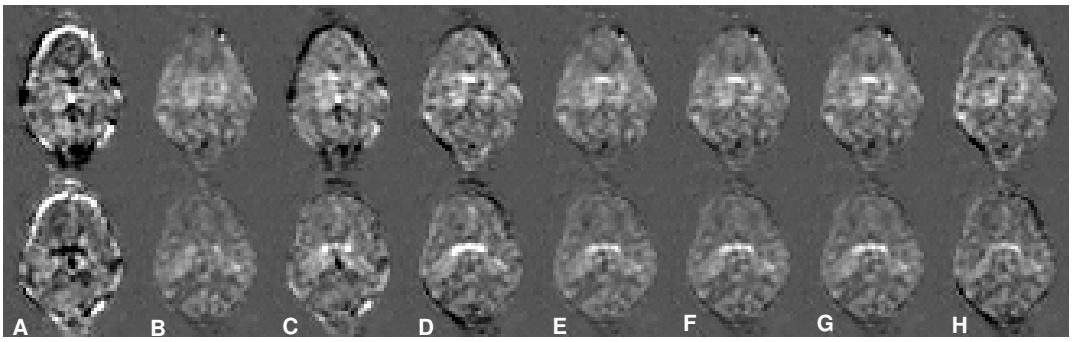

Figure 7.11: *2 slices of PWI with severe motion; A - G different method of outliers detection (see text for more details)*

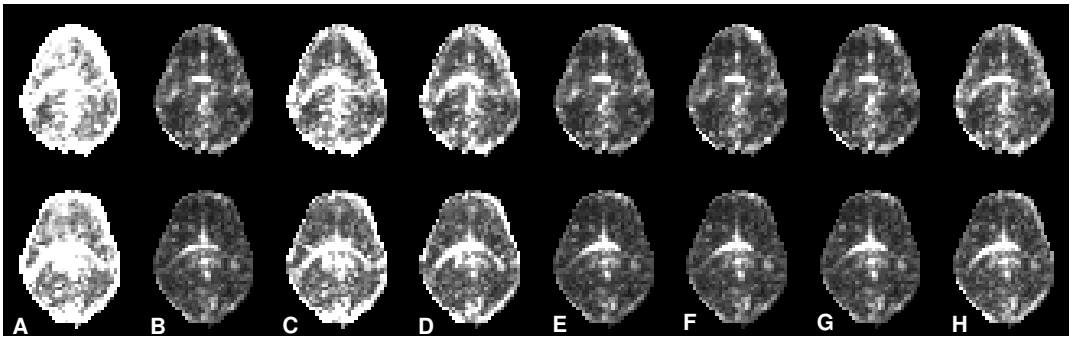

Figure 7.12: *2 slices of tSD with severe motion; A - G different method of outliers detection (see text for more details)*

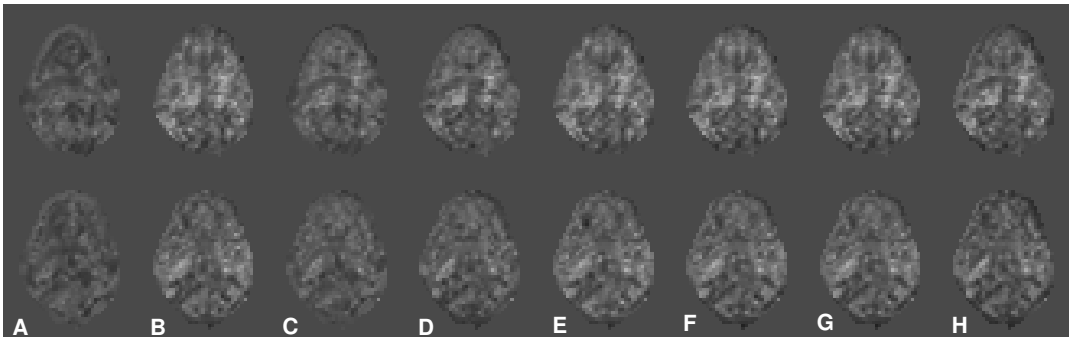

Figure 7.13: *2 slices of SNR with severe motion; A - G different method of outliers detection (see text for more details)*

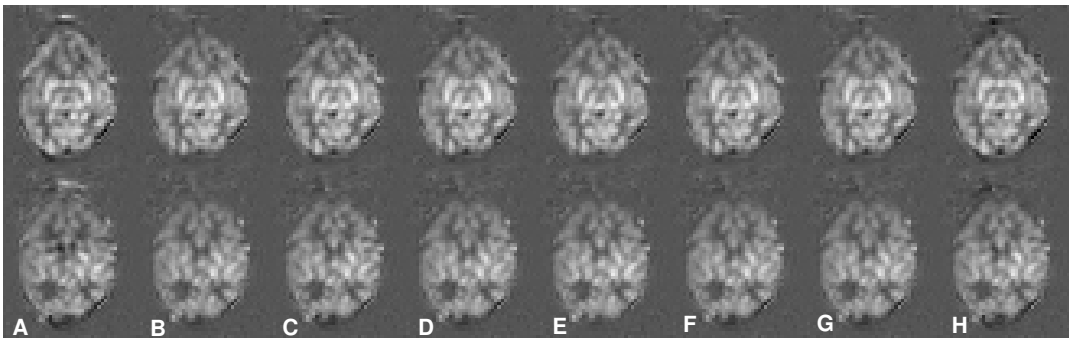

Figure 7.14: *2 slices of PWI with moderate motion; A - G different method of outliers detection (see text for more details)*

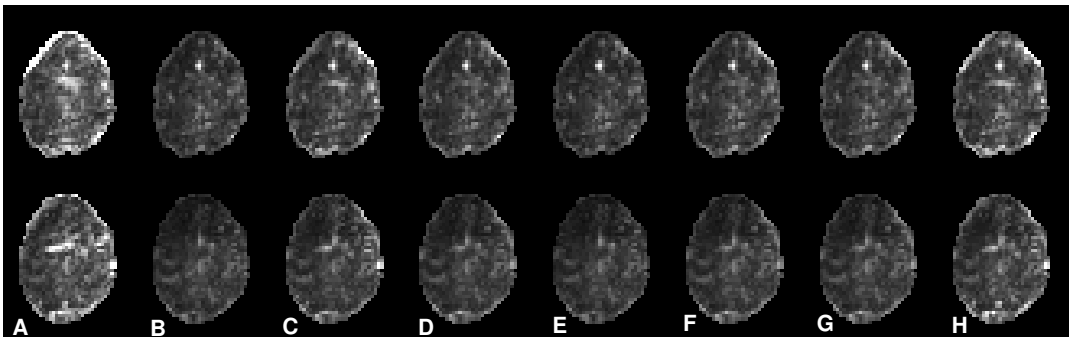

Figure 7.15: *2 slices of tSD with moderate motion; A - G different method of outliers detection (see text for more details)*

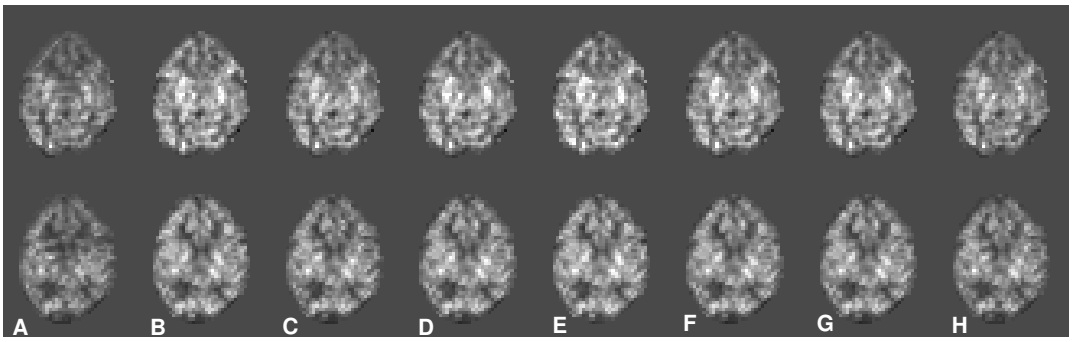

Figure 7.16: *2 slices of SNR with moderate motion; A - G different method of outliers detection (see text for more details)*

Registration with outlier rejection. Method E and F were found to be most effective in identifying motion corrupted volumes and were selected for further testing with registrations. The performance of the registration before and after outliers exclusion for severe motion can be visualised in figures 7.17 and 7.18 for the registration to the first and to the mean respectively. The qualitative data are also given in tables 7.2, 7.3 and 7.4 for severe, moderate and motion free data sets respectively.

It can be seen in figures 7.17 and 7.18, that SD reduces after the registration compared with images 7.12 and 7.15 before registration, however, the misalignment is still present, causing changes to the mean and SD of images contributing to PWI.

For both severe and moderate motion, a further improvement in SNR was achieved after registration, but only after exclusion of mis-aligned data was also performed (see tables 7.2 and 7.3). Registration to the mean paired with SD rejection seems to improve the quality of the PWI as well as SNR the most. For moderate motion, the choice of the target image doesn't seem to influence the PWI. In both cases, the registration paired with SD rejection produced higher SNR of PWI compared to no registration. In case of the data without any motion, the registration slightly reduced the SNR, however there was no difference in the mean PWI value.

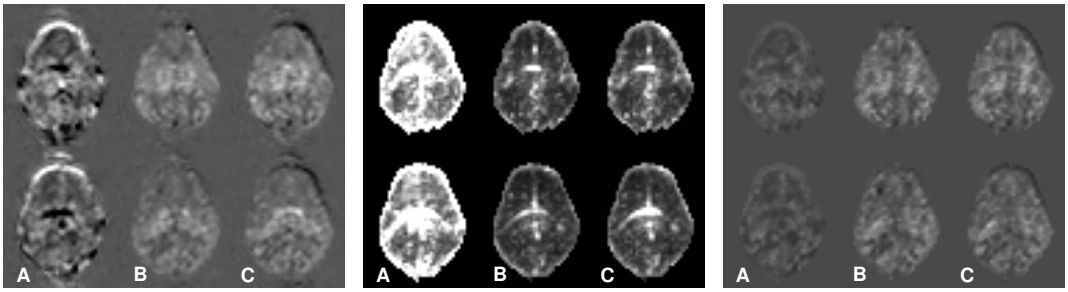

Figure 7.17: *2 slices of PWI, SD and SNR with severe motion after registration to the* **first** *volume and before outlier rejection (A), mean + SD + loop rejection (B) and SSD rejection (C)*

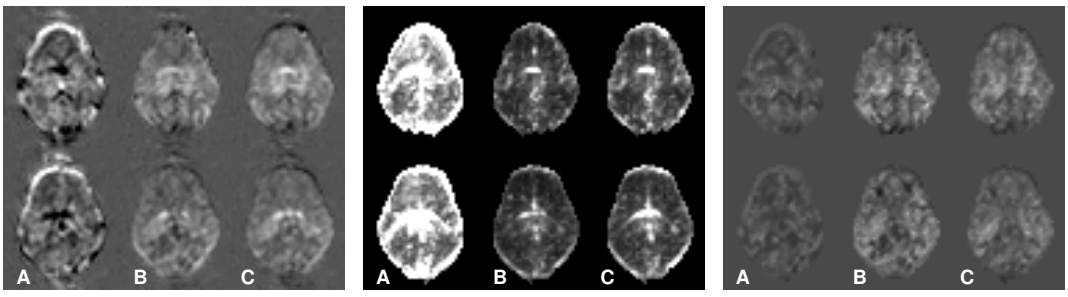

Figure 7.18: *2 slices of PWI, SD and SNR with severe motion after registration to the* **mean** *volume and A: before outlier rejection (method A), B:mean + SD + loop rejection (method E) and C: SSD rejection (method F)*

Method	No Pairs Used	Mean PWI (SD)	SNR = PWI / tSD
Registration to the first			
No exclusion (A)	40	0.5930 (0.7679)	0.1744
Mean + SD + loop (E)	24	0.3936 (0.3807)	**0.3588**
SSD (F)	31	**0.4118 (0.3922)**	0.3420
Registration to the mean			
No exclusion (A)	40	0.6362 (0.7942)	0.1863
Mean + SD + loop (E)	23	**0.4634 (0.4219)**	**0.4279**
SSD (F)	31	0.4295 (0.3982)	0.3340

Table 7.2: *Severe motion: summary of mean, standard deviation and SNR of the whole brain PWI for 2 registration methods.*

Method	No Pairs Used	Mean PWI (SD)	SNR = PWI / tSD
Registration to the first			
None (A)	40	0.6462 (0.4938)	0.5727
Mean + SD + loop (E)	31	**0.6556 (0.4646)**	**0.9434**
SSD (F)	37	0.6421 (0.4715)	0.8275
Registration to the mean			
None (A)	40	0.6365 (0.4790)	0.5727
Mean + SD + loop (E)	31	**0.6386 (0.4520)**	**0.9246**
SSD (F)	37	0.6361 (0.4638)	0.8213

Table 7.3: *Moderate motion: summary of mean, standard deviation and SNR of the whole brain PWI for 2 registration methods.*

Method	No Pairs Used	Mean PWI (SD)	SNR = PWI / tSD
No Registration	40	0.6253 (0.4673)	0.9145
Registration to the first	40	0.6228 (0.4523)	0.8532
Registration to the mean	40	0.6203 (0.4454)	0.8570

Table 7.4: *Motion free: summary of mean, standard deviation and SNR of the whole brain PWI for 2 registration methods.*

Validation. Method E for outlier exclusion was chosen for validation against previously published method D, with and without registration to refined mean image. The results of analysis averaged across all 12 datasets are given in table 7.5. In terms of motion, three datasets were categorised as motion free, 5 as mild and 4 as severe. The break-down for mean, SD and SNR for each motion category are shown in figures 7.19, 7.20 and 7.21, showing mean, SD and SNR respectively.

	No Pairs Used	Mean PWI (SD)	SNR= PWI / tSD	No loops	Accepted datasets
No registration					
No exclusion (A)		1.95 (2.93)	0.49		7
Mean + SD (D)	41.25	1.85 (2.70)	0.53	1.00	9
Mean + SD + loop (E)	31.75	1.89 (2.35)	0.58	3.75	11
With registration					
No exclusion (A)		1.95 (2.29)	0.51		7
Mean + SD (D)	41.25	1.90 (2.17)	0.55	1.00	9
Mean + SD + loop (E)	**33.67**	**1.89 (2.07)**	**0.61**	**2.58**	**12**

Table 7.5: *Summary of mean, standard deviation and SNR of the whole brain PWI for the full dataset*

The findings after analysing 12 datasets were consistent with those described above. Data exclusion significantly reduced presence of big motion artefacts, which was especially visible in datasets included in 'moderate' and 'severe motion' group. This is reflected in reduction of mean SD and increase SNR in figures 7.20 and 7.21 respectively for these categories. The best improvement was achieved for proposed method E. In all cases, registration improved definition of the anatomy, i.e. cortical ribbon and deep grey matter and in some cases reduced some motion artefacts, which resulted in reduced SD and improved SNR in 'moderate' and 'severe motion' groups.

Out of all different methods motion correction, only a combination or registration and proposed method E allowed inclusion of all twelve datasets to the study (based on visual inspection). Using method D with or without registration, would have resulted in exclusion of 3 datasets (25%).

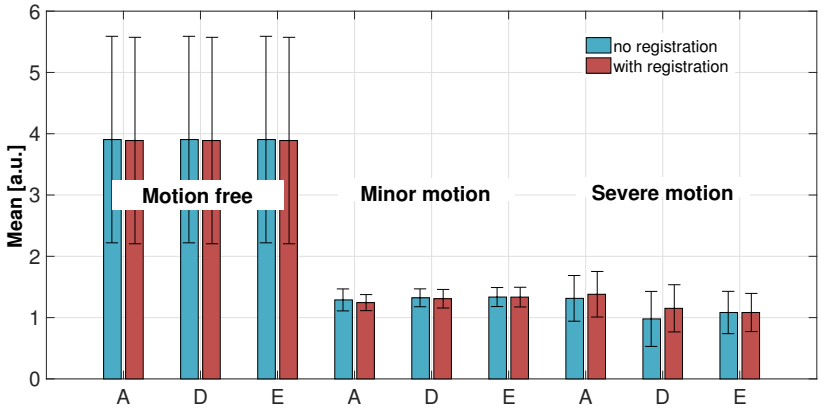

Figure 7.19: *Mean PWI averaged across different motion groups for 3 methods with and without registration. (A): no outlier exclusion, (D): mean + SD, (E): mean + SD + loop; error bars represent standard error.*

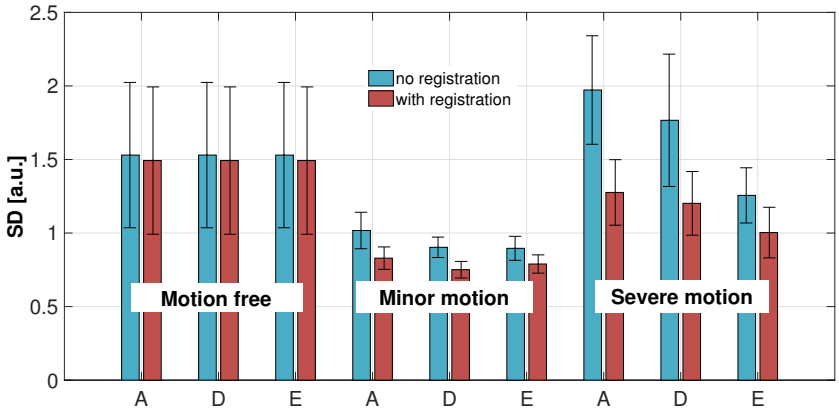

Figure 7.20: *Mean SD of PWI averaged across different motion groups for 3 methods with and without registration. (A): no outlier exclusion, (D): mean + SD, (E): mean + SD + loop; error bars represent standard error.*

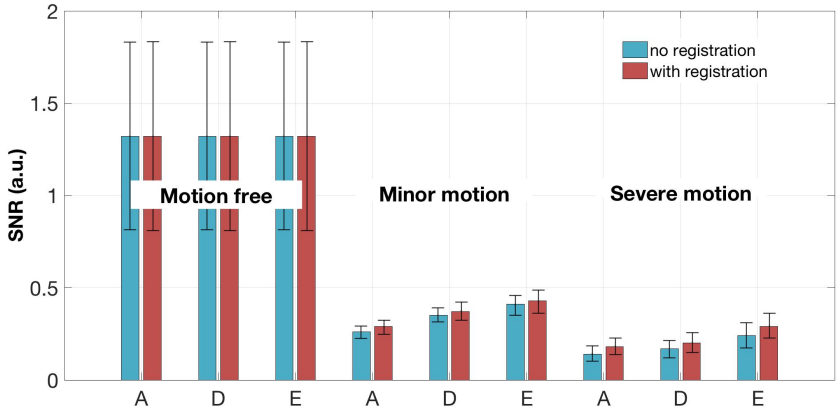

Figure 7.21: *SNR averaged across different motion groups for 3 methods with and without registration. (A): no outlier exclusion, (D): mean + SD, (E): mean + SD + loop; error bars represent standard error.*

7.3.4 Discussion

The above analysis shows, that identification and exclusion of motion corrupted data significantly improves the quality of the data in case of both severe and moderate motion. Reduction in number of averages used to compute PWI did not result in decreased SNR, confirming, that the data removed from analysis had undesired effect on PWI. All proposed methods resulted in improved quality of PWI, with proposed method E performing the best qualitatively and quantitatively. There are two advantages of using this method. Firstly, it does not require rejection of any dataset if the motion is not present (condition 7.9). Secondly, it performs rejection until all datasets are considered stable. This allows to overcome the issue of increased standard deviation in a presence of outliers. With this additional condition the number of images rejected was similar for both severe and moderate motion.

The registration paired with misaligned data exclusion improves the quality and SNR of PWI, especially in case of severe and moderate motion. The choice of the template for the registration is important when a severe motion is present the "average head position" should be chosen as a common space for the registration. However, this choice is less important for less severe motion. The registration algorithm is not always able to align the volumes, and therefore additional exclusion is necessary.

Both improvements: first, it the image registration and second, in identification of corrupted data resulted in 100% success rate, which compares favourably with previously published research.

An additional improvement of the registration performance could be achieved for the registration of control and images separately and this will be investigated in the future work. Another improvement might be to perform a distortion correction using acquired B_0 map. However, this might be not practical for 2 reasons: first, in case of large motion the acquired map might not match the image to be corrected and secondly, it requires additional time for acquisition.

However, in some cases the registration might not result in a good alignment. This is because of the low resolution of ASL images in combination with poor contrast and non-isotropic voxels. Therefore, after the registration, those images that are still not aligned, should be identified and excluded.

7.4 Summary and conclusions

This chapter presents development and optimisation of ASL protocol for neonatal scanning and motion correction. Two main issues that can significantly alter the estimated CBF have been identified:

1. Arterial Transit Time range: ATT

   Arterial Transit time varies between the babies. This variation might be visualised by acquisition of a single slice image at multiple delay times. This might be then used to adjust the PLD appropriately to avoid arterial artefacts.

2. Motion correction with outlier rejection

   Motion correction is essential to compute meaningful PWI for neonates that moved during acquisition. This can be achieved by efficient rejection of corrupted datasets or image registration. The best performance is achieved when these two techniques are combined. Creating an "average head position" as a common space improves the registration. However, this improvement is more subtle than data rejection.

List of abstracts that benefited from work presented in this chapter:

M. Sokolska, X. Golay, and D. Thomas *Effect of labelling plane angulation on pCASL labelling efficiency does it really matter?*. Proceedings of 23rd ISMRM 2015

M. Sokolska, C. Uria-Avellanal, M.J. Cardoso, M. Proisy, A. Bainbridge, S. Ourselin, D.Thomas, N. Robertson, and X. Golay *Assessing brain damage after perinatal hypoxic-ischaemia using an automated protocol for combined regional analysis of the Cerebral Blood Flow and MR spectroscopy*. Proceedings of 23rd ISMRM 2015

C. Godi*, **M. Sokolska***, F. Kennedy, S. Fallatah, X. Golay and R. Jäger *"Quantification of cerebral haemodynamics with QUASAR Arterial Spin Labelling (ASL) in patients with carotid atherosclerotic stenosis"*. Proceedings of 32nd Annual Scientific Meeting ESMRMB 2015

L. Haddow, **M. Sokolska**, S. Fallatah, R. Gilson, R. Jäger, X. Golay *"A study of the effect of early, untreated HIV on cerebral perfusion and arterial transit time in the basal ganglia using arterial spin labelling"*. 15th European AIDS Conference 2015

M. Sokolska, Maia Proisy, Cristina Uria-Avellanal, Alan Bainbridge, Ernest Cady, David Thomas,

Nicola Robertson, and Xavier Golay *Combined use of arterial spin labeling and MRS to determine the severity of injury in neonates with hypoxic-ischaemic encephalopathy* . ISMRM 2014

M. Sokolska, D. Thomas, A. Bainbridge, X. Golay, S. Taylor, S. Punwani, D. Pendse *Renal Perfusion Imaging with Pseudo-continuous Arterial-Spin Labelling (pCASL) at 3.0T: Repeatability in Healthy volunteers.* Proceedings of 22nd ISMRM 2014

M. Sokolska, D. Thomas, A. Bainbridge, X. Golay, S. Taylor, S. Punwani, D. Pendse *"Renal Pseudo- continuous Arterial Spin Labelling (pCASL) MRI: A Repeatability Study".* ERC 2014

Chapter 8

Clinical application of pCASL in neonates with hypoxic-ischaemic encephalopathy

8.1 Introduction

In this chapter, a detailed analysis of CBF maps acquired from neonates who experienced a peri-natal hypoxic-ischaemic event will be presented. This will be combined with brain MRS data acquired during the same scanning session in order to compare the abnormal regional CBF values to the outcome biomarker derived from MRS and investigate the added value of ASL and to link the physiological and biochemical changes after hypoxia-ischaemia in neonatal brain.

8.2 Background

Perinatal hypoxia-ischemia (HI) can cause severe alteration of brain metabolism and physiology [17], resulting in neonatal encephalopathy. Metabolic changes detected using magnetic resonance spectroscopy (MRS) have been used as a reliable predictor of clinical outcome [131]. Abnormalities in cerebral blood flow (CBF), reflecting cerebral physiology, have also been linked to HI [34]. Our group proposed combining these two MR biomarkers [132], which was subsequently shown by another group to increase the predictive power of MRS in deep grey matter (DGM) [133]. The CBF analysis in [133] was limited to DGM; extending this analysis to other brain regions might provide further insights into different patterns and severity of the

pathology resulting from HI.

Regional CBF analysis can be achieved by manually placing regions of interest (ROI) directly on the CBF map, using high resolution scans used as a guidance. However, this approach requires an expert knowledge of neonatal brain anatomy. Additionally, it is likely that this approach will produce biased CBF values if identification of the regions is based only on voxels' intensity in the CBF maps. A different solution to this problem is to define ROIs on high resolution structural images, either manually [134] or automatically, using available atlases, and then propagate the labels to the perfusion maps. Recently, two new neonatal atlases have become available: one containing probabilistic tissue segmentation of 5 tissue classes[1] [135] and one consisting of manual segmentations of neonatal brain into 50 regions called ALBERT[2] [136]. They have been shown to be useful for segmentation and percellation of high resolution data for volumetric studies [135],[137], but their potential for ASL has not yet been explored.

The aim of this work was to develop an automated framework for regional analysis of CBF and to investigate the added value of combining thalamic MRS with such detailed regional CBF analysis as a potential biomarker of outcome in HIE.

8.3 Methods

Arterial Spin Labelling is a part of the ongoing "UCH Baby Brain Study", led by Prof Nicola Robertson and Dr Cristina Uria-Avellanal, who received ethical approval for the study from the NRES Committee London - Bloomsbury (Research Ethics Committee (REC) Reference number: 13/LO/0225) and from UCLH. Written consent was obtained from the parents before enrolment of any neonate in the study. The MR images were scored by Dr. Maïa Proisy, UCL honorary clinical research fellow (now Centre Hospitalier Universitaire de Rennes-Hôpital Sud, Rennes, France). The clinical MR report on the scans was provided by a consultant neonatologist as part of clinical care and management.

Subjects. Neonates that fulfilled the following criteria were considered eligible for the study: "All term and pre-term babies born at UCH or transferred to UCH for treatment of acute brain injury without life threatening congenital malformations and considered likely to survive". Some of the neonates were also recruited to the Total Body with Xenon gas (ToBy Xenon) clinical trial (REC reference: 10/H0707/33) and, apart from the standard care, were administered Xenon dur-

[1] http://biomedic.doc.ic.ac.uk/brain-development/index.php?n=Main.Neonatal2

[2] http://biomedic.doc.ic.ac.uk/brain-development/index.php?n=Main.Neonatal3

ing the first days of life. The detailed inclusion criteria were defined for the ToBy Xenon trial and were followed in all cases [3]:

1. Infant is 36 to 43 weeks gestation with at least one of the following:
   - Apgar score of < 5 at 10 minutes after birth;
   - Continued need for resuscitation, including endotracheal or mask ventilation, at 10 minutes after birth;
   - Acidosis defined as pH < 7.00 and/or base deficit > 15mmol/L in umbilical cord blood sample or any blood sample within 60 minutes of birth (arterial or venous blood).
2. Moderate to severe encephalopathy consisting of altered state of consciousness (reduced or absent response to stimulation) and hypotonia, and abnormal primitive reflexes (weak or absent suck or Moro response).
3. At least 30 minutes duration of amplitude integrated EEG (aEEG) recording that shows moderately abnormal or suppressed background aEEG activity or seizures.

Twenty two neonates with suspicion of acute brain injury were enrolled in the study. The data from one neonate were excluded due to severe motion artefacts. The characteristics of all accepted neonates are given in table 8.1. Although four neonates: two pre-term (N 18 and 19) and two with neonatal seizures (N 20 and 21) presented a different clinical picture and were not included in the final HIE cohort analysis, the data contributed to the development of the final protocol.

Classification. Neonates admitted to the neonatal unit were assessed by the clinical team and initially scored in terms of severity of the injury based on the clinical history, blood pH, EEG (electroencephalography) signal. The final classification was given based on the improvement in terms of EEG, imaging and spectroscopy results.

MR protocol and processing. The infants were appropriately prepared for the MRI examination, placed in an MR-compatible incubator, equipped with ear protection and monitored throughout the scan. Scanning was performed on a 3T Philips Achieva. Twenty out of 21 infants were sedated either with an oral dose of chloral hydrate (n = 10) or intravenous morphine

[3] https://www.npeu.ox.ac.uk/toby-xe

N	GA (weeks + days)	Gender	Birth Weight [g]	PNA (days)	Initial classification	Treatment
1	39 + 2	F	2814	7	HIE 1	Cooling
2	41	M	3670	3	HIE 1	Cooling
3	41	F	3800	4	HIE 1	Cooling + Xenon
4	36 + 3	M	2440	7	HIE 1	Cooling
5	38 + 2	F	3034	5	HIE 1	Cooling
6	40 + 3	F	3930	5	HIE 2	Cooling
7	40 + 2	F	3020	4	HIE 2	Cooling
8	38 + 6	M	2850	4	HIE 2	Cooling
9	41 + 6	F	3630	6	HIE 2	Cooling
10	39	M	2250	3	HIE 2	Cooling
11	40 + 2	M	3110	6	HIE3	Cooling + Xenon
12	39 + 2	M	3060	7	HIE3	Cooling + Xenon
13	38	F	1770	4	HIE3	Cooling + Xenon
14	39 + 5	M	3640	4	HIE3	Cooling
15	40	M	3310	13	HIE 1	Cooling
16	36+3	M	3034	9	HIE 1	Cooling
17	41 + 1	M	3140	2	HIE 3	Cooling + Xenon
18	26	F	890	64	pre-term	
19	32 + 5	F	1890	24	pre-term	
20	41	F	3775	7	neonatal seizures	
21	40 + 3	M	3186	8	neonatal seizures	

Table 8.1: *Summary of subjects. N - neonate number, GA - gestational age, PNA - postnatal age, HIE - hypoxy-ischemic encepalopathy grade[13] (grading details given in table 2.2 in chapter 2). Neonates 18-21 were excluded from HIE cohort analysis.*

in the case of ventilated babies (n = 10). Blood testing was also performed around the time of the MRI examination. In addition to standard structural imaging, 19 neonates underwent MRS and 21 underwent the ASL protocol.

1. Structural scans. The standard protocol included T_1, T_2 weighted (axial and coronal) high resolution and diffusion weighted structural scans. Neonates that were also enrolled to the Toby Xenon trial additionally received a T_2 weighted Pseudo 3D scan. Apparent diffusion coefficient (ADC) and exponential ADC, eADC (calculated as exp(-b*ADC))

maps were generated on the scanner. In case of motion, structural scans were repeated using single shot, motion resistant sequences. All sequence parameters are given in table 8.2. Images were scored by trained neuroradiologist using the Barkovich scoring system (see table 2.4 in the chapter 2 details of the scoring system).

2. MRS. The MRS voxel was positioned in the left thalamus as shown in figure 8.1. Water-suppressed spectra were acquired using point resolved spectroscopy (PRESS, 64 averages, TR/TE = 2288/288ms, voxel size 15x15x15mm, scan time ∼7 min). The spectra were manually corrected for phase and frequency shifts and fitted using the AMARES algorithm as implemented in the jMRUI[4] software package. Lactate to N-acetylaspartate (Lac/NAA) peak-area ratio were calculated.

3. ASL. A pseudo-continuous ASL (pCASL) scans and post processing were performed as described in 4.2. The labelling plane was positioned based on ToF angiography images to ensure that it was perpendicular to the feeding arteries, as shown in figure 8.1. The labelling duration was 1.7s with a post-labelling delay of 1.5-2s. A proton density (PD) image was also acquired (19 neonates), with the same acquisition parameters as the pCASL readout. Since the protocol was under development, some improvements (longer PLD, fat saturation and background suppression pulses) were introduced during the duration of the study and therefore not present in scans for all subjects. Motion Correction was performed as described in chapter 7.3.1. In short, images were first rigidly registered using normalised mutual information based rigid registration to a subject template created from every other control image using DTI-TK[5]. Next, pairwise subtraction was performed and any outliers were removed before averaging using method E described in section 7.3.1. The schematic of motion correction procedure is shown in figure 8.1. The single compartment kinetic model was used for CBF quantification (equation 4.10 [71]) using Matlab and was calculated for each baby based on measured hematocrit values according to equation 4.11: $1/T_{blood}$ = 0.5*Hct +0.37[89]. Labelling efficiency was set to 0.77, as estimated by numerical simulations of Bloch Equations in chapter 5, or 0.69 if the background suppression was used (i.e. accounting for the efficiency of two background suppression pulses assumed to be 0.95 each). All ASL parameters for each baby are given in table 8.3.

[4]http://sermn02.uab.es/mrui/mrui_Overview.shtml

[5]http://dti-tk.sourceforge.net/pmwiki/pmwiki.php

Name	Type	Fast mode (factor)	FA°	TR [ms]	TE [ms]	Total time [min]	Acq matrix	Voxel size [mm]	Slice thickness [mm]	Slice gap [mm]	SENSE	Half Scan	NA	Other
Multishot														
T_1 MPRAGE (3D)	FFE	TFE (16)	13	3000	4.1	8	256x 163	0.82x 0.82	1.00	n/a	no	no	1	IR, TI= 1465
T_2 (2D)	SE	TSE (11)	90	7026	130	6	280x 275	0.50x 0.50	3.00	0.30	no	no	2	
T_2 (Pseudo3D)	SE	TSE (16)	90	15715	160	3.5	192x 186	0.86x 0.86	2.00	-1.00	2 (AP)	no	1	
Single shot														
T_1 (2D)	SE	TSE (53)	13.5 [nT]	22000	6.1	6.5	204x 164	0.98x 0.98	2.00	-1.00	2 (RL)	0.6	2	IR, TI= 400
T_2 (2D)	SE	TSE (201)	90	22200	130	2	280x 275	0.50x 0.50	3.00	-1.00	2 (RL)	0.65	2	
Other														
DTI (2D)	SE	EPI (59)	90	7857	49	6	112x 110	2.00x 2.00	2.00	0	2 (AP)	0.61	1	b750, 32 dirs
pCASL (2D)	FFE	EPI (31)	90	4500	20	7	64x 64	3.75x 3.75	6.00	1.00	2.3 (AP)	no	45	

Table 8.2: *Summary of sequences. FA - flip angle, TR- repetition time, TE - echo time, NA - number of averages, IR - inversion recovery, TI - delay time after inversion pulse, b - diffusion weighting [s/mm^2], dirs - diffusion-weighted directions.*

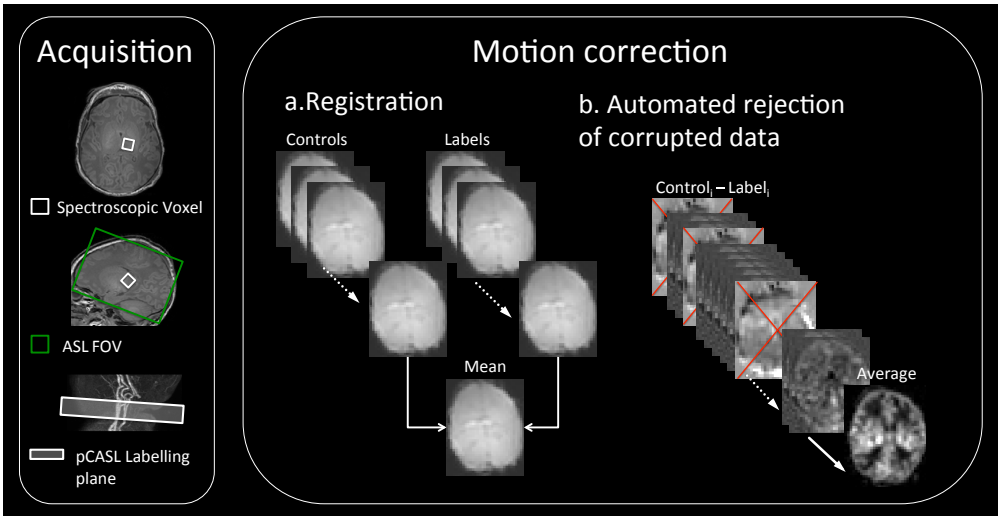

Figure 8.1: *Acquisition: positioning of the thalamic voxel, ASL FOW and the labelling plane (left) and motion correction procedure: a - registration and b - automated rejection of the corrupted data (right).*

4. Regional CBF quantification. Regional CBF was calculated in Regions of Interest (ROIs) defined automatically based on both an atlas based probabilistic tissue segmentation of 5 tissue classes[6] and on a joint multi-atlas label propagation and fusion of 50 neonatal brain[7] [136]. After affine and non-linear registration (Nifty-Reg[8]) of the T_2-weighted atlas images to the T_2-weighted image of each neonate, the probabilistic maps and parcellations were propagated to individual subject space. Probability maps were used to segment T_2 images using AdaPT algorithm [137] (Nifty-Seg[9]). The segmentations were reviewed and manually corrected when necessary. Finally,T_2-weighted subject images were co-registered to the CBF maps using rigid registration, with the tissue segmentations and brain parcellation propagated to CBF space. Global grey matter (GM) and deep grey matter (DGM) CBF were quantified in the regions using tissue segmentations. Subsets of the parcellated areas were combined to create larger regions, corresponding to the main cerebral lobes (frontal, temporal, occipital, parietal) plus cingulate cortex and insula. Left and right sides were added together to create a single mask for each region. The ROIs were then used together with the GM mask to determine cortical regions. Similarly, the left and right parcellation of the deep grey matter nuclei (thalami, caudate and lentiform nuclei) were combined and CBF quantified within the DGM seg-

[6]http://biomedic.doc.ic.ac.uk/brain-development/index.php?n=Main.Neonatal2
[7]http://biomedic.doc.ic.ac.uk/brain-development/index.php?n=Main.Neonatal3
[8]http://sourceforge.net/projects/niftyreg/
[9]http://sourceforge.net/projects/niftyseg/

N	LD [ms]	PLD [ms]	Fat Sat	BS	Reps	Hct [%]	T1 [s]	Sedation
1	1700	2000	Yes	1750 / 2974	29	46	1.67	Chloral
2	1700	1500	No	n/a	44	60	1.49	Chloral
3	1700	1700	No	1750 / 2674	38	39	1.77	Morphine
4	1700	2000	Yes	1750 / 2974	38	35	1.84	Morphine
5	1700	2000	Yes	1750 / 2974	33	36	1.82	Morphine
6	1700	1700	No	n/a	45	40	1.75	Morphine
7	1700	2000	Yes	1750 / 2974	32	45	1.68	Morphine+ Chloral
8	1700	2000	Yes	1750 / 2974	36	45	1.68	Chloral
9	1700	1500	No	n/a	23	45	1.68	Chloral
10	1700	2000	Yes	1750 / 2974	45	32	1.89	Morphine+ Chloral
11	1700	2000	Yes	1750 / 2974	45	46	1.67	Morphine
12	1700	2000	Yes	1750 / 2974	23	33	1.87	Morphine
13	1700	2000	No	1750 / 2974	30	35	1.84	Chloral
14	1700	2000	Yes	1750 / 2974	40	36	1.82	Morphine
15	1700	2000	Yes	1750 / 2974	40	46	1.67	Chloral
16	1700	2000	Yes	1750 / 2974	35	41	1.74	Chloral
17	1700	1500	No	n/a	60	42	1.72	Morphine
18	1700	1500	No	n/a	20	30	1.92	Chloral
19	1700	2000	Yes	1750 / 2974	14	36	1.82	None
20	1700	1700	No	n/a	17	45	1.68	Chloral
21	1700	1500	No	n/a	42	29	1.94	Chloral

Table 8.3: *Summary of ASL parameters. N - neonate number consistent with table 8.1 Hct and sedation agents administered during the scan. LD - labelling duration, PLD - post-labelling delay, BS - background suppression, Reps - number of control-label pairs accepted for final averaging, Hct - haematocrit,* T_1 *calculated from Hct based on equation 4.11.*

mentation mask. The generated segmentations and parcellations were checked for the quality and manually edited if necessary.

Analysis. The analysis was performed in three steps: i. general analysis (all subjects), ii. qualitative analysis (case study), iii. regional analysis (chosen subgroup).

The aim of the general analysis was to find different patterns in regional CBF visually and quantitatively for all neonates. Additionally, an analysis was performed to investigate any dependencies that could influence the finding, such as PLD, days of life at scan (DOL), administered sedation.

Next, cases with imaging findings (Barkovich score > 0) were qualitatively analysed. CBF maps were compared with the structural scans (T_1, T_2 and diffusion weighted) to assess the correspondence of the pathology observed in the anatomical scans and CBF maps.

Finally, a subgroup of 14 neonates (indicated by N = 1 to 14 in table 8.1) was chosen for in depth analysis. The criteria for the choice included: PNA (4-7), gestation age at birth ($\geqslant$ 38), and initial classification (excluding neonates diagnosed with neonatal seizures and without clinical presentation typical for HI). Subjects were divided into two groups based on Lac/NAA peak-area ratio: below 0.3 = likely favourable outcome (n=9) and above 0.3 = high risk of poor outcome. T-tests and F-tests were computed to investigate the statistical differences in mean and variance of CBF values between low- and high-risk groups in terms of prognosis.

8.4 Results

All CBF maps and MR spectra were successfully produced in all neonates. On average, 20% (range: 0-70%) of motion corrupted data was rejected. An example of MR spectra showing low and high level of lactate relative to NAA is shown in figure 8.2 and an example segmentation and parcellation is shown in figure 8.3 and 8.4 respectively, whereas figure 8.5 shows an example of segmentation and parcellation combined which was used for the final analysis.

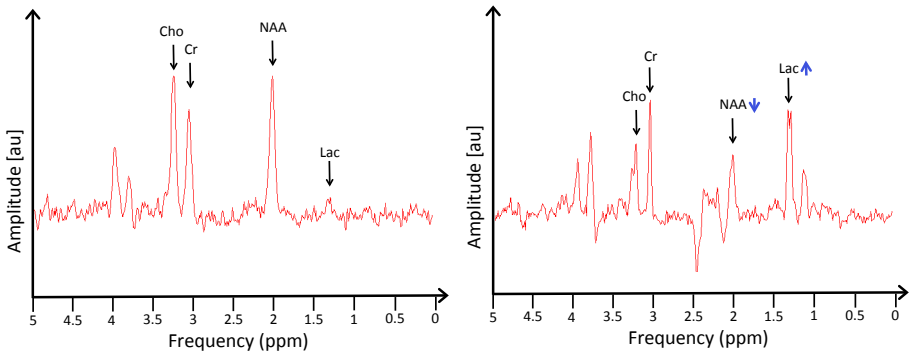

Figure 8.2: *Examples of MRS spectra from two neonates showing normal (left) and abnormal (right) levels of lactate and NAA. Blue arrow indicate direction of change*

Figure 8.3: *Example of GM and DGM segmentation overlaid on a CBF map*

Figure 8.4: *Example of GM and DGM parcellation overlaid on a CBF map*

Figure 8.5: *Example of the ROI used for the analysis overlaid on a CBF map*

8.4.1 General analysis findings

The CBF maps for all neonates are presented in figure 8.6. The order of the images is consistent with the order in tables 8.1 and 8.3.

Visual analysis. Upon visual inspection of the maps, two main observations can be made. First, the distribution of CBF varied considerably between neonates with different degrees of HIE. Second, some parts of the brain were more likely to be characterised by high CBF. Specifically:

- Most of the CBF maps showed:
    1. High CBF in basal ganglia / thalamus in relation to the average cortical CBF (see 8.7 a);
    2. High signal in the area of MCA (see 8.7 b);
    3. High signal in the area of Circle of Willis, indicating arterial artefact originating from the posterior circulation; this usually coincided with high signal from occipital lobe and low signal in the PCA/MCA watershed regions (see 8.7 c);
- Some of the CBF maps showed:
    1. High signal in the region of ACA and pericallosal artery; this coincided with high signal in cingulate cortex and low signal in pericallosal/MCA borderzone (see 8.7 d);
    2. Unevenly distributed signal in the basal ganglia, i.e. some nuclei perfused more than others (see 8.7 e);

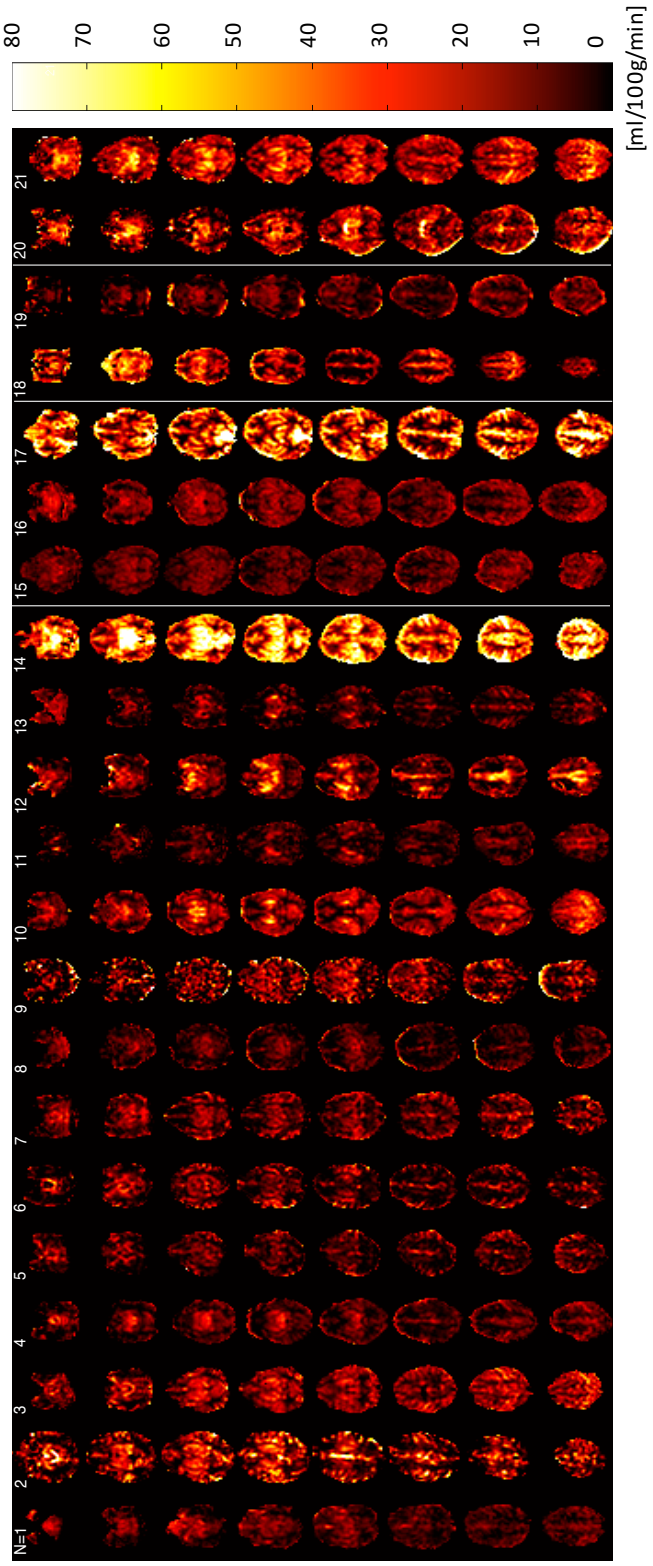

Figure 8.6: *CBF maps for all babies in the order given by table 8.1. N and lines consistent with numbering in table. N=1-5 HIE1; N=6-10 HIE2, N=11-14 HIE3; N=15-16 HIE1, N=17 HIE3 N=18-19 pre-terms, N=20-21 neonatal seizures.*

3. High signal in cingulate and perirolandic cortex (see 8.7 f and g);

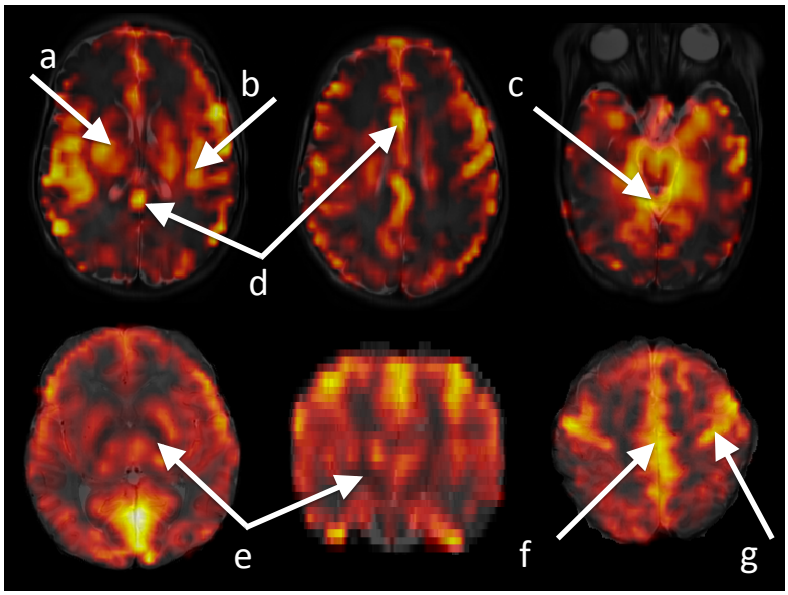

Figure 8.7: *Example images representing common (a-c) and less common (e-h) findings. CBF maps of neonate 2 and 17 displayed on the high resolution structural scans for easier localisation*

Quantitative analysis. The findings from the visual analysis were confirmed quantitatively in figures 8.8, 8.9 and 8.10, which show the CBF values in the various regions of interest in the whole brain, grey matter (GM) and deep grey matter (DGM) (figure 8.8), in sub-regions of the cortex expressed as percent of the CBF value in GM (figure 8.9) and in deep grey matter sub-regions, expressed as percent of the CBF value in DGM (figure 8.10). Two outliers seen in figure 8.8: neonate 14 and 17 are two out of three neonates with the highest Lac/NAA peak-area ratios in this cohort, suggesting the most severe effect of the hypoxia-ishaemia (Lac/NAA = 1.32 and 1.94 for neonate 14 and 17 respectively). This dramatic increase in CBF was most likely caused by vasoparalysis and loss of the vessel tone. Neonate 17 passed away a day after the scan (neonate 14 was transported to a different hospital and their final outcome is unknown). In the cortical sub-regions in some neonates, CBF in cingulate, parietal cortex and insula is noticeably increased. In deep grey matter, CBF in caudate nuclei is consistently lower compared to the mean DGM and the other nuclei and lentiform nucleus has the highest CBF. All the CBF values for each region, subregion, Lac/NAA peak-area ratio, detail Barkovich scores and the final classification are given in table 8.4.

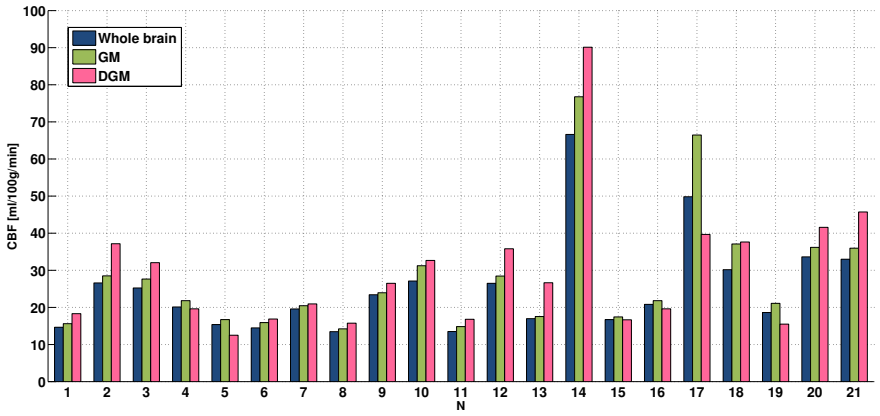

Figure 8.8: *CBF in the whole brain, mean cortical grey matter (GM) and the deep grey matter (DGM) by subject*

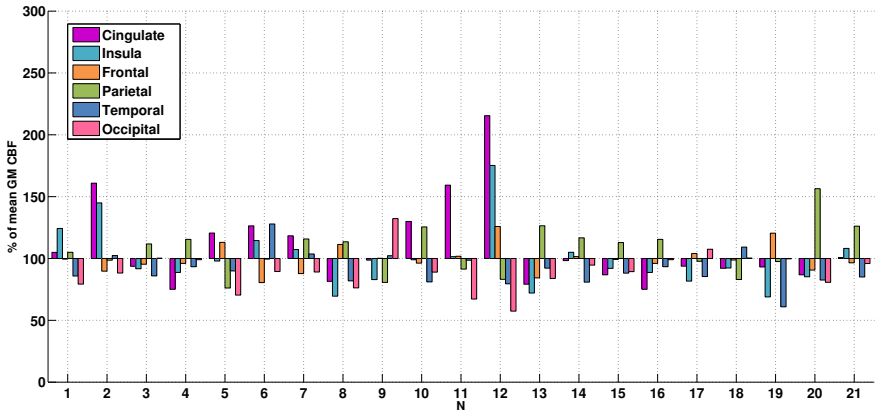

Figure 8.9: *CBF in cortical sub-regions expressed as a percent of the CBF value in the mean cortical GM, by subject*

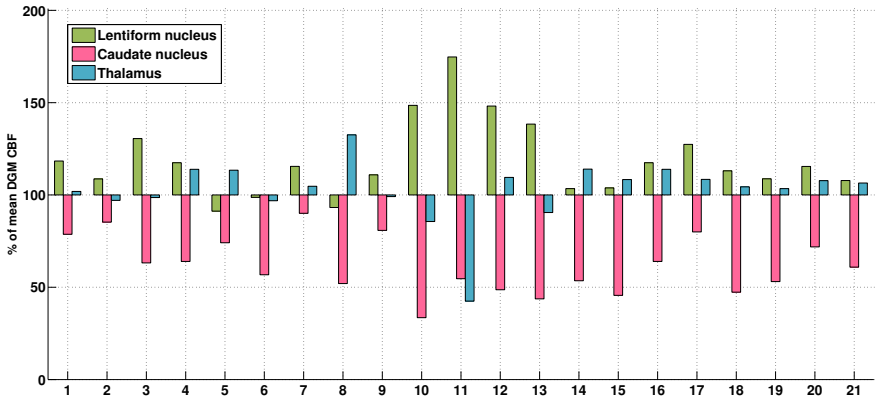

Figure 8.10: *CBF in sub-regions of deep grey matter expressed as a percent of the CBF value in the whole DGM by subject*

Dependencies of CBF on other factors. The initial analysis of the dependencies did not show any significant correlation between CBF and sedation agents administered (figure 8.11) gestation age (GA) at birth (figure 8.12), GA at scan (figure 8.13), postnatal age at scan (figure 8.14, 8.15 and 8.16 for whole brain, grey and deep grey matter respectively). The high spread of CBF values for the neonates receiving morphine during the scan, as seen in the figure 8.11, is likely to be explained by the severity of the HI. Babies receiving morphine were the most affected and required ventilator support.

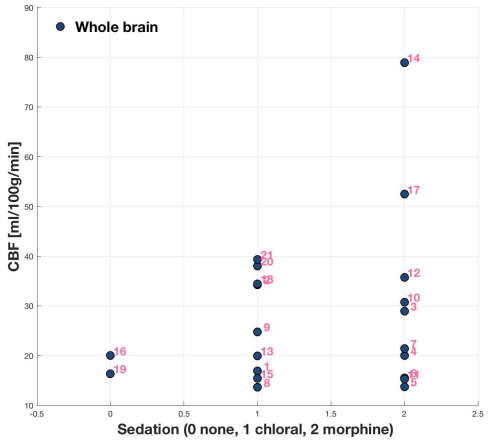

Figure 8.11: *Whole brain CBF vs sedation agent*

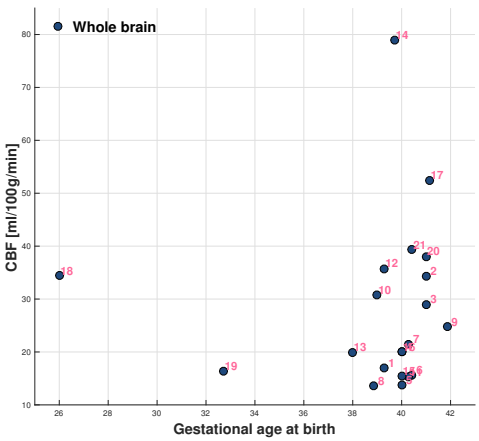

Figure 8.12: *Whole brain CBF vs. gestation age at birth*

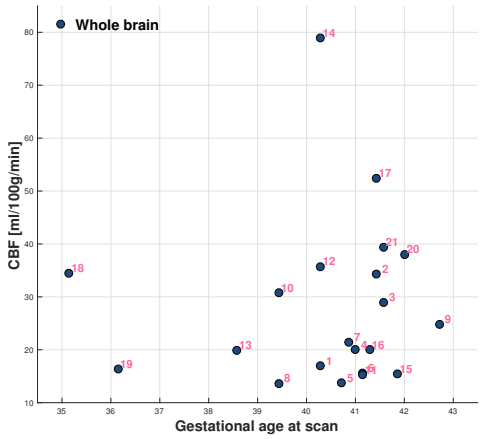

Figure 8.13: *Whole brain CBF vs. gestation age at scan*

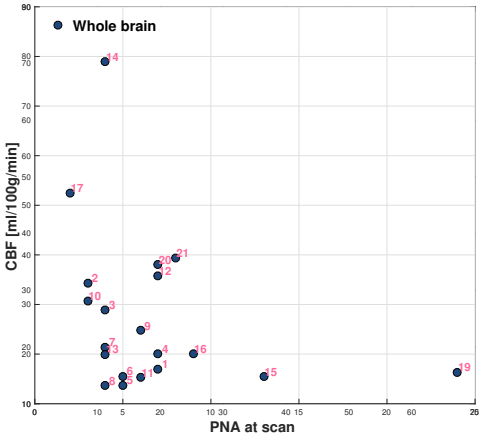

Figure 8.14: *Whole brain CBF vs postnatal age*

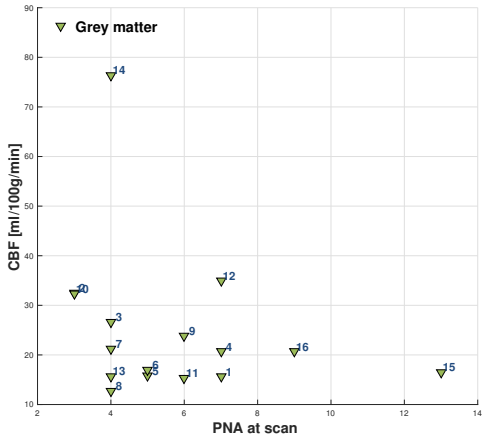

Figure 8.15: *Grey matter CBF vs. postnatal age*

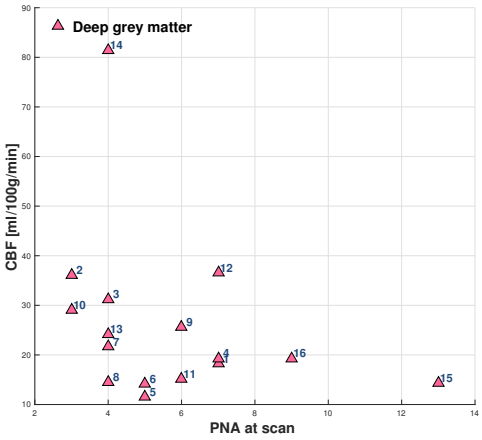

Figure 8.16: *Deep grey matter CBF vs. postnatal age*

N	WB	GM	DGM	WM	Fron-tal	Cingu-late	Parie-tal	Tem-poral	Occi-pital	Brain Stem	Insu-la	Cau-date	Lenti-form	Thal-amus	Lac NAA	BG	WM	BG W	Tot	Final grade
1	14.7	15.6	18.3	8.6	15.5	16.4	16.4	13.4	12.4	27.2	19.4	14.4	21.7	18.7	0.13	0	0	0	0	1
2	26.6	28.5	37.2	16.1	25.6	45.9	28.1	29.2	25.1	50.3	41.3	31.7	40.4	36.1	0.15	0	0	0	0	1
3	25.2	27.6	32.1	18.8	26.4	25.9	30.9	23.7	27.7	34.6	25.3	20.3	41.9	31.6	0.20	0	0	0	0	1
4	20.1	21.8	19.6	15.4	21.0	16.4	25.2	20.4	21.6	32.3	19.4	12.6	23.0	22.3	0.20	0	0	0	0	1
5	15.4	16.7	12.5	12.3	18.9	20.2	12.7	15.0	11.8	19.9	16.4	9.3	11.4	14.2	0.28	0	0	0	0	1
6	14.5	15.9	16.9	8.3	12.8	20.1	15.8	20.3	14.2	11.2	18.2	9.6	16.6	16.3	0.12	0	0	0	0	2
7	19.6	20.5	20.9	13.7	18.0	24.2	23.7	21.2	18.2	31.3	21.9	18.9	24.2	21.9	0.15	0	0	0	0	1
8	13.5	14.2	15.7	8.1	15.8	11.6	16.1	11.6	10.8	18.5	9.9	8.2	14.7	20.9	0.16	0	0	0	0	1
9	23.4	24.0	26.5	16.2	24.0	23.6	19.3	24.5	31.7	26.4	19.9	21.4	29.4	26.3	0.18	0	0	0	0	2
10	27.1	31.2	32.7	21.8	30.1	40.6	39.2	25.3	27.8	35.9	30.9	11.0	48.5	28.0	1.80	4	0	3	7	3
11	13.5	14.8	16.8	10.5	15.1	23.6	13.6	14.6	10.0	16.2	15.1	9.2	29.4	7.1	0.39	4	3	3	10	2
12	26.5	28.4	35.8	17.0	35.8	61.3	23.7	22.6	16.3	36.7	49.8	17.4	53.1	39.2	0.76	2	5	3	10	3
13	17.0	17.5	26.6	10.8	14.8	13.9	22.2	16.2	14.7	28.7	12.6	11.6	36.9	24.1	0.77	2	0	0	2	2
14	66.6	76.8	90.1	40.3	77.9	75.4	89.6	62.1	72.7	130.5	80.6	48.2	93.2	102.8	1.32	4	3	3	10	3
15	16.7	17.4	16.7	13.4	17.3	15.1	19.7	15.4	15.6	23.3	16.0	7.6	17.3	18.1	0.16	0	0	0	0	1
16	20.8	21.8	19.6	15.4	21.0	16.4	25.2	20.4	21.6	32.3	19.4	12.6	23.0	22.3	0.22	0	0	0	0	1
17	49.8	66.5	39.7	32.9	69.1	62.3	65.0	56.7	71.4	38.5	54.3	31.7	50.6	43.0	1.94	4	5	4	13	3
18	30.2	37.1	37.6	22.7	36.6	34.2	30.8	40.5	37.2	52.2	34.2	17.8	42.5	39.3	0.00	0	0	0	0	0
19	18.6	21.1	15.5	13.5	25.4	19.6	20.6	12.9	21.0	20.0	14.5	8.2	16.8	16.0	0.00	0	0	0	0	0
20	33.6	36.2	41.6	22.9	32.8	31.4	56.6	29.9	29.2	57.0	30.8	29.9	48.0	44.8	0.12	0	0	0	0	0
21	33.0	36.0	45.7	24.1	34.7	36.2	45.3	30.6	34.5	70.3	38.9	27.9	49.3	48.7	0.14	0	0	0	0	0

Table 8.4: *CBF [ml/100g/min]] for all subjects and sub-regions, Lac/NAA peak-area ratio, Barkovich score (BG- basal ganglia, W - watershed, BG/W - basal ganglia/watershed)*

8.4.2 Cases with abnormalities in imaging

CBF maps of six neonates with imaging findings (Barkovich score > 0) were compared to standard structural scans (T_1, T_2 and diffusion weighted) to assess the correspondence of the pathology observed in the anatomical scans and CBF maps. These neonates also had increased thalamic Lac/Naa peak-area ratios and regional CBF values, which is provided in description of each subject for convenience. All results are given in table 8.4. Direct citations from the radiology report is given in quotation marks.

Case 1 (Neonate 10)

CBF maps and matching slices of the structural scans: T_1 weighed, T_2 weighted, eADC and ADC are shown in figure 8.17. Lac/NAA peak-area for this neonate was 1.8, mean whole brain (WB) CBF = 27 ml/100g/min and CBF in the lentiform nucleus = 48 ml/100g/min.

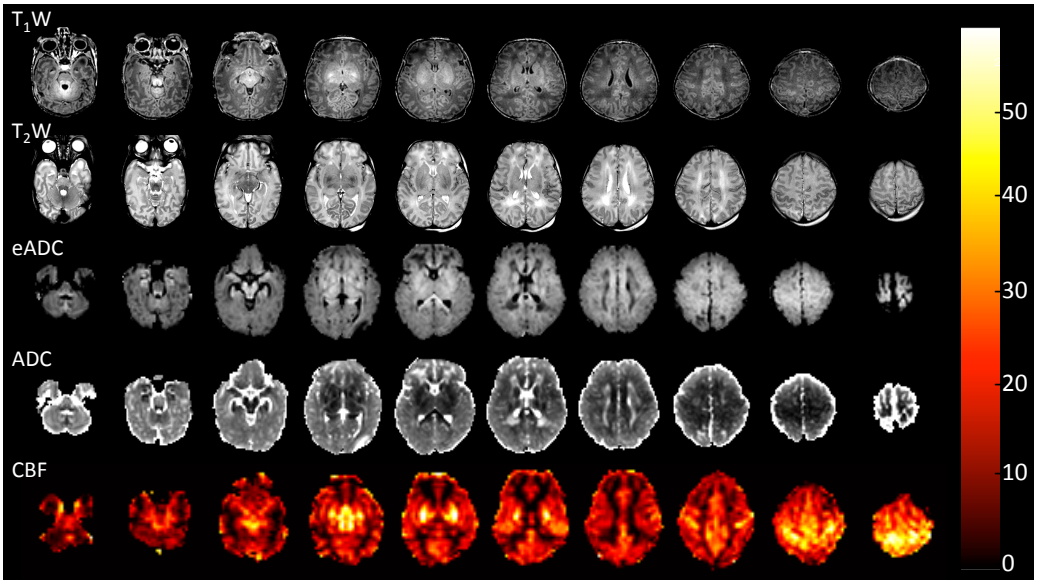

Figure 8.17: *Neonate 10. Matching slices of structural scans and CBF map. From the top: T_1 weighed, T_2 weighted, eADC, ADC, CBF [ml/100g/min].*

Structural imaging shows widespread abnormal signal intensities (Barkovich score 7: BG = 4 and BG/W = 3). All regions of the cortex are clearly visible in the CBF map, which results from both high contrast between grey and white matter and homogenous distribution of the label across and within grey matter, reflecting increased perfusion. Regions of low mean diffusitivity in the ADC map coincide with increased CBF. An expert radiologist also noted that "the white matter changes are quite extensive for an isolated acute hypoxic ischaemic event. The image

findings would be associated with a poor outcome with both motor and cognitive impairment. [...] There may be prolonged feeding difficulties."

Case 2 (Neonate 11)

CBF maps and matching slices of the structural scans: T_1 weighed, T_2 weighted, eADC and ADC are shown in figure 8.18. Lac/NAA peak-area for this neonate was 0.39, mean WB CBF = 13 ml/100g/min and CBF in the lentiform nucleus = 30 ml/100g/min.

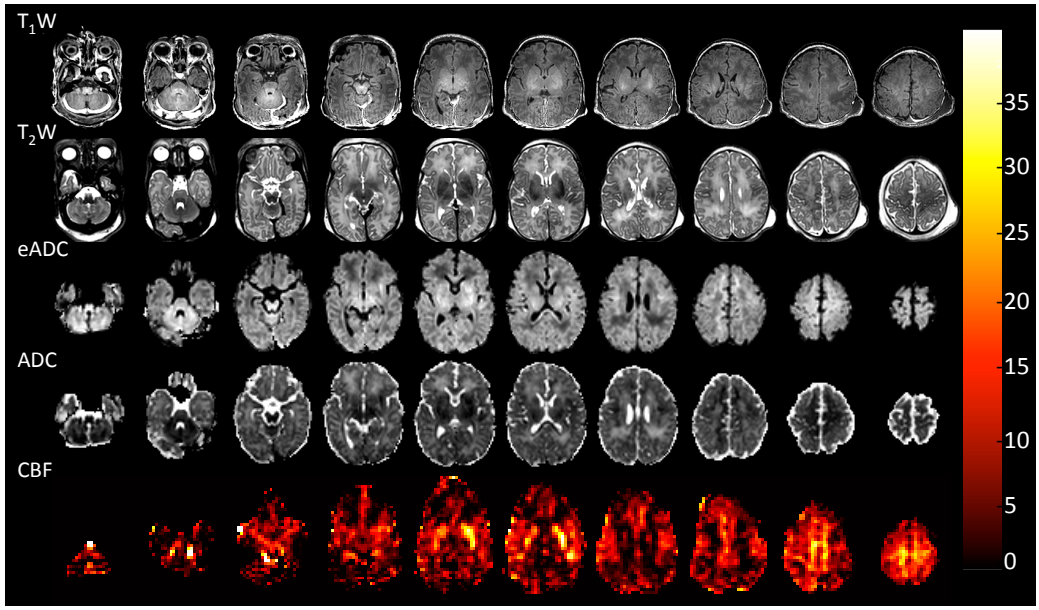

Figure 8.18: *Neonate 11. Matching slices of structural scans and CBF map. From the top: T_1 weighed, T_2 weighted, eADC, ADC, CBF [ml/100g/min].*

Structural scans show widespread abnormal signal intensities (Barkovich score 10: BG = 4, WM = 3 and BG/W = 3). It was reported that "The multifocal cortical involvement is not typical of an isolated acute hypoxic ischaemic encephalopathy secondary to a sentinel event.[...] These imaging findings are likely to be associated with later motor and cognitive impairment." Cingulate cortex and lentiform nucleus show restricted diffusion (decreased ADC), which coincides with elevated CBF. There seems to be decrease in the CBF in anterior and posterior watershed grey matter regions.

Case 3 (Neonate 12)

CBF maps and matching slices of the structural scans: T_1 weighed, T_2 weighted, eADC and ADC are shown in figure 8.19. Lac/NAA peak-area for this neonate was 0.76, mean WB CBF = 27 ml/100g/min and CBF in the lentiform nucleus = 53 ml/100g/min, para sagittal cortex CBF = 60 ml/100g/min, Barkovich score 10: BG = 2, WM = 5 and BG/W = 3.

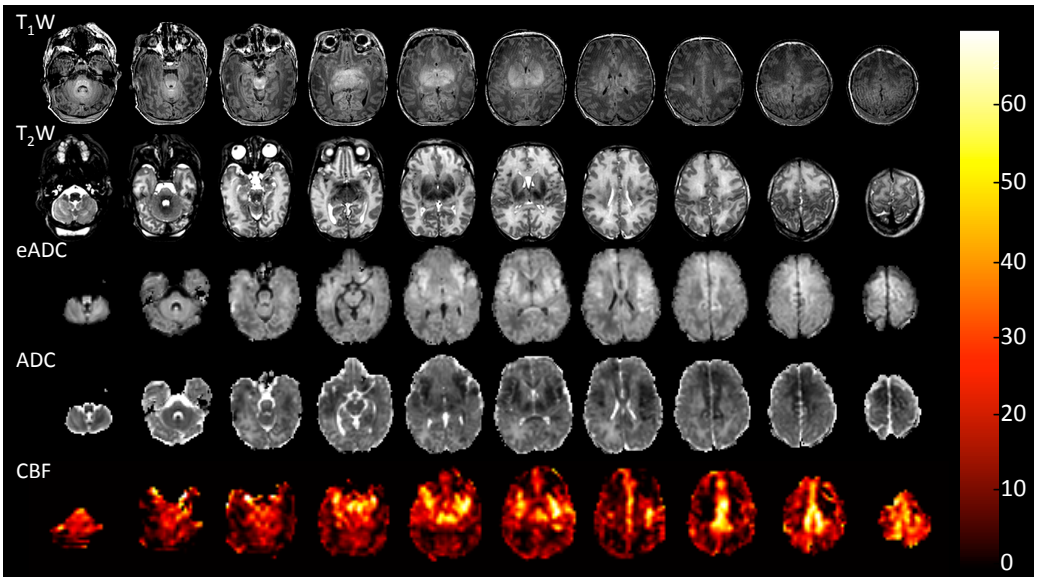

Figure 8.19: *Neonate 12. Matching slices of structural scans and CBF map. From the top: T_1 weighed, T_2 weighted, eADC, ADC, CBF [ml/100g/min].*

The structural scans showed "widespread abnormal signal intensities consistent with severe hypoxic ischaemic brain injury and likely to be associated with severe neurodevelopmental impairment. The white matter changes are atypical for an isolated acute hypoxic ischaemic event, particularly the anterior cerebral artery changes". Decreased ADC in the regions supplied by ACA and MCA are consistent with increased CBF in these regions.

Case 4 (Neonate 13)

CBF maps and matching slices of the structural scans: T_1 weighed, T_2 weighted, eADC and ADC are shown in figure 8.20. Lac/NAA peak-area for this neonate was 0.77, mean WB CBF = 17 ml/100g/min and CBF in the lentiform nucleus = 36 ml/100g/min and Barkovich score 2 (BG = 2).

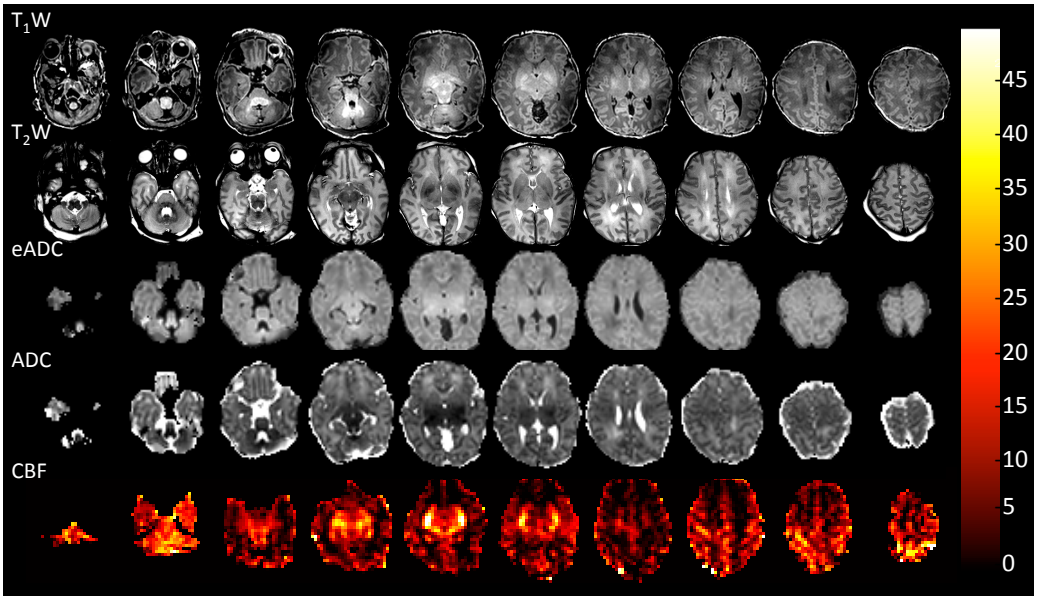

Figure 8.20: *Matching slices of structural scans and CBF map. From the top: T_1 weighed, T_2 weighted, eADC, ADC, CBF [ml/100g/min].*

Abnormal signal intensity was found "within the basal ganglia and thalami, PLIC, brainstem and the white matter, and within the cortex of the medial temporal lobes . This is consistent with a perinatal hypoxic ischaemic injury. These imaging findings would be associated with neurodevelopmental impairment in both motor and cognitive domains". CBF maps show increased CBF mainly within the lentiform nucleus, which is coincides with decreased ADC.

Case 5 (Neonate 14)

CBF maps and matching slices of the structural scans: T_1 weighed, T_2 weighted, eADC and ADC are shown in figure 8.21. Lac/NAA peak-area for this neonate was 1.32, mean WB CBF = 67 ml/100g/min and in the lentiform nucleus = 93 ml/100g/min and Barkovich score 11 (BG = 4, W = 3, BG/W = 3).

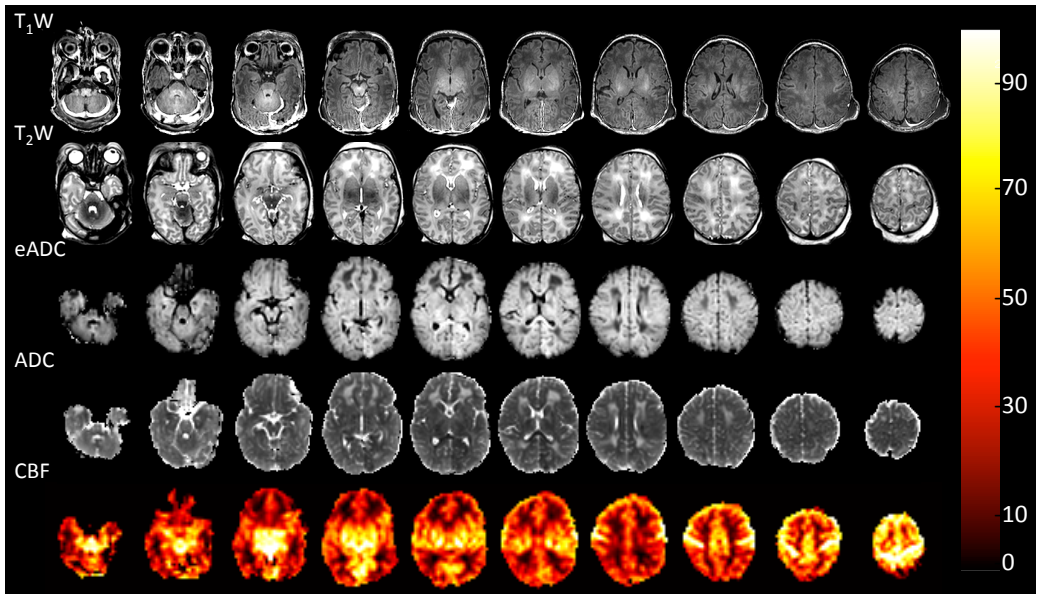

Figure 8.21: *Neonate 14. Matching slices of structural scans and CBF map. From the top: T_1 weighed, T_2 weighted, eADC, ADC, CBF [ml/100g/min].*

There are "widespread abnormal signal intensities consistent with severe perinatal hypoxic ischaemic injury involving the white matter, cortex, basal ganglia and thalami, PLIC and the brainstem. (...) The diffusion weighted ADC map shows widespread low signal intensity with reduced ADC values consistent with infarction.These image findings would be associated with significant motor and cognitive impairments.(...) We also noted a splitting of the choline peak [in MR spectra, shown in figure 8.22] which we see in severe HIE and is consistent with membrane breakdown as part of axonal and neuronal injury." CBF map shows very high CBF throughout the brain, with high values in the basal ganglia and thalami, occipital and cingulate cortex, concurrent with decreased ADC.

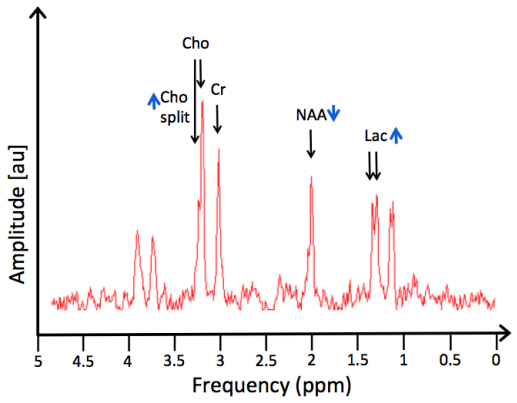

Figure 8.22: *MR spectroscopy for neonate 14 showing splitting choline peak.*

Case 6 (Neonate 17)

CBF maps and matching slices of the structural scans: T_1 weighed, T_2 weighted, eADC and ADC are shown in figure 8.23. Lac/NAA peak-area for this neonate was 1.94, mean WB CBF = 50 ml/100g/min and in the lentiform nucleus = 51 ml/100g/min, occipital cortex 71 ml/100g/min and Barkovich score 11 (BG = 4, W = 5, BG/W = 4).

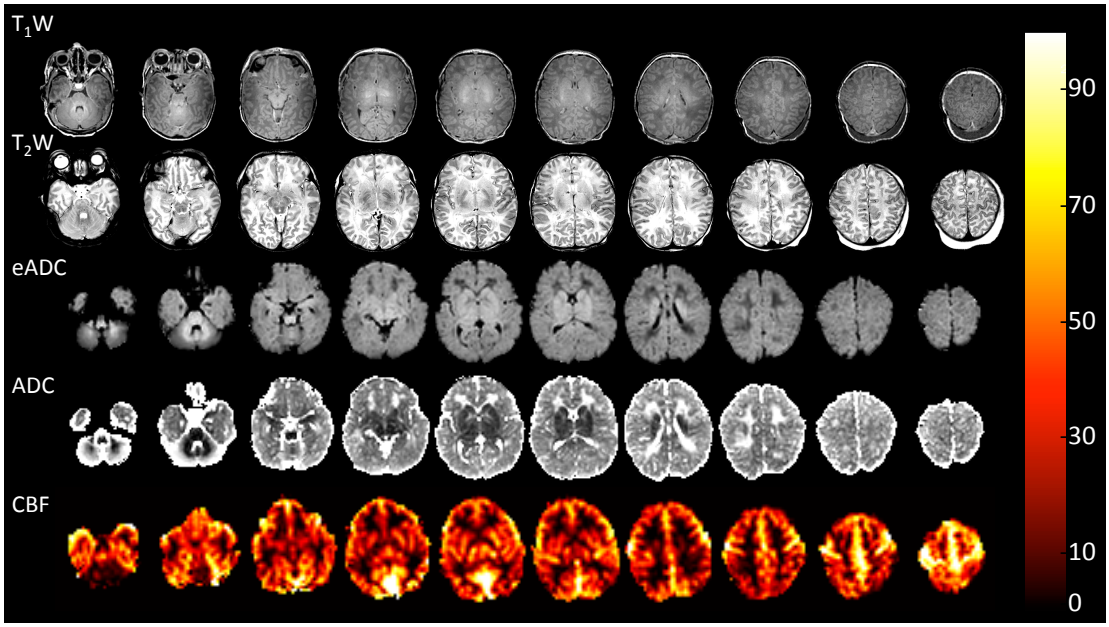

Figure 8.23: *Neonate 17 (excluded). Matching slices of structural scans and CBF map. From the top: T_1 weighed, T_2 weighted, eADC, ADC, CBF [ml/100g/min].*

The radiology report noted "marked diffuse swelling and oedema of the basal ganglia, tha-

lami and PLICS in keeping with profound, severe HIE. There is diffuse cerebral hemisphere swelling of the cortex and white matter. Some oedema is seen within the midbrain, pons and medulla and there is definite restricted diffusion within the midbrain." CBF maps shows increased CBF in occipital and peri-Rolandic cortex as well as basal ganglia and cortex.

8.4.3 Subgroup analysis

The analysis of the subgroup data showed that the whole brain CBF values for neonates with low Lac/NAA peak-area ratio and low Barkovich score are all below 40 ml/100g/min, whereas in some neonates with elevated Lac/NAA peak-area ratio can reach much higher values, as presented in figures 8.24 and 8.25.

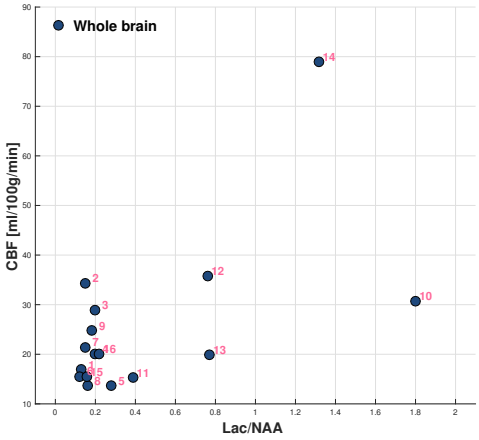

Figure 8.24: *CBF vs Lac/NAA peak-area ratio for the selected cohort*

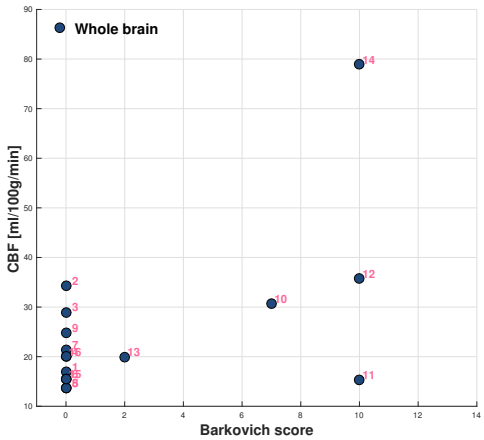

Figure 8.25: *CBF vs Barkovich score for the selected cohort*

After division of the neonates into two groups based on the Lac/NAA peak-area ratio (below or above 0.3), the difference in the distribution of the CBF values across different brain regions can be clearly seen (see figure 8.26). The boxes represent the 25th and 75th percentile, the band the median and the whiskers the spread of the data. In the low risk group, all CBF estimations are within a tight range for all brain regions (8-47ml/100g/min), whereas in the high-risk group, the range is much broader: (7-128ml/100g/min). In this group, the CBF of lentiform nuclei and cingulate cortex have the most elevated values. There were statistical differences for CBF in the lentiform nuclei between the high- and low-risk groups (t-test, F-test $p<0.05$) but not in the cingulate cortex (t-test $p=0.07$, F-test $p<0.05$), suggesting that CBF in the lentiform nucleus has good potential for outcome prediction in HIE neonates.

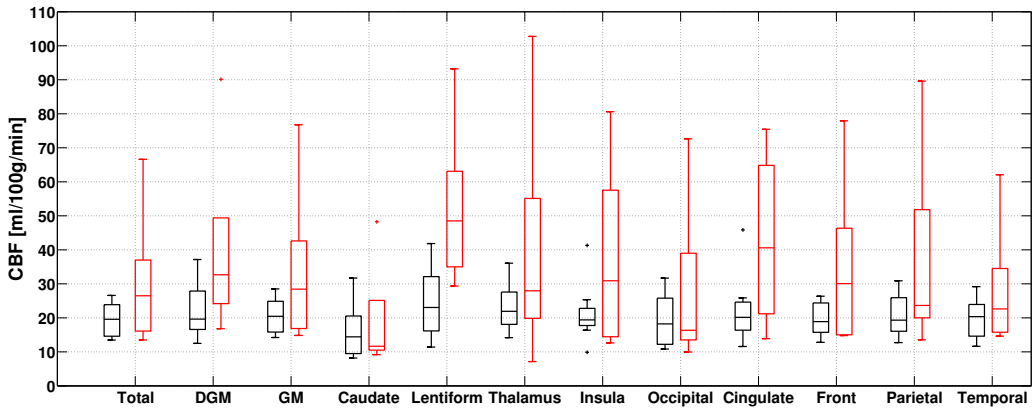

Figure 8.26: *Results of detailed regional CBF analysis; neonates with thalamic Lac/NAA peak ratio below (black) and above (red) predictive value of 0.3*

8.5 Discussion

This study presents a detailed analysis of regional CBF in conjunction with Lac/NAA peak-area ratio. ASL provides a window to the physiology of the brain, over and above the information from structural, T_1 / T_2 / diffusion weighted scans. Generally, an increase in CBF accompanies an increase in Lac/NAA, most notably within the lentiform nuclei and cingulate cortex. This increase in CBF could be related to the loss of autoregulation in severely affected babies, and this information has the possibility to further separate this group of patients from the moderately affected, usually evenly split by current imaging and clinical criteria between mild and severe HIE.

8.5.1 Acquisition and processing

ASL Protocol and CBF quantification.

For each neonate, quantification was done according to the performed protocol and hematocrit measured on the day of the scan. The protocol used here evolved through the study, therefore not all neonates were scanned with identical parameters (e.g. PLD, background suppression and fat saturation). For later scans, PLD was increased to avoid suspected artefacts from large arteries whereas the fat saturation was added to reduce the fat artefact arising from incorrect SENSE encoding of the fat frequency due to the chemical shift. However, the CBF quantification accounted for all the changes and no relation between the parameters and CBF was found. It is therefore believed that any artificial variation of CBF due to to the protocol adjustment

was much smaller than the genuine variation of CBF between neonates. Some quantification error could have been introduced by the uncertainty of the Hct measurement. In this study, a constant labelling efficiency was assumed for all babies. Please see section 5.5 for more details and further discussion on this topic.

In some cases, the signal seemed to originate from arteries, even after 1.5-2s PLD, which indicates very low blood velocities in the main supplying arteries or dispersion of the labelled blood bolus. This could have given rise to overestimation of flow in the voxels including the large arteries, while at the same time underestimating the CBF in the voxels containing the terminating branches of these large arteries. This could explain the regions of low CBF in the arterior and posterior cortex coinciding with high signal in the regions of ACA and PCA respectively.

Very high CBF values were found in the brainstem. For the majority of the neonates, this was the highest value in the brain and was much higher than in other brain ROIs. This could be the reflection of the damage done to that structure. However, it is more likely that the origin of the high signal lies in the arterial artefact in the PCA, i.e. the presence of the labelled blood that still occupied the posterior circulation at the time of scan. For that reason, the quantitative values for that region were not included in the graphs and were not commented on in the case analysis.

Motion correction

Registration and outlier rejection were essential to produce good quality maps for the majority of subjects. However, some residual motion artefacts could still be present, especially at the edges of the brain in the region of frontal cortex, where motion correction is the most challenging. This could have affected CBF quantification in those regions.

Automated segmentation and parcellation

Although challenging, a good match was achieved between atlases and structural subject scans, and between the structural and CBF maps, resulting in good quality ROIs.

Segmentation. Good quality segmentations were produced, despite using a priori template created from the scans of the pre-term babies. The anatomical features of pre-term brain at birth equivalent age differ from that of a term infant, mainly in the CSF spaces around the brain tissue at the top of the brain. In the brains of HIE neonates, especially the badly affected

ones, tissue is swollen, leaving little or no space for CSF. Additionally, the tissue contrast of the basal ganglia and thalamus differ from that of healthy (pre-)term babies. These differences influenced the accuracy of the registration, i.e. finding the spatial correspondence between the template and the subjects' structural images. To overcome this, a relaxed prior segmentation AdaPT algorithm was used, and most of the DGM structures were manually corrected. The relaxation of the prior has been shown to significantly improve the success of segmentations in babies with structural abnormalities like ventriculomegaly and has proven to improve the segmentations compared to no-relaxation approach [137]. All segmentations were guided by the T_2 weighted images as they were found to be of better quality across the cohort compared to the T_1 weighted images (less motion artefacts), and are thought to provide better contrast [138].

Parcellation. The propagation of a manually segmented atlas of a term infant was sufficient to provide multiple ROIs within grey and deep grey matter.

Registration. The accuracy of the registrations between the high resolution structural images and low resolution perfusion maps was carefully checked for all cases and it was found to be satisfactory based on visual inspection. Finding the geometrical correspondence between structural and perfusion scans can be challenging due to the non-linear distortions of EPI images. This could be improved if a B_0 field map was used to reduce distortions of the EPI images [139]. This is a common practice in fMRI studies [140], where the final activation mask is displayed on the high resolution anatomical image to identify the activated brain regions. In the present study, however, acquisition of the field maps was not possible due to restricted protocol time. Additionally, any movement between the acquisition of the map and EPI images will reduce the efficacy of the method.

8.5.2 Clinical findings

General findings

Overall, the CBF maps showed large variability between neonates. The CBF findings were consistent with those previously reported in neonates in terms of range and location, as shown in table 8.4. No clear relationship between CBF values and GA at birth, GA at scan or postnatal age at scan was found. The relationship between CBF and PNA was reported in healthy term neonates over a period of 7 [141] and 20 days [121] of life using Doppler ultrasonography and during the first days of life in pre-terms measured with NIRS [142]. The changes in CBF

with GA were reported in pre-term neonates between pre-term age, term age and three months equivalent age using ASL [143] and in the first weeks [144] and months of life [48] using PET. The lack of this relationship in this study suggests, that any CBF changes due to maturation are likely to be much smaller compared to that resulting from the perinatal brain injury, and therefore the CBF values reported in this study reflect perfusion abnormalities.

Case study

The case studies showed the extent of variability of brain damage as a result of HI, as can be seen from the structural images as well as the CBF maps. Most of the imaging findings, i.e. abnormal signal intensities seen in the structural scans, correspond to elevated CBF values.

Abnormal CBF and its distribution coincides with abnormal tissue appearance in DWI/ADC images. This is consistent with the previous findings in HIE neonates [93]. The behaviour of DWI signal in neonates is very different from that of a typical adult arterial ischaemic stroke. In stroke, the ADC is reduced rapidly after the artery occlusion and the volume of the lesion seen in DWI is closely related to the volume of the final lesion, indicating an acute necrosis. In contrast, in HIE neonates cell death is a dynamic process [145] lasting days after the injury, which results in constant changes of DWI signal [146]. The relationship between CBF and ADC is also very different when comparing stroke and HIE. In adult stroke, the decrease in ADC is usually explained by cytotoxic oedema, caused by complete reduction in the blood flow by a focal arterial occlusion. In neonates at the time of the scan, the flow is usually fully restored and usually increased in the affected tissue.

Subgroup analysis

This study has found a statistically significant difference in the CBF levels of the lentiform nuclei between neonates with elevated and normal levels of Lac/NAA ratio, which can be considered consistent with the very recent findings found in [133]. In [133], the low Lac/NAA ratio were also linked to low CBF in the majority of cases. However, there are a number of differences between [133] and the study presented here. In [133], a PASL technique was employed, as opposed to pCASL that was used here. It is reassuring that both ASL approaches used in neonates led to similar quantitative results, regardless of differences in the method for ROI placement. In [133], a manual method was used. Here, an automated method was chosen for two reasons: (i) the ability to define a larger number of regions quickly and (ii) avoidance of the segmentation bias. The segmentation bias could result in ROIs being chosen based on the

high CBF, therefore not representing the underlying anatomy and potentially overestimating the findings. Lastly, in [133] the one year outcome of all the neonates was available, which is the most important measure from the clinical perspective. Here, the Lac/NAA peak-area ratios were used as a surrogate measure of outcome predictor, as the 1 year outcome data was not yet available. However, the findings presented here are consistent with [133], when considering only CBF and Lac/NAA data, i.e. the increase of the Lac/NAA peak-area ratio generally follows increased CBF values.

Only a limited number of cases were available for the sub-group analysis (n=14) with unknown long term clinical outcomes. It is expected that long-term follow-up data of these neonates will enable correlation between CBF findings and clinical outcome.

8.6 Summary

This chapter presents an in depth analysis of cerebral blood flow in neonates with perinatal brain injury and its relation to thalamic metabolic changes. The study takes advantage of an optimised acquisition protocol and image processing pipeline, which enabled non-biased regional CBF quantification. The proposed automated method of segmentation and parcellation increases the objectivity of ROI placement, making it user-independent. It is less labour intensive and time consuming, and therefore more appropriate for implementation in clinical practice. It also allows for the objective analysis of a much larger number of regions.

List of abstracts that benefited from work presented in this chapter:

M. Sokolska, C. Uria-Avellanal, M.J. Cardoso, M. Proisy, A. Bainbridge, S. Ourselin, D.Thomas, N. Robertson, and X. Golay *Assessing brain damage after perinatal hypoxic-ischaemia using an automated protocol for combined regional analysis of the Cerebral Blood Flow and MR spectroscopy*. Proceedings of 23rd ISMRM 2015

M. Sokolska, Maia Proisy, Cristina Uria-Avellanal, Alan Bainbridge, Ernest Cady, David Thomas, Nicola Robertson, and Xavier Golay *Combined use of arterial spin labeling and MRS to determine the severity of injury in neonates with hypoxic-ischaemic encephalopathy* . ISMRM 2014

Chapter 9

Conclusions and future work

9.1 Thesis summary

The aim of this thesis was to develop a clinically feasible framework for non invasive mapping of cerebral blood flow in neonates with presumed hypoxy-ischemic encephalopathy.

The following objectives have been achieved:

pCASL labelling efficiency in neonates was estimated in chapter 5, which described the theory, implementation, validation and usage of the Bloch equation simulator for pCASL labelling. Implementation of the simulator enabled estimation of labelling efficiency for measured blood velocities in neonates, as well as enabled estimation of labelling efficiency for not perpendicular labelling plane orientations and in renal pCASL.

The effect of labelling plane angulation was studied in details in chapter 6. It was shown in healthy adult volunteers, that pCASL labelling is robust against the angulation of the labelling plane, even as high as 30° and that labelling plane positioned on parallel part of vertebral arteries resulted in a large data variation. It was therefore recommended that while positioning the labelling plane, the highest attention should be given to avoid kinks on the vertebral arteries. Since the velocities of blood in neonates are much lower than these of adults, especially in posterior circulation, this indicated that an extra care should be taken when planning neonatal scan to avoid deterioration of the labelling efficiency. Additionally, the position of the neonatal head and neck in the scanner can be tilted to allow space for a tracheal tubes used as part of breathing support, which makes the position difficult to predict. Therefore a constant distance between the labelling plane and FOV could result in disadvantageous labelling plane position

on parallel part of vertebral arteries.

pCASL acoustic noise reduction of 6dB achieved without significant change in labelling efficiency and described in chapter 6. This was done by predicting the acoustic noise using the scanner transfer function and adjustments of labelling train module parameters.

In vivo imaging framework was developed for imaging neonates using pCASL in chapter 7. First, differences in arterial transit times depending on HIE severity were identified. This included optimisation of ASL protocol for neonatal scanning, motion correction and identification and exclusion of corrupted data. The best performance was achieved when motion correction was combined with extended identification and exclusion of motion corrupted data. The combination of these approaches proposed in this thesis improved the success rate and allowed all acquired datasets to be included in the final study.

pCASL was successfully applied in clinical study presented in chapter 8. This chapter showed potential benefits of using pCASL in neonates with perinatal brain injury and its relation to thalamic metabolic changes. The study took advantage of an optimised acquisition protocol and image processing pipeline, which enabled non-biased regional CBF quantification.

Renal application of pCASL in healthy adult volunteers will be presented Appendix A. This study demonstrates the feasibility of using pCASL with gradient-echo EPI in a wide bore 3T scanner to measure renal perfusion in healthy volunteers. The technique is quick to acquire and both tissue contrast and spatial resolution suggest likely utility in the clinical setting. Two important challenges are addressed: estimation of labelling efficiency and motion correction.

9.2 Future directions

The research presented in the previous chapters leaves many promising avenues open for future research. This section looks at some of the future directions in the development and applications of the framework.

1. Outcome, dataset extension and clinical practice

   A natural extension to the work presented here is further data collection and clinical follow up at one and two years of age for neonates with HIE. This will allow further investigation

of the sensitivity and specificity of pCASL for outcome prediction. Once the outcome prediction of the CBF maps is clearly demonstrated, the standard clinical protocol could easily be extended to include pCASL and CBF maps can be generated for radiological reporting.

2. New research

   Two new studies already take advantage of the proposed framework and combine information provided by pCASL with other modalities: phosphorous MRS and NIRS in HI neonates. The first study might further the understanding of HIE (measuring pH in the brain with MRS); the second might enable bedside CBF monitoring (NIRS). Although the framework was developed for HIE cohort, it could be extended to include pre-term neonates to, for example, study the relationship between regional CBF and localised cortical folding.

   A more ambitious new research direction could involve perfusion measurement in neonatal kidneys using pCASL. Renal failure can occur within 24 hours of a HI episode and can be difficult to diagnose in neonates [147]. Although renal ASL in still a relatively uncommon technique, it has been shown to be useful in evaluating renal blood flow after transplantation [148] and it might become a valuable tool in clinical practice (see Appendix A for renal pCASL study in healthy volunteers).

3. Arterial transit times

   CBF maps used in this project were calculated using a single post labelling delay. However, measuring an ATT reliably could provide additional information about the vascular response to HIE. Therefore, future work will focus on optimisation of time encoded pCASL (e.g. [141]) to enable estimation of arterial transit time in addition to CBF.

4. Imaging framework

   Further improvements to the regional CBF estimation will be made by using more sophisticated methods for automated ROI definition, by using multimodal data and using the Similarity and Truth Estimation for Propagated Segmentations (STEPS) approach [142].

5. Motion reduction

   Currently, the timing of background suppression pulses pulses was chosen to reduce the signal from the white and grey matter (WM, GM) and cerebrospinal fluid (CBF) in order

to enhance SNR. However, the manipulation of the BS pulses can be used to enhance the contrast between the tissues instead, which might improve the performance of image registration. This will be tested first in healthy volunteers. The data will be acquired with carefully controlled motion and the temporal SD of difference images will be used to assess the alignment after registration.

6. CBF and MRS

   The detailed regional analysis of CBF could provide additional information of pathophysiology, if it could be combined with regional MRS data. This could be achieved by using MRS imaging instead of a single voxel.

Appendix A

Renal pCASL: reproducibility study

A.1 Introduction

This chapter presents an application of pCASL quantification of renal blood flow, which takes advantage of the knowledge and experience gained during development of the neonatal imaging framework described in chapter 7. Although this work was not directly motivated by investigation of neonatal HIE at this stage, it might lead to future development in neonatal renal failure.

A.2 Motivation

Renal perfusion is an important indicator of renal function and its abnormalities are associated with a range of diseases [149]. Therefore measuring renal perfusion is particularly important for assessment of renal damage, recovery from the desease or transplantation. Commonly used methods for renal perfusion quantification, such as PET, CT and contrast enhanced MRI, are invasive. Furthermore, they might not be well tolerated by the patient due to nephrotoxicity or might be contraindicated in certain patient group, for example gadolinium based agents in renal failure. ASL offers a truly noninvasive alternative, therefore it has attracted attention of researchers interested in the renal function in recent years. Additionally, ASL offers quantification of renal blood flow (RBF) which may be a useful imaging biomarker.

Renal ASL using pseudocontinuous labelling has been shown feasible in 1.5T [150] and 3T [151], but it presents itself with different challenges compared to that of the brain. One of the biggest challenges in renal imaging is motion and motion related artefacts. As shown in chapter 7 in brain and by other researchers in kidneys, motion correction can increase SNR and improve reproducibility of the technique [152]. However, standard motion correction approaches devel-

oped for brain do not always produce expected results. Another challenge in renal pCASL and RBF quantification is estimation of labelling efficiency. In renal pCASL, the labelling plane is positioned on the descending aorta, where a large velocity distribution within the cardiac cycle is expected and, as seen in section 5.3.2, the labelling efficiency depends on the velocity of the moving spins. In reported studies using pCASL in kidneys at 3T [151], the labelling efficiency was estimated only based on simulations. However, it is not clear how the different velocities of blood in the descending aorta during the cardiac cycle affect the labelling efficiency.

For renal perfusion imaging with pseudo-continuous ASL (pCASL) to become a clinically useful tool, the above challenges need to be addressed and its reliability assessed. Therefore in this study the labelling efficiency for different velocities in the cardiac cycle is estimated and a new motion correction framework proposed. This is then followed by an assessment of a test-retest reproducibility in healthy volunteers.

A.3 Methods

Study design. Institutional and Research Ethics Committee approval was obtained for this study. Ten healthy volunteers were recruited to this study (3 females, age 25-35). All volunteers underwent within session scan-rescan. Additionally, seven had the scan repeated on two separate occasions (between sessions scan-rescan, at least one week apart). The schematic of the study design is shown in figure A.1.

Imaging. All subjects underwent a renal pCASL perfusion protocol in a 3.0T Phillips Ingenia wide-bore MR scanner. Volunteers were positioned with their arms extended on dedicated arm-rests above their heads. This allowed a reduction of the FOV in the phase encoding direction and the number of phase encoding steps, which in turn reduced the acquisition time of each frame. Respiration and cardiac cycles were monitored with respiratory bellows and pulse oximetry. The main protocol consisted of localiser scans, pCASL and phase contrast scans. A coronal-oblique ASL imaging volume was positioned along the long axis of both kidneys to reduce in and out of plane motion. The labelling plane was carefully positioned above the kidneys, perpendicular to the descending aorta and far away from the lungs to reduce B_0 inhomogeneities at the level of labelling. An example of planning for pCASL including FOV: labelling plane an shim box is shown in figure A.2. Labelling duration was 1.65s, post labelling delay 0.9s. The pCASL labelling train consisted of 0.5ms Hanning RF pulses with FA=18°, a maximum gradient of

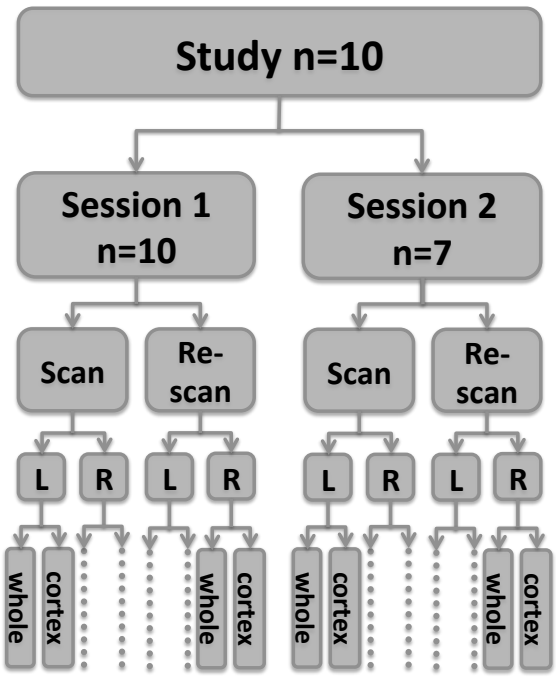

Figure A.1: *Study design.*

0.6 G/cm and Gmax/Gmean equal to 10. Gradient-echo EPI was chosen for the readout module which enabled multi-slice acquisition. EPI parameters were: 108x99 acquisition matrix, 320x320x5mm^3 FOV,10 slices (2mm gap), SENSE factor of 3, FA=90° and TE/TR = 7/4000ms and spectral adiabatic inversion recovery (SPAIR) pulses were applied for fat suppression. 20 control-label pairs were acquired for each full pCASL acquisition. To reduce motion between acquisitions, two pairs were acquired within a 16s breath-hold. M_0 proton density images were also acquired in a separate acquisition with the same readout as pCASL scans, but with TR=9s.

QFlow acqisition and velocities estimation. Quantitative cardiac-gated phase contrast scan was acquired at the exact position of labelling plane for all volunteers. The velocities of the flowing blood were measured using a flow sensitive multi-shot TFE sequence, with the following parameters: TFE factor = 9, TR/TE = 5.6/3.3ms, FOV 210x267x5 mm^3, matrix size 104x129, FA=10°, SENSE factor = 1.5, VENC = 90 or 100 cm/s, phase encoding direction: AP. All data was acquired within a single breath-hold and PPU retrospective synchronisation was used to reconstruct PC images for twelve cardiac phases.

Magnitude images from all cardiac phases were segmented using Snake ROI region growth implementation in ITK-SNAP [1]. The intensity threshold for ROI growth restriction was set to

[1] http://www.itksnap.org/pmwiki/pmwiki.php?n=Main.Credits

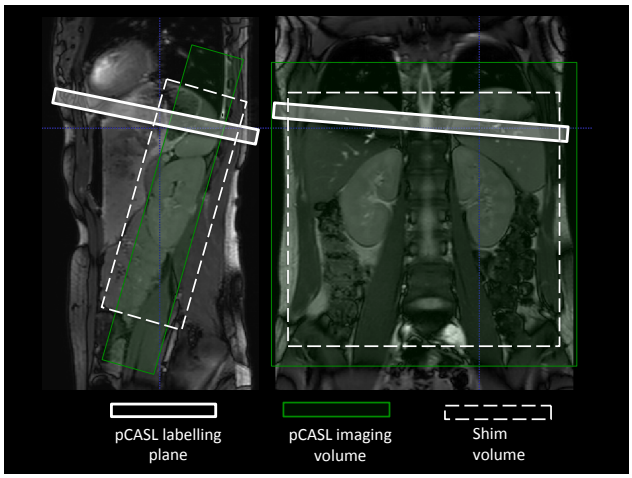

Figure A.2: *Position of the FOV (green), labelling plane (white) and shim box (white dashed line)*

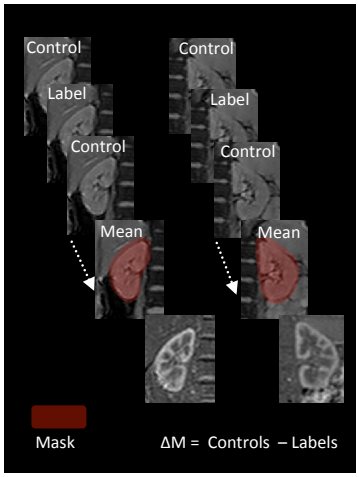

Figure A.3: *Motion correction pipeline*

include the whole lumen of the artery. Such created segmentations were then used to quantify mean and maximum velocity in phase images, as well as the lumen for each cardiac phase. An example segmentation overlaid on the magnitude and phase images is presented in figure A.4.

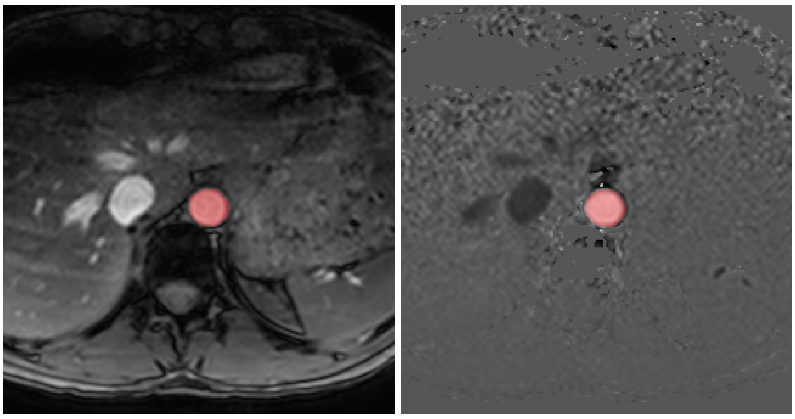

Figure A.4: *Magnitude (left) and phase (right) images acquired with QFlow sequence with overlaid manual segmentation of descending aorta.*

Labelling Efficiency estimation. Based on measured velocities across different cardiac cycle phases, laminar flow weighted labelling efficiency was estimated using a Bloch equation simulator (described previously in chapter 5). Two methods were considered. In the first method, all velocities across all cardiac cycles across all volunteers were averaged, and labelling efficiency for that velocity α_{vave} was computed. In the second method, the velocities and artery lumen for each cardiac cycle phase were averaged across all volunteers, and a total flow and total labelling

efficiency was computed using equations similar to 5.30 and 5.31 from chapter 5:

$$F_{total} = \sum_{i=1}^{12} v_{mean,i} \cdot s_i \tag{A.1}$$

$$\alpha_{total} = \sum_{i=1}^{12} \frac{v_{mean,i} \cdot s_i}{F_{total}} \cdot \alpha_{weighted}(v_{max,i}) \tag{A.2}$$

$$= \sum_{i=1}^{12} w_i \cdot \alpha_{weighted}(v_{max,i}) \tag{A.3}$$

where s_i is the artery lumen, $i = 1 : 12$ here representing each cardiac cycle and $\alpha_{weighted}$ 5.28. Weighting factor w_i was introduced here to reflect different volumes of blood delivered to the kidneys at different cardiac phases. The resulting estimated efficiencies were compared and used for RBF quantification.

Motion Correction. Although the images were acquired during multiple breath-holds, the frames acquired during different breath-holds were not aligned. To reduce this misalignment between consecutive pairs, a new post-processing motion correction procedure was developed. First, the images were cropped to restrict FOV to the region of left and right kidneys separately, which allowed for independent registration. Next, a mask was drawn manually on each kidney and used to constrain the rigid registration to the region of interest. Control and labelled images were registered to a template created by refined registration of control images using DTITK[2], similarly to that described in detail in chapter 7. Pairwise subtraction was then performed, and these were averaged to create a perfusion weighte image. A summary of the motion correction steps is shown in figure A.3.

Quantification. The general kinetic model was used to quantify RBF using equation 4.10, with blood T1 set to 1.65s and partition coefficient λ = 0.9. The mean value of M_0 within the whole kidney mask was used for calibration. Cortical RBF was calculated by averaging signal within a manually segmented cortex mask created for each kidney.

Statistical analysis. The mean and SD for all measurements of whole kidney and cortex ROIs was calculated, and a Student's t-test was used to evaluate the reproducibility of the technique. A standard deviation of the differences between repeated measurements (both within and between sessions) within and between subjects (SD_{ws}, SD_{bs}) as well as coefficient of variation (CV_{ws}, CV_{bs}) and interclass correlation coefficient ICC were computed, using analysis of variance

[2]http://dti-tk.sourceforge.net/pmwiki/pmwiki.php

(ANOVA) [153]. Coefficient of variation is defined as a ratio of SD_{ws} or SD_{bs} to the appropriate mean of repeated measurements. ICC is a measure of reliability; it typically ranges between 0-1, with 1 indicating the highest reliability (zero measurement error) [154]. It is defined as:

$$ICC = \frac{MS_{bs} - MS_{ws}}{MS_{bs} + (k-1) \cdot MS_{ws}} \tag{A.4}$$

where MS_{bs} and MS_{ws} are the mean square between and within subjects, and k is the number of repeated scans. To visualise the agreement within and between session measurements, a Bland-Altman plot [16] was provided. The 95% limits of agreements were calculated as the mean difference $\pm 1.96 \cdot SD$ of the scan-rescan difference. This represents the range within which 95% of the future scan-rescan differences will lie [155]. This was done for an average of left and right kidneys within cortex and whole kidney ROIs.

A.4 Results

Labelling Efficiency estimation.

The maximum velocity, lumen and weighted labelling efficiency for each cardiac phase for all volunteers as well as a mean across volunteers is shown in the figure A.5. Details of average cardiac cycle across all volunteers are presented in table A.1.

Labelling efficiency for average blood velocity, α_{vave} was 0.87, whereas the total efficiency α_{total} averaged across all cardiac cycle phases and volunteers was 0.81, $SD = 0.18$ (ranging from 0.77 to 0.84) and was used to quantify RBF.

RBF qualification

A typical renal perfusion map is shown in figure A.6. The mean RBF within the whole kidney ROI was 187[ml/100g/min] (range: 98-291[ml/100g/min], SD:52 [ml/100g/min]) and within the cortex: 234[ml/100g/min] (range: 86-399[ml/100g/min], SD 70). The RBF values are in agreement with previously reported renal ASL studies. There was no statisticaly significant difference between left and right kidney RBF, both whole and cortex (Student t-test p>0.05).

Reproducibility

Results of the reproducibility analysis are given in table A.2. Within-session scan-rescan coefficient of variance, was lower than that between between sessions, both within and between

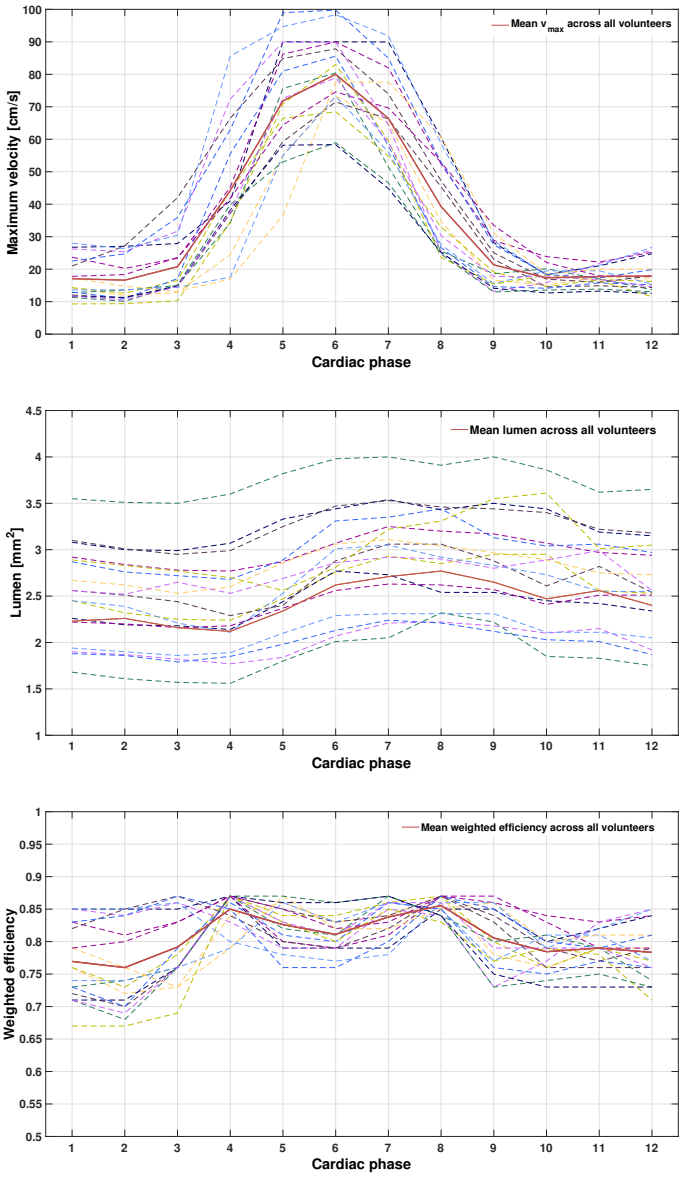

Figure A.5: *Maximum velocity (top), lumen (middle) and weighted efficiency (bottom) for each cardiac phase. The mean for all volunteers is marked in red.*

subjects. The Bland-Altman plot is shown in figure A.7. There is a small negative bias: -3.7 and -5.9 [ml/100g/in] for within and between session differences, respectively.

A.5 Discussion

This study demonstrated the feasibility of using pCASL with gradient-echo EPI in a wide bore 3T scanner to measure renal perfusion in healthy volunteers. The technique was quick to acquire

phase	v_{mean} [cm/s]	v_{max} [cm/s]	s [mm^2]	w_i	$\alpha(v_{max})$
1	10.3	17.1	2.51	0.04	0.77
2	9.9	16.6	2.46	0.03	0.76
3	13.8	20.7	2.41	0.04	0.79
4	30.4	44.2	2.39	0.07	0.85
5	52.6	71.8	2.59	0.13	0.83
6	55.7	80.0	2.84	0.18	0.81
7	43.2	66.4	2.94	0.17	0.84
8	22.9	39.3	2.92	0.12	0.86
9	10.7	21.3	2.88	0.08	0.81
10	9.2	17.3	2.77	0.05	0.78
11	10.1	17.7	2.68	0.05	0.79
12	10.9	17.9	2.59	0.04	0.78

Table A.1: *Results of estimated labelling efficiency, averaged across all volunteers*

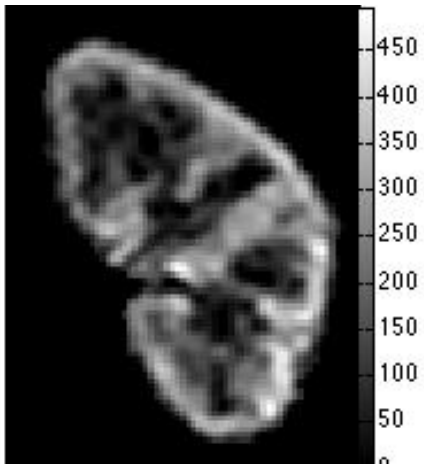

Figure A.6: *Example of renal blood flow map. Tissue contrast and spatial resolution of the imaging allowed for differentiation between cortex, medulla and renal columns*

and both tissue contrast and spatial resolution suggest fiseable utility in the clinical setting. Two important challenges were addressed: estimation of labelling efficiency and motion correction.

Labelling efficiency. Labelling efficiency of pCASL was estimated successfully for an average velocity and for all cardiac cycle phases. Additionally to laminar flow weighing, the additional weight w_i for each cardiac cycle was added to put more importance on the cardiac cycle phase that provides the highest volume of the label. This weighting was driven by the wide range of velocities and lumen within a cardiac cycle. For an average heart rate of 75 beats

		Whole Kidney	Cortex
scan - rescan	SD_{ws}[ml/100g/min]	14.8	20.14
	CV_{ws}	7.90%	8.60%
	SD_{bs} [ml/100g/min]	71.7	97.8
	CV_{bs}	38.30%	41.70%
	ICC (scan-rescan)	0.92	0.92
session1 - session 2	SD_{ws}[ml/100g/min]	60.4	80.1
	CV_{ws}	31.30%	33.00%
	SD_{bs}[ml/100g min]	48.9	70.5
	CV_{bs}	25.30%	28.90%

Table A.2: *Results of statistical analysis. SD_{ws},SD_{bs} - within subject and between subjects standard deviation CV_{ws},CV_{bs} - within subject and between subjects coefficient of variation, ICC - Interclass Correlation Coefficient*

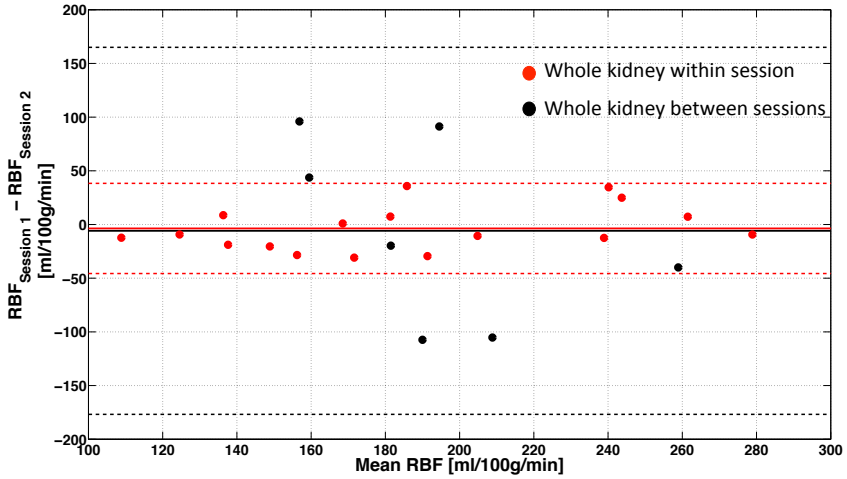

Figure A.7: *Bland-Altman plot for scan-rescan (red) and between sessions (black) variability of cortical and whole kidney perfusion (dashed lines represent 95% limits of agreement, calculated as the mean difference $\pm 1.96 \cdot SD$ of the difference between repeated measurements.*

per minute (1.25 per second) two full cardiac cycles are covered within the labelling duration of 1.65 seconds and therefore all cardiac cycle phases should be equally represented in the total acquisition of 20 controls and labels. However, using the mean flow across the cardiac cycle would result in an overestimation of renal perfusion of almost 7%, which emphasises the importance of efficiency estimation for all cardiac phases. In this study of healthy volunteers, one value of labelling efficiency was used. If the method was to be used in a patient population, it could be beneficial to estimate efficiency on a patient by patient basis.

One limitation of the estimation of α_{total} presented here is the lack of B_0 estimation from the field maps. The inhomogeneities are expected to reduce efficiency, especially for the fastest spins, as discussed in chapter 5. This will be addressed in future work.

Motion correction. The motion correction pipeline consisting of registration of each kidney separately as well as adding a mask significantly improved the quality of RBF maps. Motion artefacts could be further reduced with the use of background suppression pulses. Additionally, breath-holds could be replaced by a timed breathing - a method in which the subject synchronises their breathing with the sequence, breathing during post-labelling delay and at the end of a single frame acquisition. This method is currently being tested in a new study investigating usability of pCASL in the liver.

RBF **quantification.** The RBF values are in agreement with previously reported renal ASL studies [156].

Reproducibility. The within sessions ICC was high, indicating good reliability of the method. Between sessions limits of agreements were high, however they were similar to values previously reported at 1.5T using multiple inversion times FAIR [156]. This might have resulted from a natural variance in renal perfusion driven by food and drink (especially caffeine) uptake before the scans, which was not controlled for. Another reason for increased variance between the sessions could have been deviations of the labelling efficiency from that estimated based on measured velocities and simulations due to B0 and B1 inhomogeneity.

A.6 Summary

In summary, pCASL can be successfully used for RBF estimation. The biggest application of the method would be in cases when an asymmetrical RBF is expected, like in kidney transplantation. The scanning protocol can be easily adapted for perfusion quantification in other organs, like a liver or prostate.

List of abstracts that benefited from work presented in this chapter:

M. Sokolska, D. Thomas, A. Bainbridge, X. Golay, S. Taylor, S. Punwani, D. Pendse *Renal Perfusion Imaging with Pseudo-continuous Arterial-Spin Labelling (pCASL) at 3.0T: Repeatability in Healthy volunteers.* Proceedings of 22nd ISMRM 2014

M. Sokolska, D. Thomas, A. Bainbridge, X. Golay, S. Taylor, S. Punwani, D. Pendse *"Renal Pseudo- continuous Arterial Spin Labelling (pCASL) MRI: A Repeatability Study"*. ERC 2014

Bibliography

[1] P. W. Pires, C. M. Dams Ramos, N. Matin, and A. M. Dorrance, "The effects of hypertension on the cerebral circulation," *American Journal of Physiology - Heart and Circulatory Physiology*, vol. 304, no. 12, pp. H1598–H1614, 2013.

[2] R. B.Buxton, *INTRODUCTION TO FUNCTIONAL MAGNETIC RESONANCE IMAGING: PRINCIPLES AND TECHNIQUES*. Cambridge University Press, 2002.

[3] J. Perlman, "Intrapartum Hypoxic-Ischemic Cerebral Injury and Subsequent Cerebral Palsy: Medicolegal Issues Perlman," *Pediatrics*, no. 99, pp. 851–859, 1977.

[4] K.-A. Hossmann, "Reperfusion of the brain after global ischemia-hemodynamic disturbances.," *Shock*, vol. 8, no. 2, 1997.

[5] P. Ilves, R. Talvik, and T. Talvik, "Changes in doppler ultrasonography in asphyxiated term infants with hypoxic-ischaemic encephalopathy," *Acta Pediatrica*, vol. 87, no. 6, pp. 680–684, 1998.

[6] C. E. Williams, A. J. Gunn, C. Mallard, and P. D. Gluckman, "Outcome after ischemia in the developing sheep brain: An electroencephalographic and histological study," *Annals of Neurology*, vol. 31, no. 1, pp. 14–21, 1992.

[7] M. Rutherford, C. Malamateniou, A. McGuinness, J. Allsop, M. M. Biarge, and S. Counsell, "Magnetic resonance imaging in hypoxic-ischaemic encephalopathy.," *Early human development*, vol. 86, pp. 351–60, June 2010.

[8] L. S. de Vries and F. Groenendaal, "Patterns of neonatal hypoxic-ischaemic brain injury," *Neuroradiology*, vol. 52, pp. 555–566, June 2010.

[9] Z.-P. Liang and P. C. Lauterbur, *Principles of magnetic resonance imaging : a signal processing perspective*. IEEE Press series in biomedical engineering, Bellingham (Wash.): IEEE Press, 2000.

[10] D. W. McRobbie, *MRI from picture to proton*. Cambridge : Cambridge University Press, 2nd ed ed., 2006. Previous ed.: 2003.

[11] P. B. Barker and D. D. Lin, "In vivo proton mr spectroscopy of the human brain," *Progress in Nuclear Magnetic Resonance Spectroscopy*, vol. 49, no. 2, pp. 99 – 128, 2006.

[12] M. Bernstein, K. King, X. Zhou, and W. Fong, "Handbook of mri pulse sequences," *Medical Physics*, vol. 32, no. 1452, 2005.

[13] H. Sarnat and M. Sarnat, "Neonatal encephalopathy following fetal distress: A clinical and electroencephalographic study," *Archives of Neurology*, vol. 33, no. 10, pp. 696–705, 1976.

[14] C. M. T. Robertson and M. Perlman, "Follow-up of the term infant after hypoxic-ischemic encephalopathy," *Paediatrics & Child Health*, vol. 11, pp. 278–282, May 2006.

[15] J. Barkovich, B. L. Hajnal, D. Vigneron, a. Sola, J. C. Partridge, F. Allen, and D. M. Ferriero, "Prediction of neuromotor outcome in perinatal asphyxia: evaluation of MR scoring systems.," *AJNR. American journal of neuroradiology*, vol. 19, pp. 143–9, Jan. 1998.

[16] D. I. Altman, W. J. Powers, J. M. Perlman, P. Herscovitch, S. L. Volpe, and J. J. Volpe, "Cerebral blood flow requirement for brain viability in newborn infants is lower than in adults.," *Annals of neurology*, vol. 24, pp. 218–26, Aug. 1988.

[17] O. Pryds, "Control of cerebral circulation in the high-risk neonate," *Ann Neurol*, vol. 30, no. 8, pp. 321–329, 1991.

[18] L. Biagi, A. Abbruzzese, M. C. Bianchi, D. C. Alsop, A. Del Guerra, and M. Tosetti, "Age dependence of cerebral perfusion assessed by magnetic resonance continuous arterial spin labeling.," *Journal of magnetic resonance imaging : JMRI*, vol. 25, pp. 696–702, Apr. 2007.

[19] P. Moses, M. DiNino, L. Hernandez, and T. T. Liu, "Developmental changes in resting and functional cerebral blood flow and their relationship to the bold response," *Human Brain Mapping*, vol. 35, no. 7, pp. 3188–3198, 2014.

[20] L. Tatu, T. Moulin, J. Bogousslavsky, and H. Duvernoy, "Arterial territories of the human brain: Cerebral hemispheres," *Neurology*, vol. 50, no. 6, pp. 1699–1708, 1998.

[21] E. C. Peterson, Z. Wang, and G. Britz, "Regulation of cerebral blood flow.," *International journal of vascular medicine*, vol. 2011, p. 823525, Jan. 2011.

[22] O. Pryds and A. D. Edwards, "Cerebral blood flow in the newborn infant.," *Archives of Disease in Childhood. Fetal and Neonatal Edition*, vol. 74, pp. F63–F69, Jan. 1996.

[23] P. Jezzard, P. M. Matthews, S. M. Smith, *et al.*, *Functional MRI: an introduction to methods*, vol. 61. Oxford University Press, 2001.

[24] L. Symon, M. Branston, N, A. Strong, J, and D. Hope, T, "The concepts of thresholds of ischaemia in relation to brain structure and function," *J Clin Pathol*, no. 11, pp. 149–154, 1977.

[25] W. J. Powers, R. L. Grubb, D. Darriet, and M. E. Raiehle, "Cerebral blood flow and cerebral metabolic rate of oxygen requirements for cerebral function and viability in humans," *J Cereb Blood Flow Metab*, no. 5, pp. 600–8, 1985.

[26] J. Astrup, B. K. Siesjo, and L. Symon, "Thresholds in cerebral ischemia - the ischemic penumbra.," *Stroke*, no. 6, pp. 723–5, 1981.

[27] F. Chen and Y.-C. Ni, "Magnetic resonance diffusion-perfusion mismatch in acute ischemic stroke: An update," *World Journal of Radiology*, vol. 4, pp. 63–74, Mar. 2012.

[28] L.-A. Papile, A. M. Rudolph, and M. A. Heymann, "Autoregulation of Cerebral Blood Flow in the Preterm Fetal Lamb," *Pediatr Res*, vol. 19, pp. 159–161, Feb. 1985.

[29] P. Magistretti and I. Allaman, "A cellular perspective on brain energy metabolism and functional imaging," *Neuron*, vol. 86, no. 4, pp. 883 – 901, 2015.

[30] N. A. Lassen, "The luxury-perfusion syndrome and its possible relation to acute metabolic acidosis localised within the brain," *The Lancet*, vol. 288, no. 7473, pp. 1113–1115, 1966.

[31] M. F. Lythgoe, D. L. Thomas, M. D. King, G. S. Pell, L. van der Weerd, R. J. Ordidge, and D. G. Gadian, "Gradual changes in the apparent diffusion coefficient of water in selectively vulnerable brain regions following brief ischemia in the gerbil," *Magnetic Resonance in Medicine*, vol. 53, no. 3, pp. 593–600, 2005.

[32] C. Lou, H, A. Lassen N, A. Tweed W, G. Johnson, M. Jones, and J. Palahniuk, R, "Pressure passive cerebral blood flow and breakdown of the blood-brain barrier in experimental fetal asphyxia," *Acta Paediatr Scand*, vol. 68, pp. 57–63, 1979.

[33] H. C. Lou, N. a. Lassen, and B. Friis-Hansen, "Impaired autoregulation of cerebral blood flow in the distressed newborn infant.," *The Journal of pediatrics*, vol. 94, pp. 118–21, Jan. 1979.

[34] O. Pryds, G. Greisen, H. Lou, and B. Friis-Hansen, "Vasoparalysis associated with brain damage in asphyxiated term infants," *J. Pediatr.*, vol. 117, pp. 119–125, 1990.

[35] C. E. Williams, C. Mallard, W. Tan, and G. P. D, "Pathophysiology of perinatal asphyxia," *Clin Perinatol*, vol. 20, pp. 305–325, 1993.

[36] E. Inder, Terrie and J. Volpe Joseph, "Mechanism of perinatal brain injury," *Semin Neonatol*, vol. 5, pp. 3–26, 2000.

[37] A. Lorek, Y. Takei, E. B. Cady, W. J. S, S. Penrice J, A. D. Edwards, D. Peebles, M. Wylezinska, H. Owen-Reece, V. Kirkbride, C. E. C E Cooper, R. F. Aldridge, S. C. Roth, G. Brown, D. D. T, and E. O. R. Reynolds, "Delayed (ŇSecondaryÓ) Cerebral Energy Failure after Acute Hypoxia-Ischemia in the Newborn Piglet: Continuous 48-Hour Studies by Phosphorus Magnetic Resonance Spectroscopy," *Pediatric Research*, vol. 36, pp. 699–706, 1994.

[38] E. C. Mallard, C. E. Williams, A. J. Gunn, G. M. I, and P. D. Gluckman, "Frequent episodes of brief ischemia sensitize the fetal sheep brain to neuronal loss and induce striatal injury," *Pediatr Res*, vol. 33, pp. 61–65, 1993.

[39] R. Berger and Y. Garnier, "Pathophysiology of perinatal brain damage," *Brain Research Reviews*, vol. 30, no. 2, pp. 107 – 134, 1999.

[40] S. Jacobs, R. Hunt, W. Tarnow-Mordi, T. Inder, and P. Davis, "Cooling for newborns with hypoxic ischaemic encephalopathy (Review)," *The Cochrane Collaboration. Published by John Wiley & Sons, Ltd.*, 2008.

[41] D. Azzopardi, B. Strohm, N. Marlow, P. Brocklehurst, A. Deierl, O. Eddama, J. Goodwin, H. L. Halliday, E. Juszczak, O. Kapellou, M. Levene, L. Linsell, O. Omar, M. Thoresen, N. Tusor, A. Whitelaw, and A. D. Edwards, "Effects of hypothermia for perinatal asphyxia on childhood outcomes," *New England Journal of Medicine*, vol. 371, no. 2, pp. 140–149, 2014. PMID: 25006720.

[42] A. Jensen, Y. Garnier, J. Middelanis, and R. Berger, "Perinatal brain damage - from pathophysiology to prevention," *European Journal of Obstetrics and Gynecology and Reproductive Biology*, vol. 110, pp. S70–S79, Dec. 2014.

[43] S. Faulkner, A. Bainbridge, T. Kato, M. Chandrasekaran, A. B. Kapetanakis, M. Hristova, M. Liu, S. Evans, E. De Vita, D. Kelen, R. D. Sanders, a. D. Edwards, M. Maze, E. B. Cady, G. Raivich, and N. J. Robertson, "Xenon augmented hypothermia reduces early lactate/N-acetylaspartate and cell death in perinatal asphyxia.," *Annals of neurology*, vol. 70, pp. 133–50, July 2011.

[44] D. Azzopardi, N. J. Robertson, A. Bainbridge, E. Cady, G. Charles-Edwards, A. Deierl, G. Fagiolo, N. P. Franks, J. Griffiths, J. Hajnal, E. Juszczak, B. Kapetanakis, L. Linsell, M. Maze, O. Omar, B. Strohm, N. Tusor, and A. D. Edwards, "Moderate hypothermia within 6 h of birth plus inhaled xenon versus moderate hypothermia alone after birth asphyxia (toby-xe): a proof-of-concept, open-label, randomised controlled trial," *The Lancet Neurology*, vol. 15, no. 2, pp. 145 – 153, 2016.

[45] R. Brown, Y. Cheng, M. Haacke, M. Thompson, and R. Venkatesan, *Magnetic Resonance Imaging: Physical Principles and Sequence Design*. John Wiley & Sons Ltd, 1999.

[46] P. Mansfield, "Multi-planar image formation using NMR spin echoes," *J. Phys. C: Solid State Phys.,*, vol. 10, 1977.

[47] G. Greisen, "Cerebral blood flow in preterm infants during the first week of life.," *Acta paediatrica Scandinavica*, vol. 75, pp. 43–51, Jan. 1986.

[48] A. Kinnala, H. Suhonen-Polvi, T. Aarimaa, P. Kero, H. Korvenranta, U. Ruotsalainen, J. Bergman, M. Haaparanta, O. Solin, P. Nuutila, and U. Wegelius, "Cerebral metabolic rate for glucose during the first six months of life: an fdg positron emission tomography study.," *Archives of Disease in Childhood - Fetal and Neonatal Edition*, vol. 74, no. 3, pp. F153–F157, 1996.

[49] J. B. D. Vis, E. T. Petersen, L. S. D. Vries, F. Groenendaal, K. J. Kersbergen, T. Alderliesten, J. Hendrikse, and M. J. N. L. Benders, "Regional changes in brain perfusion during brain maturation measured non-invasively with Arterial Spin Labeling MRI in neonates," *European Journal of Radiology*, 2012.

[50] J. J. Volpe, P. Herscovitch, J. M. Perlman, and M. E. Raichle, "Positron emission tomography in the newborn: Extensive impairment of regional cerebral blood flow with intraventricular hemorrhage and hemorrhagic intracerebral involvement," *Pediatrics*, vol. 72, no. 5, pp. 589–601, 1983.

[51] J. J. Volpe, "Neurobiology of Periventricular Leukomalacia in the Premature Infant," *Pediatr Res*, vol. 50, no. 5, 2001.

[52] P. Wintermark, A. C. Moessinger, F. Gudinchet, and R. Meuli, "Perfusion-weighted magnetic resonance imaging patterns of hypoxic-ischemic encephalopathy in term neonates.," *Journal of magnetic resonance imaging : JMRI*, vol. 28, pp. 1019–25, Oct. 2008.

[53] J. J. Volpe, P. Herscovitch, J. M. Perlman, K. L. Kreusser, and M. E. Raichle, "Positron emmission tomography in the asphyxiated term newborn: Parasagittal impairment of cerebral blood flow," *Annals of Neurology*, vol. 17, no. 3, pp. 287–296, 1985.

[54] K. Borch and G. Greisen, "Blood flow distribution in the normal human preterm brain," *Pediatr Res*, no. 43, pp. 28–33, 1998.

[55] A. D. Edwards, C. Richardson, M. Cope, D. T. Delpy, and E. O. R. Reynolds, "Cot-side measurement of cerebral blood flow in ill newborns infants by near infrared spectroscopy," *The Lancet*, vol. 332, no. 8614, pp. 770 – 771, 1988.

[56] L. Skov, O. Pryds, and G. Greisen, "Estimating cerebral blood flow in newborn infants: comparison of near infrared spectroscopy and 133Xe clearance.," *Pediatric research*, vol. 30, pp. 570–3, Dec. 1991.

[57] M. Varela, A. M. Groves, T. Arichi, and J. V. Hajnal, "Mean cerebral blood flow measurements using phase contrast MRI in the first year of life.," *NMR in biomedicine*, vol. 25, pp. 1063–1072, Sept. 2012.

[58] M. J. Miranda, K. Olofsson, and K. Sidaros, "Noninvasive measurements of regional cerebral perfusion in preterm and term neonates by magnetic resonance arterial spin labeling.," *Pediatric research*, vol. 60, pp. 359–63, Sept. 2006.

[59] P. Wintermark, A. C. Moessinger, F. Gudinchet, and R. Meuli, "Temporal evolution of MR perfusion in neonatal hypoxic-ischemic encephalopathy.," *Journal of magnetic resonance imaging : JMRI*, vol. 27, pp. 1229–34, June 2008.

[60] E. T. Petersen, T. Lim, and X. Golay, "Model-free arterial spin labeling quantification approach for perfusion MRI.," *Magnetic resonance in medicine : official journal of the Society of Magnetic Resonance in Medicine / Society of Magnetic Resonance in Medicine*, vol. 55, pp. 219–32, Feb. 2006.

[61] D. S. Williams, J. a. Detre, J. S. Leigh, and a. P. Koretsky, "Magnetic resonance imaging of perfusion using spin inversion of arterial water.," *Proceedings of the National Academy of Sciences of the United States of America*, vol. 89, pp. 212–216, Jan. 1992.

[62] J. A. Detre, J. S. Leigh, D. S. Williams, and A. P. Kotersky, "Perfusion Imaging," *Magnetic resonance in medicine*, vol. 23, no. 1, pp. 37—5, 1992.

[63] R. R. Edelman, B. Siewert, D. G. Darby, V. Thangaraj, A. C. Nobre, and M. M. Mesulam, "Qualitative mapping of cerebral blood flow and functional localization with echo-planar MR imaging and signal targeting with alternating radio frequency," *Radiology*, vol. 192, no. 1, pp. 513—20, 1994.

[64] R. B. Buxton, L. R. Frank, E. C. Wong, B. Siewert, S. Warach, and R. R. Edelman, "A general kinetic model for quantitative perfusion imaging with arterial spin labeling.," *Magnetic resonance in medicine : official journal of the Society of Magnetic Resonance in Medicine / Society of Magnetic Resonance in Medicine*, vol. 40, pp. 383–396, Sept. 1998.

[65] W. Dai, D. Garcia, C. de Bazelaire, and D. C. Alsop, "Continuous flow-driven inversion for arterial spin labeling using pulsed radio frequency and gradient fields," *Magnetic Resonance in Medicine*, vol. 60, no. 6, pp. 1488–1497, 2008.

[66] K. K. Kwong, D. a. Chesler, R. M. Weisskoff, K. M. Donahue, T. L. Davis, L. Ostergaard, T. a. Campbell, and B. R. Rosen, "Mr perfusion studies with t1-weighted echo planar imaging.," *Magnetic resonance in medicine : official journal of the Society of Magnetic Resonance in Medicine / Society of Magnetic Resonance in Medicine*, vol. 34, pp. 878–87, Dec. 1995.

[67] D. C. Alsop and J. a. Detre, "Reduced transit-time sensitivity in noninvasive magnetic resonance imaging of human cerebral blood flow.," *Journal of cerebral blood flow and metabolism : official journal of the International Society of Cerebral Blood Flow and Metabolism*, vol. 16, pp. 1236–49, Nov. 1996.

[68] F. Calamante, S. R. Williams, N. van Bruggen, K. K. Kwong, and R. Turner, "A model for quantification of perfusion in pulsed labelling techniques," *NMR in Biomedicine*, vol. 9, no. 2, pp. 79–83, 1996.

[69] L. M. Parkes and P. S. Tofts, "Improved accuracy of human cerebral blood perfusion measurements using arterial spin labeling: Accounting for capillary water permeability," *Magnetic Resonance in Medicine*, vol. 48, no. 1, pp. 27–41, 2002.

[70] E. C. Wong, R. B. Buxton, and L. R. Frank, "A theoretical and experimental comparison of continuous and pulsed arterial spin labeling techniques for quantitative perfusion imaging," *Magnetic Resonance in Medicine*, vol. 40, no. 3, pp. 348–355, 1998.

[71] D. C. Alsop, J. A. Detre, X. Golay, M. Gunther, J. Hendrikse, L. Hernandez-Garcia, H. Lu, B. J. MacIntosh, L. M. Parkes, M. Smits, M. J. P. van Osch, D. J. J. Wang, E. C. Wong, and G. Zaharchuk, "Recommended implementation of arterial spin-labeled perfusion mri for clinical applications: A consensus of the ismrm perfusion study group and the european consortium for asl in dementia," *Magnetic Resonance in Medicine*, vol. 73, no. 1, pp. 102–116, 2015.

[72] E. T. Petersen, K. Mouridsen, and X. Golay, "The quasar reproducibility study, part ii: Results from a multi-center arterial spin labeling test-retest study," *NeuroImage*, vol. 49, no. 1, pp. 104 – 113, 2010.

[73] F. Q. Ye, V. S. Mattay, P. Jezzard, J. a. Frank, D. R. Weinberger, and a. C. McLaughlin, "Correction for vascular artifacts in cerebral blood flow values measured by using arterial spin tagging techniques.," *Magnetic resonance in medicine : official journal of the Society of Magnetic Resonance in Medicine / Society of Magnetic Resonance in Medicine*, vol. 37, pp. 226–35, Feb. 1997.

[74] E. C. Wong, R. B. Buxton, and L. R. Frank, "Quantitative imaging of perfusion using a single subtraction (QUIPSS and QUIPSS II).," *Magnetic resonance in medicine : of-*

ficial journal of the Society of Magnetic Resonance in Medicine / Society of Magnetic Resonance in Medicine, vol. 39, pp. 702–8, May 1998.

[75] E. C. Wong, R. B. Buxton, and L. R. Frank, "Implementation of quantitative perfusion imaging techniques for functional brain mapping using pulsed arterial spin labeling.," *NMR in biomedicine*, vol. 10, no. 4-5, pp. 237–249, 1997.

[76] J. Hrabe and D. Lewis, "Two analytical solutions for a model of pulsed arterial spin labeling with randomized blood arrival times," *Journal of Magnetic Resonance*, vol. 167, no. 1, pp. 49 – 55, 2004.

[77] M. A. Chappell, M. W. Woolrich, S. Kazan, P. Jezzard, S. J. Payne, and B. J. MacIntosh, "Modeling dispersion in arterial spin labeling: Validation using dynamic angiographic measurements," *Magnetic Resonance in Medicine*, vol. 69, no. 2, pp. 563–570, 2013.

[78] D. W. Holdsworth, C. J. D. Norley, R. Frayne, D. A. Steinman, and R. B. K, "Characterization of common carotid artery blood-flow waveforms in normal human subjects.," *Physiol. Meas.*, vol. 20, pp. 219–240, 1999.

[79] R. M. Henkelman, X. Huang, Q.-S. Xiang, G. J. Stanisz, S. D. Swanson, and M. J. Bronskill, "Quantitative interpretation of magnetization transfer," *Magnetic Resonance in Medicine*, vol. 29, no. 6, pp. 759–766, 1993.

[80] W. Zhang, a. C. Silva, D. S. Williams, and a. P. Koretsky, "NMR measurement of perfusion using arterial spin labeling without saturation of macromolecular spins.," *Magnetic resonance in medicine*, vol. 33, pp. 370–376, Mar. 1995.

[81] G. Zaharchuk, P. J. Ledden, K. K. Kwong, T. G. Reese, B. R. Rosen, and L. L. Wald, "Multislice perfusion and perfusion territory imaging in humans with separate label and image coils.," *Magnetic resonance in medicine : official journal of the Society of Magnetic Resonance in Medicine / Society of Magnetic Resonance in Medicine*, vol. 41, pp. 1093–8, June 1999.

[82] D. C. Alsop and J. A. Detre, "Multisection cerebral blood flow mr imaging with continuous arterial spin labeling.," *Radiology*, vol. 208, no. 2, pp. 410–416, 1998. PMID: 9680569.

[83] R. R. Edelman and Q. Chen, "Epistar mri: Multislice mapping of cerebral blood flow," *Magnetic Resonance in Medicine*, vol. 40, no. 6, pp. 800–805, 1998.

[84] X. Golay, M. Stuber, K. P. Pruessmann, D. Meier, and P. Boesiger, "Transfer insensitive labeling technique (TILT): application to multislice functional perfusion imaging.," *Journal of magnetic resonance imaging : JMRI*, vol. 9, pp. 454–61, Mar. 1999.

[85] X. Golay, E. T. Petersen, and F. Hui, "Pulsed star labeling of arterial regions (PULSAR): a robust regional perfusion technique for high field imaging.," *Magnetic resonance in medicine : official journal of the Society of Magnetic Resonance in Medicine / Society of Magnetic Resonance in Medicine*, vol. 53, pp. 15–21, Jan. 2005.

[86] S. G. Kim, "Quantification of relative cerebral blood flow change by flow-sensitive alternating inversion recovery (FAIR) technique: application to functional mapping.," *Magnetic resonance in medicine : official journal of the Society of Magnetic Resonance in Medicine / Society of Magnetic Resonance in Medicine*, vol. 34, pp. 293–301, Sept. 1995.

[87] E. Boudes, G. Gilbert, I. R. Leppert, X. Tan, G. B. Pike, C. Saint-Martin, and P. Wintermark, "Measurement of brain perfusion in newborns: Pulsed arterial spin labeling (pasl) versus pseudo-continuous arterial spin labeling (pcasl)," *NeuroImage: Clinical*, vol. 6, pp. 126 – 133, 2014.

[88] J. Wang, D. J. Licht, D. W. Silvestre, and J. a. Detre, "Why perfusion in neonates with congenital heart defects is negative–technical issues related to pulsed arterial spin labeling.," *Magnetic resonance imaging*, vol. 24, pp. 249–54, Apr. 2006.

[89] M. Varela, J. V. Hajnal, E. T. Petersen, X. Golay, N. Merchant, and D. J. Larkman, "A method for rapid in vivo measurement of blood T1.," *NMR in biomedicine*, vol. 24, pp. 80–8, Jan. 2011.

[90] H. Lu, C. Clingman, X. Golay, and P. C. M. van Zijl, "Determining the longitudinal relaxation time (T1) of blood at 3.0 Tesla.," *Magnetic resonance in medicine : official journal of the Society of Magnetic Resonance in Medicine / Society of Magnetic Resonance in Medicine*, vol. 52, pp. 679–82, Sept. 2004.

[91] D. J. Licht, J. Wang, D. W. Silvestre, S. C. Nicolson, L. M. Montenegro, G. Wernovsky, S. Tabbutt, S. M. Durning, D. M. Shera, J. W. Gaynor, T. L. Spray, R. R. Clancy, R. a. Zimmerman, and J. a. Detre, "Preoperative cerebral blood flow is diminished in neonates with severe congenital heart defects.," *The Journal of thoracic and cardiovascular surgery*, vol. 128, pp. 841–9, Dec. 2004.

[92] P. Wintermark, A. Hansen, M. Gregas, J. Soul, M. Labrecque, R. Robertson, and S. Warfield, "Brain perfusion in asphyxiated newborns treated with therapeutic hypothermia," *American Journal of Neuroradiology*, vol. 32, no. 11, pp. 2023–2029, 2011.

[93] R. Pienaar, M. J. Paldino, N. Madan, K. S. Krishnamoorthy, D. C. Alsop, M. Dehaes, and P. E. Grant, "A quantitative method for correlating observations of decreased apparent diffusion coefficient with elevated cerebral blood perfusion in newborns presenting cerebral ischemic insults.," *NeuroImage*, vol. 63, pp. 1510–8, Nov. 2012.

[94] a. N. Massaro, M. Bouyssi-Kobar, T. Chang, L. G. Vezina, a. J. du Plessis, and C. Limperopoulos, "Brain perfusion in encephalopathic newborns after therapeutic hypothermia.," *AJNR. American journal of neuroradiology*, vol. 34, pp. 1649–55, Aug. 2013.

[95] D. Garcia, C. de Bazelaire, and A. D, "Pseudo-continuous flow driven adiabatic inversion for arterial spin labeling," *Proceedings of the 13th Annual Meeting of ISMRM*, 2005.

[96] E. Wong, "Vessel encoded arterial spin labeling using pseudo-continuous tagging," *Proceedings of the 14th Annual Meeting of ISMRM*, 2006.

[97] Y. Jung, E. C. Wong, and T. T. Liu, "Multiphase pseudocontinuous arterial spin labeling (MP-PCASL) for robust quantification of cerebral blood flow.," *Magnetic resonance in medicine : official journal of the Society of Magnetic Resonance in Medicine / Society of Magnetic Resonance in Medicine*, vol. 64, pp. 799–810, Sept. 2010.

[98] W.-M. Luh, S. L. Talagala, T.-Q. Li, and P. A. Bandettini, "Pseudo-continuous arterial spin labeling at 7 t for human brain: Estimation and correction for off-resonance effects using a prescan," *Magnetic Resonance in Medicine*, vol. 69, no. 2, pp. 402–410, 2013.

[99] W.-C. Wu, S.-F. Jiang, S.-C. Yang, and S.-H. Lien, "Pseudocontinuous arterial spin labeling perfusion magnetic resonance imaging–a normative study of reproducibility in the human brain.," *NeuroImage*, vol. 56, pp. 1244–50, June 2011.

[100] D. D. Shin, T. T. Liu, E. C. Wong, A. Shankaranarayanan, and Y. Jung, "Pseudocontinuous arterial spin labeling with optimized tagging efficiency," *Magnetic Resonance in Medicine*, vol. 68, no. 4, pp. 1135–1144, 2012.

[101] H. Jahanian, D. C. Noll, and L. Hernandez-Garcia, "B0 field inhomogeneity considerations in pseudo-continuous arterial spin labeling (pCASL): effects on tagging efficiency and correction strategy.," *NMR in biomedicine*, vol. 24, pp. 1202–9, Dec. 2011.

[102] L. Maccotta, J. a. Detre, and D. C. Alsop, "The efficiency of adiabatic inversion for perfusion imaging by arterial spin labeling.," *NMR in biomedicine*, vol. 10, no. 4-5, pp. 216–21, 1997.

[103] P. Liu, H. Huang, N. Rollins, L. F. Chalak, T. Jeon, C. Halovanic, and H. Lu, "Quantitative assessment of global cerebral metabolic rate of oxygen (CMRO2) in neonates using MRI.," *NMR in biomedicine*, pp. 332–340, Jan. 2014.

[104] S. Aslan, F. Xu, P. L. Wang, J. Uh, U. S. Yezhuvath, M. van Osch, and H. Lu, "Estimation of labeling efficiency in pseudocontinuous arterial spin labeling.," *Magnetic resonance in medicine : official journal of the Society of Magnetic Resonance in Medicine / Society of Magnetic Resonance in Medicine*, vol. 63, pp. 765–71, Mar. 2010.

[105] P. Herscovitch and M. E. Raichle, "What is the correct value for the brain–blood partition coefficient for water?," *Journal of cerebral blood flow and metabolism : official journal of the International Society of Cerebral Blood Flow and Metabolism*, vol. 5, pp. 65–9, Mar. 1985.

[106] Y. Zhang, M. Brady, and S. Smith, "Segmentation of brain mr images through a hidden markov random field model and the expectation-maximization algorithm," *Medical Imaging, IEEE Transactions on*, vol. 20, pp. 45–57, Jan 2001.

[107] K. Philbin, M, H. Taber, K, and A. Hayman, L, "Preliminary report: Changes in vital signs of term newborns during mr," *AJNR*, vol. 17, pp. 6–10, 1996.

[108] P. Mansfield, B. Chapman, R. Bowtell, P. Glover, R. Coxon, and P. Harvey, "Active Acoustic Screening: Reduction of Noise in Gradient Coils by Lorentz Force Balancing," *Magn Reson Med*, vol. 33, pp. 276–81, Feb. 1995.

[109] A. Katsunuma, H. Takamori, Y. Sakakura, Y. Hamamura, Y. Ogo, and R. Katayama, "Quiet mri with novel acoustic noise reduction," *Magnetic Resonance Materials in Physics, Biology and Medicine*, vol. 13, no. 3, pp. 139 – 144, 2002.

[110] A. Moelker, M. W. Vogel, and P. M. T. Pattynama, "Efficacy of passive acoustic screening: Implications for the design of imager and mr-suite," *Journal of Magnetic Resonance Imaging*, vol. 17, no. 2, pp. 270–275, 2003.

[111] R. A. Hedeen and W. A. Edelstein, "Characterization and prediction of gradient acoustic noise in mr imagers," *Magnetic Resonance in Medicine*, vol. 37, no. 1, pp. 7–10, 1997.

[112] F. Hennel, F. Girard, and T. Loenneker, “"silent" mri with soft gradient pulses,” *Magnetic Resonance in Medicine*, vol. 42, no. 1, pp. 6–10, 1999.

[113] D. G. Tomasi and T. Ernst, “Echo planar imaging at 4 tesla with minimum acoustic noise,” *Journal of Magnetic Resonance Imaging*, vol. 18, no. 1, pp. 128–130, 2003.

[114] M. A. Baker, “Reduction of mri acoustic noise achieved by manipulation of scan parameters; a study using veterinary mr sequences,” *Radiography*, vol. 19, no. 1, pp. 11 – 16, 2013.

[115] J. N. Meer, D. F. R. Heijtel, G. Hest, G.-J. Plattèl, M. J. P. Osch, E. J. W. Someren, E. T. vanBavel, and A. J. Nederveen, “Acoustic noise reduction in pseudo-continuous arterial spin labeling (pcasl),” *Magnetic Resonance Materials in Physics, Biology and Medicine*, vol. 27, no. 3, pp. 269–276, 2013.

[116] F. Q. Ye, J. A. Frank, D. R. Weinberger, and A. C. McLaughlin, “Noise reduction in 3d perfusion imaging by attenuating the static signal in arterial spin tagging (assist),” *Magnetic Resonance in Medicine*, vol. 44, no. 1, pp. 92–100, 2000.

[117] W. Dixon, M. Sardashti, M. Castillo, and S. G, “Multiple inversion recovery reduces static tissue signal in angiograms.,” *Magnetic resonance in medicine : official journal of the Society of Magnetic Resonance in Medicine / Society of Magnetic Resonance in Medicine*, vol. 18, no. 2, pp. 257–268, 1991.

[118] L. Williams, N. Gelman, P. Picot, D. Lee, J. Ewing, V. Han, and R. Thompson, “Neonatal brain: Regional variability of in vivo mr imaging relaxation rates at 3.0t - initial experience,” *Radiology*, vol. 235, no. 2, pp. 595–603, 2005.

[119] K. Prabhakaran, R. Hopson, M. Elliott, K. Ruparel, R. Gur, G. R.C., and J. Detre, “Comparison of water excitation versus fat saturation in perfusion mri - effects on lipid signal, snr and cbf,” *Proc. Intl. Soc. Mag. Reson. Med. 21*, p. 2162, 2013.

[120] W. Dai, P. M. Robson, A. Shankaranarayanan, and D. C. Alsop, “Reduced resolution transit delay prescan for quantitative continuous arterial spin labeling perfusion imaging,” *Magnetic Resonance in Medicine*, vol. 67, no. 5, pp. 1252–1265, 2012.

[121] H. Bode and U. Wais, “Age dependence of flow velocities in basal cerebral arteries.,” *Archives of disease in childhood*, vol. 63, pp. 606–11, June 1988.

[122] M. Günther, M. Bock, and L. R. Schad, "Arterial spin labeling in combination with a look-locker sampling strategy: Inflow turbo-sampling epi-fair (its-fair)," *Magnetic Resonance in Medicine*, vol. 46, no. 5, pp. 974–984, 2001.

[123] B. U. Foerster, D. Tomasi, and E. C. Caparelli, "Magnetic field shift due to mechanical vibration in functional magnetic resonance imaging," *Magnetic Resonance in Medicine*, vol. 54, no. 5, pp. 1261–1267, 2005.

[124] K. K. Oguz, X. Golay, F. B. Pizzini, C. a. Freer, N. Winrow, R. Ichord, J. F. Casella, P. C. M. van Zijl, and E. R. Melhem, "Sickle cell disease: continuous arterial spin-labeling perfusion MR imaging in children.," *Radiology*, vol. 227, pp. 567–74, May 2003.

[125] H. Tan, J. A. Maldjian, J. M. Pollock, J. H. Burdette, L. Y. Yang, A. R. Deibler, and R. A. Kraft, "A fast, effective filtering method for improving clinical pulsed arterial spin labeling mri," *Journal of Magnetic Resonance Imaging*, vol. 29, no. 5, pp. 1134–1139, 2009.

[126] J. Wright, A. Ganesh, S. Rao, Y. Peng, and Y. Ma, "Robust principal component analysis: Exact recovery of corrupted low-rank matrices by convex optimization," *Proc. of Neural Information Processing Systems (NIPS)*, 2009.

[127] K. Sidaros, K. Olofsson, M. Miranda, and O. Paulson, "Arterial spin labeling in the presence of severe motion," *Journal of Cerebral Blood Flow and Metabolism*, vol. 25, 2005.

[128] P. A. Yushkevich, B. B. Avants, S. R. Das, J. Pluta, M. Altinay, and C. Craige, "Bias in estimation of hippocampal atrophy using deformation-based morphometry arises from asymmetric global normalization: An illustration in {ADNI} 3 t {MRI} data," *NeuroImage*, vol. 50, no. 2, pp. 434 – 445, 2010.

[129] M. Reuter, N. J. Schmansky, H. D. Rosas, and B. Fischl, "Within-subject template estimation for unbiased longitudinal image analysis," *NeuroImage*, vol. 61, no. 4, pp. 1402 – 1418, 2012.

[130] C. Studholme, D. Hill, and D. Hawkes, "Multireso- lution voxel similarity measures for mr-pet registration," *Information Processing in Medical Imaging*, pp. 287–298, 1995.

[131] S. Thayyil, M. Chandrasekaran, A. Taylor, A. Bainbridge, E. B. Cady, W. K. K. Chong, S. Murad, R. Z. Omar, and N. J. Robertson, "Cerebral magnetic resonance biomarkers

in neonatal encephalopathy: a meta-analysis.," *Pediatrics*, vol. 125, pp. e382–95, Feb. 2010.

[132] M. Sokolska, M. Proisy, C. Uria-Avellanal, A. Bainbridge, E. Cady, D. Thomas, N. Robertson, and X. Golay, "Combined use of arterial spin labeling and mrs to determine the severity of injury in neonates with hypoxic-ischaemic encephalopathy," *Proceedings of the 22nd Annual Meeting of ISMRM*, p. 2721, 2014.

[133] J. De Vis, J. Hendrikse, E. Petersen, L. de Vries, F. van Bel, T. Alderliesten, S. Negro, F. Groenendaal, and M. Benders, "Arterial spin-labelling perfusion mri and outcome in neonates with hypoxic-ischemic encephalopathy," *European Radiology*, pp. 1–9, 2014.

[134] A. Duncan, A. Caprihan, E. Montague, J. Lowe, R. Schrader, and J. Phillips, "Regional cerebral blood flow in children from 3 to 5 months of age," *American Journal of Neuroradiology*, vol. 35, no. 3, pp. 593–598, 2014.

[135] M. Kuklisova-Murgasova, P. Aljabar, L. Srinivasan, S. J. Counsell, V. Doria, A. Serag, I. S. Gousias, J. P. Boardman, M. A. Rutherford, A. D. Edwards, J. V. Hajnal, and D. Rueckert, "A dynamic 4d probabilistic atlas of the developing brain," *NeuroImage*, vol. 54, no. 4, pp. 2750 – 2763, 2011.

[136] I. S. Gousias, A. D. Edwards, M. A. Rutherford, S. J. Counsell, J. V. Hajnal, D. Rueckert, and A. Hammers, "Magnetic resonance imaging of the newborn brain: Manual segmentation of labelled atlases in term-born and preterm infants," *NeuroImage*, vol. 62, no. 3, pp. 1499 – 1509, 2012.

[137] M. J. Cardoso, A. Melbourne, G. S. Kendall, M. Modat, N. J. Robertson, N. Marlow, and S. Ourselin, "Adapt: An adaptive preterm segmentation algorithm for neonatal brain mri," *NeuroImage*, vol. 65, no. 0, pp. 97 – 108, 2013.

[138] F. Shi, P. T. Yap, G. Wu, H. Jia, J. H. Gilmore, W. Lin, and D. Shen, "Infant brain atlases from neonates to 1- and 2-year-olds," *PLoS ONE*, vol. 6, 2011.

[139] P. Jezzard and R. S. Balaban, "Correction for geometric distortion in echo planar images from B0 field variations.," *Magnetic resonance in medicine : official journal of the Society of Magnetic Resonance in Medicine / Society of Magnetic Resonance in Medicine*, vol. 34, pp. 65–73, July 1995.

[140] C. Hutton, A. Bork, O. Josephs, R. Deichmann, J. Ashburner, and R. Turner, "Image distortion correction in fmri: A quantitative evaluation," *NeuroImage*, vol. 16, no. 1, pp. 217 – 240, 2002.

[141] M. I. Levene, A. C. Fenton, D. H. Evans, L. N. J. Archer, D. B. Shortland, and N. A. Gibson, "Severe birth asphyxia and abnormal cerebral blood-flow velocity," *Developmental Medicine and Child Neurology*, vol. 31, no. 4, pp. 427–434, 1989.

[142] J. Meek, L. Tyszczuk, C. Elwell, and J. Wyatt, "Cerebral blood flow increases over the first three days of life in extremely preterm neonates," *Archives of Disease in Childhood. Fetal and Neonatal Edition*, vol. 78, no. 1, pp. F33–F37, 1998.

[143] J. B. D. Vis, E. T. Petersen, L. S. de Vries, F. Groenendaal, K. J. Kersbergen, T. Alderliesten, J. Hendrikse, and M. J. Benders, "Regional changes in brain perfusion during brain maturation measured non-invasively with arterial spin labeling {MRI} in neonates," *European Journal of Radiology*, vol. 82, no. 3, pp. 538 – 543, 2013.

[144] Y. Shi, J.-N. Zhao, L. Liu, Z.-X. Hu, S.-F. Tang, L. Chen, and R.-B. Jin, "Changes of positron emission tomography in newborn infants at different gestational ages, and neonatal hypoxic-ischemic encephalopathy.," *Pediatric neurology*, vol. 46, pp. 116–23, Feb. 2012.

[145] P. E. Grant and D. Yu, "Acute injury to the immature brain with hypoxia with or without hypoperfusion," *Radiologic Clinics of North America*, vol. 44, no. 1, pp. 63 – 77, 2006. Neuroradiology Essentials.

[146] M. Rutherford, S. Counsell, J. Allsop, J. Boardman, O. Kapellou, D. Larkman, J. Hajnal, D. Edwards, and F. Cowan, "Diffusion-weighted magnetic resonance imaging in term perinatal brain injury: A comparison with site of lesion and time from birth," *Pediatrics*, vol. 114, no. 4, pp. 1004–1014, 2004.

[147] B. Gupta, P. Sharma, J. Bagla, M. Parakh, and J. Soni, "Renal failure in asphyxiated neonates," *Indian pediatrics*, vol. 42, no. 9, p. 928, 2005.

[148] R. S. Lanzman, H.-J. Wittsack, P. Martirosian, P. Zgoura, P. Bilk, P. Kröpil, F. Schick, A. Voiculescu, and D. Blondin, "Quantification of renal allograft perfusion using arterial spin labeling mri: initial results," *European Radiology*, vol. 20, no. 6, pp. 1485–1491, 2010.

[149] J. L. Zhang, G. Morrell, H. Rusinek, E. E. Sigmund, H. Chandarana, L. O. Lerman, P. V. Prasad, D. Niles, N. Artz, S. Fain, P.-H. Vivier, A. K. Cheung, and V. S. Lee, "New magnetic resonance imaging methods in nephrology," *Kidney International*, vol. 85, pp. 768–778, Mar. 2016.

[150] P. M. Robson, A. J. Madhuranthakam, W. Dai, I. Pedrosa, N. M. Rofsky, and D. C. Alsop, "Strategies for Reducing Respiratory Motion Artifacts in Renal Perfusion Imaging With Arterial Spin Labeling," *Magnetic resonance in medicine*, vol. 1387, pp. 1374–1387, 2009.

[151] W.-C. Wu, M.-Y. Su, C.-C. Chang, W.-Y. I. Tseng, and K.-L. Liu, "Renal perfusion 3-t mr imaging: A comparative study of arterial spin labeling and dynamic contrast-enhanced techniques," *Radiology*, vol. 261, no. 3, pp. 845–853, 2011.

[152] A. G. Gardener and S. T. Francis, "Multislice perfusion of the kidneys using parallel imaging: image acquisition and analysis strategies.," *Magnetic resonance in medicine*, vol. 63, pp. 1627–36, June 2010.

[153] A. Rutherford, *INTRODUCING ANOVA AND ANCOVA A GLM APPROACH*. SAGE Publications, 2001.

[154] Y. Chen, D. J. Wang, and J. A. Detre, "Test-retest reliability of arterial spin labeling with common labeling strategies," *Journal of Magnetic Resonance Imaging*, vol. 33, no. 4, pp. 940–949, 2011.

[155] J. W. Bartlett and C. Frost, "Reliability, repeatability and reproducibility: analysis of measurement errors in continuous variables," *Ultrasound in Obstetrics and Gynecology*, vol. 31, no. 4, pp. 466–475, 2008.

[156] M. Cutajar, D. L. Thomas, T. Banks, C. a. Clark, X. Golay, and I. Gordon, "Repeatability of renal arterial spin labelling MRI in healthy subjects.," *Magma (New York, N.Y.)*, vol. 25, pp. 145–53, Apr. 2012.